Supramolecular Polymers under the Magnifying Glass
On the interplay between structure, dynamics and function

PROEFSCHRIFT

ter verkrijging van de graad van doctor aan de Technische Universiteit Eindhoven, op gezag van de rector magnificus prof.dr.ir. F.P.T. Baaijens, voor een commissie aangewezen door het College voor Promoties, in het openbaar te verdedigen op dinsdag 30 november 2021 om 16:00 uur

door

Sandra Maria Christina Schoenmakers

geboren te Goirle

Dit proefschrift is goedgekeurd door de promotoren en de samenstelling van de promotiecommissie is als volgt:

Voorzitter: prof. dr. ir. R.A.J. Janssen
1e promotor: prof. dr. E.W. Meijer
2e promotor: prof. dr. ir. A.R.A. Palmans
Leden: prof. dr. D.J. Pochan (University of Delaware)
                prof. dr. P. Besenius (Universität Mainz)
                dr. L. Albertazzi
                prof. dr. dr. P.Y.W. Dankers
                prof. dr. R.P. Sijbesma

Table of Contents

Chapter 1

The Structure-Dynamics-Function Relationship of Supramolecular Polymers in water

Abstract: Nature makes use of non-covalent interactions to produce functional materials from small building blocks. Many synthetic water-compatible supramolecular assemblies have been created with the aim to create biomaterials that mimic the fascinating functions found in nature. Especially one-dimensional supramolecular polymers have attracted a lot of interest due to their structural similarity to natural fibrous assemblies, for example like those found in the extracellular matrix. However, creating advanced multicomponent materials is not as straightforward as mixing building blocks in solution. Instead, a bottom-up approach is required in which first a fundamental understanding of the properties of the individual components is achieved before the step is made towards functional biomaterials. The importance of the structure-function relationship is already established for supramolecular polymers, whereas the contribution of their dynamic behavior has only recently been acknowledged. In this chapter, examples of literature will be used to illustrate the current understanding of the structure of various synthetic supramolecular polymers in water and how this is influenced by chemical changes to the monomer. Additionally, the current techniques used for the characterization of the dynamics of supramolecular assemblies will be discussed in some detail.
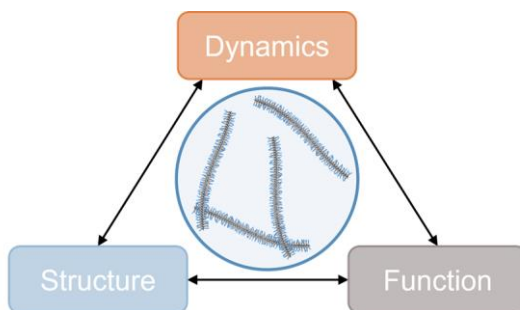
1.1 Introduction

Supramolecular polymers distinguish themselves from covalent polymers by their dynamic behavior, originating from the reversibility of the non-covalent interactions. Whereas individual non-covalent interactions are not as strong as their covalent counterparts, the combination of many weak inter- and intramolecular interactions is enough to create complex materials with properties that cannot be predicted by the simple summation of the properties of the individual building blocks. Supramolecular polymers are ubiquitous in nature and often fulfill important structural functions, such as collagen in the extracellular matrix (ECM).[1] Other examples of natural supramolecular polymers include the microtubules[2–4] and actin filaments[5,6] in the cytoskeleton which are involved in cell division and cell motility, respectively. The dynamicity of those polymers can only be achieved by the use of non-covalent interactions, underlining the importance of supramolecular chemistry in nature.

Inspired by the complex systems found in nature, scientists have started a quest to mimic the supramolecular materials in nature with synthetic ones.[7–10] Especially water-compatible supramolecular polymers assembled from small molecules have gained a lot of interest as these resemble the fibrous assemblies found in nature.[11] Although a few examples have been reported in which functional supramolecular materials are reaching the clinic, most synthetic materials still lack a lot of functionality compared to nature.[12] The reason for this is that the creation of multicomponent supramolecular materials is not as trivial as mixing all components in solution due to the intricate interplay of interactions between the different components. Instead, a bottom-up approach should be adopted in which first a fundamental understanding of the individual supramolecular assemblies is established before the number of components is increased.

The structure-function relationship in supramolecular polymers is well-studied for various supramolecular motifs. The use of non-covalent interactions makes the supramolecular polymers intrinsically dynamic. However, the dynamics of the supramolecular polymers are generally overlooked during the characterization of new materials, partly due to a lack of suitable characterization techniques. Recently, new methods have been introduced to probe the dynamic behavior of supramolecular polymers in solution. These reports emphasize the importance of studying the dynamics of supramolecular polymers next to their structure and function.

In this introductory chapter the structure and dynamics of synthetic supramolecular polymers in water will be discussed. First, general principles of supramolecular self-assembly will be introduced. Several well-studied water-compatible supramolecular polymers based on different motifs and interactions will be discussed with a focus on their supramolecular structure and how this is influenced by chemical modifications. Next, the current methods available for the characterization of the dynamics of those polymers will be compared. Finally, the aim and outline of this thesis will be presented.

1.2 Introduction to supramolecular self-assembly in water

The first man-made supramolecular polymers were created to assemble in organic solvents via hydrogen bonding, π-π stacking, electrostatic interactions or metal-ligand complexation.[13] However, water-compatibility is essential for the application of supramolecular polymers as biomaterials since nearly all biological processes take place in an aqueous environment.[8,14–16] This led to the development of new water-compatible building blocks and the redesign of existing motifs. Supramolecular polymers designed for organic solvents generally comprise a hydrophobic periphery making them insoluble in water. Several solvating moieties have therefore been added to the periphery of the building blocks, including but not limited to hydrophilic oligomers, crown ethers, carbohydrates, amino acids and charged groups.[11]

One of the main challenges in the design of water-compatible supramolecular polymers lies in the competition of water molecules with the attractive hydrogen bonds that hold many supramolecular motifs together. Additionally, solvophobic effects play a prominent role in self-assembly in water as hydrophobic solutes tend to aggregate and release their hydration water into the bulk.[17,18] This hydrophobic effect generally lacks the directionality and controllability as observed for other non-covalent interactions and it remains therefore challenging to predict its effects. Scientists have used this effect to their advantage as it can create a hydrophobic pocket that shields the vulnerable hydrogen bonds from the solvent. This requires a very careful monomer design as the hydrophobic groups should be balanced by enough hydrophilic groups to prevent the formation of ill-defined assemblies and to ensure water-compatibility.

1.2.1 The self-assembly of linear amphiphiles

One of the simplest and best understood examples of supramolecular self-assembly in water is that of linear amphiphiles or surfactants, comprising a hydrophobic chain and a hydrophilic headgroup. These molecules assemble into a range of morphologies depending on the balance between attractive hydrophobic interactions of the chain and repulsive steric or electrostatic interactions of the headgroup.[19–22] The work of Israelachvili introduced a model to predict the supramolecular structure of the aggregates depending on the structure of the amphiphile.[23] For each amphiphile, a packing parameter, P, can be defined as:

$$P = \frac{V}{a_0 l_c} \tag{1.1}$$

with V the volume of the hydrophobic chain, a_0 the optimum area of the hydrophilic headgroup and l_c the critical length of the alkyl chain. The optimum area refers to the transition region between the hydrophilic and hydrophobic parts of the molecule and is mainly determined by the nature of the headgroup. Depending on the packing parameter, the amphiphiles assemble into a micellar, cylindrical, vesicle or lamellar morphology (Figure 1).

Figure 1. Illustration of different morphologies observed for linear amphiphiles in water and their dependence on the packing parameter.[20]

For the remainder of this chapter, we will focus on one dimensional supramolecular polymers that consist of small building blocks that assemble via intermolecular interactions in one direction. Although supramolecular polymers generally consist of more complex monomers with multiple types of interactions, the theory described here also helps to understand those assemblies. The hydrophilic/hydrophobic balance is extremely delicate in aqueous self-assembly as small deviations in the size or spatial arrangement of hydrophobic and hydrophilic parts could disturb the supramolecular morphology. In general, a balance should be found between attractive and repulsive interactions such that the desired supramolecular structure is found. However, it remains one of the challenges in the field to predict supramolecular morphologies based on the chemical structure of their monomers.

1.2.2 Mechanisms of supramolecular polymerization

The length of the supramolecular polymers cannot be measured directly due to their dynamicity and is therefore defined as a virtual degree of polymerization. In general, supramolecular polymerization is promoted by an increase of concentration or a decrease in temperature.[24] An additional driving force for supramolecular polymerization in water is a change in solvent composition as some motifs cannot be directly combined with water and instead are injected into water from a concentrated solution in a good solvent.[25]

Two major supramolecular polymerization mechanisms have been described, namely isodesmic and cooperative polymerization (Figure 2).[24,26,27] During an isodesmic polymerization, the affinity of a monomer to the growing polymer chain is independent of the polymer length and the association constant, K, is identical for each step. As a consequence, high concentrations, low temperatures or high association constants are required to reach a high degree of polymerization. The isodesmic self-assembly mechanism is generally associated with disordered polymers. Cooperative

polymerizations on the other hand are defined by two phases and therefore two association constants. The initial nucleation phase is characterized by a low association constant, K_n. When a critical temperature or concentration is reached (indicated by the star in Figure 2) the elongation phase follows which is characterized by a high association constant, K_e. In contrast to isodesmic polymerizations, only two populations exist in this elongation phase: elongated supramolecular polymers and monomers. Cooperatively assembled polymers are more ordered than isodesmic ones, and the higher the order the more cooperative the polymerization mechanism becomes.
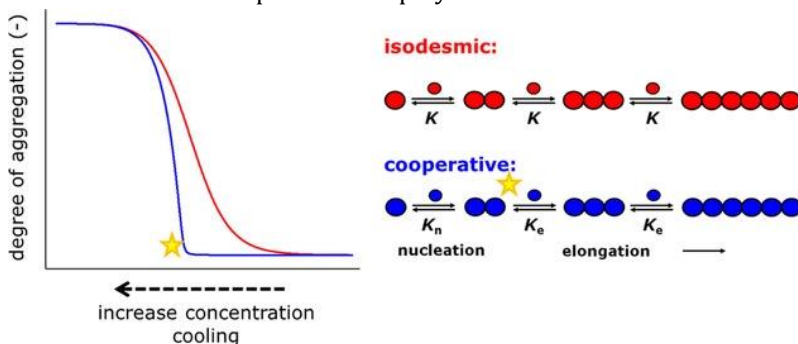
Figure 2. Schematic representation of supramolecular polymerization following an isodesmic or cooperative mechanism.[26]

1.2.3 Supramolecular copolymerization

The multivalent presentation of functional groups on supramolecular polymers is essential for their application as biomaterials. In general, only a fraction of the monomers is required to bear a functionality to prevent steric effects and solubility problems. Supramolecular copolymerization of unfunctional and functional monomers is therefore an often-used strategy to create functional materials.[28,29] A library of supramolecular materials with different degrees of functionality can relatively easily be obtained by mixing two monomers in solution in the desired ratios.[30] Additionally, supramolecular copolymers have been reported in which functional monomers that cannot polymerize on their own due to steric constraints or solubility issues are incorporated.[31,32]

Several types of supramolecular copolymers can be formed upon combination of two monomers in solution (Figure 3).[33] Self-sorting will occur in the absence of any interaction between two supramolecular polymers, for example when supramolecular polymers with a large mismatch in self-assembling motifs are combined.[34,35] This type of self-assembly could be used to create a network of fibers each with distinct properties and functions, similar to the ECM.[36] Supramolecular monomers will copolymerize when they have compatible interactions and the more alike the motifs are, the higher the tendency for copolymerization.[37] The order of molecules within the polymers will depend on the interaction strength between the two types of monomers.

In practice, the number of reports in which the order of molecules within copolymers is elucidated is still limited, partly since there is not a straightforward experimental technique to study the arrangement. Most reports therefore focus on a combination of experimental techniques and computational modelling. A few examples of water-compatible copolymers with elucidated internal structure were found in literature. Alternating copolymers can be obtained when strong complementary interactions are incorporated in the monomers such as opposite charges[38–40] or specific hydrogen bonding arrays.[41] Periodic copolymers are obtained when there are less interactions between the different monomers, for example when twisted and planar cores are mixed.[42] Block copolymers are often created via a multistep self-assembly protocol, such as the stepwise addition of monomers to an unidirectionally growing polymer.[43]
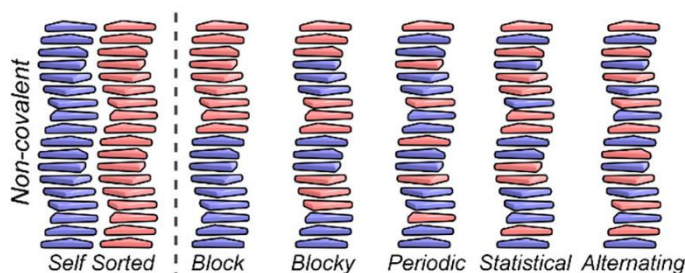
Figure 3. Schematic representation of different types of supramolecular copolymers, ordered from no interaction on the left to high degree of interaction on the right. Image is adapted from reference 33.

1.3 The impact of chemical modifications on the structure of 1D supramolecular polymers

Due to the growing interest in supramolecular polymers as multicomponent biomaterials various water-compatible motifs have been developed in recent years. Some of these motifs will be discussed here with a special focus on changes in their morphology due to chemical modification as elucidated with cryogenic transmission electron microscopy (cryoTEM). This microscopy technique has already been proven to be suitable for the structural characterization of soft matter, as illustrated for example by the group of Pochan with the visualization of block copolymer nanoparticles,[44,45] peptide assemblies[46] and copolypeptide hydrogels.[47–49] This technique permits to study the material in near-native state and is therefore very useful for the structural characterization of supramolecular polymers in aqueous solution.

1.3.1 Peptide amphiphiles

Supramolecular polymers based on peptide amphiphiles were first introduced by the group of Stupp.[50,51] These linear amphiphiles consist of a hydrophobic alkyl chain and a hydrophilic head group of a modifiable peptide sequence. These amphiphiles assemble into rod-like micelles, similar to the ones described in section 1.2.1. Although

peptide amphiphiles have been synthesized with various chemical structures, they all have in common that they consist of four domains (Figure 4A). Domain I comprises the linear alkyl chain that forms the hydrophobic interior of the polymer. The hydrophobic β-sheet forming amino acids in domain II provide structural support and removal of their hydrogen-bonding ability leads to the formation of spherical micelles through the hydrophobic effect.[52] Water-solubility is ensured by the charged amino acids in domain III. Domain IV on the surface of the supramolecular polymers is optionally used for the functionalization of the polymers. CryoTEM images confirm the formation of supramolecular polymers with a diameter of 7 nm. The large amount of natural amino acids and synthetic modifications possible makes the peptide amphiphile design extremely versatile. For example, decreasing the number of amino acids results in the association of various polymers into ribbons[53] and changing the order of amino acids changes the structure from fibers to ribbons or nanobelts depending on the formed β-sheets (Figure 4B).[54] Supramolecular polymers based on peptide amphiphiles have already been investigated as scaffolds for cartilage[55] and bone regeneration,[56] for targeted therapy for atherosclerosis[57] and for the promotion of angiogenesis.[58]
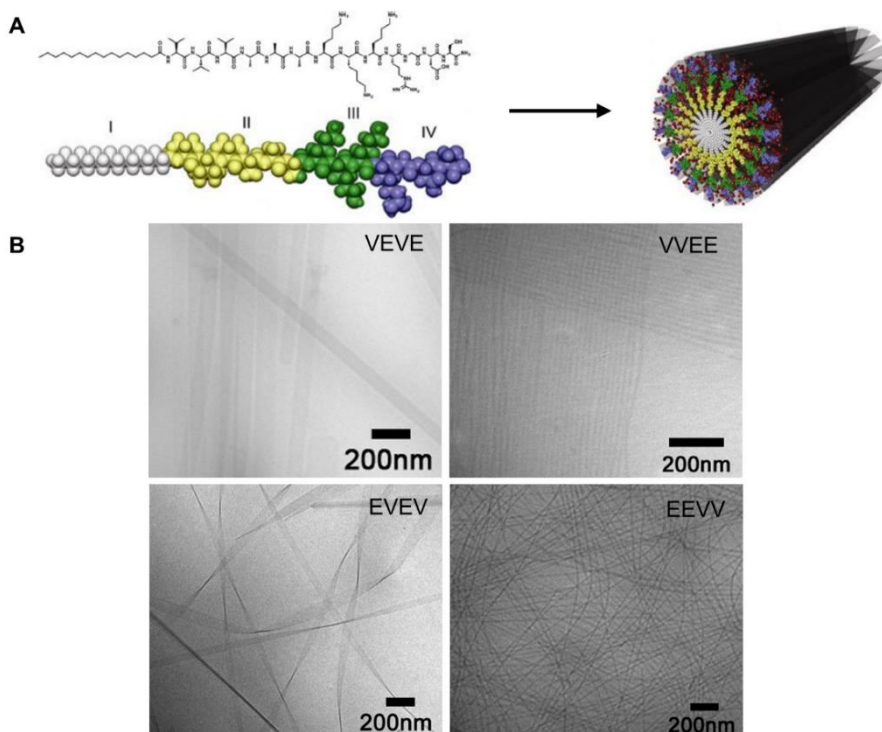
Figure 4. (A) Left: Chemical structure and space-filling model of a peptide amphiphile, highlighting the four structural domains. Right: Schematic representation of the self-assembly of a peptide amphiphile. Water molecules are represented as red spheres. Image adapted from reference 59. (B) CryoTEM images of peptide amphiphiles in water with a C_{15} chain and 4 amino acids in various order as indicated in the figure. Image is adapted from reference 54.

1.3.2 Bis-urea motifs

The urea motif combines a C=O hydrogen bond acceptor with two strong N-H hydrogen bond donors to induce stacking of molecules. When combined in a bis-urea setting, these hydrogen bonding motifs are known to create supramolecular polymers via a cooperative mechanism in organic solvents.[60,61] The group of Boutellier used bis-urea motifs to create supramolecular polymers that can assemble in a range of solvents, from water to toluene (Figure 5A).[62] The bis-urea motifs were placed in between hydrophobic alkyl chains to protect the hydrogen bonds from the water. By increasing the length of the ethylene glycol periphery from 3 to 7 units the molecules became compatible with water, while still maintaining its ability to assemble in organic solvents. The more polar the solvent, the longer and thicker the supramolecular polymers. The hydrophobic interactions in water result in the additional lateral packing of several stacks of molecules such that thicker supramolecular polymers are formed. CryoTEM images revealed the presence of 2 populations in water with varying number of molecules in the cross-section (Figure 5B).[63]
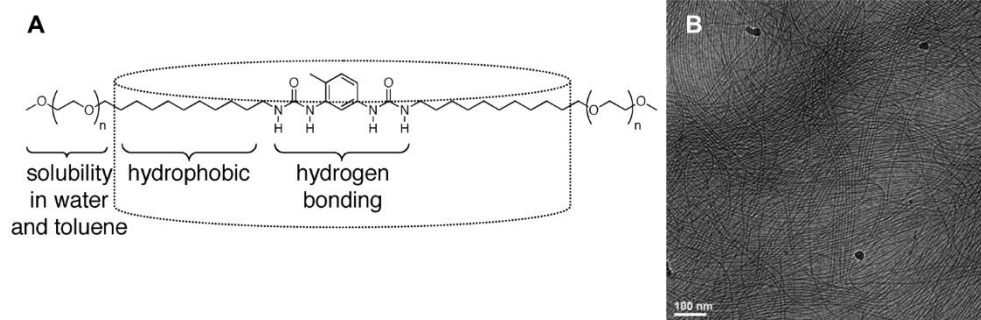
Figure 5. (A) Chemical structure of a water-compatible bis-urea based monomer (n = 3 or 7).[62] (B) CryoTEM image of supramolecular polymers based on a bis-urea motif in water.[63]

Sijbesma and co-workers created water-compatible supramolecular polymers from bola-amphiphiles with bis-urea motifs separated by linear alkyl chains.[64] Additionally, they showed with a systematic study that increasing the size of the hydrophobic pocket resulted in less bundling and that increasing the size of the hydrophilic periphery resulted in a morphological transition to spherical aggregates (Figure 6).[65] In other studies, they installed diacetylene moieties between the bis-urea groups to create supramolecular polymers of laterally associated stacks that can covalently be fixated.[66–68] The introduction of acetylene or azide groups at the end of the side chains allows for cross-linking such that strain-stiffening networks were obtained that resemble biological fibrous networks were obtained.

P8-10 OMe p_a = 8, m = 10, R = CH$_3$; **P8-6 OMe** p_a = 8, m = 6, R = CH$_3$
P8-12 OMe p_a = 8, m = 12, R = CH$_3$; **P12-10 OMe** p_a = 12, m = 10, R = CH$_3$
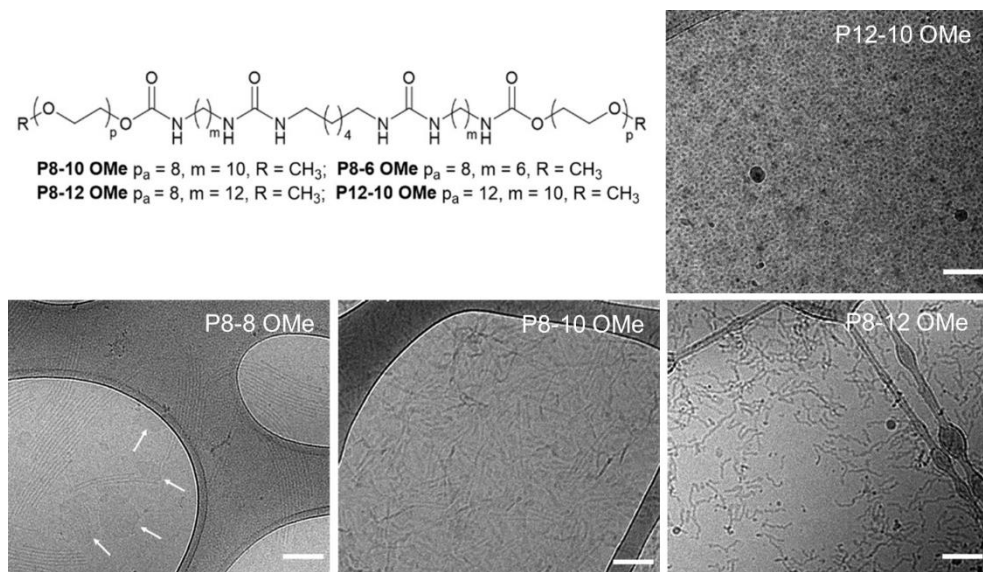
Figure 6. Chemical structure of a bis-urea based bola-amphiphile with various lengths of hydrophobic chains and polydisperse oligo(ethylene glycol). CryoTEM images show their self-assembly in water. Scale bar is 100 nm. Image is adapted from reference 65.

1.3.3 Hydrogen bonding arrays

A general approach to increase the strength and directionality of hydrogen bonds is to position them in complementary arrays. These arrays of hydrogen bond donors and acceptors require careful design as secondary repulsive interactions should be minimized to obtain the most stable self-assembled materials. Ureidopyrimidinone (UPy) motifs are such hydrogen bonded arrays which can dimerize via self-complementary quadrupole hydrogen bonding.[69] One dimensional supramolecular polymers in water were obtained by equipping both sides of linear hydrophilic polymers with UPy moieties protected from the solvent with linear alkyl chains (Figure 7A). Urea groups were introduced for additional lateral hydrogen bonds (Figure 7B-C).[70,71] Later, monomers were introduced with a UPy moiety on only one side (Figure 7A, bottom) which resulted in longer and thicker fibers due to bundling of several UPy stacks (Figure 7D).[72,73] Mixing of those moieties results in cross-linked hydrogels with tunable mechanical properties.[72] Additionally, the free end of the monovalent UPy-based monomer can be used for the attachment of functional motifs such as peptide sequences or catechols, a strategy that is often used by the group of Dankers.[74–76] Additonally, they have created UPy-based hydrogels for in vitro and in vivo studies on renal and cardiac regeneration.[77–80]
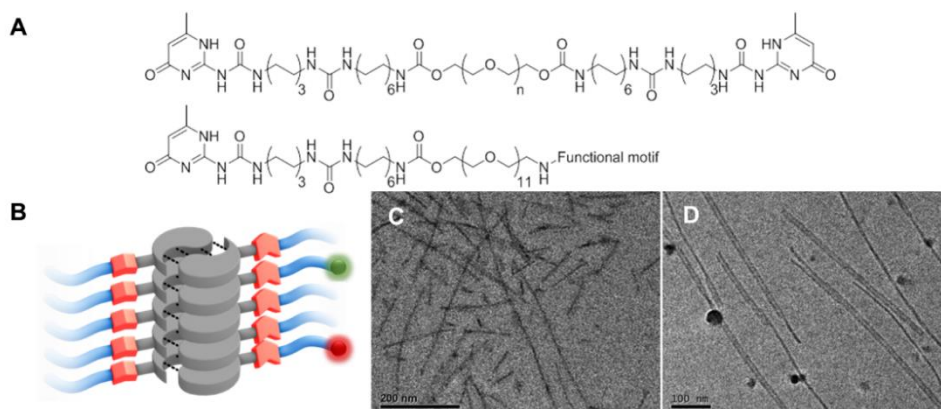
Figure 7. (A) Chemical structure of bivalent (top) and monovalent (bottom) UPy-based monomers that can self-assemble in water via dimerization and bis-urea hydrogen bonding.[12] (B) Schematic representation the stacking of UPy moieties (grey) and bis-ureas (red).[12] (C-D) CryoTEM images of (C) bivalent and (D) monovalent UPy moieties in water.[73]

1.3.4 Supramolecular discotics

Many examples exist of supramolecular polymers based on the stacking of discotic molecules with a C_3-symmetrical core surrounded by amides for intermolecular hydrogen bonding. All of these molecules have in common that they only assemble into supramolecular polymers when the cores are surrounded by a hydrophobic pocket for protection from the water and by a hydrophilic periphery for water-solubility. Several design strategies have been applied and a few of them will be discussed below.

An often-used strategy to induce supramolecular polymerization is to functionalize discotics with hydrophobic amino acids. The group of van Esch studied C_3-symmetrical 1,3,5-trihexyltricarboxamides with various amino acids and showed that supramolecular polymers were formed with phenylalanine and methionine but not with glycine or serine as these lack sufficient hydrophobic interactions.[81] These molecules stack on top of each other and bundle into supramolecular polymers with a diameter of 10-500 nm when a linear ethylene glycol periphery is added.[34,82–84] The structure of the assemblies can be controlled by the covalent attachment of a surfactant to one side chain, which results in the formation of a tape-like structure (Figure 8A, B left).[85] Thin fibers are obtained again upon addition of a linear surfactant (Figure 8B, middle), whereas small micelles were formed upon addition of a solvent that competes for hydrogen bond formation (Figure 8B, right).[86]
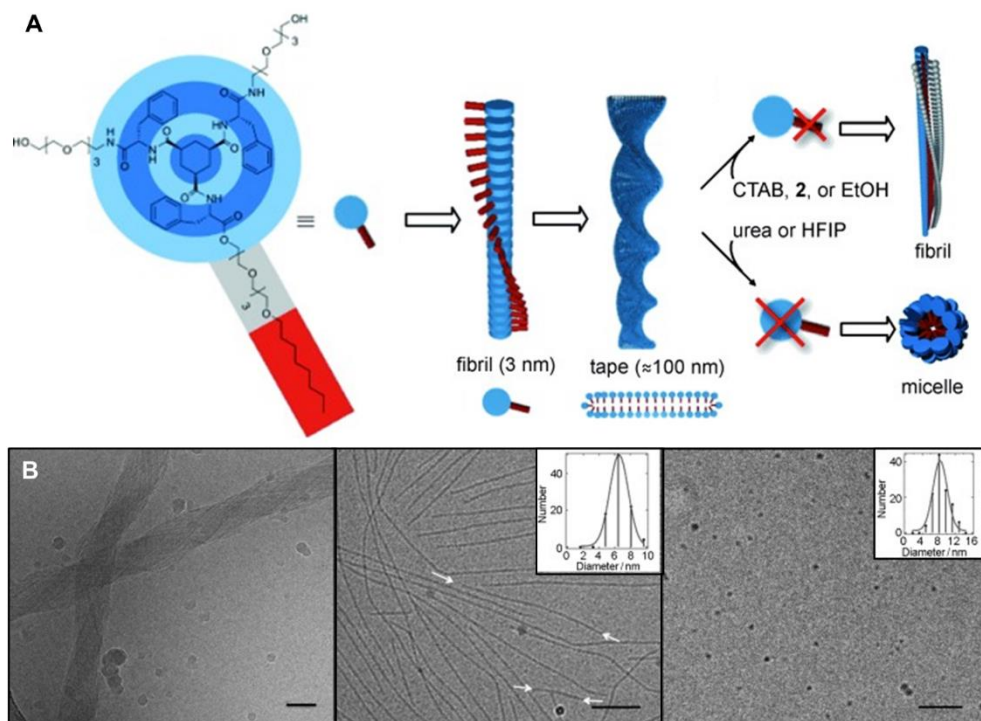
Figure 8. (A) Chemical structure of a 1,3,5-cyclohexyltricarboxamide monomer with peripheral aliphatic chain and a schematic representation of its self-assembly in water. (B) CryoTEM images of the 1,3,5-cyclohexyltricarboxamide derivative in pure water (left), in the presence of CTAB (middle) and in the presence of HFIP (right). Scale bars are 100 nm. Images are adapted from reference 86.

Besenius and co-workers introduced a short sequence of alternating hydrophobic and charged amino acids to the side chains of benzene-1,3,5-tricarboxamides (BTAs) to induce β-sheet formation. Monomers with opposite charge could copolymerize in alternating fashion at neutral pH.[39] When a branched ethylene glycol periphery was used, the monomers could homopolymerize in their uncharged form due to hydrophobic interactions between the phenylalanine (Figure 9A-B).[40] This results in a pH-dependent changes in morphology. At low pH, glutamic acid is protonated and monomer 2 assembles into micrometer long supramolecular polymers with a left-handed helicity, whereas the self-assembly of monomer 1 is prevented by electrostatic repulsion (Figure 9C, left). At neutral pH both monomers are charged and will assemble into short alternating copolymers with an average length of 56 nm and right-handed helicity (Figure 9C, middle). At high pH lysine is deprotonated and monomer 1 assembles into short polydisperse supramolecular polymers while monomer 2 suffers from electrostatic repulsions (Figure 9C, right). Additionally, the group reported several examples of frustrated self-assembly in which they controlled the length of BTA-

based supramolecular polymers by balancing the attractive supramolecular interactions with repulsive electrostatic interactions.[87–90]
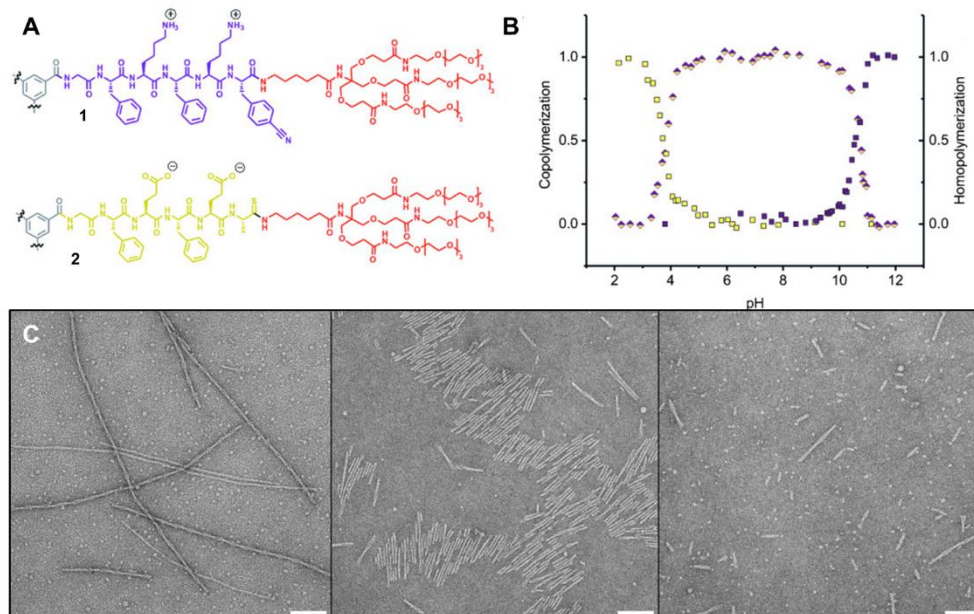
Figure 9. (A) Chemical structure of BTAs with oppositely charged amino acids. (B) Normalized CD spectra for the individual BTA polymers and their 1:1 mixture. The colors correspond to the monomers in A. (C) TEM images of the the 1:1 mixture of 1 and 2 at different pH values. Left: pH 2.0 with homopolymer 2 and monomer 1; Middle: pH 7.4 with the alternating copolymer of 1 and 2; Right: pH 11.0 with homopolymer 1 and monomer 2. Scale bar is 100 nm.[40]

The group of Brendel created supramolecular polymer bottlebrushes from 1,3,5-substituted benzene trisureas (BTUs) with one long poly(ethylene glycol) (PEG) chain and two short hydrophobic chains (Figure 10A).[91] The trisurea groups drive the self-assemble of BTUs with dodecyl chains and 2k PEG towards cylindrical structures with a length of several hundreds of nanometers (Figure 10B, middle). The cross-section of these assemblies corresponds to four BTU moieties. A transition to tightly packed spherical assemblies was observed when the length of the PEG chains was increased, since the amphiphilic character of the molecule becomes stronger than its hydrogen-bonding ability (Figure 10B, left). When the number of PEG chains was increased the lateral interactions were hampered due to steric effects. This also limits the number of directional hydrogen bonds and therefore results in spherical assemblies with two BTU molecules in the cross-section (Figure 10B, right). When the BTU core was replaced with a BTA core the hydrogen bonds were not strong enough to drive self-assembly and the molecules self-assemble based on their packing parameter instead, which mainly results in spherical structures.[92]
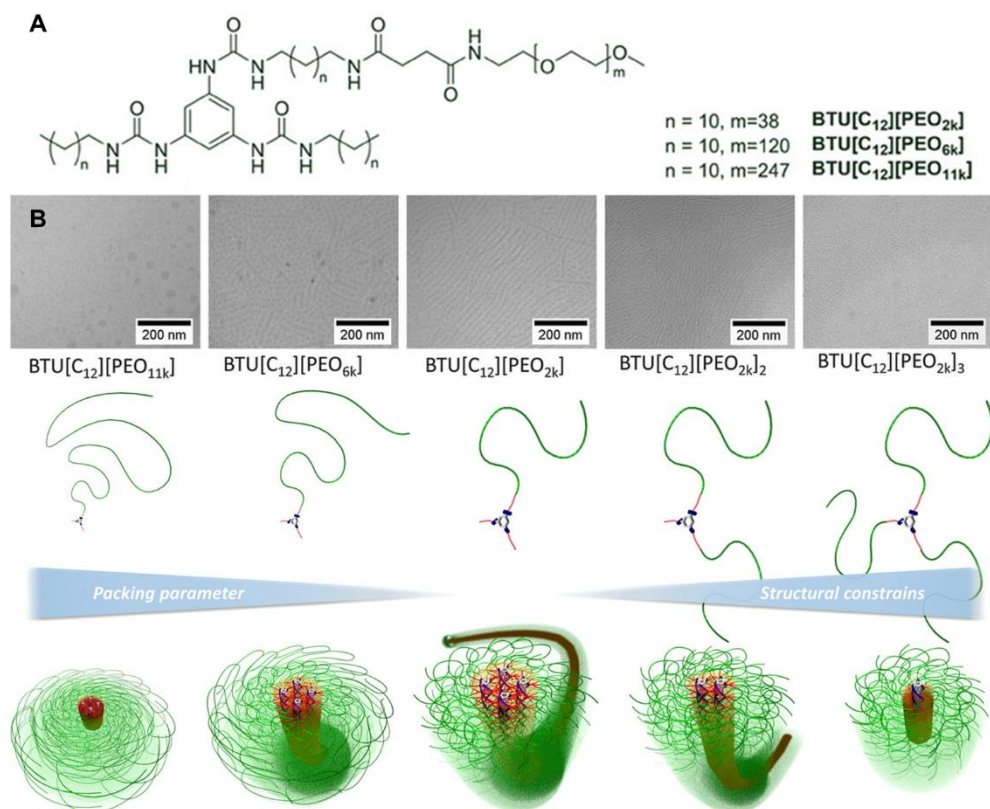
Figure 10. (A) Chemical structure of a BTU molecule with various lengths of ethylene glycol chains. (B) CryoTEM images and a schematic representation of supramolecular polymer bottlebrushes formed with BTU molecules with increasing PEG lengths and with an increasing number of PEG chains. Images are adapted from reference 91.

Finally, our group observed micrometer long supramolecular polymers with a radius of 3.3 nm when BTAs were decorated with a dodecyl chain for the creation of a hydrophobic pocket around the hydrogen-bonding amides and with tetra(ethylene glycol) as a water-compatible periphery (Figure 11A-B).[93,94] Supramolecular polymers of similar dimensions were observed for BTAs with a undecyl or tridecyl chain, but short stacks, referred to as BTA micelles (Figure 11C), were observed for BTAs with an decyl chain due to insufficient hydrophobic protection of the intermolecular hydrogen bonds.[95,96] Similarly, supramolecular polymerization was prevented when the size of the hydrophilic periphery was increased by replacing the linear ethylene glycol with a dendritic one.[31] These examples illustrate the delicate balance between hydrophobic and hydrophilic interactions that determine the ability of the monomer to polymerize in water. A large part of this thesis will focus on these water-compatible BTAs and their properties will be elucidated in more detail in the following chapters.
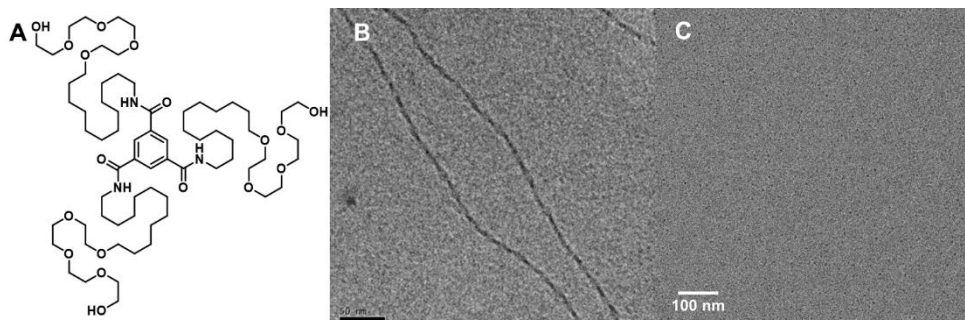
Figure 11. (A) Chemical structure of a water-compatible BTA with dodecyl and tetra(ethylene glycol) side chains. (B) CryoTEM image of a BTA-based supramolecular polymer in water. Scale bar is 50 nm.[93] (C) Representative cryoTEM image of micelles formed by BTAs in water.

1.4 Characterization of the dynamics of supramolecular polymers

A plethora of techniques are available to study the static structure of supramolecular polymers in solution, including light or X-ray scattering, fluorescent microscopy and cryoTEM. In contrast, the added value of characterizing the dynamics of supramolecular systems was only recently realized and the understanding of supramolecular dynamics and the number of experimental techniques available to study this property is therefore still lagging behind. Three types of dynamics can be distinguished in supramolecular polymers in water: conformation dynamics, hydration water dynamics and molecular exchange dynamics.[97] In this section, several techniques used for the characterization of these different types of dynamics will be discussed.

1.4.1 Electron paramagnetic resonance

Conformation dynamics, that is the time-dependent fluctuation of molecular conformation, can be measured with electron paramagnetic resonance (EPR) spectroscopy and site-directed spin labeling. EPR spectroscopy is widely used in biochemistry[98–101] and has recently been adapted to be used in synthetic supramolecular chemistry.[102–105] This technique measures the rotational diffusion rate (typically in the range from megahertz to gigahertz) of radical nitroxyl spin labels in an applied magnetic field and can thereby provide information on local conformational dynamics within a supramolecular polymer on a nanometer length scale.[106] This technique requires the spin labeling of a fraction of the monomers within the polymer.

Ortony *et al.* introduced (2,2-6,6-tetramethylpiperidin-1-yl)oxyl (TEMPO) spin labels at specific positions along the axis of a peptide amphiphile to reveal heterogeneity in the conformational dynamics through the cross-section of the self-assembled polymer.[107] The spin labels at the core and surface of the polymers showed the fastest, most liquid-like dynamics, whereas the spin labels in the β-sheet region showed the slowest, most solid-like dynamics due to the hydrogen bonding of the amino acids (Figure 12A). Copolymerization with a peptide amphiphile that has one of its

amino acids methylated resulted in weaker β-sheets and therefore a more liquid-like interior of the polymers (Figure 12B).
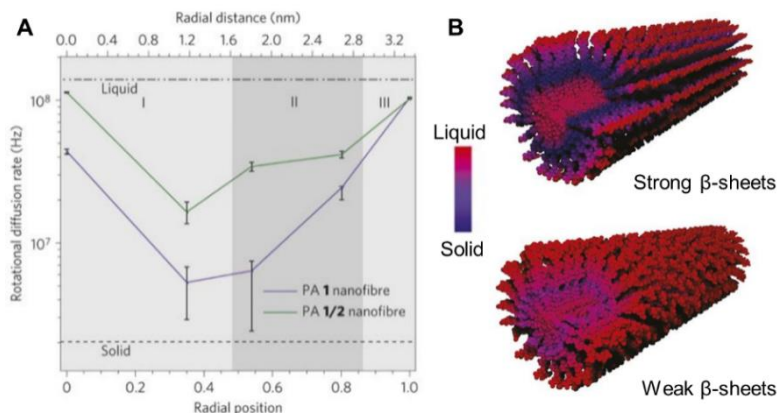
Figure 12. (A) Rotation diffusion rates extracted from EPR measurements of peptide amphiphile polymers with 0.4% of the monomers labeled with spin labels at different radial positions. The aliphatic core domain (I), β-sheet forming domain (II) and charged corona (III) are indicated. The purple line corresponds to a peptide amphiphile polymer with strong β-sheets and the green line corresponds to a peptide amphiphile copolymer with weak β-sheets. (B) Schematic representation of peptide amphiphiles with strong and weak β-sheets. The vertical bar indicates the gradient of solid- to liquid-like dynamics. Image is adapted from reference 107.

1.4.2 Overhauser dynamic nuclear polarization relaxometry

Overhauser dynamic nuclear polymerization (ODNP) relaxometry[108] has been used to quantify the diffusion of water molecules around biomolecules.[109–111] Water molecules around biological supramolecular structures greatly influence their function and structure and similar effects are expected for synthetic supramolecular materials. ODNP combines EPR and NMR to capture the translational diffusion rate of water molecules within a nanometer distance from a spin label. ODNP can provide information on water dynamics on very small length scales, but similar to EPR it requires the introduction of spin labels.

ODNP has been used to study the water dynamics through the cross-section of the same peptide amphiphile polymer as used for EPR measurements in the previous section.[112] The measured water correlation times reveal that water is moving fast in the aliphatic core and slow at the surface of the polymer (Figure 13). It seems that water molecules become trapped in the highly hydrophilic and charged corona of the polymer, which is likely to influence the ligand-receptor binding affinities when functionalized monomers are incorporated. Additionally, it was shown that the surface water dynamics significantly decrease upon cross-linking the polymer with Ca^{2+}.
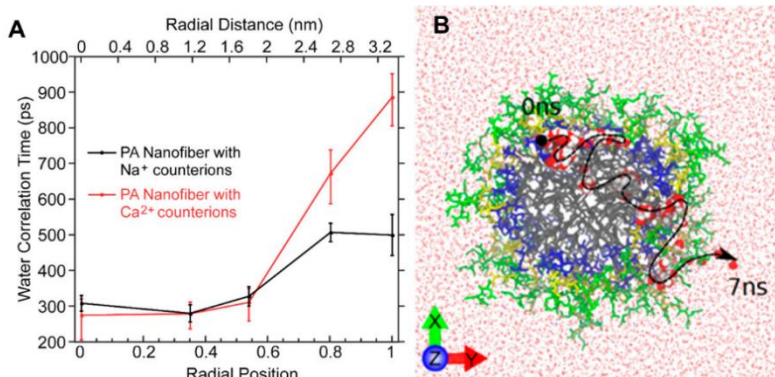
Figure 13. (A) Water correlation times measured with ODNP for peptide amphiphile polymers with less than 0.1% of the monomers labelled with spin labels at different radial positions. Either Na^+ or Ca^{2+} counterions were added resulting in the formation of single and bundled fibers, respectively. (B) Molecular dynamics simulation to illustrate the diffusion of a water molecule (red with white) across the polymer in 7 ns of simulation. Image is adapted from reference 112.

1.4.3 Stochastic optical reconstruction microscopy

The following techniques will all focus on the characterization of molecular exchange dynamics, that is the physical movement of monomers between supramolecular polymers. Stochastic optical reconstruction microscopy (STORM) is a super-resolution optical microscopy technique that can achieve resolutions below the diffraction limit by subsequently activating and deactivating different fluorophores and by overlaying their localizations.[113–115] STORM can be used to visualize the exchange of dye-labeled monomers between polymers. To this end, separate solutions of supramolecular polymers with 2-5% of different fluorescent dyes have to be prepared, which are then mixed and visualized with STORM (Figure 14A). Repetitive imaging of polymers absorb on a glass surface can provide information on the time needed for complete exchange as well as spatial information about the positions of monomer exchange along the polymer.

The exchange of monomers between Cy3- and Cy5-labeled BTA supramolecular polymers was followed with STORM by Albertazzi *et al.*[116] Already after 1 hour some Cy5-labeled BTAs could be observed within Cy3-labeled polymers and vice versa, but 24 hours were required for full exchange (Figure 14B). These experiments revealed that BTA-based supramolecular polymers exchange monomers homogeneously over their length. Homogeneous exchange was also observed for UPy-based supramolecular polymers. Monomer exchange of bivalent UPy motifs occurs within minutes, but barely any exchange was observed after 20 hours for monovalent UPy motifs.[73] In contrast, a heterogeneous exchange of monomers along a polymer was observed for peptide amphiphiles, with regions that barely showed monomer exchange over the course of 48 hours.[117] Additionally, STORM was used to show that supramolecular polymers based

on self-assembling peptides only grown on their ends.[118] Whereas STORM can provide an indication of the timescale needed for complete exchange, it cannot be used to accurately quantify the rate of exchange due to its low time resolution (around 10 min). Additionally, it only provides information on the fraction of the monomers that is covalently labelled with a dye.
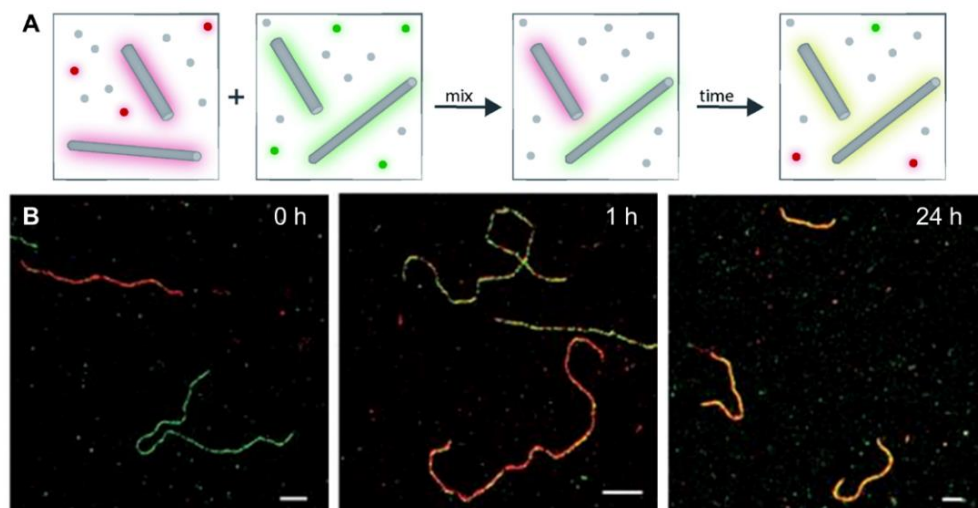
Figure 14. (A) Schematic representation of a STORM and FRET experiment.[119] (B) Merged STORM images of Cy3- (green) and Cy5-labeled (red) polymers (5% labeling) at different time points after equimolar mixing. The scale bars are 1 μm. Image is adapted from reference 116.

1.4.4 Förster resonance energy transfer

Quantitative information on the rate of monomer exchange can be obtained with Förster resonance energy transfer (FRET). This technique is often used in biochemistry and relies on the transfer of energy from a donor to and acceptor fluorophore, which can be a chemical dye or fluorescent protein.[120,121] The efficiency of the energy transfer depends on the spectral overlap between the donor and acceptor, their distance and their orientation with respect to each other.[122] When the donor is excited in the absence of an acceptor it will emit photons of its own characteristic wavelength. However, when an acceptor is in close proximity it will be excited by the photons of the donor and will emit photons with a different wavelength. FRET can be used to study the dynamics of supramolecular polymers after mixing of two solutions with donor or acceptor fluorophore (Figure 14A). As monomers exchange between polymers the fluorophores come in close proximity, resulting in excitation of the acceptor due to photon transfer. The FRET ratio, that is the ratio between acceptor and donor emission, upon donor emission can be measured with fluorescent spectroscopy to obtain the rate of exchange.

FRET experiments with Cy3- and Cy5-labeled BTAs revealed a complete exchange of monomers within an hour.[123] The introduction of chirality into the side chains

significantly slowed down the exchange of monomers.[94] The decrease of a dodecyl to undecyl chain did not have any effect on the rate of exchange, whereas a further decrease to decyl chain leads to irreproducible FRET ratios as ill-defined micelles are formed instead of stable polymers (Figure 15).[95] FRET is a solution-based technique, in contrast to STORM, and could therefore be used to study environmental conditions. Changes in concentration did not have an effect on the exchange dynamics, but the monomer exchange was found to be complete within an hour upon increase of temperature.[123] Additionally, FRET experiments confirmed the clustering of monomers upon addition of an RNA recruiter[124] as well as the reversibility of clustering after the binding of single stranded DNA.[123] FRET experiments with Cy-labeled bivalent UPy monomers revealed a complete monomer exchange within minutes, which could be slowed down by the incorporation of monovalent UPy monomers.[73]
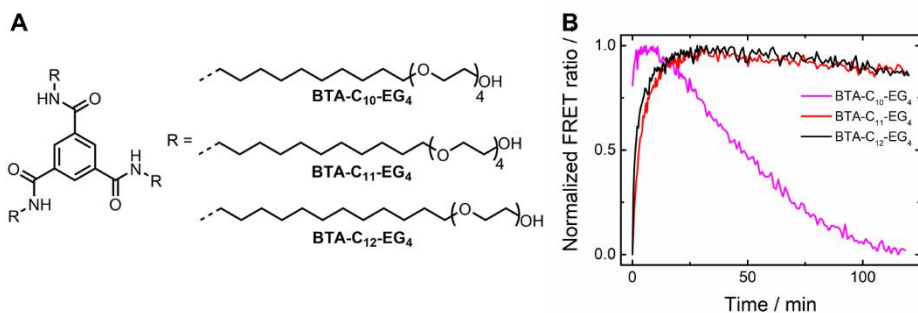
Figure 15. (A) Chemical structure of water-compatible BTAs with varying hydrophobic chain length. BTA-C_{11}-EG_4 and BTA-C_{12}-EG_4 assemble into supramolecular polymers, but BTA-C_{10}-EG_4 assembles into ill-defined micelles. (B) FRET ratio upon mixing of Cy3- and Cy5-labeled BTAs with different hydrophobic chain length. Image is adapted from reference 95.

1.4.5 Hydrogen/deuterium exchange followed by mass spectrometry

The previously described techniques all rely on the covalent attachment of bulky molecular probes to study the exchange of only a fraction of the molecules. In contrast, hydrogen/deuterium exchange (HDX) followed by mass spectrometry (MS) can be used for the characterization of the monomer exchange of all monomers between supramolecular polymers with only minimal perturbation of the chemical structure. This technique is inspired by biochemistry as it is often used for the characterization of the structure and dynamics of proteins.[125–130] Upon dilution of a protein into D_2O the labile amide hydrogen atoms in the backbone exchange for deuterium atoms, which results in a mass increase that is detectable with MS. Hydrogen atoms on the outside of the protein are easily accessible for the solvent and undergo immediate H/D exchange. However, the exchange of hydrogen atoms that are contained in the hydrophobic interior of the protein or that are hydrogen bonded can only undergo H/D exchange when part of the protein is unfolded, thereby providing a method for the

characterization of protein folding and dynamics. HDX-MS was, for example, used to understand the assembly of amyloid fibrils.[131–133]

HDX-MS was first introduced in synthetic supramolecular chemistry to study the movement of crown ethers over dendrimers.[134–136] Our group used the technique to study the monomer exchange between BTA-based supramolecular polymers.[96] Upon dilution of these polymers from water into D_2O two isotope distribution can be observed in the MS spectra. The hydroxyl hydrogen atoms immediately exchange as they are on the outside of the polymer and in direct contact with the solvent, resulting in a BTA with 3 deuterium atoms (Figure 16A). The amide hydrogen atoms are responsible for hydrogen bonding and are inside the hydrophobic pocket, hence they are protected from immediate exchange. When monomers move between polymers, the amide hydrogen atoms come in contact with the solvent and will exchange for deuterium atoms, resulting in a BTA with 6 deuterium atoms. The percentage of BTAs with only the hydroxyl hydrogen atoms was calculated from the MS spectra at different timepoints to reveal an exchange profile described by several rate constants (Figure 16B). It was thereby revealed that the BTA polymers contain regions that undergo fast and regions that undergo slow monomer exchange. Such a heterogeneity in the monomer exchange rate was also observed bis-urea bolaamphiphiles.[65] Additionally, it was revealed for BTAs that the monomer exchange slows down upon increasing the hydrophobic chain length (Figure 16B),[96] an effect that was previously overlooked with FRET as this technique only studies a subset of monomers (Figure 15B). The absence of supramolecular polymers, as is the case for a BTA with decyl hydrophobic chain results in an immediate exchange of all labile hydrogen atoms. Additionally, HDX-MS is uniquely suited to study the effect of copolymerization as the exchange of all types of monomers within the copolymer can be studied separately. In case of the BTAs, it was revealed that supramolecular polymers can be either stabilized[31] or destabilized[32] upon copolymerization with micellar BTAs.
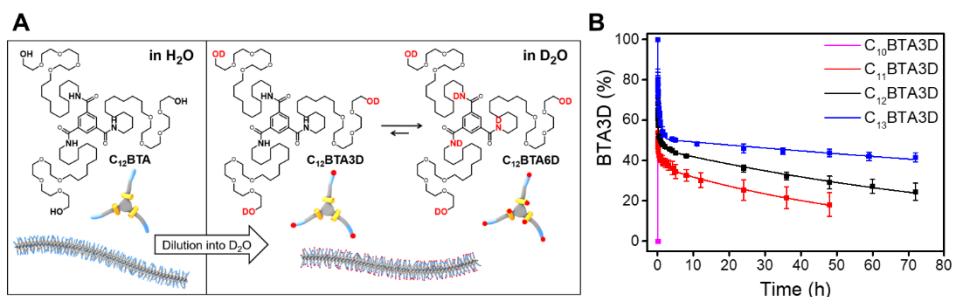
Figure 16. (A) Schematic representation of an HDX-MS experiment of BTA-based supramolecular polymers. The polymers are diluted from H_2O into D_2O and the exchange of labile hydrogen atoms is subsequently followed by MS. Exchangeable hydrogen atoms are indicated in red. (B) The percentage of different BTA molecules with only their hydroxyl hydrogen atoms exchanged for deuterium as a function of time.[96]

1.5 Aim and outline of this thesis

In the previous sections several water-compatible supramolecular polymers were presented which have the potential to be used as functional biomaterials. The structure-function relationship of these materials has already been studied and the impact of chemical modifications on the supramolecular structure has been described in detail. However, studies on the molecular exchange dynamics of supramolecular polymers have only been reported sporadically and they are usually disconnected from studies on the structure and function. However, these three properties are at constant interplay and changing one of them will influence the others. A proper understanding of the structure-dynamics-function relationship of supramolecular polymers would therefore benefit their future application in biomedical settings but is unfortunately still missing. In this thesis the structure and dynamics of several supramolecular polymers will therefore be studied in detail with the aim to ultimately gain a better understanding of the structure-dynamics-function relationship (Figure 17).
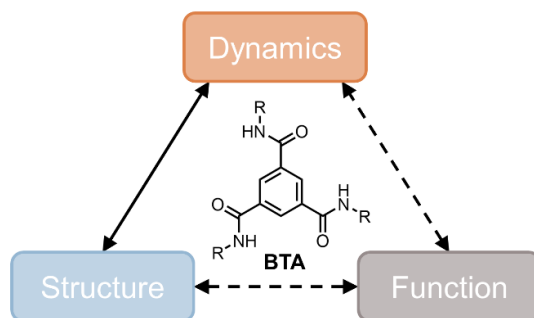
Figure 17. Schematic illustration of the structure-dynamics-function relationship of supramolecular polymers. This thesis will focus on the structure-dynamics relation for BTAs.

In the first part of this thesis relevant techniques for the characterization of structure and dynamics will be discussed and they will be applied in the characterization of several supramolecular building blocks. These techniques will then be applied in the second part to study supramolecular assemblies based on water-compatible benzene-1,3,5-tricarboxamides (BTAs) with small variations in their chemical structure with the aim to establish a structure-dynamics relationship for those assemblies. In the final part of this thesis we will work with functionalized supramolecular polymers for biomedical applications based on BTAs to make the first steps towards understanding the structure-dynamics-function relationship.

In **Chapter 2**, the application of cryogenic transmission electron microscopy (cryoTEM) for the visualization of supramolecular assemblies in their near-native hydrated state is illustrated. We use the technique to confirm the self-assembly of new supramolecular motifs. In addition, the structure of BTA-based polymers is studied in detail with a single particle analysis method and it is shown that these polymers consist of two stacks that rotate around each other as a double helix.

Chapter 3 describes the application of hydrogen/deuterium exchange followed by mass spectrometry (HDX-MS) to characterize the molecular exchange dynamics of supramolecular polymers with only a minimal perturbation of their chemical structure. This technique is used to compare the dynamics of supramolecular polymers based on different motifs and different self-assembly mechanisms. Characterization of the dynamics is possible as long as exchangeable hydrogen atoms are sufficiently protected from the solvent and the monomer concentration is sufficiently high to ensure the presence of supramolecular polymers during dilution.

The techniques described in previous chapters are used in **Chapter 4** to study the effect of chirality on the structure and dynamics of BTA-based polymers. The introduction of deuterium atoms as stereogenic centers results in an increase in order over time which is accompanied by a tightening of the double helix structure and a decrease of exchange dynamics. The use of methyl groups as stereogenic centers changes the packing of the molecules such that they assemble into a single stack with a different mechanism of monomer exchange. Additionally, this BTA with additional methyl groups can be used to invers the helicity of the stacks in a double helix structure.

Chapter 5 explores the potential use of saccharides as a water-compatible and potentially functional periphery for BTAs. The attachment of monosaccharides to the hydrophobic chains leads to the formation of bundled supramolecular polymers due to saccharide-saccharide interactions. However, attachment of saccharides to the tetra(ethylene glycol) chains disrupts the hydrophilic/hydrophobic balance and results in the formation of small micelles. These monomers could still be included into supramolecular polymers via copolymerization

In **Chapter 6** a novel synthetic pathway towards monofunctionalized BTAs is presented, starting from a desymmetrized core. This inevitably leads to the inversion of one of the amide bonds, which results in a slight decrease in solubility when these motifs are homopolymerized. Solubility problems are overcome upon copolymerization and the successful incorporation of functional monomers into BTA polymers without altering the structure and dynamics is confirmed.

Chapter 7 describes various interactions between BTAs and charged surfactants. First, it will be shown that uncharged BTA polymers are disrupted by charged surfactants, but polymers are reobtained by dilution. Secondly, it will be shown that surfactants are required to promote the elongation of C_3-symmetrical charged BTAs. Finally, one of the side chains of the charged BTAs is replaced by a hydrophobic chain, such that the molecule can assemble either as a surfactant or as a BTA. Interesting morphological transitions are obtained based on the addition of salt or a surfactant.

Finally, in **Chapter 8** the first steps towards using BTAs in functional biomaterials are discussed. The covalent attachment of dyes and polymers decreases the length of polymers and increases their monomer exchange. In addition, the effect of small molecules, proteins and complex media on the structure will be covered, as well their application in responsive hydrogels.

1.6 References

1   J. K. Mouw, G. Ou and V. M. Weaver, *Nat. Rev. Mol. Cell Biol.*, 2014, **15**, 771–785.
2   R. D. Vale, *Cell*, 2003, **112**, 467–480.
3   D. Sept, *Curr. Biol.*, 2007, **17**, 764–766.
4   S. Forth and T. M. Kapoor, *J. Cell Biol.*, 2017, **216**, 1525–1531.
5   F. Van den Ent, L. A. Amos and J. Löwe, *Nature*, 2001, **413**, 39–44.
6   T. D. Pollard and J. A. Cooper, *Science*, 2009, **326**, 1208–1212.
7   T. Aida, E. W. Meijer and S. I. Stupp, *Science*, 2012, **335**, 813–817.
8   J. Boekhoven and S. I. Stupp, *Adv. Mater.*, 2014, **26**, 1642–1659.
9   S. I. Stupp, *Nano Lett.*, 2010, **10**, 4783–4786.
10   T. D. Clemons and S. I. Stupp, *Prog. Polym. Sci.*, 2020, **111**, 101310.
11   E. Krieg, M. M. C. Bastings, P. Besenius and B. Rybtchinski, *Chem. Rev.*, 2016, **116**, 2414–2477.
12   O. J. G. M. Goor, S. I. S. Hendrikse, P. Y. W. Dankers and E. W. Meijer, *Chem. Soc. Rev.*, 2017, **46**, 6621–6637.
13   L. Brunsveld, B. J. B. Folmer, E. W. Meijer and R. P. Sijbesma, *Chem. Rev.*, 2001, **101**, 4071–4098.
14   E. A. Appel, J. del Barrio, X. J. Loh and O. A. Scherman, *Chem. Soc. Rev.*, 2012, **41**, 6195–6214.
15   R. Dong, Y. Zhou, X. Huang, X. Zhu, Y. Lu and J. Shen, *Adv. Mater.*, 2015, **27**, 498–526.
16   A. Noro, M. Hayashi and Y. Matsushita, *Soft Matter*, 2012, **8**, 6416–6429.
17   D. Chandler, *Nature*, 2005, **437**, 640–647.
18   N. T. Southall, K. A. Dill and A. D. J. Haymet, *J. Phys. Chem. B*, 2002, **106**, 521–533.
19   B. Parshad, S. Prasad, S. Bhatia, A. Mittal, Y. Pan, P. K. Mishra, S. K. Sharma and L. Fruk, *RSC Adv.*, 2020, **10**, 42098–42115.
20   B. N. S. Thota, L. H. Urner and R. Haag, *Chem. Rev.*, 2016, **116**, 2079–2102.
21   D. Lombardo, M. A. Kiselev, S. Magazù and P. Calandra, *Adv. Condens. Matter Phys.*, 2015, **2015**, 1–22.
22   J. P. Hill, L. K. Shrestha, S. Ishihara, Q. Ji and K. Ariga, *Molecules*, 2014, **19**, 8589–8609.
23   J. N. Israelachvili, D. J. Mitchell and B. W. Ninham, *J. Chem. Soc. Faraday Trans. 2 Mol. Chem. Phys.*, 1976, **72**, 1525–1568.
24   T. F. A. De Greef, M. M. J. Smulders, M. Wolffs, A. P. H. J. Schenning, R. P. Sijbesma and E. W. Meijer, *Chem. Rev.*, 2009, **109**, 5687–5754.
25   R. P. M. Lafleur, X. Lou, G. M. Pavan, A. R. A. Palmans and E. W. Meijer, *Chem. Sci.*, 2018, **9**, 6199–6209.
26   T. Aida and E. W. Meijer, *Isr. J. Chem.*, 2020, **60**, 33–47.
27   M. M. J. Smulders, M. M. L. Nieuwenhuizen, T. F. A. De Greef, P. Van Der Schoot, A. P. H. J. Schenning and E. W. Meijer, *Chem. - A Eur. J.*, 2010, **16**, 362–367.
28   K. Petkau-Milroy, M. H. Sonntag, A. H. A. M. Van Onzen and L. Brunsveld, *J. Am. Chem. Soc.*, 2012, **134**, 8086–8089.
29   P. Y. W. Dankers, M. C. Harmsen, L. A. Brouwer, M. J. A. Van Luyn and E. W. Meijer, *Nat. Mater.*, 2005, **4**, 568–574.
30   P. Besenius, *J. Polym. Sci. Part A Polym. Chem.*, 2017, **55**, 34–78.
31   B. N. S. Thota, X. Lou, D. Bochicchio, T. F. E. Paffen, R. P. M. Lafleur, J. L. J. van Dongen, S. Ehrmann, R. Haag, G. M. Pavan, A. R. A. Palmans and E. W. Meijer, *Angew. Chemie - Int. Ed.*, 2018, **57**, 6843–6847.
32   S. I. S. Hendrikse, L. Su, T. P. Hogervorst, R. P. M. Lafleur, X. Lou, G. A. van der Marel, J. D. C. Codee and E. W. Meijer, *J. Am. Chem. Soc.*, 2019, **141**, 13877–13886.
33   B. Adelizzi, N. J. Van Zee, L. N. J. De Windt, A. R. A. Palmans and E. W. Meijer, *J. Am. Chem. Soc.*, 2019, **141**, 6110–6121.
34   A. Heeres, C. Van Der Pol, M. Stuart, A. Friggeri, B. L. Feringa and J. Van Esch, *J. Am. Chem. Soc.*, 2003, **125**, 14252–14253.
35   A. Pal, S. Karthikeyan and R. P. Sijbesma, *J. Am. Chem. Soc.*, 2010, **132**, 7842–7843.
36   S. Onogi, H. Shigemitsu, T. Yoshii, T. Tanida, M. Ikeda, R. Kubota and I. Hamachi, *Nat. Chem.*, 2016, **8**, 743–752.
37   R. P. M. Lafleur, S. M. C. Schoenmakers, P. Madhikar, D. Bochicchio, B. Baumeier, A. R. A. Palmans, G. M. Pavan and E. W. Meijer, *Macromolecules*, 2019, **52**, 3049–3055.
38   P. Ahlers, H. Frisch and P. Besenius, *Polym. Chem.*, 2015, **6**, 7245–7250.
39   H. Frisch, J. P. Unsleber, D. Lüdeker, M. Peterlechner, G. Brunklaus, M. Waller and P. Besenius, *Angew. Chemie - Int. Ed.*, 2013, **52**, 10097–10101.
40   H. Frisch, Y. Nie, S. Raunser and P. Besenius, *Chem. - A Eur. J.*, 2015, **21**, 3304–3309.

41   B. J. Cafferty, I. Gállego, M. C. Chen, K. I. Farley, R. Eritja and N. V. Hud, *J. Am. Chem. Soc.*, 2013, **135**, 2447–2450.
42   D. Görl, X. Zhang, V. Stepanenko and F. Würthner, *Nat. Commun.*, 2015, **6**, 7009.
43   W. Zhang, W. Jin, T. Fukushima, A. Saeki, S. Seki and T. Aida, *Science*, 2011, **334**, 340–343.
44   J. Zhu, S. Zhang, K. Zhang, X. Wang, J. W. Mays, K. L. Wooley and D. J. Pochan, *Nat. Commun.*, 2013, **4**, 2297.
45   H. Cui, Z. Chen, S. Zhong, K. L. Wooley and D. J. Pochan, *Science*, 2007, **317**, 647–650.
46   Y. Tian, F. B. Polzer, H. V. Zhang, K. L. Kiick, J. G. Saven and D. J. Pochan, *Biomacromolecules*, 2018, **19**, 4286–4298.
47   B. Ozbas, J. Kretsinger, K. Rajagopal, J. P. Schneider and D. J. Pochan, *Macromolecules*, 2004, **37**, 7331–7337.
48   M. S. Lamm, K. Rajagopal, J. P. Schneider and D. J. Pochan, *J. Am. Chem. Soc.*, 2005, **127**, 16692–16700.
49   R. A. Hule, R. P. Nagarkar, B. Hammouda, J. P. Schneider and D. J. Pochan, *Macromolecules*, 2009, **42**, 7137–7145.
50   J. D. Hartgerink, E. Beniash and S. I. Stupp, *Science*, 2001, **294**, 1684–1688.
51   J. D. Hartgerink, E. Beniash and S. I. Stupp, *Proc. Natl. Acad. Sci.*, 2002, **99**, 5133–5138.
52   S. E. Paramonov, H. Jun and J. D. Hartgerink, *J. Am. Chem. Soc.*, 2006, **128**, 7291–7298.
53   T. J. Moyer, H. Cui and S. I. Stupp, *J. Phys. Chem. B*, 2013, **117**, 4604–4610.
54   H. Cui, A. G. Cheetham, E. T. Pashuck and S. I. Stupp, *J. Am. Chem. Soc.*, 2014, **136**, 12461–12468.
55   R. N. Shah, N. A. Shah, M. M. D. R. Lim, C. Hsieh, G. Nuber and S. I. Stupp, *Proc. Natl. Acad. Sci.*, 2010, **107**, 3293–3298.
56   A. Mata, Y. Geng, K. J. Henrikson, C. Aparicio, S. R. Stock, R. L. Satcher and S. I. Stupp, *Biomaterials*, 2010, **31**, 6004–6012.
57   N. A. Mansukhani, E. B. Peters, M. M. So, M. S. Albaghdadi, Z. Wang, M. R. Karver, T. D. Clemons, J. P. Laux, N. D. Tsihlis, S. I. Stupp and M. R. Kibbe, *Macromol. Biosci.*, 2019, **19**, 1900066.
58   R. Mammadov, B. Mammadov, S. Toksoz, B. Aydin, R. Yagci, A. B. Tekinay and M. O. Guler, *Biomacromolecules*, 2011, **12**, 3508–3519.
59   J. B. Matson, R. H. Zha and S. I. Stupp, *Curr. Opin. Solid State Mater. Sci.*, 2011, **15**, 225–235.
60   B. Isare, S. Pensec, M. Raynal and L. Bouteiller, *Comptes Rendus Chim.*, 2016, **19**, 148–156.
61   V. Simic, L. Bouteiller and M. Jalabert, *J. Am. Chem. Soc.*, 2003, **125**, 13148–13154.
62   E. Obert, M. Bellot, L. Bouteiller, F. Andrioletti, C. Lehen-Ferrenbach and F. Boué, *J. Am. Chem. Soc.*, 2007, **129**, 15601–15605.
63   M. Tharcis, T. Breiner, J. Belleney, F. Boué and L. Bouteiller, *Polym. Chem.*, 2012, **3**, 3093–3099.
64   N. Chebotareva, P. H. H. Bomans, P. M. Frederik, N. A. J. M. Sommerdijk and R. P. Sijbesma, *Chem. Commun.*, 2005, 4967.
65   J. Liu, M. J. G. Schotman, M. M. R. M. Hendrix, X. Lou, P. P. Marín San Román, I. K. Voets and R. P. Sijbesma, *J. Polym. Sci.*, 2021, **59**, 1162–1170.
66   M. Fernandez-Castano Romera, R. P. M. Lafleur, C. Guibert, I. K. Voets, C. Storm and R. P. Sijbesma, *Angew. Chemie - Int. Ed.*, 2017, **56**, 8771–8775.
67   M. Fernández-Castaño Romera, X. Lou, J. Schill, G. Ter Huurne, P. P. K. H. Fransen, I. K. Voets, C. Storm and R. P. Sijbesma, *J. Am. Chem. Soc.*, 2018, **140**, 17547–17555.
68   M. Fernández-Castano Romera, R. Göstl, H. Shaikh, G. Ter Huurne, J. Schill, I. K. Voets, C. Storm and R. P. Sijbesma, *J. Am. Chem. Soc.*, 2019, **141**, 1989–1997.
69   R. P. Sijbesma, F. H. Beijer, L. Brunsveld, B. J. B. Folmer, J. H. K. K. Hirschberg, R. F. Lange, J. K. L. Lowe and E. W. Meijer, *Science*, 1997, **278**, 1601–1604.
70   P. Y. W. Dankers, T. M. Hermans, T. W. Baughman, Y. Kamikawa, R. E. Kieltyka, M. M. C. Bastings, H. M. Janssen, N. A. J. M. Sommerdijk, A. Larsen, M. J. A. Van Luyn, A. W. Bosman, E. R. Popa, G. Fytas and E. W. Meijer, *Adv. Mater.*, 2012, **24**, 2703–2709.
71   A. C. H. Pape, M. M. C. Bastings, R. E. Kieltyka, H. M. Wyss, I. K. Voets, E. W. Meijer and P. Y. W. Dankers, *Int. J. Mol. Sci.*, 2014, **15**, 1096–1111.
72   R. E. Kieltyka, A. C. H. Pape, L. Albertazzi, Y. Nakano, M. M. C. Bastings, I. K. Voets, P. Y. W. Dankers and E. W. Meijer, *J. Am. Chem. Soc.*, 2013, **135**, 11159–11164.
73   S. I. S. Hendrikse, S. P. W. Wijnands, R. P. M. Lafleur, M. J. Pouderoijen, H. M. Janssen, P. Y. W. Dankers and E. W. Meijer, *Chem. Commun.*, 2017, **53**, 2279–2282.
74   M. Diba, S. Spaans, S. I. S. Hendrikse, M. M. C. Bastings, M. J. G. Schotman, J. F. van Sprang, D. J. Wu, F. J. M. Hoeben, H. M. Janssen and P. Y. W. Dankers, *Adv. Mater.*, 2021, 2008111.
75   I. De Feijter, O. J. G. M. Goor, S. I. S. Hendrikse, M. Comellas-Aragonès, S. H. M. Söntjens, S. Zaccaria,

P. P. K. H. Fransen, J. W. Peeters, L. G. Milroy and P. Y. W. Dankers, *Synlett*, 2015, **26**, 2707–2713.

76   R. C. van Gaal, B. D. Ippel, S. Spaans, M. I. Komil and P. Y. W. Dankers, *J. Polym. Sci.*, 2021, **59**, 1253–1266.

77   M. M. C. Bastings, S. Koudstaal, R. E. Kieltyka, Y. Nakano, A. C. H. Pape, D. A. M. Feyen, F. J. van Slochteren, P. A. Doevendans, J. P. G. Sluijter, E. W. Meijer, S. A. J. Chamuleau and P. Y. W. Dankers, *Adv. Healthc. Mater.*, 2014, **3**, 70–78.

78   M. J. G. Schotman, M. M. C. Peters, G. C. Krijger, I. van Adrichem, R. de Roos, J. L. M. Bemelmans, M. J. Pouderoijen, M. G. T. A. Rutten, K. Neef, S. A. J. Chamuleau and P. Y. W. Dankers, *Adv. Healthc. Mater.*, 2021, **10**, 2061987.

79   D. E. P. Muylaert, G. C. van Almen, H. Talacua, J. O. Fledderus, J. Kluin, S. I. S. Hendrikse, J. L. J. van Dongen, E. Sijbesma, A. W. Bosman, T. Mes, S. H. Thakkar, A. I. P. M. Smits, C. V. C. Bouten, P. Y. W. Dankers and M. C. Verhaar, *Biomaterials*, 2016, **76**, 187–195.

80   M. Dong, M. G. Wessels, J. Y. Lee, L. Su, H. Wang, R. A. Letteri, Y. Song, Y. N. Lin, Y. Chen, R. Li, D. J. Pochan, A. Jayaraman and K. L. Wooley, *ACS Nano*, 2019, **13**, 5147–5162.

81   K. J. C. Van Bommel, C. Van Der Pol, I. Muizebelt, A. Friggeri, A. Heeres, A. Meetsma, B. L. Feringa and J. Van Esch, *Angew. Chemie - Int. Ed.*, 2004, **43**, 1663–1667.

82   A. M. Brizard, M. C. A. Stuart and J. H. Van Esch, *Faraday Discuss.*, 2009, **143**, 345–357.

83   J. Boekhoven, A. M. Brizard, M. C. A. Stuart, L. Florusse, G. Raffy, A. Del Guerzo and J. H. Van Esch, *Chem. Sci.*, 2016, **7**, 6021–6031.

84   A. Brizard, M. Stuart, K. Van Bommel, A. Friggeri, M. De Jong and J. Van Esch, *Angew. Chemie - Int. Ed.*, 2008, **47**, 2063–2066.

85   J. Boekhoven, P. Van Rijn, A. M. Brizard, M. C. A. Stuart and J. H. Van Esch, *Chem. Commun.*, 2010, **46**, 3490–3492.

86   J. Boekhoven, A. M. Brizard, P. Van Rijn, M. C. A. Stuart, R. Eelkema and J. H. Van Esch, *Angew. Chemie - Int. Ed.*, 2011, **50**, 12285–12289.

87   M. Von Gröning, I. De Feijter, M. C. A. Stuart, I. K. Voets and P. Besenius, *J. Mater. Chem. B*, 2013, **1**, 2008–2012.

88   P. Besenius, G. Portale, P. H. H. Bomans, H. M. Janssen, A. R. A. Palmans and E. W. Meijer, *Proc. Natl. Acad. Sci.*, 2010, **107**, 17888–17893.

89   R. Appel, S. Tacke, J. Klingauf and P. Besenius, *Org. Biomol. Chem.*, 2015, **13**, 1030–1039.

90   P. Ahlers, H. Frisch, D. Spitzer, Z. Vobecka, F. Vilela and P. Besenius, *Chem. - An Asian J.*, 2014, **9**, 2052–2057.

91   F. V. Gruschwitz, M. C. Fu, T. Klein, R. Takahashi, T. Higashihara, S. Hoeppener, I. Nischang, K. Sakurai and J. C. Brendel, *Macromolecules*, 2020, **53**, 7552–7560.

92   T. Klein, F. V. Gruschwitz, S. Rogers, S. Hoeppener, I. Nischang and J. C. Brendel, *J. Colloid Interface Sci.*, 2019, **557**, 488–497.

93   C. M. A. Leenders, L. Albertazzi, T. Mes, M. M. E. Koenigs, A. R. A. Palmans and E. W. Meijer, *Chem. Commun.*, 2013, **49**, 1963–1965.

94   M. B. Baker, L. Albertazzi, I. K. Voets, C. M. A. Leenders, A. R. A. Palmans, G. M. Pavan and E. W. Meijer, *Nat. Commun.*, 2015, **6**, 6234.

95   C. M. A. Leenders, M. B. Baker, I. A. B. Pijpers, R. P. M. Lafleur, L. Albertazzi, A. R. A. Palmans and E. W. Meijer, *Soft Matter*, 2016, **12**, 2887–2893.

96   X. Lou, R. P. M. Lafleur, C. M. A. Leenders, S. M. C. Schoenmakers, N. M. Matsumoto, M. B. Baker, J. L. J. van Dongen, A. R. A. Palmans and E. W. Meijer, *Nat. Commun.*, 2017, **8**, 15420.

97   Y. Cho, T. Christoff-Tempesta, S. J. Kaser and J. H. Ortony, *Soft Matter*, 2021, **17**, 5850–5863.

98   C. B. Karim, T. L. Kirby, Z. Zhang, Y. Nesmelov and D. D. Thomas, *Proc. Natl. Acad. Sci.*, 2004, **101**, 14437–14442.

99   I. D. Sahu, R. M. McCarrick and G. A. Lorigan, *Biochemistry*, 2013, **52**, 5967–5984.

100   Y. Sato, H. Hayashi, M. Okazaki, M. Aso, S. Karasawa, S. Ueki, H. Suemune and N. Koga, *Magn. Reson. Chem.*, 2008, **46**, 1055–1058.

101   N. A. Eschmann, T. D. Do, N. E. LaPointe, J. E. Shea, S. C. Feinstein, M. T. Bowers and S. Han, *J. Phys. Chem. B*, 2015, **119**, 14421–14432.

102   N. S. Schauser, D. J. Grzetic, T. Tabassum, G. A. Kliegle, M. L. Le, E. M. Susca, S. Antoine, T. J. Keller, K. T. Delaney, S. Han, R. Seshadri, G. H. Fredrickson and R. A. Segalman, *J. Am. Chem. Soc.*, 2020, **142**, 7055–7065.

103   F. Liu, H. Karoui, A. Rockenbauer, S. Liu, O. Ouari and D. Bardelang, *Molecules*, 2020, **25**, 776

104   A. Carageorgheopol, W. Edwards, J. G. Hardy, D. K. Smith and V. Chechik, *Langmuir*, 2014, **30**, 9210–9218.

105   R. Öztürk, S. Güner, B. Aktaş and A. Gül, *Supramol. Chem.*, 2005, **17**, 233–241.

106   M. M. Roessler and E. Salvadori, *Chem. Soc. Rev.*, 2018, **47**, 2534–2553.

107   J. H. Ortony, C. J. Newcomb, J. B. Matson, L. C. Palmer, P. E. Doan, B. M. Hoffman and S. I. Stupp, *Nat. Mater.*, 2014, **13**, 812–816.

108   J. R. Biller, R. Barnes and S. Han, *Curr. Opin. Colloid Interface Sci.*, 2018, **33**, 72–85.

109   J. M. Franck, Y. Ding, K. Stone, P. Z. Qin and S. Han, *J. Am. Chem. Soc.*, 2015, **137**, 12013–12023.

110   R. Barnes, S. Sun, Y. Fichou, F. W. Dahlquist, M. Heyden and S. Han, *J. Am. Chem. Soc.*, 2017, **139**, 17890–17901.

111   J. Song, B. Allison and S. Han, *MRS Bull.*, 2014, **39**, 1082–1088.

112   J. H. Ortony, B. Qiao, C. J. Newcomb, T. J. Keller, L. C. Palmer, E. Deiss-Yehiely, M. Olvera De La Cruz, S. Han and S. I. Stupp, *J. Am. Chem. Soc.*, 2017, **139**, 8915–8921.

113   B. Huang, M. Bates and X. Zhuang, *Annu. Rev. Biochem.*, 2009, **78**, 993–1016.

114   M. J. Rust, M. Bates and X. Zhuang, *Nat. Methods*, 2006, **3**, 793–795.

115   M. Bates, B. Huang, G. T. Dempsey and X. Zhuang, *Science*, 2007, **317**, 1749–1753.

116   L. Albertazzi, D. van der Zwaag, C. M. A. Leenders, R. Fitzner, R. W. van der Hofstad and E. W. Meijer, *Science*, 2014, **344**, 491–495.

117   R. M. P. da Silva, D. van der Zwaag, L. Albertazzi, S. S. Lee, E. W. Meijer and S. I. Stupp, *Nat. Commun.*, 2016, **7**, 11561.

118   L. H. Beun, L. Albertazzi, D. Van Der Zwaag, R. De Vries and M. A. Cohen Stuart, *ACS Nano*, 2016, **10**, 4973–4980.

119   S. Pujals, K. Tao, A. Terradellas, E. Gazit and L. Albertazzi, *Chem. Commun.*, 2017, **53**, 7294–7297.

120   M. Dimura, T. O. Peulen, C. A. Hanke, A. Prakash, H. Gohlke and C. A. Seidel, *Curr. Opin. Struct. Biol.*, 2016, **40**, 163–185.

121   K. Petkau-Milroy, D. A. Uhlenheuer, A. J. H. Spiering, J. A. J. M. Vekemans and L. Brunsveld, *Chem. Sci.*, 2013, **4**, 2886.

122   L. Wu, C. Huang, B. P. Emery, A. C. Sedgwick, S. D. Bull, X. P. He, H. Tian, J. Yoon, J. L. Sessler and T. D. James, *Chem. Soc. Rev.*, 2020, **49**, 5110–5139.

123   L. Albertazzi, F. J. Martinez-Veracoechea, C. M. A. Leenders, I. K. Voets, D. Frenkel and E. W. Meijer, *Proc. Natl. Acad. Sci.*, 2013, **110**, 12203–12208.

124   L. Albertazzi, N. van der Veeken, M. B. Baker, A. R. A. Palmans and E. W. Meijer, *Chem. Commun.*, 2015, **51**, 16166–16168.

125   T. E. Wales and J. R. Engen, *Mass Spectrom. Rev.*, 2006, **25**, 158–170.

126   L. Konermann, J. Pan and Y.-H. Liu, *Chem. Soc. Rev.*, 2011, **40**, 1224–1234.

127   S. W. Englander, *Annu. Rev. Biophys. Biomol. Struct.*, 2000, **29**, 213–238.

128   D. L. Smith, Y. Deng and Z. Zhang, *J. mass Spectrom.*, 1997, **32**, 135–146.

129   Y.-H. Liu, A. Belcheva, L. Konermann and D. Golemi-Kotra, *J. Mol. Biol.*, 2009, **391**, 149–163.

130   A. N. Hoofnagle, K. A. Resing and N. G. Ahn, *Annu. Rev. Biophys. Biomol. Struct.*, 2003, **32**, 1–25.

131   I. Kheterpal, S. Zhou, K. D. Cook and R. Wetzel, *Proc. Natl. Acad. Sci. U. S. A.*, 2000, **97**, 13597–13601.

132   N. Carulla, G. L. Caddy, D. R. Hall, J. Zurdo, M. Gairí, M. Feliz, E. Giralt, C. V. Robinson and C. M. Dobson, *Nature*, 2005, **436**, 554–558.

133   N. Carulla, M. Zhou, M. Arimon, M. Gairi, E. Giralt, C. V. Robinson and C. M. Dobson, *Proc. Natl. Acad. Sci.*, 2009, **106**, 7828–7833.

134   Z. Qi, C. Schlaich and C. A. Schalley, *Chem. - A Eur. J.*, 2013, **19**, 14867–14875.

135   L. Cera and C. A. Schalley, *Chem. Soc. Rev.*, 2014, **43**, 1800.

136   H. D. F. Winkler, E. V. Dzyuba and C. A. Schalley, *New J. Chem.*, 2011, **35**, 529.

Chapter 2

Cryogenic Transmission Electron Microscopy as a Versatile Tool for the Structural Characterization of Supramolecular Assemblies

Abstract: The structure and function of supramolecular materials are closely related. Detailed characterization of the structure of such assemblies is therefore important for their application as new biomaterials. Most microscopy techniques require the introduction of dyes or the drying of the specimen on a surface, but most self-assembled structures are only stable in their native solution conditions. Cryogenic transmission electron microscopy (cryoTEM) allows the direct visualization of supramolecular assemblies in their hydrated state trough a thin layer of vitrified solvent. In this chapter, the cryoTEM technique will be introduced and its application in the structural characterization of various aqueous supramolecular systems will be illustrated. CryoTEM is used to visualize the micellization of various polyurethane ionomers and to study the morphology of hydrogen-bonded supramolecular assemblies based on new motifs. Finally, an in-depth analysis of the structure of supramolecular polymers based on benzene-1,3,5-tricarboxamides (BTAs) will be presented. It was previously believed that those molecules assemble into a single stack, but image reconstruction based on single particle analysis methods reveals the presence of a double helix structure. Several BTAs were analyzed with this method to illustrate that this secondary structure is very delicate and small deviations in the chemical structure result in a different morphology.

2.1 Introduction

The function of natural supramolecular assemblies is largely determined by their structure. Fibers provide support for cells, vesicles transport cargo and bilayers are used to separate the cell interior from the outside. A similar structure-function relationship is observed for synthetic supramolecular assemblies: polymers have been used as support during cell growth,[1] stimuli-responsive vesicles have been designed for targeted drug delivery[2] and tubular structure have been used for the transport of ions across a membrane.[3] A direct and high resolution method for the characterization of these nanoscale structures is essential for their applications as synthetic biomaterials.

Most supramolecular assemblies are only stable in their native solvated conditions, requiring an imaging technique that applies only minimal perturbations. Fluorescent microscopy is a versatile technique but with a resolution limit around 200 nm and it requires the introduction of bulky fluorescent dyes that could interfere with the supramolecular structure.[4] Even super-resolution techniques, such as stochastic optical reconstruction microscopy (STORM) with a resolution limit around 20 nm,[4,5] do not have sufficient resolution to elucidate some of the nanometer-sized features of supramolecular assemblies. Atomic resolutions can be obtained with atomic force microscopy (AFM) but this generally requires the specimen to be adhered to a surface and to be in direct contact with the cantilever, both of which could distort the soft nature of many supramolecular assemblies.[6] Samples can be imaged on a nanometer scale with transmission electron microscopy (TEM) in a dried state on a surface. Although drying effects can be minimalized by a negative stain based on heavy metals, the native state of the sample cannot always be preserved and information about the internal structure is lost.[7] These drying problems are overcome with cryogenic transmission electron microscopy (cryoTEM) for which samples are vitrified into a thin film before imaging. CryoTEM has already been used to elucidate the structure of various biological macromolecules.[8] Recent advances in image analysis even allow for single-particle cryoTEM at an atomic resolution by the imaging of many identical copies of biological macromolecules and their subsequent combination during analysis.[9]

In this chapter, the application of cryoTEM for the structural characterization of synthetic supramolecular assemblies will be discussed. In the first part, some important aspects of the technique and the interpretation of the images will be described. Next, several examples will be presented in which cryoTEM was used for the visualization of supramolecular assemblies. This involves the characterization of polyurethane ionomers and several new supramolecular motifs from our group that assemble via hydrogen bonding. Whereas image capturing is enough to prove the self-assembly of those materials, sometimes more detailed image analysis is required to extract information about the self-assembly on the nanoscale. In the final part, image reconstruction will be used to elucidate the presence of a double helix in supramolecular assemblies that were previously believed to consist of single stacks.

2.2 Experimental aspects and analysis of cryoTEM

CryoTEM differs from conventional TEM in that the sample is thermally fixated into a thin film without additional staining and is handled under cryogenic conditions. This has the advantage that the sample can be studied in its hydrate state and it is less susceptible to beam damage.[7] A typical cryoTEM experiment is depicted in Figure 1. A successful experiment relies on careful grid preparation, on an understanding of the mechanism of contrast generation and on the recognition of artefacts during image analysis.[7,10–17] All of these aspects will be discussed in this section.
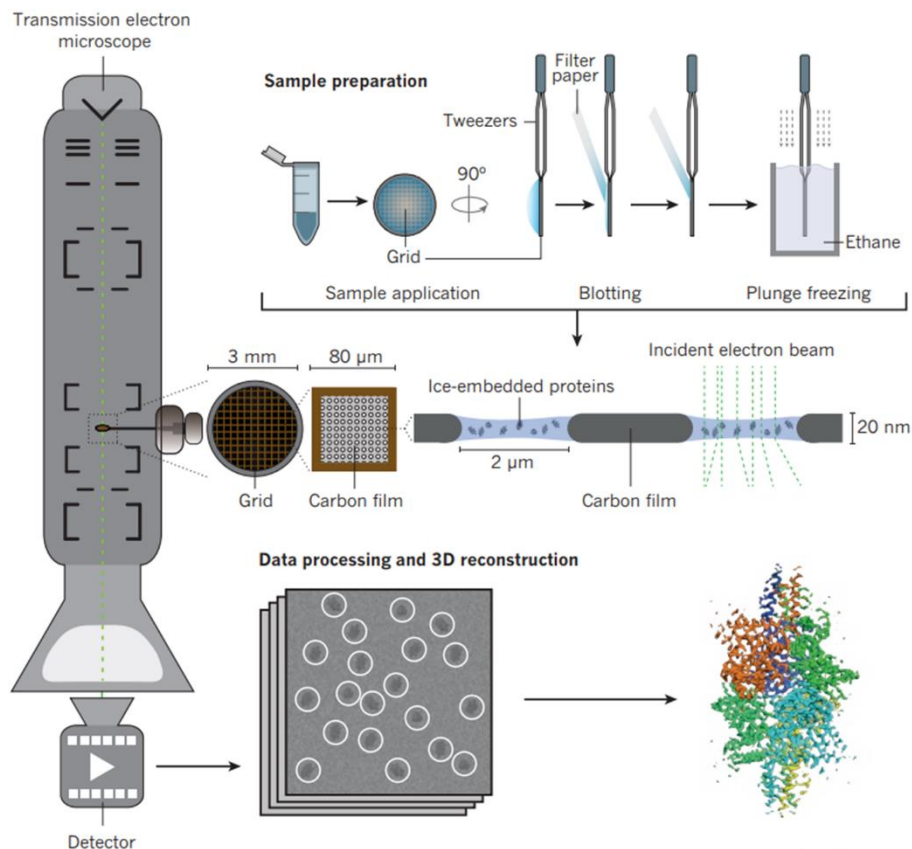
Figure 1. Schematic representation of a typical cryoTEM experiment, including grid preparation, data acquisition and single-particle analysis of a protein. Image is adapted from reference 8.

Grid preparation starts with the application of a sample on a copper mesh grid covered in a holey carbon support film. Wettability of the support film is improved by oxygen-plasma treatment prior to the application of the sample such that the sample spreads across the holes of the film.[18] Typically, a few microliters of a sample is applied to form a thin film that supports the specimen. The concentration of the sample should

be sufficiently high to see enough material after blotting but it should not be too high as viscous samples are more resistant to blotting, resulting in thick films that are not transparent for electrons. Excess fluid is blotted away with solvent-absorbent filter paper for several seconds to yield a film of less than 300 nm in thickness. A few seconds of wait time between blotting and vitrification can prevent alignment of the sample due to sheer stress caused by the flow of excess fluid to the blotting paper. Sample application and blotting occurs under controlled temperature, humidity and solvent composition to prevent water evaporation. Immediately after blotting the grid is plunged into a cryogen such that the solvent vitrifies into an amorphous state that is transparent for electrons. An extremely fast cooling rate is required to avoid freezing of the solvent as this would induce crystallization. Vitrification with liquid nitrogen is prone to the Leiden frost effect, which results in the formation of a film of vapor around the sample that decreases the rate of heat transfer and promotes undesired freezing. Liquid ethane just above its melting temperature is therefore the most used cryogen for aqueous samples due to its rapid cooling rate (about 10^5 K/s), whereas liquid nitrogen is the cryogen of choice for organic solvents due to the solubility of ethane in those solvents.[11] Vitrified grids are stored below -140 °C in liquid nitrogen until imaging to prevent recrystallization of the amorphous film.

Grids are imaged in the high vacuum of a cooled transmission electron microscope under liquid nitrogen conditions. Traces of solid ethane will sublime due to this high vacuum and are therefore not observed as artefacts. A correctly prepared grid should have a thin enough vitrified film such that electrons are transmitted through the sample. The contrast in cryoTEM images arises from both mass-thickness contrast and phase-contrast. Mass-thickness contrast originates from a decrease of the intensity of transmitted electrons due to their scattering after interaction with the sample. Larger, heavier atoms, thicker samples or the denser packing of hydrophobic moieties contribute to this type of contrast. However, organic supramolecular structures mainly consist of low molecular weight atoms such as C, H, N or O, which provide only minimal contrast compared to the solvent. The imaging of those samples therefore relies on phase contrast which originates from interference of transmitted electrons and scattered electrons after interaction with the sample. A phase shift of the scattered electrons can be induced by under-focusing the objective lens such that phase contrast is enhanced.[14] However, increased contrast due to defocusing comes at the expense of a reduced spatial resolution. The need for defocusing is overcome by the introduction of the Volta phase plate which provides an additional phase shift to the central electron beam to increase the phase contrast.[19]

Even in case of a careful grid preparation some artefacts can occur which can be misleading during image interpretation and the most common ones will be discussed here. Hexagonal ice is formed when the cooling rate during vitrification is too low and cubic ice is the result of devitrification during sample transfer, both of which could obscure the analysis of the particles of interest. Atmospheric water vapor deposited on

the grid during preparation or transfer to the microscope results in the formation of hexagonal or spherical ice crystals on top of the vitreous ice. Especially the electron-dense spherical ice particles can easily be mistaken for nanoparticles from the sample but due to their position on top of the vitreous film instead of inside they are more out of focus than the sample, resulting in white contours. The vitrified film has a slightly biconcave surface when it spans the holes as the film thickness decreases towards the middle of a hole. This can result in size sorting with larger objects on the outside of the hole and small objects in the middle, which could bias statistical analysis of the particle size. The limited thickness of the film could exclude or deform particles and some larger particles could even protrude from the film. Both the sample and the vitreous film suffer from degradation due to the focused high energy electron beam. Such radiation damage could lead to the loss of structural details or even the introduction of circular voids. Low-dose techniques should be used to minimize the electron dose prior to image acquisition to prevent damage to the sample.

The high resolution and high magnification of cryoTEM permits a detailed structural characterization of various materials. Recent advances in both instrumentation and image analysis have made it possible to elucidate the structure of biological macromolecules with atomic resolution.[8,9] Single-particle cryoTEM is based on the alignment of many 2D images of randomly oriented particles to obtain a 3D reconstruction (Figure 1). Subsequent multivariate statistical analysis (MSA) is used to identify similarities in a large heterogeneous dataset of images and to cluster those images based on recurring motifs. Thus far, this technique has only sparsely been used for the structural characterization of synthetic supramolecular assemblies.[20]

2.3 CryoTEM for the visualization of supramolecular assemblies

CryoTEM is an often-used technique in our department for the characterization of soft matter in aqueous solution. In this section several examples will be presented in which I measured cryoTEM to characterize new materials. The first part will focus on micelles based on waterborne polyurethanes and the second part on new water-compatible supramolecular motifs that assemble via hydrogen bonds.

2.3.1 Characterization of polyurethane ionomers

Polyurethanes represent an important class of materials found in various applications such as coatings and paints.[21] Waterborne polyurethanes are generally dispersions of polyurethane ionomers (PUIs) with a random distribution of hydrophilic (dimethylpropionic acid (DMPA)) and hydrophobic units (isophorone diamine (IPDA) and poly-tetrahydrofuran (THF)) along the polymer chain.[22] Understanding the structure-function relationship in those systems is complicated as the macromolecules are often disperse in length and composition, and the influence of each component cannot be studied individually. Lisa Timmers, Michel Fransen, dr. ir. Henk Janssen and

prof. dr. Ilja Voets therefore designed small sequence-defined PUI materials to gain an understanding of the complexation of various PUIs in solution.

First, doubly charged asymmetric (**PUI-A2**) and symmetric (**PUI-S2**) PUIs (Figure 2A) were studied in aqueous 0.1 triethylamine (TEA) solutions.[23] Both molecules assemble into micelles above their critical micelle concentration (CMC) as was visualized by cryoTEM. Micelles of **PUI-A2** (Figure 2B) and **PUI-S2** (Figure 2C) have an average radius of 7.2 nm and 5.2 nm, respectively. This difference originates from the different packing of those molecules: **PUI-A2** resembles a classical surfactant architecture, whereas the bola-amphiphile **PUI-S2** acts as a more complex surfactant.
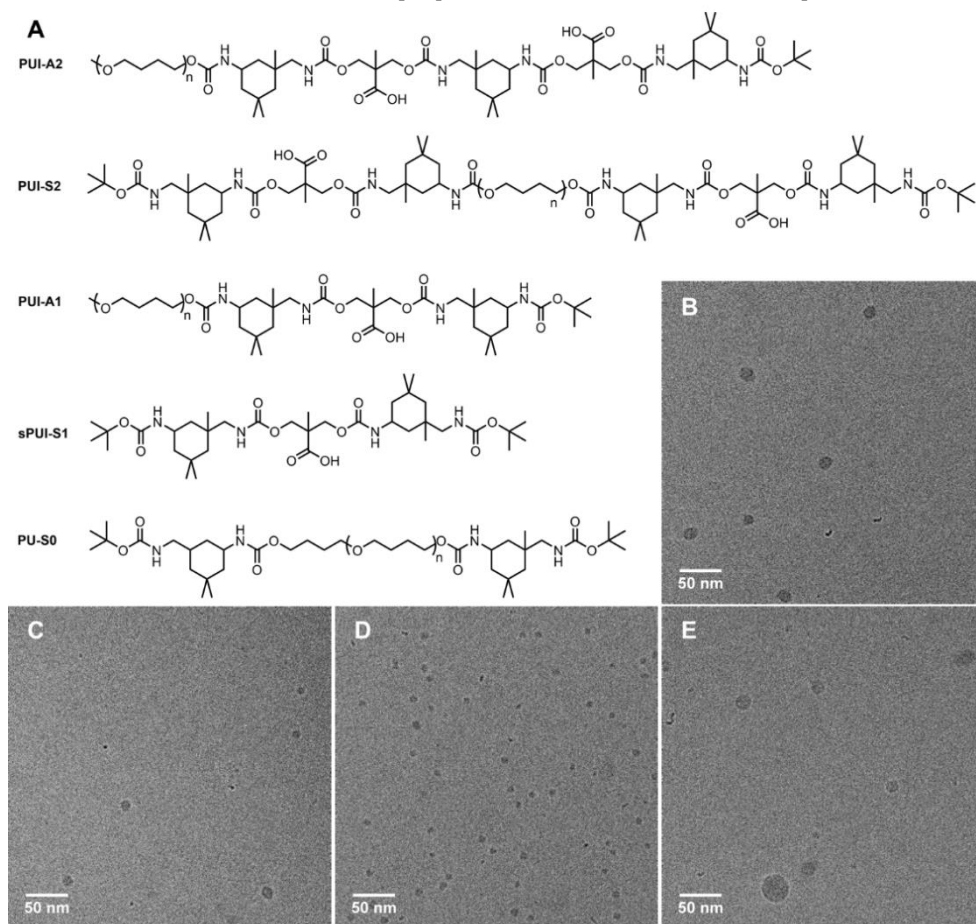
Figure 2. (A) Chemical structure of **PUI-A2**, **PUI-S2**, **PUI-A1**, **sPUI-S1** and **PU-S0**. n = 28 for 2 kDa poly-THF. (B) CryoTEM image of **PUI-A2** in aqueous 0.1 M TEA solution (c = 2.5 mg/ml). Dark objects of around 5 nm are crystalline ice particles. (C) CryoTEM image of **PUI-S2** in aqueous 0.1 M TEA solution (c = 2.5 mg/ml). (D) CryoTEM image of **PUI-A1** and **sPUI-S1** in a 1:6 molar ratio in aqueous 0.1 M TEA solution (c_{total} = 2.5 mg/mL). (E) CryoTEM image of **PUI-A1** and **sPUI-S1** in a 1:6 molar ratio with **PU-S0** as a guest in aqueous 0.1 M TEA solution (c_{total} = 2.5 mg/mL, $f_{guest} \approx$ 0.2).

Surfactant formulations are often used for the encapsulation of lipophilic compounds. The poly-THF sequence-defined PUIs resemble the alkyl chains of typical surfactants, thereby creating micelles with a hydrophobic core that is suited for the incorporation of hydrophobic guests. The asymmetric PUI with one charge (**PUI-A1**) and small symmetric PUI with one charge (**sPUI-S1**, Figure 2A) are both unable to assemble into micelles on their own due to a lack of charge and lack of surfactant architecture, respectively.[23] However, together they can form stable micelles with a radius of roughly 4.0 nm (Figure 2D). The symmetrical neutral polymer **PU-S0** (Figure 2A) is too hydrophobic to assemble into micelles on its own, but it could function as a guest molecule that incorporates into the hydrophobic core of host micelles. CryoTEM measurements confirmed that the radius of the **PUI-A1/sPUI-S1** micelles increase to an average of 7.1 nm upon addition of **PU-S0** ($f_{guest} \approx 0.2$), although there are variations in the particle size. This experiment confirm guest encapsulation (Figure 2E).

Co-assembly of ionic surfactants with ionic-neutral copolymers results in surfactant-polymer complexes with a mixed core composed of a coacervate phase with polyelectrolyte-decorated surfactant micelles.[24] This micellar core is known to be capable of solubilizing both hydrophilic and hydrophobic cargo and these co-assemblies are therefore interesting candidates for the formation of modular drug delivery systems. The anionic **PUI-A2** and **PUI-S2** were co-assembled with the cationic-neutral poly(N-methyl-2-vinylpyridinium iodide)$_{29}$-b-poly(ethylene oxide)$_{204}$ (PMVP$_{29}$-b-PEO$_{204}$) to study the effect of amphiphile sequence on the core structure of the surfactant-polymer complexes.[25] Both PUI assemblies significantly increase in size upon addition of PMVP$_{29}$-b-PEO$_{204}$ (Figure 3), confirming its incorporation. Interestingly, the assemblies became more irregular in their shape. Additionally, both mixtures contained some micelles with internal compartments, as is illustrated for **PUI-A2**:PMVP$_{29}$-b-PEO$_{204}$ in Figure 3B, which could not be revealed with other techniques.
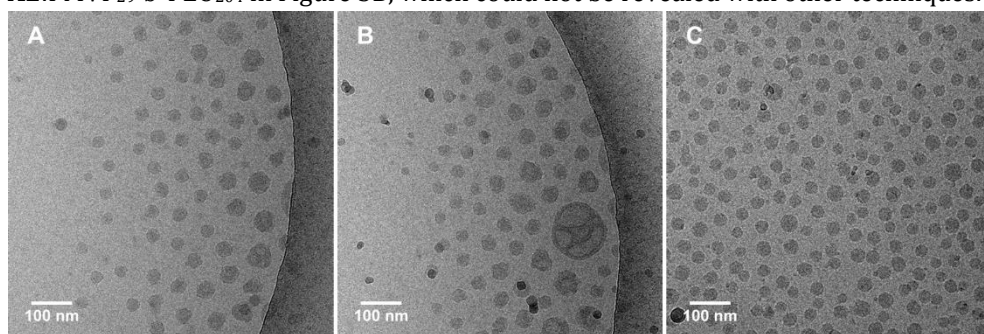
Figure 3. (A-B) CryoTEM image of **PUI-A2**:PMVP$_{29}$-b-PEO$_{204}$ complexes in water with 0.1% THF and 10 mM NaNO$_3$ (c = 10 mg/mL). (C) CryoTEM image of **PUI-S2**:PMVP$_{29}$-b-PEO$_{204}$ complexes in water with 0.1% THF and 10 mM NaNO$_3$ ($c_{total, polymer}$ = 10 mg/mL). The dark objects are crystalline ice particles.

2.3.2 Characterization of supramolecular assemblies based on new hydrogen-bonded motifs in water

CryoTEM is a useful technique to confirm that newly designed supramolecular motifs are able to assemble into larger structures. Whereas scattering or spectroscopy experiments give a first hint for the occurrence of aggregation, cryoTEM can provide direct visual confirmation of the morphologies formed. Several examples of new supramolecular building blocks and their characterization by cryoTEM will be discussed in this section.

A first example comprises the self-assembly of phthalhydrazides in water. Due to their self-complementary hydrogen bond motifs, the phthalhydrazides are able to assemble into trimeric disk in their lactim-lactam tautomeric form (Figure 4A).[26] These trimeric disks were shown to stack on top of one another via hydrophobic interactions such that columnar liquid crystals[27] or long supramolecular polymers[28–32] were obtained. We envisioned that such a hierarchical self-assembly could be useful for the creation of biomaterials, which requires water-compatibility. The phthalhydrazide motif was therefore redesigned to contain a hydrophobic dodecyl chain and hydrophilic tetra(ethylene glycol). This **PH-C$_{12}$-EG$_4$** (Figure 4A) was synthesized by dr. ir. Bas van Genabeek. Absorption spectra of this molecule in water did not match with any of the spectra reported in literature and were therefore inconclusive about the aggregation of the molecules. CryoTEM images revealed the presence of long supramolecular polymers in water (Figure 4B). No ends were observed in the images made, also not at lower magnification (6500x), from which it can be concluded that the length of those assemblies is in the range of several micrometers. The diameter of those fibers is roughly 7 nm, which matches with the diameter of a trimeric disk.
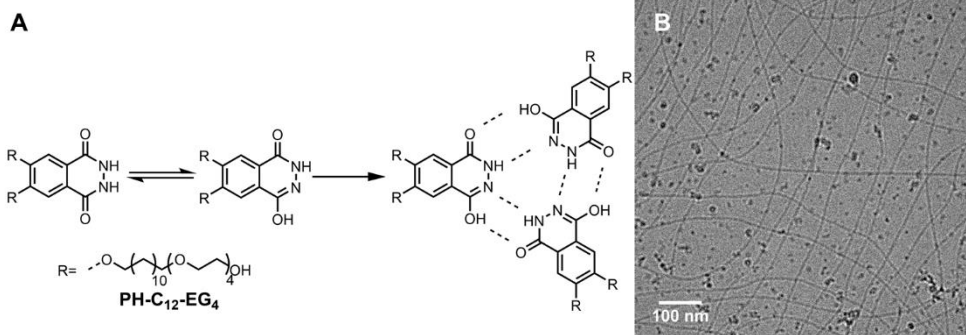
Figure 4. (A) Chemical structure of **PH-C$_{12}$-EG$_4$** that can form trimeric disks after tautomerization to its lactim-lactam form. (B) CryoTEM image of **PH-C$_{12}$-EG$_4$** in water (c = 500 μM). The dark objects are spherical ice particles.

Our group showed some interesting properties of supramolecular polymers based on biphenyl tetracarboxamides (BPTAs) in organic solvents. These molecules form multiple helical states depending on the temperature and water content in the organic

solvent.[33,34] Tomo Iseki aimed to use these interesting motifs for the formation of water-compatible supramolecular polymers. The amides of the core were therefore equipped with a dodecyl chain for hydrophobic protection and tetra(ethylene glycol) for water-compatibility (Figure 5A). **BPTA-C$_{12}$-EG$_4$** precipitated upon addition to pure water, possibly due to the hydrophobic nature of the molecule. It was therefore required to dissolve the molecule in THF before injection of this stock solution into water. The presence of 20% THF did not hinder the vitrification process for cryoTEM since water is still the excess solvent. CryoTEM images revealed the presence of supramolecular polymers of several micrometers in length and roughly 4.5 nm in width (Figure 5B-C). Additionally, those images show that some material had the tendency to precipitate instead of assembling into supramolecular polymers (Figure 5B). This was corroborated by the scattering at higher wavelengths in the UV spectrum of **BPTA-C$_{12}$-EG$_4$** in water with 20% THF. However, higher percentage of cosolvent, for example 30% THF, hampered the formation of supramolecular polymers, illustrating a delicate balance between solvation and supramolecular self-assembly.
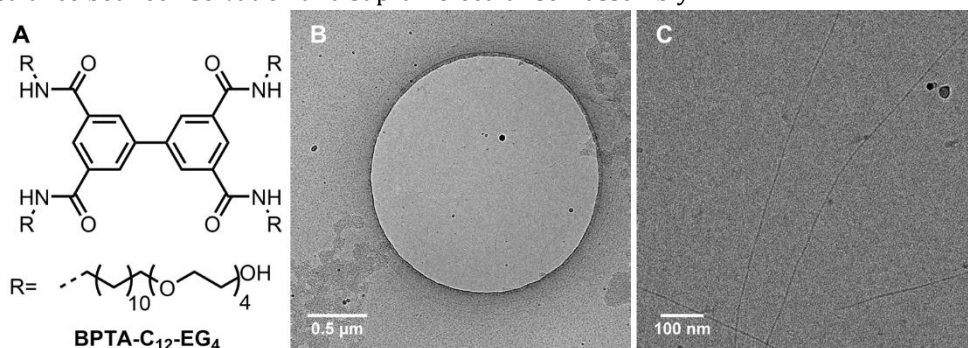
Figure 5. (A) Chemical structure of **BPTA-C$_{12}$-EG$_4$**. (B-C) CryoTEM images of **BPTA-C$_{12}$-EG$_4$** in water with 20% THF (c = 500 μM). The dark objects are spherical ice particles.

Next, the ability of triphenylene-2,6,10-tricarboxamides (TTAs) to self-assemble in water was explored. These molecules assemble into columnar helical stacks in organic solvents through hydrogen bonding and π-π stacking.[35] Dr. Marcin Ślęczkowski synthesized a TTA with dodecyl and tetra(ethylene glycol) chains, but this molecule could not be dissolved in water due to its large hydrophobicity. Ir. Gilian Klerks therefore introduced various oligo-2-oxazolines as a hydrophilic periphery. The hydrophilicity as well as the thermal properties of the oxazolines are influenced by the length of their side groups.[36,37] A disperse 2-methyl-2-oxazoline periphery (**TTA-C$_{12}$-MeOx$_{\sim5}$**, Figure 6A) was found to facilitate the formation of elongated supramolecular assemblies which I proved with cryoTEM (Figure 6B). The elongated assemblies are all less than a micrometer long and resemble twisted ribbons. However, not all TTAs assemble into those twisted ribbons as the presence of micelles can also be observed.

This could be an effect of a disbalance between hydrophilic and hydrophobic interactions or it could be a steric effect from the bulky oxazoline periphery.
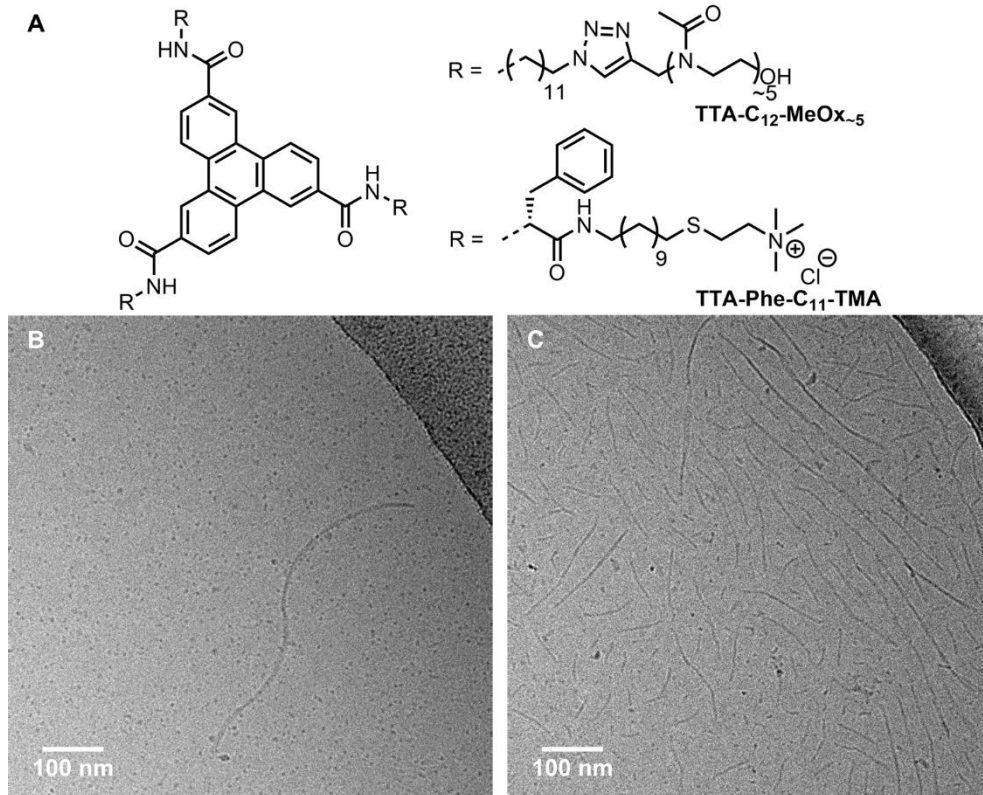
Figure 6. (A) Chemical structures of **TTA-C$_{12}$-MeOX$_{\sim5}$** and **TTA-Phe-C$_{11}$-TMA**. (B) CryoTEM image of **TTA-C$_{12}$-MeOx$_{\sim5}$** in water (c = 1 mM). (C) CryoTEM image of **TTA-Phe-C$_{11}$-TMA** in water (c = 500 µM).

Dr. Jesús Mosquera proposed to use a charged periphery for the promotion of TTA self-assembly in water. He therefore introduced a trimethylammonium (TMA) group at the periphery via thiol-ene click chemistry (see Chapter 7 for more details). Additionally, he modified the hydrophobic chain such that it includes a D-phenylalanine moiety for more hydrophobic interactions and an amide group for additional hydrogen bonding. Aggregation of this **TTA-Phe-C$_{11}$-TMA** (Figure 6A) was observed in water without additional counterions for charge screening. CryoTEM revealed elongated supramolecular assemblies with a polydisperse length of less than one micrometer (Figure 6C). Size sorting can be observed in this image with the larger assemblies on the edge (top right) and the smaller assemblies closer to the center of the hole (bottom left). Interestingly, some of the assemblies on the edge of the hole appear to have a ribbon structure similar to **TTA-C$_{12}$-MeOx$_{\sim5}$**, whereas some thinner assemblies are observed towards the middle. This demonstrates the large variety of moprhologies

formed by this motif, which could not be revealed with averaging techniques such as spectroscopy or scattering measurements.

In a final example, the aim was to introduce pH-responsiveness into benzene-1,3,5-tricarboxamide (BTA) based supramolecular polymers. The dodecyl side chains of a BTA were therefore decorated with carboxylic acid groups (**BTA-C$_{12}$-COOH**, Figure 7A) by ir. Laura Rijns. The presence of aggregation was suggested by UV spectroscopy when the pH was increased to 11 by the addition of NaOH. However, light scattering experiments suggested the formation of larger assemblies with a morphology that does not resemble supramolecular polymers. CryoTEM images showed that this BTA assembles into sheets of various dimensions (Figure 7B). Additionally, these sheets appear to fold into a tubular structure. Similar sheet-like structures were previously observed for a BTA with one carboxylic acid group,[38] suggesting that electrostatic interactions are responsible for sheet-formation. The influence of charges on the self-assembly and structure of BTAs will be further explored in Chapter 7.
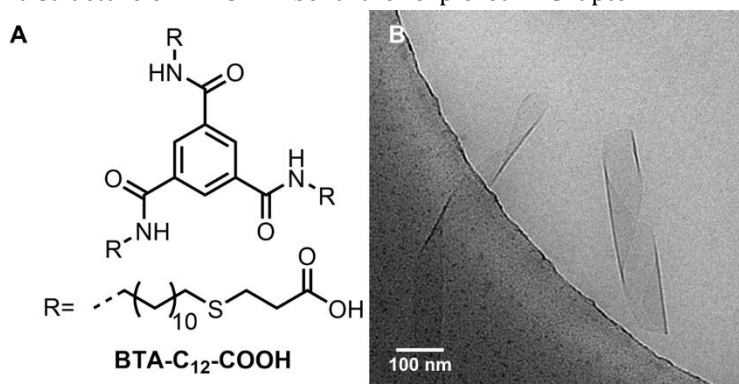
Figure 7. (A) Chemical structure of **BTA-C$_{12}$-COOH**. (B) CryoTEM image of **BTA-C$_{12}$-COOH** in water with pH 11 (c = 500 μM).

All of these examples show that cryoTEM is a suitable technique to characterize the structure of supramolecular polymers based on hydrogen-bonded motifs. **PH-C$_{12}$-EG$_4$** and **BPTA-C$_{12}$-EG$_4$** both have a length of several micrometers that resembles the previously studied supramolecular polymers based on BTAs with the same side chains.[39] However, a TTA with the same side chains was not soluble in water and only short polymers were found for the other side chains that provided enough water-compatibility. These experiments also showed that the BPTA motif is only slightly soluble in water. All of the experiments in this section indicate that the number of hydrogen bonds, their directionality, the strength of the π-π stacking and the strength of the hydrophobic effect drastically influences the ability of supramolecular motifs to self-assemble. The constant interplay between those interactions makes it difficult to predict which side chain is required for a new supramolecular motif a priori. Since it remains difficult to decouple the interactions between the cores that govern

supramolecular self-assembly we will for now focus on the influence of the side chains. Therefore, a systematic study on the influence of the hydrophobic chain length as well as its spatial arrangement on the self-assembly of BTAs will be presented in the next section.

2.4 In-depth cryoTEM analysis of supramolecular polymers based on BTAs

Synthetic supramolecular polymers based on BTAs have been studied for many years in our group. The molecules have been equipped with dodecyl and tetra(ethylene glycol) side chains (**BTA-C$_{12}$-EG$_4$**, Figure 8A) such that supramolecular polymerization in water was ensured.[39] Various biological recognition motifs were attached to the side chains to create new biomaterials after copolymerization with **BTA-C$_{12}$-EG$_4$**.[40–43] CryoTEM images of **BTA-C$_{12}$-EG$_4$** revealed micrometer long supramolecular polymers. Interestingly, all images of **BTA-C$_{12}$-EG$_4$** showed a periodic variation in the diameter of the polymer (see Figure 8B for an example).[39] In case of a thin vitrified film a fingerprint-like pattern can be observed, which is attributed to ordered BTA molecules that are assembled at the air-water interface.[44] The hydrophobic parts of the molecule provide the most contrast and should result in a diameter of 2-2.5 nm. However, the diameter observed with cryoTEM is twice this value, prompting dr. ir. René Lafleur to start a deeper investigation into the structure of supramolecular polymers based on **BTA-C$_{12}$-EG$_4$**. Cryogenic electron tomography (cryo-ET) experiments revealed that the assemblies of **BTA-C$_{12}$-EG$_4$** consist of two strands that wrap around one another to form a double helix.
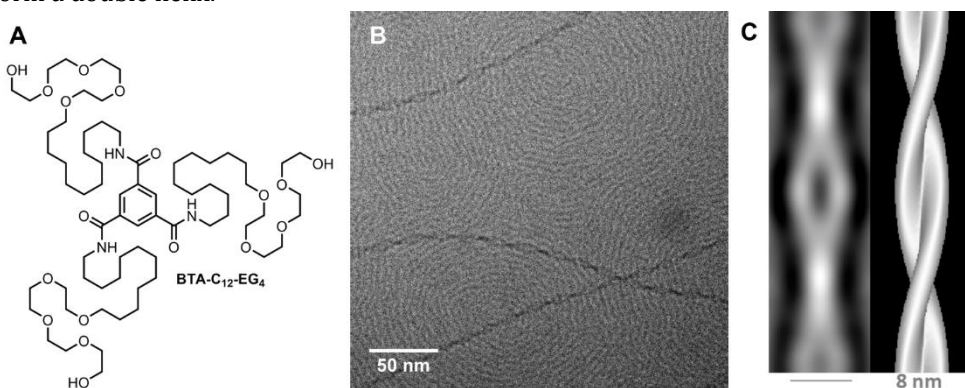
Figure 8. (A) Chemical structure of **BTA-C$_{12}$-EG$_4$**. (B) CryoTEM image of **BTA-C$_{12}$-EG$_4$** in water made with a 61000x magnification (c = 582 µM). Image was acquired by René Lafleur. (C) Class sum image of the 100 best aligned extracts of **BTA-C$_{12}$-EG$_4$** and the surface representation of the volume reconstruction based on this sum image.

Following the revelations of the cryo-ET experiments, we collaborated with dr. Christoph Böttcher and dr. Svenja Herziger for further analysis of the double helix

structure of **BTA-C$_{12}$-EG$_4$**. Additional 2D images were recorded with a Volta phase plate for enhanced contrast and these new images were used for detailed image analysis and reconstruction based on single-particle cryoTEM. To this end, 380 extracts of the supramolecular assemblies were taken, band-pass-filtered to remove low- and high-frequency noise and then translationally and rotationally aligned into a sum image. Obvious misaligned fibers, for example due to bending, tilting or too much distortion from the fingerprint-pattern, were removed with MSA. For clarity, the contrast was inverted, resulting in bright supramolecular structures on a dark background. The double helix repeat becomes clearly visible from this processing and could be used for 3D volume reconstruction (Figure 8C).[45] No helical inversion was observed within the polymers with this analysis. The two strands have a diameter around 3.5 nm, matching with the diameter of a single stack. The area between the stacks is not completely black which indicates that the stacks are not always completely separated. With the class sum images the half helical pitch could be determined, that is the distance between two knots. For **BTA-C$_{12}$-EG$_4$** this was determined to be 19.9 nm with an uncertainty of one pixel, approximately 0.4 nm. The image reconstruction could not be used to determine the handedness of the double helix, but it is expected that equal amounts of P and M helices are present since the building blocks are achiral.

Intrigued by the secondary structure found for **BTA-C$_{12}$-EG$_4$** other BTAs with variations in their side chain were studied in more detail by me (Figure 9A). 2D images of all assemblies were made with a Volta phase plate for increased contrast. BTAs with a decyl chain do not assemble into elongated structures due to a lack of hydrophobic interactions. Instead, small assemblies with a diameter of roughly 10 nm are formed by **BTA-C$_{10}$-EG$_4$** (Figure 9B). An undecyl chain is long enough to create a hydrophobic pocket that can protect the intermolecular hydrogen bonds such that micrometer long supramolecular polymers can be observed.[46] The polymers of **BTA-C$_{11}$-EG$_4$** (Figure 9C) do not express the same separation of strands as observed for **BTA-C$_{12}$-EG$_4$** (Figure 9D). However, the assemblies have a diameter of 6.0 ± 0.4 nm, which is larger than expected for a single stack of molecules. It is hypothesized that **BTA-C$_{11}$-EG$_4$** also assembles into two strands that are closely associated such that no separation of strands can be observed. Further increase of the hydrophobic chain length to a tridecyl chain, **BTA-C$_{13}$-EG$_4$**, results in even thicker supramolecular polymers with a diameter of 8.2 ± 0.4 nm (Figure 9E). A periodicity in the diameter is also observed for these assemblies with a half helical pitch of 22.4 ± 0.4 nm. The knots appear to be thicker in the assemblies of **BTA-C$_{13}$-EG$_4$** than in the assemblies of **BTA-C$_{12}$-EG$_4$** but this could also be an artefact from image reconstruction since less fibers were available for **BTA-C$_{13}$-EG$_4$**, thereby limiting the analysis. A BTA with a branched hydrophobic chain was studied as well. Image analysis of the supramolecular polymers formed by this **BTA-(S)-Me-C$_{12}$-EG$_4$** surprisingly reveals the presence a straight fiber with a diameter of 3.5 ± 0.4 nm. This diameter corresponds to that of a single stack of molecules. Although **BTA-(S)-Me-C$_{12}$-EG$_4$** has the same number of carbon atoms in its side chain as **BTA-C$_{13}$-EG$_4$** it assembles

into a completely different structure. The properties of **BTA-(S)-Me-C$_{12}$-EG$_4$** will be discussed in more detail in Chapter 4.
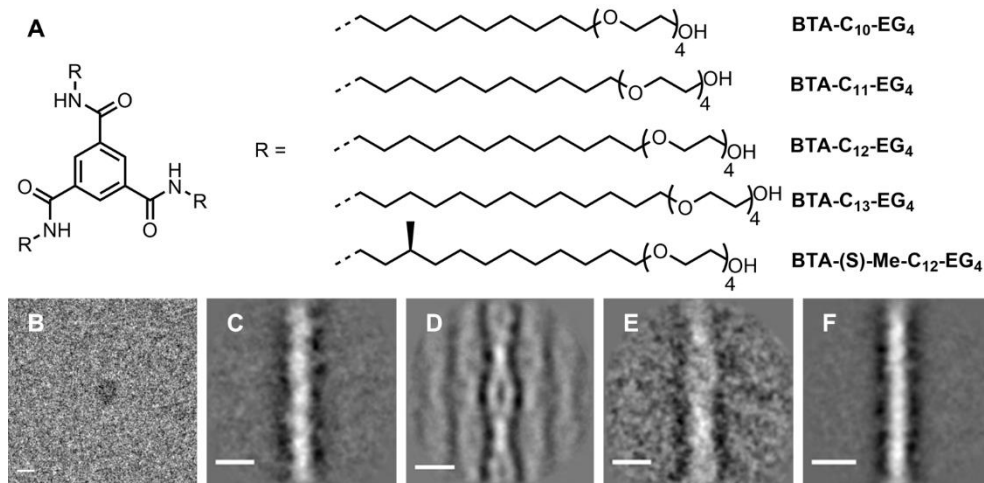
Figure 9. Chemical structure of **BTA-C$_{10}$-EG$_4$**, **BTA-C$_{11}$-EG$_4$**, **BTA-C$_{12}$-EG$_4$**, **BTA-C$_{13}$-EG$_4$** and **BTA-(S)-Me-C$_{12}$-EG$_4$**. (B) Zoom-in on a supramolecular assembly of **BTA-C$_{10}$-EG$_4$** in water (c = 500 μM). (C) Class sum image of the 150 best aligned extracts of **BTA-C$_{11}$-EG$_4$** in water (c = 500 μM). (D) Class sum image of the 380 best aligned extracts of **BTA-C$_{12}$-EG$_4$** in water (c = 582 μM). (E) Class sum image of the 90 best aligned extracts of **BTA-C$_{13}$-EG$_4$** in water (c = 500 μM). (F) Class sum image of the 400 best aligned extracts of **BTA-(S)-Me-C$_{12}$-EG$_4$** in water with 2% ACN (c = 500 μM). The scale bar is 10 nm in all images.

The absence of a double helix structure in assemblies of **BTA-(S)-Me-C$_{12}$-EG$_4$** illustrates how delicate the self-assembly process is as small deviations in the chemical structure prevent the formation of a secondary structure. From the image analysis of the BTAs with linear alkyl chains it can be concluded that the diameter as well as the helical pitch increases with hydrophobic chain length. It is hypothesized that the hydrophobic effect has an influence on the association of two strands. The formation of a double helix by achiral molecules is rarely reported in literature, but in all cases it is suggested that bundling is used to reduce solvent exposure of hydrophobic parts.[47–49] A proposal for the molecular packing of water-compatible BTAs into a double helix will be presented in Chapter 4.

Dr. Svenja Herziger studied the effect of supramolecular co-assembly on the structure using the same image analysis techniques.[44] **BTA-C$_{12}$-G1** contains a dendritic periphery which is more hydrophilic and results in more steric hinderance compared to a linear ethylene glycol periphery. As a result, **BTA-C$_{12}$-G1** does assemble into small micellar assemblies instead of supramolecular polymers.[50] Supramolecular polymers with slower exchange dynamics were found when this molecule was mixed with **BTA-C$_{12}$-EG$_4$**. CryoTEM and consecutive image analysis revealed that all co-assemblies have a double helix structure but their helical pitch decreases with increasing amounts of

BTA-C$_{12}$-G1 (Figure 10A). Additionally, the separation of strands becomes less prominent in the 1:2 sample, similar to **BTA-C$_{11}$-EG$_4$**. The addition of a BTA that assembles into small micelles seems to lead to a tightening of the double helix.

The opposite effect was observed with **BTA-C$_{16}$-G1**. This redesign of **BTA-C$_{12}$-G1** contains a longer hydrophobic chain to compensate for the increased hydrophilicity of the dendritic periphery. **BTA-C$_{16}$-G1** is able to assemble into micrometer supramolecular polymers but image analysis revealed that those polymers consist of two parallel stacks that do not rotate around each other.[44] Co-assembly of **BTA-C$_{12}$-EG$_4$** with increasing amounts of **BTA-C$_{16}$-G1** results in an increase of the helical pitch until parallel pairs are found at a 1:2 ratio, which resembles a double helix with an infinitely long pitch (Figure 10B). The addition of **BTA-C$_{16}$-G1** thus leads to the unraveling of the double helix. The co-assembly of supramolecular motifs can be used as a strategy to control the secondary structure of the supramolecular assemblies.
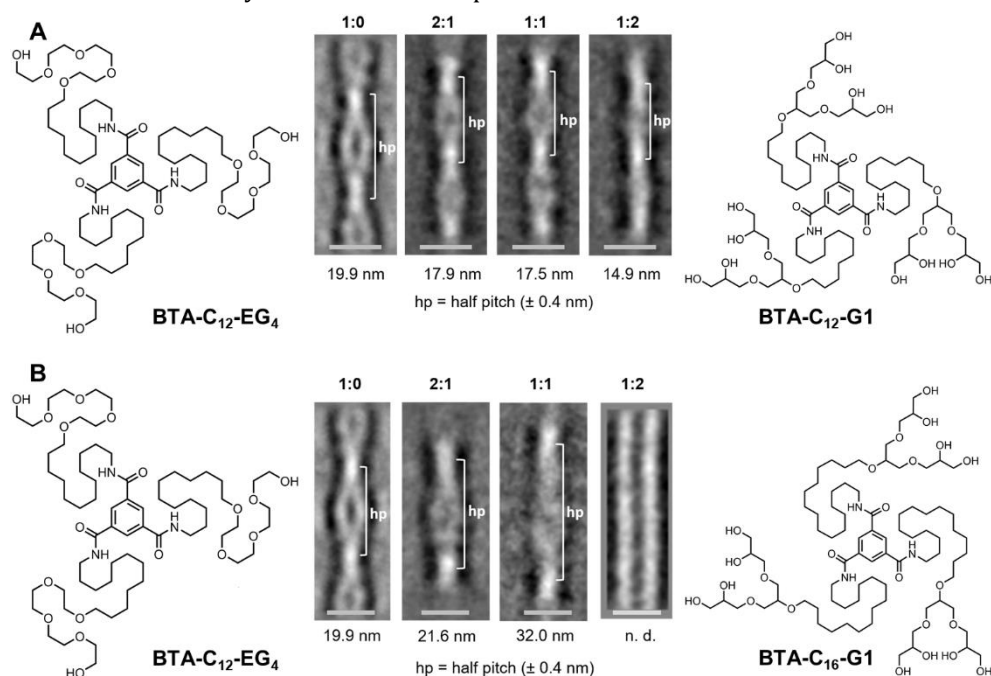
Figure 10. (A) Class sum images of different mixtures of **BTA-C$_{12}$-EG$_4$** and **BTA-C$_{12}$-G1**. The amount of **BTA-C$_{12}$-G1** increases from left to right. (B) Class sum images of different mixtures of **BTA-C$_{12}$-EG$_4$** and **BTA-C$_{16}$-G1**. The amount of **BTA-C$_{16}$-G1** increases from left to right. The corresponding half helical pitches are indicated. The scale bar is 10 nm in all images and the half helical pitches are indicated below the images. Images were acquired and analyzed by dr. Svenja Herziger.

2.5 Conclusions

In conclusion, cryoTEM is very well-suited for the structural characterization of supramolecular assemblies in water. The vitrification process of the samples prevents changes in sample composition and aggregation due to solvent drying and allows for the direct examination of the assemblies in their near-native state. Nevertheless, care should be taken during the interpretation of the results to prevent erroneous conclusions as one should be aware of artefacts introduced by atmospheric deposition of water and electron beam radiation. Images can be taken to study the structural features of individual assemblies in solution. However, this can also be one of the weaknesses of the techniques as it does not provide information about the whole population within the sample and many images are required for statistical analysis on the size of the assemblies, especially for supramolecular polymers with a length beyond the scale of one image. Ideally, characterization of supramolecular assemblies should be based on several complementary techniques, including cryoTEM.

Several supramolecular assemblies were analyzed in this chapter with cryoTEM. Supramolecular polymers of various lengths were observed for new phthalhydrazide, BPTA and TTA motifs, but these results also illustrate that the design of new water-compatible motifs is still based on a trial-and-error approach as basic design rules are still missing. Whereas high-magnification images suffice to prove the self-assembly of new supramolecular materials in solution, in-depth image analysis techniques based on single particle analysis are required to elucidate the secondary structure of BTAs. Although these BTA molecules were previously believed to assemble into a single stack, a double helix structure with a regular helical pitch was observed in some of the assemblies. This secondary structure can be influenced by chemical modifications to the monomer as was demonstrated for BTAs with various hydrophobic chain lengths. Interestingly, **BTA-(S)-Me-C$_{12}$-EG$_4$** with its branched hydrophobic chain lacks a secondary structure and assembles into a single stack of molecules. Additionally, the helical pitch could be tuned by co-assembly as both tightening and unraveling of the double helix was observed. These results show that the structure of the supramolecular polymers can be more complex than previously believed and careful analysis is required. We suggest that the association of two BTA strands originates from hydrophobic interactions and the molecular packing inside a double helix or single strand will be discussed in more detail in Chapter 4.

2.6 Experimental section
2.6.1 Materials and Methods

All solvents and chemicals used were of reagent grade quality or better and purchased from Biosolve or Sigma-Aldrich at the highest purity available and used without further purification unless otherwise noted. Reactions were followed by thin-layer chromatography (TLC) using 60-F$_{254}$ silica gel plates from Merck and visualized by UV light at 254 nm and/or staining (ninhydrin, bromocresol green, potassium permanganate, iodine chamber). **BTA-C$_{10}$-EG$_4$**,[46] **BTA-C$_{11}$-EG$_4$**,[46]

BTA-C$_{12}$-EG$_4$,[39] **BTA-C$_{13}$-EG$_4$**,[51] **BTA-(S)-Me-C$_{12}$-EG$_4$**[39] and the PUIs[23,25] were synthesized according to literature procedure by Jolanda Spiering, Nicolas Matsumoto and Michel Fransen. Water for aqueous samples was purified on an EMD Millipore Milli-Q Integral Water Purification System. The sample preparation of the aqueous samples of PUIs is reported in literature.[23,25]

Sample preparation of PH-C$_{12}$-EG$_4$, TTA-C$_{12}$-MeOx$_{\sim 5}$, BTA-C$_{10}$-EG$_4$, BTA-C$_{11}$-EG$_4$ and BTA-C$_{12}$-EG$_4$: the solid material was weighed into a glass vial equipped with a magnetic stirring bar. MQ-water was added to obtain the desired concentration. The sample was subsequently stirred at 80 °C for 15 minutes and the hot and hazy sample was vortexed immediately afterwards for 15 seconds. All samples were left to equilibrate overnight at room temperature.

Sample preparation of TTA-Phe-C$_{11}$-TMA: the solid material was weighed into a glass vial. MQ-water was added to obtain the desired concentration. The sample was subsequently vortexed for 15 seconds and was left to equilibrate overnight at room temperature. The synthesis of this molecule was developed by Jesús Mosquera and has not been published yet.

Sample preparation of BTA-C$_{12}$-COOH: the solid material was weighed into a glass vial equipped with a magnetic stirring bar. MQ-water (pH adjusted to 11 with NaOH) was added to obtain the desired concentration. The sample was subsequently stirred at 80 °C for 15 minutes and the hot and hazy sample was vortexed immediately afterwards for 15 seconds. All samples were left to equilibrate overnight at room temperature.

Sample preparation of BTA-C$_{13}$-EG$_4$: roughly 2 mg the solid material was weighed into a 15 mL glass vial with a magnetic stirring bar. Approximately 300 μL CHCl$_3$ was added and the sample was vortexed for 15 seconds. The solvent was evaporated by blowing a constant stream of N$_2$ (g) above the solvent. 15 mL MQ-water was added and the sample was stirred at 80 °C for 15 minutes. Subsequently, the hot and hazy mixture was vortexed for 15 seconds and was left to equilibrate at room temperature overnight. The next day the sample was filtered with a 0.2 μm syringe filter. Water was evaporated by blowing a stream of N$_2$ (g) over the sample, while stirring, thereby increasing the concentration. UV spectroscopy was used to determine the concentration using a calibration curve based on the absorbance of **BTA-C$_{12}$-EG$_4$** at 250 nm: conc = (0.00434 + A$_{250}$)/0.001615. The concentration was increased to 500 μM with this method.

Sample preparation of BPTA-C$_{12}$-EG$_4$ and BTA-(S)-Me-C$_{12}$-EG$_4$: the solid material was weighed into a glass vial equipped with a magnetic stirring bar. ACN (for **BTA-(S)-Me-C$_{12}$-EG$_4$**) or THF (for **BPTA-C$_{12}$-EG$_4$**) was added to obtain a concentrated stock solution (25 mM for **BTA-(S)-Me-C$_{12}$-EG$_4$** and 2.5 mM for **BPTA-C$_{12}$-EG$_4$**). Stock solutions were vortexed for 1 minute and left to equilibrate at room temperature for at least 2 hours. A small aliquot of such a stock solution was injected into a separate vial with MQ-water and a magnetic stirring bar to obtain the desired concentration. The sample was subsequently stirred at 80 °C for 15 minutes and the hot and hazy sample was vortexed immediately afterwards for 15 seconds. All samples were left to equilibrate overnight at room temperature.

2.6.2 Instrumentation

Cryogenic transmission electron microscopy (cryoTEM) images were made of vitrified samples. Vitrified films were prepared in a 'Vitrobot' instrument (FEI Vitrobot™ Mark IV, FEI Company) at 22 °C and at a relative humidity of 100%. In the preparation chamber of the 'Vitrobot', 3 μL samples were applied on Quantifoil grids (R 2/2, Quantifoil Micro Tools GmbH) or Lacey grids (LC200-Cu, Electron Microscopy Sciences), which were surface plasma treated just prior to use (Cressington 208 carbon coater operating at 5 mA for 40 s). Excess sample was

removed by blotting using filter paper for 3 s with a blotting force of -1, and the thin film thus formed was plunged (acceleration about 3 g) into liquid ethane just above its freezing point. Vitrified films were transferred into the vacuum of a CryoTITAN equipped with a field emission gun that was operated at 300 kV, a post-column Gatan energy filter, and a 2048 x 2048 Gatan CCD camera. Virtrified films were observed in the CryoTITAN microscope at temperatures below -170 °C. Micrographs were taken at low dose conditions at a magnification of 6500x with a defocus of -40 μm, at a magnification of 24000x with a defocus of -10 or -5 μm or at a magnification of 48000x with a defocus of -5 or -2.5 μm.

2D image reconstruction was performed in Berlin on samples with a concentration of 500 μM. Vitrified films were prepared in a 'Vitrobot' instrument (Vitrobot™ Mark IV, Thermo Fisher Scientific) at 22 °C and at a relative humidity of 100%. In the preparation chamber of the 'Vitrobot', 4 μL samples were applied on Quantifoil grids (R 1/4) which were surface plasma treated with a BALTEC MED 020. Excess sample was removed by blotting using filter paper for 3.5 s, with a drain time of 1.0 s, a wait time of 1.0 s and with a blotting force of -13. The thin film thus formed was plunged (acceleration about 3 g) into liquid ethane just above its freezing point. Vitrified films were imaged with a Talos Arctica™ TEM (Thermo Fisher Scientific) at 200 kV accelerating voltage at temperatures below -170 °C. Image recording was done using a Falcon3EC direct electron detector (Thermo Fisher Scientific). Micrographs were taken at low dose conditions at a magnification of 28000x with a defocus setting around -5 μm. Some images were made with a Volta phase plate for enhanced contrast. The objective aperture was replaced by the phase plate which was aligned using the alignment module of the microscope software. After an activation time of several minutes, the phase shift was measured and the astigmatism was corrected using "AutoCTF" (Thermo Fisher). As long as the phase shift stayed close to 0.5 π, micrographs were taken and with a defocus of around -300 nm. In case of significant higher or lower phase shift the position at the phase plate was shifted. From cryoTEM images, individual motifs (128 x 128 pixels, 0.373 nm/pixel) were extracted using the EMAN tool *boxer*.[52] Utilizing the software package IMAGIC-5[79],[53] images were aligned with respect to one or multiple reference images, using cross-correlation techniques. The images were furthermore band-pass filtered to exclude low and high spacial frequencies, thus reducing unspecific noise. Subsequently, a mask image was generated, isolating the area of interest in the images. This mask was applied to all images and the multivariate statistical analysis was computed.

Normal phase column chromatography was performed on a Grace Reveleris X2 chromatography system using Reveleris Silica Flash cartridges. **Reversed phase column chromatography** was achieved using a reversed phase KP-C_{18}-HS SNAP column or a Reveleris C_{18} reversed-phase flash cartridge.

Nuclear magnetic resonance (NMR) spectra were recorded on Bruker Ultrashield 400 MHz spectrometers (400 MHz for ^{1}H NMR; 100 MHz for ^{13}C NMR). Deuterated solvents used are indicated in each case. Proton chemical shifts are reported in ppm (δ) downfield from trimethyl silane (TMS) using the resonance frequency of the deuterated solvent ($CDCl_3$ 7.26 ppm; DMSO-d_6 2.50 ppm; CD_3OD; 3.31 ppm) as the internal standard. Peak multiplicities are abbreviated as s: singlet; d: doublet; m: multiplet; t: triplet, p: pentet, dd: double doublet. Carbon chemical shifts are reported in ppm (δ) downfield from TMS using the resonance frequency of the deuterated solvents ($CDCl_3$ 77.16 ± 0.06 ppm; DMSO-d_6; 39.52 ± 0.06 ppm; 49.00 ± 0.06 ppm) as the internal standard.

Fourier-transform infrared (FT-IR) spectra were recorded on a Perkin Elmer Spectrum Two FT-IR spectrometer. Solid state samples were measured at room temperature from 4000 cm^{-1} to 450 cm^{-1} over 16 scans.

Liquid chromatography mass spectroscopy (LC-MS) spectra were acquired using a device consisting of multiple components: Shimadzu SCL-10 A VP system controller with Shimadzu LC-10AD VP liquid chromatography pumps (with an Alltima C18 3 u (50 x 2.1 mm) reversed-phase column and gradients of water, a Shimadzu DGU 20A3 prominence degasser, a Thermo Finnigan surveyor auto sampler, a Thermo Finnigan surveyor PDA detector and a Thermo Scientific LCW Fleet. All samples were dissolved in 1:1 H$_2$O:acetonitrile in ca. 0.1 mg/mL concentration.

Matrix assisted laser absorption/ionization mass time of flight mass spectroscopy (MALDI-TOF-MS) spectra were obtained on a Bruker Autoflex Speed. α-Cyano-4-hydroxycinnamic acid (CHCA) or trans-2-[3-(4-tert-butylphenyl)-2-methyl-2-propenylidene]malononitrile (DCBT) were used as matrices. All samples were dissolved in either chloroform or methanol with a concentration of 1.0 mg/mL.

2.6.3 Synthetic procedures
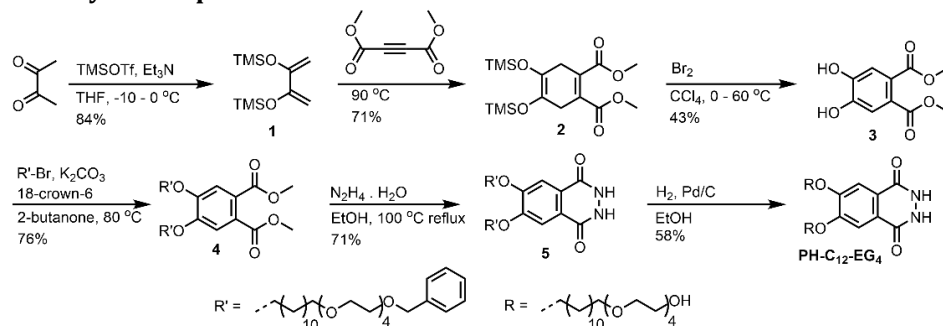
2,3-bis(trimethylsilyloxy)butadiene (1)

The synthesis was adapted from literature.[54] A three-neck round bottom flask was charged with 2,3-butanedione (1.57 g, 18.3 mmol), triethylamine (4.620 g, 45.7 mmol) and THF (20 mL) under argon atmosphere. The mixture was placed in an ice bath and trimethylsilyl triflate (TMSOTf, 9.42 g, 45.7 mmol) was added dropwise. The solution turned from clear yellow to turbid yellow and then light brown. The ice bath was removed and the mixture was allowed to warm up to room temperature. Ice cold NaHCO$_3$ (sat., 25 mL), brine (25 mL), pentane (25 mL) and ice (25 g) were added and the solution was extracted with ice cold pentane (3x 20 mL). The pentane layer was washed with ice cold brine (25 mL), dried with MgSO$_4$ and was concentrated in vacuo. **1** was obtained as a brown liquid (3.54 g, 84%). ^{1}H NMR (400 MHz, CDCl$_3$ δ): 4.84 (s, 2H, C=CH$_2$), 4.35 (s, 2H, C=CH$_2$), 0.25 (s, 18H, TMS CH$_3$).

1,2-bis(trimethylsilyloxy)-1,4-cyclohexadiene-4,5-dicarboxylic Acid Dimethyl Ester (2)

The synthesis was adapted from literature.[55] A 250 mL round bottom flask was charged with **1** (3.36 g, 14.6 mmol) and dimethyl but-2-ynedioate (2.28 g, 16.0 mmol) under argon. The mixture was heated to 90 °C and the color changed to dark brown. The reaction was stirred overnight and the product was purified by vacuum distillation (Kugelruhr Aldrich, 25 mL flask). The product was collected at 120-140 °C and 0.08 mbar. **2** was obtained as a light yellow liquid (3.85 g, 71%). ^{1}H NMR (400 MHz, CDCl$_3$ δ): 3.69 (s, 6H, OCH$_3$), 3.09 (s, 4H, CCH$_2$C), 0.19 (s, 18H, TMS CH$_3$).

Dimethyl 4,5-dihydroxyphthalate (3)

The synthesis was adapted from literature.[55] A 5 wt% solution of Br_2 (1.93 g, 12.1 mmol) in CCl_4 (38.6 g) was prepared. **2** (3.75 g, 10.07 mmol) was dissolved in CCl_4 (10 mL) in a 250 mL three-neck round bottom flask in an ice bath. The Br_2 solution was added dropwise and the solution turned orange. Roughly 80% of the Br_2 solution was added when precipitation was observed. Addition of Br_2 was stopped and the mixture was stored at 60 °C. After 2 hours the mixture was cooled down to room temperature. The solids were collected by filtration and were washed with ice cold CCl_4 (15 mL). The crude material was purified by column chromatography (DCM/MeOH 90/10), yielding **3** (1.60 g, 43%). ^{1}H NMR (400 MHz, acetone-d$_6$ δ): 8.95 (b, 2H, O$\underline{H}$), 7.18 (s, 2H, Ar), 3.77 (s, 6H, C$\underline{H_3}$). ^{13}C NMR (100 MHz, acetone-d$_6$ δ): 206.79, 168.22, 148.08, 125.52, 116.73, 111.38, 52.76, 52.49, 49.81.

Dimethyl 4,5-bis((1-phenyl-2,5,8,11,14-pentaoxahexacosan-26-yl)oxy)phthalate (4)

A 50 mL round bottom flask was charged with **3** (50 mg, 0.22 mmol), 26-bromo-1-phenyl-2,5,8,11,14-pentaoxahexacosane[39] (249 mg, 0.55 mmol), K_2CO_3 (powdered, 122 mg, 0.88 mmol) and 18-crown-6 (29 mg, 0.11 mg) dissolved in 2-butanone (5 mL) under argon. The yellow reaction mixture was stirred at 80 °C overnight. The reaction mixture was filtered through filter paper, washed with ethyl acetate (20 mL) and the filtrate was concentrated in vacuo. The crude material was purified by column chromatography (DCM/MeOH 100/0 – 94/6, 10 CV). A light brown oil with some impurities was obtained. The crude was purified again by column chromatography (CHCl$_3$/ethyl acetate 700/0 – 70/30, 5 CV, 70/30 – 20/80, 5CV), yielding **4** (189 mg, 76%). ^{1}H NMR (400 MHz, CDCl$_3$ δ): 7.44-7.36 (m, 12H, Ar), 4.65 (s, 4H, OC$\underline{H_2}$Ar), 4.12 (t, 4H, ArOC$\underline{H_2}$CH$_2$), 3.96 (s, 6H, C$\underline{H_3}$), 3.79-3.62 (m, 32H, OC$\underline{H_2}$CH$_2$), 3.52 (t, 4H, CH$_2$C$\underline{H_2}$O), 1.91 (p, 4H, ArOCH$_2$C$\underline{H_2}$), 1.65 (p, 4H, C$\underline{H_2}$CH$_2$O), 1.54 (m, 4H, ArOCH$_2$CH$_2$C$\underline{H_2}$), 1.48-1.30 (m, 28H, aliphatic). ^{13}C NMR (100 MHz, CDCl$_3$ δ): 168.00, 150.73, 138.29, 128.34, 127.71, 127.56, 124.88, 113.05, 73.23, 71.53, 70.66, 70.63, 70.62, 70.07, 69.45, 69.28, 60.36, 52.51, 29.67, 29.63, 29.59, 29.53, 29.33, 29.00, 26.12, 25.92, 21.04, 14.22. MALDI-TOF-MS: m/z calculated for $C_{64}H_{102}O_{16}$+Na$^+$: 1149.71 [M+Na]$^+$; observed 1149.74.

6,7-bis((1-phenyl-2,5,8,11,14-pentaoxahexacosan-26-yl)oxy)-2,3-dihydrophthalazine-1,4-dione (5)

A 10 mL round bottom flask was charged with **4** (99 mg, 0.088 mmol), hydrazine hydrate (64% hydrazine, 88 mg, 1.76 mmol) and a few drops of EtOH. The mixture was stirred at 100 °C under reflux conditions for 2 hours. The mixture was cooled down to room temperature and a white precipitate was observed. The crude was purified by column chromatography (DCM/MeOH 96/4 – 90/10, 10 CV). The crude still contained some starting material so it was purified by column chromatography again (DCM/MeOH 100/0 – 90/10, 10 CV), yielding **5** as a semi-transparent waxy material (68 mg, 71%). ^{1}H NMR (400 MHz, CDCl$_3$ δ): 12.91 (b, 2H, N$\underline{H}$), 7.44 (s, 2H, Ar phthalhydrazide), 7.36-7.23 (m, 10H, Ar benzyl), 4.56 (s, 4H, OC$\underline{H_2}$Ar), 4.09 (t, 4H, ArOC$\underline{H_2}$CH$_2$), 3.71-3.53 (m, 32H, OC$\underline{H_2}$CH$_2$), 3.44 (t, 4H, CH$_2$C$\underline{H_2}$O), 1.89 (p, 4H, ArOCH$_2$C$\underline{H_2}$), 1.62-1.45 (m, 8H, C$\underline{H_2}$CH$_2$O, ArOCH$_2$CH$_2$C$\underline{H_2}$), 1.44-1.19 (m, 28H, aliphatic). ^{13}C NMR (100 MHz, CDCl$_3$ δ): 157.40, 153.47, 138.31, 128.38, 127.76, 127.61, 121.46, 106.30, 73.27, 71.59, 70.69, 70.65, 70.10, 69.48, 69.21, 32.85, 29.74, 29.73, 29.62, 29.53, 29.02, 26.19, 26.13, 26.08. MALDI-TOF-MS: m/z calculated for $C_{62}H_{98}N_2O_{14}$+Na$^+$: 1117.69 [M+Na]$^+$; observed 1117.73.

PH-C$_{12}$-EG$_4$

Compound **5** (60 mg, 0.055 mmol) was dissolved in ethyl acetate (2 mL). Pd/C (10 wt%, 6 mg, 0.005 mmol) was added and the mixture was purged with H$_2$. The reaction mixture was stirred at room temperature under H$_2$ atmosphere (with a balloon). Extra Pd/C (50 mg, 0.042 mmol) was added after 8 hours and the reaction mixture was stirred overnight at room temperature under H$_2$ atmosphere. The reaction mixture was filtered through filter paper, washed with DCM (20 mL) and concentrated in vacuo. The crude was purified with column chromatography (DCM/MeOH 98/2 – 88/12, 10 CV), yielding **PH-C$_{12}$-EG$_4$** (29 mg, 58%). ^{1}H NMR (400 MHz, CDCl$_3$ δ): 12.92 (b, 2H, N$\underline{H}$), 7.45 (s, 2H, Ar), 4.09 (t, 4H, ArOC$\underline{H_2}$CH$_2$), 3.74-3.54 (m, 32H, OC$\underline{H_2}$CH$_2$), 3.43 (t, 4H, CH$_2$C$\underline{H_2}$O), 1.88 (p, 4H, ArOCH$_2$C$\underline{H_2}$), 1.62-1.44 (m, 8H, C$\underline{H_2}$CH$_2$O, ArOCH$_2$CH$_2$C$\underline{H_2}$), 1.43-1.21 (m, 28H, aliphatic). ^{13}C NMR (100 MHz, CDCl$_3$ δ): 157.49, 153.62, 121.58, 106.46, 72.68, 71.67, 70.71, 70.67, 70.65, 70.43, 70.14, 69.34, 61.81, 29.77, 29.75, 29.73, 29.65, 29.54, 29.03, 26.22, 26.10. MALDI-TOF-MS: *m/z* calculated for C$_{48}$H$_{86}$N$_2$O$_{14}$+Na$^+$: 937.60 [M+Na]$^+$; observed 937.62.
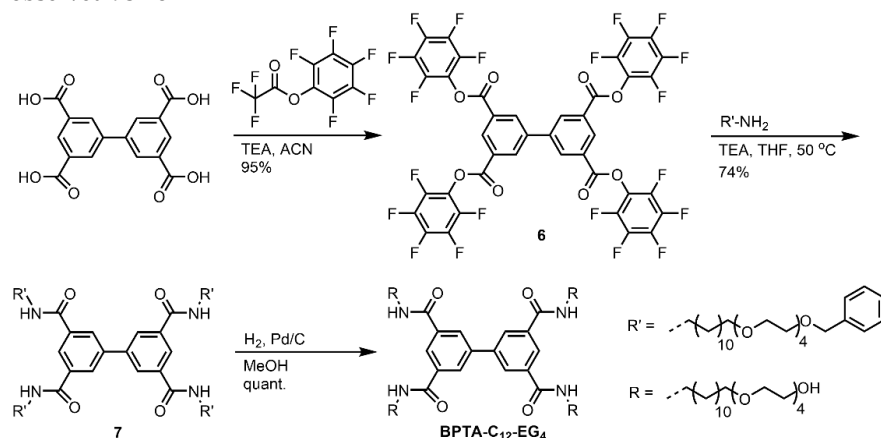
Tetrakis(perfluorophenyl) [1,1'-biphenyl]-3,3',5,5'-tetracarboxylate (6)

A round bottom flask was charged with [1,1'-biphenyl]-3,3',5,5'-tetracarboxylic acid[56] (650 mg, 1.97 mmol), triethylamine (1.59 g, 15.7 mmol) and ACN (60 mL). A solution of perfluorophenyl 2,2,2-trifluoroacetate (3.31 g, 11.8 mmol) in ACN (10 mL) was added dropwise. The reaction mixture was stirred under Ar atmosphere at room temperature overnight. The mixture was cooled with an ice bath afterwards. The solids were collected by vacuum filtration and were washed with cold ACN, yielding **6** (1.85 g, 95%). ^{1}H NMR (400 MHz, CDCl$_3$ δ): 9.07 (s, 2H, Ar), 8.81 (s, 4H, Ar). ^{19}F NMR (375 MHz, CDCl$_3$ δ): -152.14 (m, 8F), -156.48 (t, 4F), - 161.46 (m, 8F).

N^3,N$^{3'}$,N^5,N$^{5'}$-tetrakis(1-phenyl-2,5,8,11,14-pentaoxahexacosan-26-yl)-[1,1'-biphenyl]-3,3',5,5'-tetracarboxamide (7)

A flame-dried two-neck round bottom flask was charged with **6** (200 mg, 0.20 mmol) and dry THF (20 mL). The solution was stirred in an ice bath and a solution of 1-phenyl-2,5,8,11,14-pentaoxahexacosan-26-amine[39] (0.75 g, 1.61 mmol) and triethylamine (0.16 g, 1.61 mmol) in dry THF (3 mL) was added dropwise. After 10 minutes the reaction mixture was allowed to heat up to 50 °C and the mixture was stirred overnight. The yellowish solution was concentrated in vacuo and the crude material was dissolved in CHCl$_3$. The solution was washed with NaOH (1M), HCl

(1M) and brine. The organic layer was dried with MgSO$_4$, filtered and the solvent was removed in vacuo. The resulting solid was further purified by column chromatography (CHCl$_3$/MeOH 97/3) to yield **7** (0.32 g, 75%). ^{1}H NMR (400 MHz, CDCl$_3$ δ): 8.24 (s, 6H, Ar biphenyl), 7.35-7.28 (m, 20H, Ar benzyl), 6.89-6.81 (m, 4H, amides), 4.52 (s, 8H, OC$\underline{H}_2$Ar), 3.67-3.50 (m, 64H, OC$\underline{H}_2$C$\underline{H}_2$), 3.46 (q, 8H, NHC$\underline{H}_2$CH$_2$), 3.42-3.34 (t, 8H, CH$_2$C$\underline{H}_2$O), 1.63 (q, 8H, NHCH$_2$C$\underline{H}_2$), 1.52 (q, 8H, C$\underline{H}_2$CH$_2$O), 1.44-1.19 (m, 64H, aliphatic). ^{13}C NMR (100 MHz, CDCl$_3$ δ): 166.26, 140.23, 138.14, 135.71, 128.56, 128.33, 127.74, 127.59, 124.98, 73.24, 71.54, 70.64, 70.62, 70.60, 70.02, 69.40, 40.39, 39.70, 29.61, 29.56, 29.49, 29.44, 29.40, 29.38, 29.22, 26.96, 26.04. MALDI-TOF-MS: m/z calculated for C$_{124}$H$_{198}$N$_4$O$_{24}$+Na$^+$: 2150.43 [M+Na]$^+$; observed 2150.42; m/z calculated for C$_{124}$H$_{198}$N$_4$O$_{24}$+K$^+$: 2166.54 [M+K]$^+$; observed 2166.40.

BPTA-C$_{12}$-EG$_4$

A round bottom flask was charged with **7** (300 mg, 0.14 mmol) and methanol (15 mL). The flask was flashed with N$_2$ (g) and Pd/C (10 wt%, 141 mg) was added. The reaction mixture was stirred at room temperature under H$_2$ atmosphere (with a balloon) overnight. The mixture was filtered over celite and concentrated in vacuo, yielding **BPTA-C$_{12}$-EG$_4$** (262 mg, quant.). ^{1}H NMR (400 MHz, CDCl$_3$ δ): 8.29 (s, 4H, Ar biphenyl), 8.27 (s, 2H, Ar biphenyl), 7.12-7.06 (m, 4H, amides), 3.73-3.69 (m, 8H, CH$_2$C$\underline{H}_2$OH), 3.67-3.54 (m, 56H, OC$\underline{H}_2$C$\underline{H}_2$), 3.51-3.38 (m, 16H, NHC$\underline{H}_2$CH$_2$, CH$_2$C$\underline{H}_2$O), 1.64 (q, 8H, NHCH$_2$C$\underline{H}_2$), 1.53 (q, 8H, C$\underline{H}_2$CH$_2$O), 1.43-1.18 (m, 64H, aliphatic). ^{13}C NMR (100 MHz, CDCl$_3$ δ): 166.50, 140.04, 135.60, 128.48, 125.14, 72.58, 71.56, 70.58, 70.53, 70.51, 70.24, 69.99, 61.65, 40.41, 29.55, 29.50, 29.45, 29.43, 29.37, 29.24, 26.99, 26.02. MALDI-TOF-MS: m/z calculated for C$_{96}$H$_{174}$N$_4$O$_{24}$+Na$^+$: 1790.24 [M+Na]$^+$; observed 1790.24.
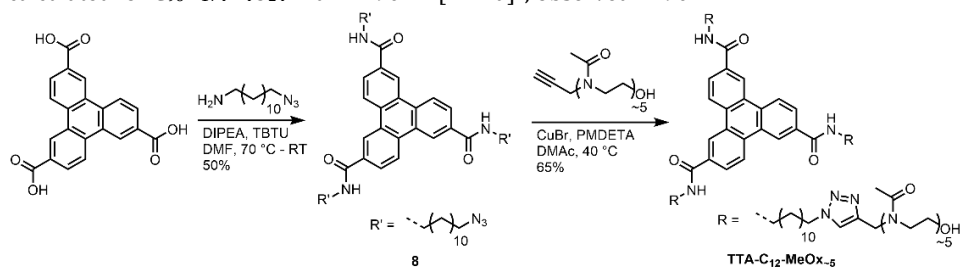
N^2,N^6,N^{10}-tris(12-azidododecyl)triphenylene-2,6,10-tricarboxamide (8)

Triphenylene-2,6,10-tricarboxylic acid[57] (49.9 mg, 0.14 mol) was dissolved in dry DMF (0.5 mL) in a 10 mL round bottom flask at 70 °C under argon atmosphere. Then DIPEA (0.15 mL, 0.86 mmol) was added to help dissolve the acid and after it was fully dissolved, TBTU (158.4 mg, 0.49 mmol) dissolved in 0.5 mL of DMF was added. The reaction was taken from the heating plate and after one minute of cooling down, 12-azidododecan-1-amine[58] (110 mg, 0.52 mmol) dissolved in 0.2 mL DMF was added to the reaction. After 3 hours of stirring, the reaction was diluted in 50 mL ethyl acetate and washed with water, 1 M HCl, 1 M NaOH, water and brine. The organic layer was dried with MgSO$_4$. The ethyl acetate was evaporated in vacuo giving the crude product, which was loaded onto silicon to be purified with column chromatography. The automated column was performed with DCM/EtOAc (gradient 100/0 to 90/10 v/v), yielding **8** (68 mg, 50%). ^{1}H NMR (400 MHz, DMSO-d$_6$ δ): 9.30 (s, 3H, triphenylene), 9.00 (d, , 3H, triphenylene), 8.90 (m, 3H, triphenylene), 8.27 (m, 3H, amides), 3.25 (t, 6H, CH$_2$C$\underline{H}_2$N$_3$), 1.62 (q, 6H, NHC$\underline{H}_2$CH$_2$), 1.50–1.42 (m, 6H, C$\underline{H}_2$CH$_2$N$_3$), 1.23 (m, 54H, aliphatic). FT-IR (ATR) ν (cm-1): 3244, 3074, 2923, 2853, 2092, 1717, 1631, 1576, 1547, 1498, 1465, 1340, 1313, 1282, 1153, 891, 838, 787, 739, 704, 647, 631,

557, 476. MALDI-TOF-MS: m/z calculated for $C_{57}H_{84}N_{12}O_3+Na^+$: 1007.67 [M+Na]$^+$; observed 1007.68.

TTA-C$_{12}$-MeOx$_{~5}$

8 (20.1 mg, 0.020 mmol), PMDETA (35 μL, 0.17 mmol) and disperse, alkyne-functionalized penta-2-methyloxazoline (obtained from the group of prof. Richard Hoogenboom, 60.02 mg, 0.12 mmol) were dissolved in DMAc (2 mL) in a 10 mL round bottom flask. The reaction mixture was deoxygenated by bubbling argon for 20 minutes. Copper(I) bromide (7.80 mg, 0.054 mmol) was added and the reaction mixture turned slightly turquoise/green. The reaction was stirred overnight under argon atmosphere. The material was purified by dialysis against water (molecular weight cut-off (MWCO) = 1000 Da, Spectra/Por Biotech CE Membranes) for 2 days, after which the material was dried by lyophilization, yielding **BTA-C$_{12}$-MeOx$_{~5}$** as a fluffy white solid that became a brittle brown solid over time (32 mg, 64.7 %). ^{1}H NMR (400 MHz, DMSO-d$_6$ δ): 9.30 (s, 3H, triphenylene), 9.00 (d, 3H, triphenylene) 8.91 (m, 3H, triphenylene), 8.27 (m, 3H, amides), 8.17–7.56 (m, 3H, triazole), 4.90-4.67 (m, 3H, CH$_2$O$\underline{H}$), 4.60-4.44 (m, 6H, triazole-C$\underline{H}_2$-N), 4.35-4.22 (m, 6H, CH$_2$C$\underline{H}_2$-triazole), 3.56-3.11 (m, disperse NC$\underline{H}_2$C$\underline{H}_2$N), 2.06-1.91 (m, disperse oxazoline CH$_3$), 1.76 (m, 6H, NHC$\underline{H}_2$CH$_2$), 1.61 (m, 6H, NHCH$_2$C$\underline{H}_2$), 1.42-1.08 (m, 54H, aliphatic). FT-IR (ATR) ν (cm-1): 3650-3100, 2925, 2853, 1633, 1573, 1548, 1475, 1419, 1363, 1318, 1258, 1035, 968, 911, 848, 608, 500. MALDI-TOF-MS: m/z calculated for $C_{126}H_{201}N_{27}O_{21}+Na^+$: 2451.54 [BTA-C$_{12}$-MeOx$_5$+Na]$^+$; observed 2451.57. The dispersity of the blocks can be seen from the other peaks of m/z 85.04 more or less, corresponding to one oxazoline unit.
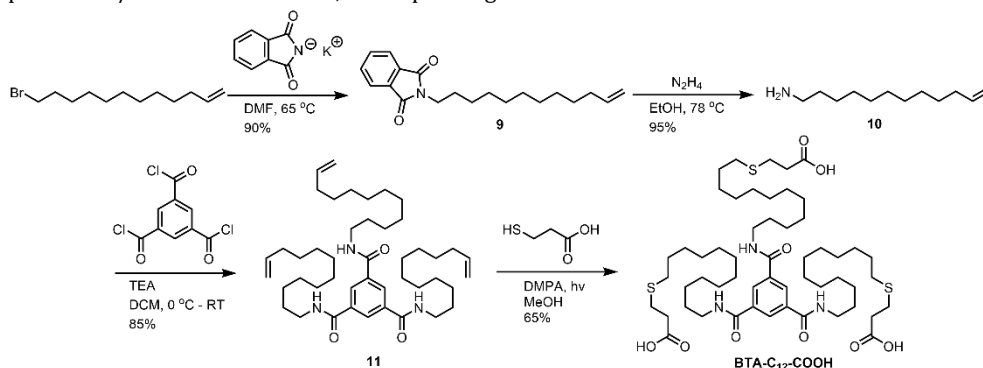
2-(dodec-11-en-1-yl)isoindoline-1,3-dione (9)

The synthesis was adapted from a literature protocol.[59] A 250 mL round bottom flask was charged with 12-bromododec-1-ene (7.5 g, 30.3 mmol), potassium phthalimide (8.4 g, 45.5 mmol) and DMF (45 mL). The reaction mixture was heated to 60 °C and stirred under an atmosphere of dry argon for 2 hours. DCM (30 mL) was added to the mixture and was extracted with HCL (aq. pH = 2). The aqueous layers were extracted two times with DCM. The organic fractions were combined and dried with MgSO$_4$. The mixture was then filtered and concentrated *in vacuo* to yield **9** as white crystals (8.55 g, 90%). ^{1}H NMR (400 MHz, CDCl$_3$ δ): 7.91 – 7.79 (dd, 2H, phthalimide), 7.71 (dd, 2H, phthalimide), 5.81 (m, 1H, CH$_2$C$\underline{H}$=CH$_2$), 4.99- 4.92 (m, 2H, CH$_2$CH=C$\underline{H}_2$), 3.71 – 3.63 (m, 2H, CH$_2$C$\underline{H}_2$N), 2.08 – 1.98 (m, 2H, C$\underline{H}_2$CH=CH$_2$), 1.67 (t, 2H, C$\underline{H}_2$CH$_2$N), 1.36-1.23 (m, 14H, aliphatic). ^{13}C NMR (100 MHz, CDCl$_3$ δ): 168.49, 139.27, 133.83, 132.21, 123.15, 114.09, 38.10, 33.81, 29.50, 29.46, 29.44, 29.19, 29.12, 28.93, 28.61, 26.87. FT-IR

(ATR) ν (cm⁻¹): 3454, 3062, 2916, 2849, 1774, 1696, 1614, 1595, 1465, 1436, 1400, 1374, 1337, 1287, 1189, 1055, 921, 900, 868, 793, 719, 625, 531.

dodec-11-en-1-amine (10)

The synthesis was adapted from a literature protocol.[59] To a stirred solution of **9** (8.35 g, 26.6 mmol) in a 250 mL round bottom flask in 65 mL ethanol, hydrazine monohydrate (1.7 g, 53.3 mmol) was added. The reaction mixture was allowed to stir overnight at reflux. The reaction mixture was filtered to remove the white precipitation that was formed during the reaction. DCM (50 mL) was subsequently added to the filtrate and it was extracted with NaOH (1M, 100 mL) solution. The organic fraction was collected, dried with MgSO₄, filtered and concentrated *in vacuo* to obtain compound **10** as a slightly yellow-colored liquid (4.85 g, 95%). ^{1}H NMR (400 MHz, CDCl₃ δ): 5.81 (m, 1H, CH₂C$\underline{H}$=CH₂), 5.04 – 4.89 (m, 2H, CH₂CH=C$\underline{H}_2$), 2.67 (t, 2H, CH₂C$\underline{H}_2$NH₂), 2.04 (m, 2H, C$\underline{H}_2$CH=CH₂), 1.48-1.16 (m, 16H, aliphatic). ^{13}C NMR (100 MHz, CDCl₃, δ): 139.27, 114.10, 42.26, 33.83, 29.63, 29.56, 29.50, 29.15, 28.95, 26.90. FT-IR (ATR) ν (cm⁻¹): 3327, 3290, 3077, 2921, 2851, 1828, 1642, 1628, 1543, 1462, 1368, 1304, 1255, 1152, 992, 909, 729, 639. MALDI-TOF-MS: *m/z* calculated for $C_{12}H_{25}N+H^+$: 184.21 [M+H]⁺; observed 184.14.

N¹,N³,N⁵-tri(dodec-11-en-1-yl)benzene-1,3,5-tricarboxamide (11)

An oven-dried 250 mL round bottom flask was charged with **10** (4.1 g, 22.4 mmol), triethylamine (7.12 mL, 51.2 mmol) and 75 mL dry DCM and was allowed to stir at 0 °C in an ice bath. Benzene-1,3,5-tricarbonyl trichloride (1.7 g, 6.4 mmol) was added dropwise from DCM, while the reaction mixture was allowed to stir and warm up to room temperature. The crude was a blurry suspension and therefore TEA salts were first removed by filtration. Then, the reaction product was isolated by automated column chromatography (MeOH/DCM 0/100 – 15/85 v/v) and the pure and impure fractions were collected separately. Again, automated column chromatography was performed to purify the impure fraction further (MeOH/DCM 0/100/0 – 5/95 v/v). The pure fractions were combined and concentrated *in vacuo* and **11** was obtained as a white solid (3.8 g, 85%). However, small traces of phthalimide impurity (<10%) were visible with ^{1}H NMR. Therefore, compound **11** was split in half. One fraction was purified further by recrystallization using MeOH/H₂O (90/10, v/v), which resulted in a totally pure reaction product. ^{1}H NMR (400 MHz, CDCl₃ δ): 8.32 (s, 3H, Ar), 7.76 (t, 3H, amides), 5.81 (ddt, 3H, CH₂C$\underline{H}$=CH₂), 4.96 (m, 6H, CH₂CH=C$\underline{H}_2$), 3.44 (m, 6H, NHC$\underline{H}_2$CH₂), 2.04 (q, 6H, C$\underline{H}_2$CH=CH₂), 1.63 (q, 6H, NHCH₂C$\underline{H}_2$), 1.43-1.23 (m, 42H, aliphatic). ^{13}C NMR (100 MHz, CDCl₃, δ): 166.20, 139.22, 134.94, 128.25, 114.13, 40.52, 33.82, 29.58, 29.50, 29.47, 29.35, 29.16, 28.95, 27.07. FT-IR (ATR) ν (cm⁻¹): 3302, 3261, 3078, 2920, 2850, 1827, 1659, 1636, 1545, 1466, 1437, 1373, 1300, 1160, 992, 909, 721, 698, 551. MALDI-TOF-MS: *m/z* calculated for $C_{45}H_{75}N_3O_3+H^+$: 706.59 [M+H]⁺; observed 706.61; *m/z* calculated for $C_{45}H_{75}N_3O_3+Na^+$: 728.57 [M+Na]⁺; observed 728.57;

BTA-C₁₂-COOH

A 15 mL glass vial with stirring bean was charged with **11** (0.15 g, 0.212 mmol), DMPA (0.077 g, 0.319 mmol), 3-mercaptopropanoic acid (0.156 mL, 1.91 mmol) and 10 mL methanol. The solution was deoxygenated with argon bubbling for 15 minutes and subsequently transferred to an UV chamber for irritation with 365 nm UV light (315 – 400 nm) while stirring for 2 h. The reaction mixture was followed by TLC and it was concluded that the reaction product was precipitated out of the reaction mixture. Thus, compound **BTA-C₁₂-COOH** was conveniently

purified by paper filtration and drying overnight and was obtained as a white powder (0.143 g, 65%). ^{1}H NMR (400 MHz, CDCl$_3$ δ): 8.65 (t, 3H, amides), 8.36 (s, 3H, Ar), 3.43-3.16 (m, 6H, NHC$\underline{H}_2$CH$_2$), 2.64 (t, 6H, SC$\underline{H}_2$CH$_2$), 2.55-2.41(t, 12H, C$\underline{H}_2$SCH$_2$C$\underline{H}_2$), 1.56-1.41 (m, 12H, NHCH$_2$C$\underline{H}_2$, CH$_2$C$\underline{H}_2$S), 1.37-1.17 (m, 48H, aliphatic). ^{13}C NMR (100 MHz, CDCl$_3$, δ): 173.51, 165.89, 135.61, 128.75, 35.07, 31.51, 29.54, 29.48, 29.45, 29.26, 29.09, 28.67, 26.95, 26.87. FT-IR (ATR) ν (cm^{-1}): 3382, 2918, 2848, 1708, 1644, 1590, 1540, 1465, 1402, 1298, 1238, 1223, 925, 889, 816, 722, 684, 617, 469. LC-MS: m/z calculated for C$_{54}$H$_{93}$N$_3$O$_9$+H$^+$: 1024.62 [M+H]$^+$; observed 1024.75.

2.7 References

1   G. A. Silva, C. Czeisler, K. L. Niece, E. Beniash, D. A. Harrington, J. A. Kessler and S. I. Stupp, *Science*, 2004, **303**, 1352–1355.
2   P. Xing and Y. Zhao, *Small Methods*, 2018, **2**, 1700364.
3   P. Tripathi, L. Shuai, H. Joshi, H. Yamazaki, W. H. Fowle, A. Aksimentiev, H. Fenniri and M. Wanunu, *J. Am. Chem. Soc.*, 2020, **142**, 1680–1685.
4   B. Huang, M. Bates and X. Zhuang, *Annu. Rev. Biochem.*, 2009, **78**, 993–1016.
5   M. J. Rust, M. Bates and X. Zhuang, *Nat. Methods*, 2006, **3**, 793–795.
6   P. Nguyen-Tri, P. Ghassemi, P. Carriere, S. Nanda, A. A. Assadi and D. D. Nguyen, *Polymers*, 2020, **12**, 1142.
7   L. E. Franken, E. J. Boekema and M. C. A. Stuart, *Adv. Sci.*, 2017, **4**, 1600476.
8   R. Fernandez-Leiro and S. H. W. Scheres, *Nature*, 2016, **537**, 339–346.
9   T. Nakane, A. Kotecha, A. Sente, G. McMullan, S. Masiulis, P. M. G. E. Brown, I. T. Grigoras, L. Malinauskaite, T. Malinauskas, J. Miehling, T. Uchański, L. Yu, D. Karia, E. V. Pechnikova, E. de Jong, J. Keizer, M. Bischoff, J. McCormack, P. Tiemeijer, S. W. Hardwick, D. Y. Chirgadze, G. Murshudov, A. R. Aricescu and S. H. W. Scheres, *Nature*, 2020, **587**, 152–156.
10   C. J. Newcomb, T. J. Moyer, S. S. Lee and S. I. Stupp, *Curr. Opin. Colloid Interface Sci.*, 2012, **17**, 350–359.
11   H. Cui, T. K. Hodgdon, E. W. Kaler, L. Abezgauz, D. Danino, M. Lubovsky, Y. Talmon and D. J. Pochan, *Soft Matter*, 2007, **3**, 945–955.
12   H. Friedrich, P. M. Frederik, G. De With and N. A. J. M. Sommerdijk, *Angew. Chemie - Int. Ed.*, 2010, **49**, 7850–7858.
13   N. D. Burrows and R. L. Penn, *Microsc. Microanal.*, 2013, **19**, 1542–1553.
14   C. Böttcher, in *Analytical Methods in Supramolecular Chemistry, 1&2, Second edition*, ed. C. A. Schalley, John Wiley & Sons, Ltd, 2012, pp. 629–709.
15   K. Murata and M. Wolf, *Biochim. Biophys. Acta - Gen. Subj.*, 2018, **1862**, 324–334.
16   H. Weissman and B. Rybtchinski, *Curr. Opin. Colloid Interface Sci.*, 2012, **17**, 330–342.
17   S. Zhong and D. J. Pochan, *Polym. Rev.*, 2010, **50**, 287–320.
18   K. A. Taylor and R. M. Glaeser, *Rev. Sci. Instrum.*, 1973, **44**, 1546–1547.
19   R. Danev, B. Buijsse, M. Khoshouei, J. M. Plitzko and W. Baumeister, *Proc. Natl. Acad. Sci.*, 2014, **111**, 15635–15640.
20   H. V. Berlepsch, K. Ludwig, B. Schade, R. Haag and C. Böttcher, *Adv. Colloid Interface Sci.*, 2014, **208**, 279–292.
21   O. Jaudouin, J. J. Robin, J. M. Lopez-Cuesta, D. Perrin and C. Imbert, *Polym. Int.*, 2012, **61**, 495–510.
22   P. Król, *Prog. Mater. Sci.*, 2007, **52**, 915–1015.
23   E. M. Timmers, P. M. Fransen, Á. González Gariá, S. M. C. Schoenmakers, J. R. Magana, J. W. Peeters, R. Tennebroek, I. Van Casteren, R. Tuinier, H. M. Janssen and I. K. Voets, *Polym. Chem.*, 2021, **12**, 2891–2903.
24   A. . Kabanov, T. K. Bronich, V. A. Kavanov, K. Yu and A. Eisenberg, *J. Am. Chem. Soc.*, 1998, **120**, 9941–9942.
25   E. M. Timmers, J. R. Magana, S. M. C. Schoenmakers, P. Michel Fransen, H. M. Janssen and I. K. Voets, *Int. J. Mol. Sci.*, 2021, **22**, 337.
26   J. A. Elvidge and A. P. Redman, *J. Chem. Soc.*, 1960, 1710–1714.
27   M. Suárez, J. M. Lehn, S. C. Zimmerman, A. Skoulios and B. Heinrich, *J. Am. Chem. Soc.*, 1998, **120**, 9526–9532.
28   T. Kaseyama, S. Furumi, X. Zhang, K. Tanaka and M. Takeuchi, *Angew. Chemie*, 2011, **123**, 3768–3771.

29   R. Inoue, M. Hasegawa and Y. Mazaki, *Chem. Lett.*, 2015, **44**, 448–450.
30   J. Otsuki, Y. Okabe, S. Eitaki, Y. Sei and K. Yamaguchi, *Chem. Lett.*, 2006, **35**, 1256–1257.
31   B. M. Schulze, N. T. Shewmon, J. Zhang, D. L. Watkins, J. P. Mudrick, W. Cao, R. Bou Zerdan, A. J. Quartararo, I. Ghiviriga, J. Xue and R. K. Castellano, *J. Mater. Chem. A*, 2014, **2**, 1541–1549.
32   N. T. Shewmon, D. L. Watkins, J. F. Galindo, R. B. Zerdan, J. Chen, J. Keum, A. E. Roitberg, J. Xue and R. K. Castellano, *Adv. Funct. Mater.*, 2015, **25**, 5166–5177.
33   N. J. Van Zee, B. Adelizzi, M. F. J. Mabesoone, X. Meng, A. Aloi, R. H. Zha, M. Lutz, I. A. W. Filot, A. R. A. Palmans and E. W. Meijer, *Nature*, 2018, **558**, 100–103.
34   N. J. Van Zee, M. F. J. Mabesoone, B. Adelizzi, A. R. A. Palmans and E. W. Meijer, *J. Am. Chem. Soc.*, 2020, **142**, 20191–20200.
35   M. L. Ślęczkowski, M. F. J. Mabesoone, P. Ślęczkowski, A. R. A. Palmans and E. W. Meijer, *Nat. Chem.*, 2021, **13**, 200–207.
36   R. Hoogenboom, *Angew. Chemie - Int. Ed.*, 2009, **48**, 7978–7994.
37   M. Grube, M. N. Leiske, U. S. Schubert and I. Nischang, *Macromolecules*, 2018, **51**, 1905–1916.
38   N. M. Matsumoto, R. P. M. Lafleur, X. Lou, K. C. Shih, S. P. W. Wijnands, C. Guibert, J. W. A. M. Van Rosendaal, I. K. Voets, A. R. A. Palmans, Y. Lin and E. W. Meijer, *J. Am. Chem. Soc.*, 2018, **140**, 13308–13316.
39   C. M. A. Leenders, L. Albertazzi, T. Mes, M. M. E. Koenigs, A. R. A. Palmans and E. W. Meijer, *Chem. Commun.*, 2013, **49**, 1963–1965.
40   S. P. W. Wijnands, W. Engelen, R. P. M. Lafleur, E. W. Meijer and M. Merkx, *Nat. Commun.*, 2018, **9**, 65.
41   G. Morgese, B. F. M. Waal, S. Varela-Aramburu, A. R. A. Palmans, L. Albertazzi and E. W. Meijer, *Angew. Chemie*, 2020, **132**, 17382–17386.
42   S. I. S. Hendrikse, L. Su, T. P. Hogervorst, R. P. M. Lafleur, X. Lou, G. A. van der Marel, J. D. C. Codee and E. W. Meijer, *J. Am. Chem. Soc.*, 2019, **141**, 13877–13886.
43   M. H. Bakker, C. C. Lee, E. W. Meijer, P. Y. W. Dankers and L. Albertazzi, *ACS Nano*, 2016, **10**, 1845–1852.
44   R. P. M. Lafleur, S. Herziger, S. M. C. Schoenmakers, A. D. A. Keizer, J. Jahzerah, B. N. S. Thota, L. Su, P. H. H. Bomans, N. A. J. M. Sommerdijk, A. R. A. Palmans, R. Haag, H. Friedrich, C. Böttcher and E. W. Meijer, *J. Am. Chem. Soc.*, 2020, **142**, 17644–17652.
45   C. Boettcher, H. Stark and M. Van Heel, *Ultramicroscopy*, 1996, **62**, 133–139.
46   C. M. A. Leenders, M. B. Baker, I. A. B. Pijpers, R. P. M. Lafleur, L. Albertazzi, A. R. A. Palmans and E. W. Meijer, *Soft Matter*, 2016, **12**, 2887–2893.
47   B. Kemper, L. Zengerling, D. Spitzer, R. Otter, T. Bauer and P. Besenius, *J. Am. Chem. Soc.*, 2018, **140**, 534–537.
48   J. Liang, J. Liang, A. Hao and P. Xing, *Nanoscale*, 2021, **13**, 12929-12937.
49   O. Zagorodko, T. Melnyk, O. Rogier, V. J. Nebot and M. J. Vicent, *Polym. Chem.*, 2021, **12**, 3478–3487.
50   B. N. S. Thota, X. Lou, D. Bochicchio, T. F. E. Paffen, R. P. M. Lafleur, J. L. J. van Dongen, S. Ehrmann, R. Haag, G. M. Pavan, A. R. A. Palmans and E. W. Meijer, *Angew. Chemie - Int. Ed.*, 2018, **57**, 6843–6847.
51   X. Lou, R. P. M. Lafleur, C. M. A. Leenders, S. M. C. Schoenmakers, N. M. Matsumoto, M. B. Baker, J. L. J. van Dongen, A. R. A. Palmans and E. W. Meijer, *Nat. Commun.*, 2017, **8**, 15420.
52   S. J. Ludtke, P. R. Baldwin and W. Chiu, *J. Struct. Biol.*, 1999, **128**, 82–97.
53   M. Van Heel, G. Harauz, E. V. Orlova, R. Schmidt and M. Schatz, *J. Struct. Biol.*, 1996, **116**, 17–24.
54   L. Hansson, R. Carlson, S. Sjöberg, E. Huskowska, M. Lounasmaa, J. Krätsmar-Smogrovic, A. Valent, T. Alminger, M. Erickson, I. Grundevik, I. Hagin, K.-J. Hoffman, S. Johansson, S. Larsson, I. Löfberg, K. Ohlson, B. Persson, I. Skånberg and L. Tekenbergs-Hjelte, *Acta Chem. Scand.*, 1989, 43, 304–306.
55   A. S. Drager and D. F. O'Brien, *J. Org. Chem.*, 2000, **65**, 2257–2260.
56   M. Mazik, A. Ko and R. V May, *J. Org. Chem.*, 2006, **71**, 7854–7857.
57   Y. N. Gong, X. W. Wei, L. H. He, Y. Q. Wen, Y. W. Ren, Y. R. Xie and D. C. Zhong, *Dalt. Trans.*, 2017, **46**, 7403–7407.
58   C. M. A. Leenders, G. Jansen, M. M. M. Frissen, R. P. M. Lafleur, I. K. Voets, A. R. A. Palmans and E. W. Meijer, *Chem. - A Eur. J.*, 2016, **22**, 4608–4615.
59   M. Tanaka, T. Sawaguchi, Y. Sato, K. Yoshioka and O. Niwa, *Langmuir*, 2011, **27**, 170–178.

Chapter 3

Elucidating the Dynamic Behavior of Synthetic Supramolecular Polymers in Water by Hydrogen/ Deuterium Exchange Mass Spectrometry

Abstract: A comprehensive understanding of the structure, mechanism of self-assembly and dynamics of one-dimensional supramolecular polymers in water is essential for their application as biomaterials. Although a plethora of techniques are available to study the first properties, there is a paucity in the possibilities to study dynamic exchange of monomers between supramolecular polymers in solution. Recently hydrogen/deuterium exchange mass spectrometry (HDX-MS) was introduced by our group to characterize the dynamic nature of synthetic supramolecular polymers in water with only a minimal perturbation of the chemical structure. To further expand the application of this powerful technique some essential experimental aspects have been reaffirmed and the technique has been applied to a diverse library of assemblies. HDX-MS is widely applicable if there are exchangeable hydrogen atoms protected from direct contact with the solvent and if the monomer concentration is sufficiently high to ensure the presence of supramolecular polymers during dilution. We demonstrate that the dynamic behaviour as probed by HDX-MS is influenced by the internal order within the supramolecular polymers and by the self-assembly mechanism. In addition, we show that HDX-MS is a valuable technique to confirm the co-assembly of supramolecular building blocks and to evaluate the dynamics of the individual components within the co-assemblies.
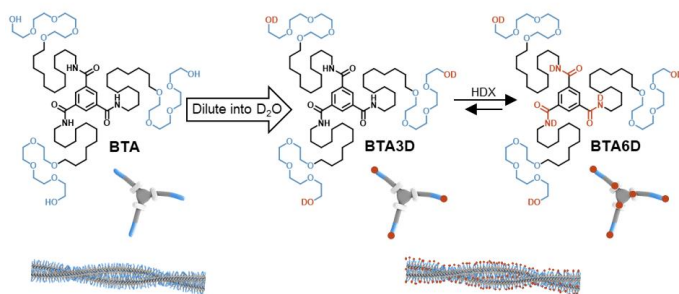
3.1 Introduction

Supramolecular assemblies in water attract a great deal of interest because a versatile library of assemblies can be formed depending on the molecular structure of the monomer.[1–3] Particularly promising are one-dimensional fibrillar structures that can be applied as synthetic biomaterials due to their resemblance to natural fibrillar assemblies and due to their modularity, which permits the introduction of a variety of functional groups.[4–12] Both the mechanism of formation of the assemblies as well as the rate of the dynamic exchange of monomers between the assemblies has been used as a handle to tune the resulting structures.[13–15] In theory, the dynamic behavior of supramolecular systems could be tuned to match the inherent dynamic behavior of the supramolecular interactions in living tissues.[16–18] A fundamental understanding of their structure, mechanism of self-assembly and dynamic behavior is therefore essential for the creation of such intricate biomaterials.

Understanding the interplay between molecular structure, formation mechanism, and dynamic exchange is important to guide the application of one dimensional fibrillar assemblies in adaptive biomaterials. As a result, it is important to evaluate these properties simultaneously without changing the nature of the supramolecular assemblies. Microscopy techniques such as cryogenic transmission electron microscopy (cryoTEM) are available that visualize on nanometer length scales the morphologies formed by supramolecular systems close to their native state (Chapter 2).[19,20] In addition, spectroscopy techniques such as UV-Vis and CD spectroscopy allow to elucidate the mechanism with which monomers form supramolecular polymers in solution.[21] In contrast, analytical methods that accurately quantify the dynamic behavior of a monomer exchanging between polymers, or the movement of a monomer along a polymer chain, typically require the attachment of molecular probes to the monomer of interest, such as spin labels or fluorescent dyes.[22–26] These probes are often rather bulky, which may have a significant influence on the local intermolecular interactions and may change the hydrophobic/hydrophilic balance within the monomer. As a result, the solubility and dynamic behavior of the monomer with the probe attached may be significantly altered compared to the "bare" monomer.

To avoid the need for molecular probes that change the monomer's character, our group started to explore hydrogen/deuterium exchange followed by mass spectrometry (HDX-MS) to track the dynamic behavior of supramolecular polymers in water.[27] HDX-MS is a key technique for studying the structural and dynamic aspects of proteins.[28–36] Hydrogen atoms in OH, NH and SH groups are labile and can exchange with labile hydrogen atoms of the surrounding solvent. Whereas the exchange of H to H is undetectable, exposing molecules with labile hydrogen atoms to a D_2O environment will lead to H to D replacements that increase the mass of the molecule by one unit per exchange event. The rate of molecular mass increase can be accurately monitored by MS. In the case of proteins, amide hydrogen atoms exhibit rapid exchange rates if they

are accessible to the solvent but show reduced exchange rates if they are hydrogen bonded and/or buried in hydrophobic regions. It is nowadays possible to obtain HDX structural resolution close to the amino acid level and to elucidate protein dynamics.[37–40] Additionally, HDX-MS has been used to reveal the mechanism of assembly and to quantify the rate constants of growth and disassembly of amyloid fibrils in solution.[41,42]

Schalley *et al* adapted HDX-MS to study supramolecular systems, and found that hydrogen bonding was important for the organization of their building blocks.[43–45] Inspired hereby, we applied HDX-MS to elucidate the dynamic behavior of benzene-1,3,5-tricarboxamide (BTA)-based supramolecular polymers in water.[27] Later, HDX-MS was used to reveal a stabilization of the exchange dynamics when BTAs with a linear periphery were co-assembled with BTAs with a dendritic periphery.[46] Although the HDX processes for supramolecular polymers and for proteins share a lot of similarities, they also have some important differences. Most notably, the HDX events in proteins are generally mediated by conformational fluctuations without changing the primary structure of the proteins, whereas H/D exchange in supramolecular assemblies occurs after the release of a monomer into the solution. Accordingly, experimental aspects which have been optimized and widely accepted in HDX-MS for protein samples need to be re-evaluated for supramolecular polymers.

In this chapter, HDX-MS will be applied to previously studied BTA-based supramolecular polymers in water[27,47] to address the effect of dilution on the HDX-MS analysis and to describe an analysis method that quantifies the abundances of all deuterated species as a function of time. Then, we compare the dynamic behavior of **BTA** (Figure 1) to that of 3 other supramolecular monomers that polymerize via different formation mechanisms, cooperative or isodesmic, and form intrinsically different morphologies as revealed by cryoTEM. We recently elucidated that **BTA** forms a double helical structure in water.[48] In contrast, diacetylene bis-urea amphiphile (**BU**) forms fibrous bundles,[49] and the two benzotrithiophenes (**BTT-5F** and **BTT**) form single fibers (Figure 1).[13] **BTT-5F** polymerizes via an isodesmic mechanism, whereas all other monomers polymerize via a cooperative mechanism. We find that there is a correlation between the rate and degree of H/D exchange, the formation mechanism and the morphology. Additionally, we show that HDX-MS can help in the evaluation of the exchange dynamics of supramolecular copolymers. All in all, we conclude that HDX-MS is applicable to all supramolecular polymers in water, as long as there are exchangeable hydrogen atoms in the monomer protected from direct contact with water in the polymer and the monomer concentration is sufficient to ensure the presence of supramolecular polymers during the H/D exchange in the solution.
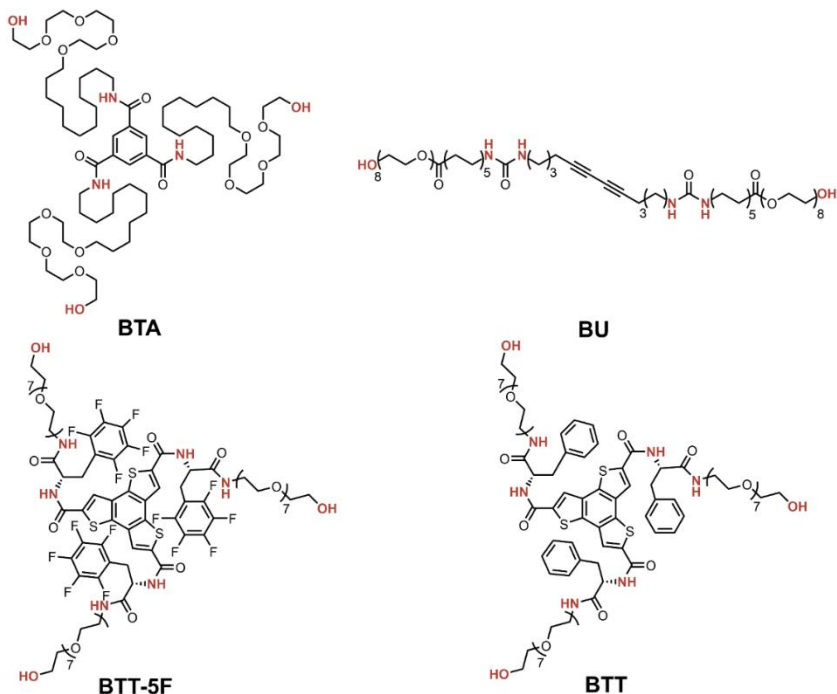
Figure 1. Chemical structures of the supramolecular building blocks of **BTA**, **BU**, **BTT-5F** and **BTT**. Hydrogen atoms prone to H/D exchange are shown in red.

3.2 Experimental aspects and analysis of HDX-MS in synthetic supramolecular polymers

Before discussing the interplay between morphology, mechanism of formation and dynamic behavior in the compounds shown in Figure 1, we first address some fundamental aspects of the HDX-MS analysis used in this work. The aim of this assessment is to ensure that HDX-MS can be widely and reliably used, and that the information obtained on exchange rates does not depend on the experimental parameters applied. For this purpose, we select the well-studied **BTA**, which contains 6 labile hydrogen atoms: 3 OH groups in the periphery and 3 NH groups in the core. Our previous results showed that dilution of a 500 μM solution of assembled **BTA** in H_2O 100x into D_2O showed two distinct distributions corresponding to BTA3D and BTA6D when analyzed with electrospray ionization MS (ESI-MS). BTA3D is formed instantaneously upon dilution by the exchange of the three peripheral OH groups into three OD groups (Figure 2A). BTA6D is formed over time as also the three labile NH hydrogen atoms get exchanged into deuterium atoms.
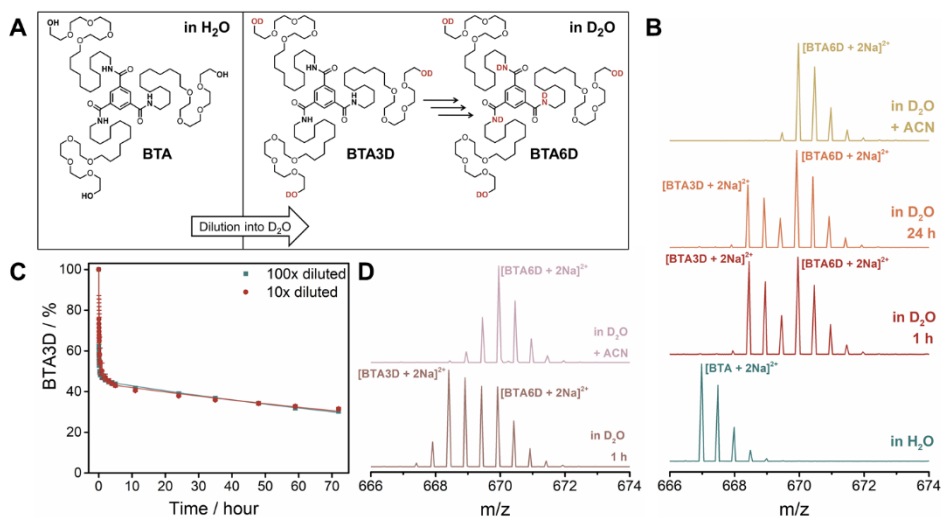
Figure 2. (A) Schematic representation of the HDX-MS process of **BTA** including the chemical structures of **BTA** analogues before and after dilution into D_2O. (B) ESI-MS spectra of the doubly charged ions of **BTA** after 100x dilution of a 500 μM sample into H_2O, D_2O or a 1/1 D_2O/ACN mixture. (C) HDX-MS curves of a 500 μM sample of **BTA** after 100x dilution and 10x dilution into D_2O (T = room temperature). The percentage of BTA3D is plotted over time, calculated from three separate experiments. Error bars represent the standard deviation and lines are added to guide the eye. (D) ESI-MS spectra of the doubly charged ions of **BTA** after 10x dilution of a 500 μM sample diluted into D_2O or a 1/1 D_2O/ACN mixture.

An important aspect of HDX-MS is to accurately extract the abundance of the differently deuterated species from the high-resolution MS spectra especially when remnant H_2O is present after dilution into D_2O. We therefore here devise a method to track the deuterated species over time and we will illustrate the calculations with **BTA**. Figure 2B shows the MS spectra of **BTA** after dilution in H_2O, D_2O and D_2O/acetonitrile (ACN). The latter solvent combination serves as a reference as **BTA** is molecularly dissolved herein.[50] In fact, BTA6D with its ^{13}C isotopes is the dominant distribution observed after 100x dilution in D_2O/acetonitrile (yellow spectrum), indicating that all labile hydrogen atoms are immediately exchanged when the BTAs are molecularly dissolved. However, the small peak at m/z 669.48 is indicative for BTA5D which is there because of D/H exchange from remnant H_2O after dilution. After 1 hour in D_2O, the peak corresponding to BTA3D has the same intensity as the peak corresponding to BTA6D (red spectrum), and after 24 hours the peak for BTA6D has grown at the expense of the peak for BTA3D (orange spectrum). The peaks between the monoisotopic peaks of BTA3D and BTA6D coincide with the isotope distribution of BTA3D and with artefacts introduced by D/H exchange of the deuterium atoms of BTA6D caused by a trace amount of H_2O present after the dilution. Therefore, we correct for the isotope distributions that overlap with the peaks of more deuterated BTAs and subtract the

theoretical percentage of BTAs formed by remnant H_2O such that only the percentage of intermediates that truly originate from H/D exchange is presented (see section 3.9.3 for details on the calculations). The result of the percentage of BTA3D as a function of time, corrected for isotopes and small amounts of H_2O after 100x dilution, is shown in Figure 2C. It is very similar to the previously reported results.[27]

Because of the non-covalent nature of the bonds holding supramolecular polymers together, the reduction in concentration by diluting a solution from H_2O into D_2O might affect the stability of the supramolecular polymers and thereby their dynamic behavior. Thus, an important experimental aspect to take into consideration is if the degree of dilution of the sample into D_2O affects the exchange. We compared the distribution of BTA3D when diluting an aqueous 500 μM sample of **BTA** 100x with that diluted 10x into D_2O. When a 10x dilution is used, the MS spectra are more complicated and contain prominent distributions of BTA2D, BTA4D and BTA5D (Figure 2D) because the H_2O concentration is about 10 vol% and cannot be ignored. When the statistical distributions for D/H exchange are taken into account, the abundance of the deuterated species can accurately be calculated (see section 3.9.3). Figure 2C shows that the percentage of BTA3D of a 100x and 10x diluted sample shows no significant differences as a function of time.

Finally, we observed for **BTA** that 100x dilution of samples with different starting concentrations (1 mM, 0.5 mM or 0.1 mM, Figure 3) does not affect the HDX exchange profile. The association constant in supramolecular polymers based on **BTA** is very high and the critical aggregation concentration (CAC) is well below 5 μM. Thus, the kinetic profiles are not affected by the start and end concentrations as long as the final concentration is above the CAC of the supramolecular polymer and the percentage of H_2O is taken into account during the analysis. When less-stable systems are considered (as in the case of **BTT-5F**, *vide infra*) care should be taken to ensure that the concentration is above the CAC to keep the molecules assembled after dilution into D_2O.
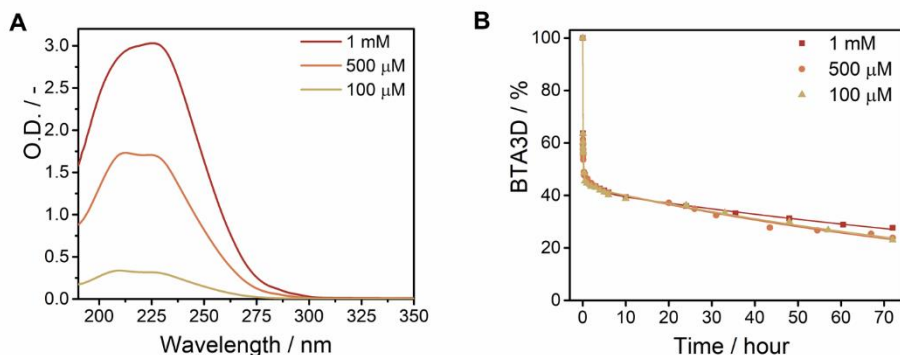
Figure 3. (A) UV spectra of **BTA** at different concentrations in H_2O. The UV spectra show the same maxima so **BTA** assembles independent of concentration in this range (l = 1 mm, T = 20 °C). (B) HDX-MS curves of 100x diluted samples of **BTA** with different initial concentrations (T = room temperature). The percentage of BTA3D is plotted over time and lines are added to guide the eye.

3.3 Analysis of the HDX experiments of several supramolecular polymers

To enable a proper comparison of the HDX-MS results between our four compounds, which all have different amounts of labile hydrogen atoms, the HDX data are visualized in such a way that we can track all species as a function of time. In this way, the information on the internal order and H/D exchange mechanism can be extracted. We first show the percentage of all deuterated species of **BTA** after 100x dilution into D_2O in the time-dependent HDX-MS experiments (Figure 4). This method of plotting reveals that there is a small percentage of BTA4D and BTA5D in the beginning of the experiment which was previously overlooked. After 1 hour, the percentage of BTA4D and BTA5D has decreased and the H/D exchange is dominated by either BTA3D or BTA6D.
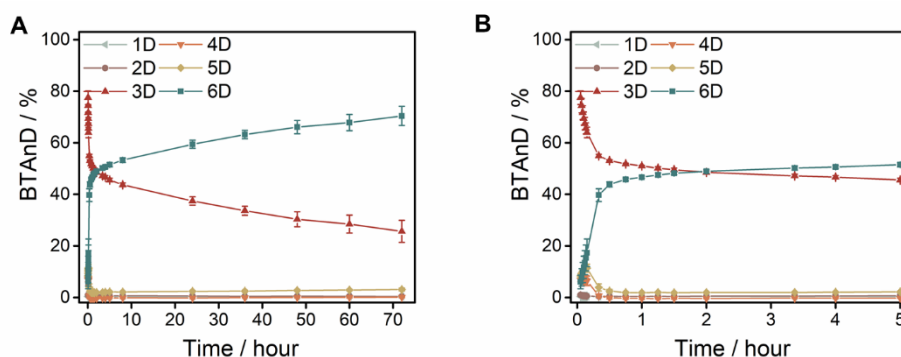
Figure 4. (A) The percentage of different deuterated analogues of **BTA** as a function of time after the 100x dilution of an aqueous 500 µM sample into D_2O (T = room temperature). (B) Zoom-in of the first 5 hours. The symbols represent the average and the error bars the standard deviation calculated from three independent measurements. The lines are added to guide the eye.

Next, we study supramolecular assemblies based on diacetylene bis-urea amphiphiles (**BU**). These linear molecules stack on top of each other via urea hydrogen bonding and hydrophobic interactions and associate laterally to form supramolecular polymers in water.[49] **BU** has two peripheral OH atoms that are on the outside of the assemblies and are easily accessible for D_2O, which would lead to the formation of BU2D (Figure 5A). The four bis-urea NHs are not in direct contact with the solvent and form hydrogen bonds to allow for linear stacking.[51] Only BU6D is observed after 100x dilution in 1/1 D_2O/ACN mixture, in which **BU** is molecularly dissolved, since all interactions are broken and all labile hydrogen atoms are immediately accessible for the solvent (Figure 5B). In contrast, after 1 hour of H/D exchange in D_2O, BU2D and BU6D are the most abundant species in the ESI-SM spectra, whereas BU6D is the major component after 24 hours and only a small amount of BU2D remains.
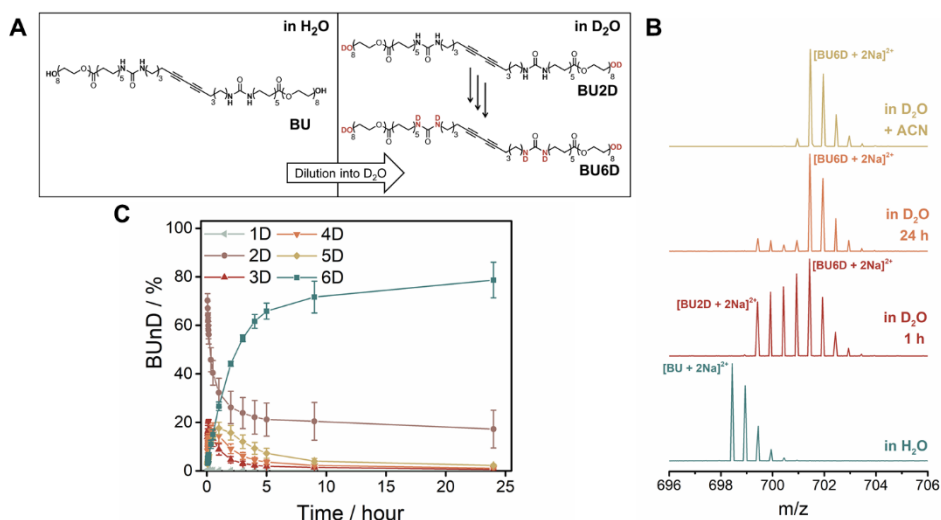
Figure 5. (A) Schematic representation of the HDX-MS process of **BU** including the chemical structures of **BU** analogues before and after dilution into D_2O. (B) ESI-MS spectra of the doubly charged ions of **BU** after 100x dilution of a 500 μM sample into H_2O, D_2O or a 1/1 D_2O/ACN mixture. (C) The percentage of different deuterated analogues of **BU** as a function of time after the 100x dilution of an aqueous 500 μM sample into D_2O (T = room temperature). The symbols represent the average and the error bars the standard deviation calculated from three independent measurements. The lines are added to guide the eye.

The percentages of different deuterated analogous of **BU** are shown in Figure 5C. The results show that the percentage of BU2D rapidly decreases in the first 5 hours, after which it stabilizes. The percentage of BU3D, BU4D and BU5D increases at the start of the experiment, until a maximum is reached and then the percentage decreases. The time needed to reach the maximum percentage increases with the number of deuterium labels that is incorporated: BU3D reaches its maximum after 10 minutes, BU4D after 30 minutes and BU5D after 1 hour. After 8 hours the contributions of BU3D, BU4D and BU5D remains constant and are almost negligible. The amount of BU1D is negligible during the whole experiment.

The two C_3-Symmetrical benzotrithiophenes (BTTs) have similar molecular structures but because the hydrophobic interactions are altered by replacing L-pentafluorophenylalanine (**BTT-5F**) with L-phenylalanine (**BTT**) the mechanism of self-assembly changed. **BTT-5F** assembles via an isodesmic mechanism, whereas **BTT** assembles via a cooperative mechanism.[13] Since isodesmic supramolecular polymers are sensitive to concentration[21] the degree of dilution has to be carefully. UV spectroscopy experiments showed that **BTT-5F** requires a concentration higher than 25 μM to remain polymerized (Figure 6). Thus, in this case, a 10x dilution from 500 μM to 50 μM was required for the HDX-MS experiments. We also selected a 10x dilution from 500 μM to 50 μM in the case of **BTT**.
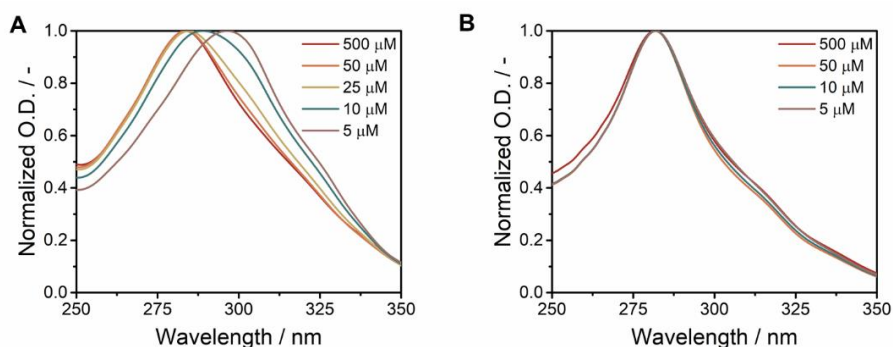
Figure 6. Normalized UV spectra of aqueous solutions of (A) **BTT-5F** and (B) **BTT** at different concentrations (l = 1 mm for 500 μM, l = 1 cm for 50 μM and 25 μM and l = 5 cm for 10 μM and 5 μM, T = 20 °C).

BTT-5F and **BTT** molecules have 9 labile hydrogen atoms: three alcohol hydrogen atoms at the periphery, 3 NH atoms of the L-phenylalanine derivatives and 3 NH atoms next to the benzotrithiophene core (Figure 7A). Interestingly, for **BTT-5F** fully deuterated BTT-5F9D is the major isotope distribution observed after 3 minutes of H/D exchange (Figure 7B). Only a small peak is observed for BTT-5F3D and this peak does not disappear after 24 hours. The exact origin of this peak is currently unknown but it can be explained by the formation of a more stable conformation or by the presence of a small impurity in the sample. The fast exchange of the amide hydrogen atoms of **BTT-5F** is not caused by a too low concentration, since UV spectroscopy experiments indicate that HDX-MS experiments are conducted at a concentration where the monomers are aggregated (Figure 6A). Additionally, the ESI-MS spectrum in D_2O does not completely overlap with the reference spectrum of the molecularly dissolved state (Figure 7B), indicating that some of the molecules are still assembled after dilution.
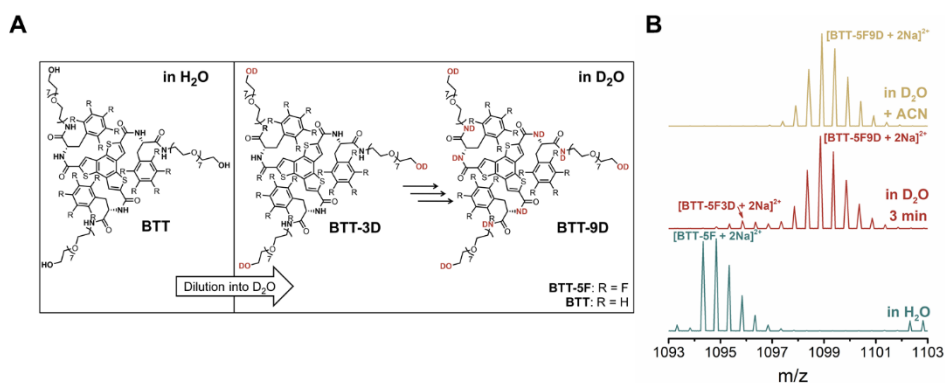
Figure 7. (A) Schematic representation of the HDX-MS process of **BTT-5F** and **BTT** including the chemical structures of BTT analogues before and after dilution into D_2O. (B) ESI-MS spectra of the doubly charged ions of **BTT-5F** after 10x dilution of a 500 μM sample into H_2O, D_2O or a 1/1 D_2O/ACN mixture.

In contrast to **BTT-5F**, the amide hydrogen atoms of **BTT** do not immediately exchange into NDs. For **BTT**, we expect BTT3D with all the three peripheral hydroxyl hydrogens replaced by deuterium, to be present immediately after 10x dilution into D_2O, while BTT9D is present when complete H/D exchange is achieved (Figure 7A). Indeed, after 24 hours, BTT9D dominates, indicating that almost all hydrogen atoms have exchanged (Figure 8A). Interestingly, BTT4D is the most prominent species after 3 minutes of exchange in D_2O and many other intermediates between BTT3D and BTT9D can be observed. Calculating and plotting the percentage of deuterated species versus time shows that the contribution of the deuterated intermediates first increases. Similar to **BU**, the more deuterium atoms are exchanged, the longer it takes to reach the maximum percentage (Figure 8B). The reason for this delayed exchange of the core amide hydrogen atoms remains to be investigated. Even after 7 hours of H/D exchange, there is a significant percentage of **BTT** molecules of which the core amide hydrogen atoms have only been partly exchanged for deuterium atoms, which is remarkably different from the other molecules studied here.

The HDX-MS experiments presented above indicate that there are noticeable differences in the exchange dynamics of the different compounds. The compound **BTT-5F**, which has an isodesmic formation mechanism, shows an immediate exchange of all labile hydrogens. **BTA**, **BU** and **BTT**, which all show cooperative formation mechanisms, require longer times for the labile NHs to exchange. The implications of those differences in the mechanism of formation and differences in the formed morphologies on the mechanism of H/D exchange will be discussed in the next section.
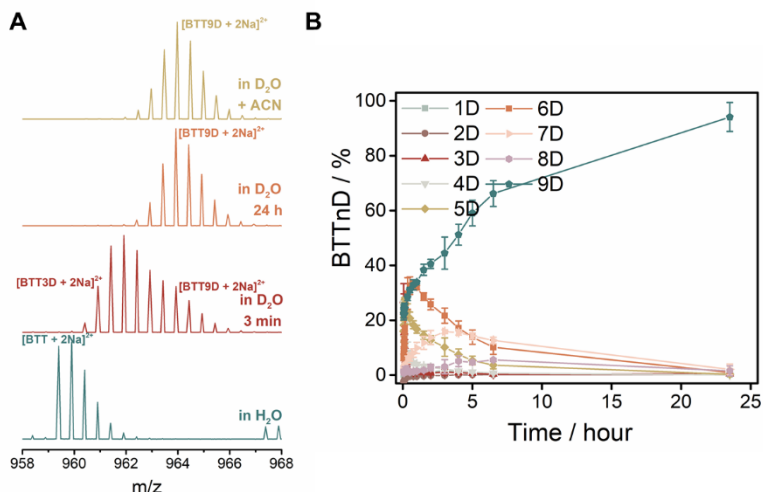
Figure 8. (A) ESI-MS spectra of the doubly charged ions of **BTT** after 10x dilution of a 500 µM sample into H_2O, D_2O or a 1/1 D_2O/ACN mixture. (B) The percentage of different deuterated analogues of **BTT** as a function of time after the 10x dilution of an aqueous 500 µM sample into D_2O (T = room temperature). The symbols represent the average and the error bars the standard deviation calculated from three independent measurements. The lines are added to guide the eye.

3.4 Consequences of the mechanism of exchange on the HDX dynamics

The time-dependent HDX-MS experiments shown in Figures 4, 5C and 8B permit to extract information about the mechanism of H/D exchange. The peripheral hydrogen atoms are immediately exchanged for deuterium atoms due to their constant accessibility to the solvent whereas two mechanism can cause the conversion of labile hydrogen atoms buried in the hydrophobic pocket. Firstly, a D_2O molecule can penetrate the hydrophobic parts of the supramolecular polymers and exchange the NHs in theory one at the time, forming intermediate deuterated species. Secondly, the release of a supramolecular monomer into the solution results in the exchange of all labile NHs to NDs at the same time. This last process has previously been proposed to occur for **BTA** during several hours with super resolution microscopy.[23] Obviously, these two exchange mechanisms cannot be completely isolated from each other because the monomers exchanged by D_2O penetration can also be released later via the monomer releasing mechanism. Since we now have access to the percentage of all deuterated species during HDX as a function of time, we can elucidate which process may be dominant in each of the systems studied. In addition, we can evaluate how the mechanism of formation and the nature of morphologies formed affect the HDX kinetic profile.

For **BTA**, the analysis of the percentage of BTA4D and BTA5D shows that in the first few minutes there is around 7-12% of BTA4D and BTA5D (Figure 4B) The percentage of BTA4D decreases within the first 20 minutes of the experiment from 7.4% to 0.1 %, but the percentage of BTA5D increases in the first 10 minutes to 11.5 % before it decreases in the following 35 minutes to 2.0 %. From this, we conclude that D_2O molecules penetrate into some less-ordered assemblies in the first hour, leading to the exchange of one amide hydrogen atom at a time until these assemblies are fully deuterated. After 1 hour the percentage of BTA4D and BTA5D is constant and negligible, suggesting that the part of the sample that undergoes H/D exchange via solvent molecule penetration has completely exchanged and that the remainder of the formation of BTA6D occurs via a monomer-release mechanism. The constant presence of trace amounts of BTA2D and BTA5D after 1 hour is attributed to an underestimation of the percentage of H_2O in the sample during the calculations. In addition, the percentage of BTA6D rapidly increases in the first hour and then the increase levels off. After 24 hours of H/D exchange, 59% of **BTA** is fully deuterated. After 72 hours, this percentage increased to 70% and the H/D exchange was still not complete. This implicates that part of the BTA assemblies does not easily releases its monomers into the solution. **BTA** assembles into long one-dimensional polymers as shown with cryoTEM (Figure 9A). In Chapter 2, it was revealed that those polymers consist of two strand that rotate around each other as a double helix.[48] We hypothesize that the formation of a double helix stabilizes the interactions between the BTAs, which would

prevent them from moving into the solvent and therefore a slowing down of the H/D exchange of the core amides can occur.
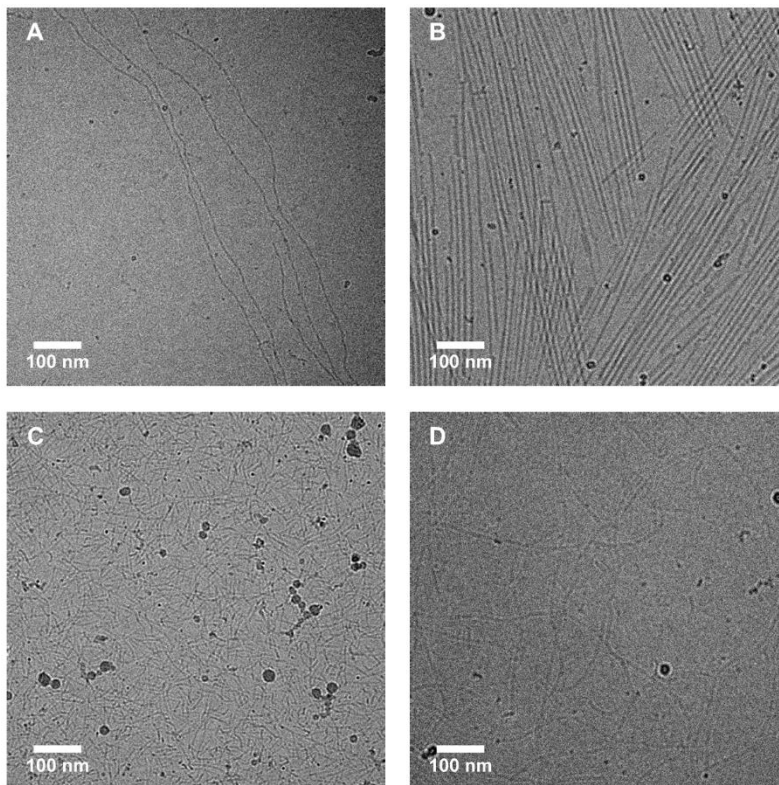
Figure 9. CryoTEM images of (A) **BTA**, (B) **BU**, (C) **BTT-5F** and (D) **BTT** in water (c = 500 µM). The dark spherical objects are ice contamination.

In the case of **BU** the high percentage of intermediate species BU3D, BU4D and BU5D over a long period of time shows that solvent penetration has a significant contribution to the H/D exchange. The extended time needed to exchange all hydrogen atoms of these intermediates indicates that there is a difference in solvent accessibility between the molecules within the assemblies. It is known that bis-urea bola-amphiphiles are able to form supramolecular polymers via the aggregation of 9-10 stacks into one bundled structure.[49] CryoTEM images show that **BU** assembles into elongated supramolecular assemblies with a diameter of roughly 6 nm (Figure 9B). This value is in agreement with the diameter of similar compounds that have been reported to consist of multiple ribbons,[49] confirming that **BU** adopts the same morphology. Stacks that are situated more on the inside of the bundles will take longer to have their hydrogen atoms exchanged than stacks that are closer to the surface of the assemblies, resulting in a longer period in which the solvent penetration mechanism can be observed. Previous sonication experiments confirm that the supramolecular

assemblies are reversible and that molecules can move between assemblies.[52] Initially, the H/D exchange of **BU** is dominated by the penetration of D_2O but after 5 hours the monomer-release mechanism is proposed to be the main mechanism for H/D exchange.

BTT-5F assembles into short fibrillar supramolecular polymers in water as shown with cryoTEM (Figure 9C). However, the H/D exchange seems to be very fast and already after 3 minutes BTT-5F9D is the dominant species (Figure 7B). Previous MD simulations revealed that the hydrophobic interaction between the L-pentafluorophenylalanines is the main interaction in the **BTT-5F** assemblies instead of the hydrogen bonds between the core amides.[13] From these experiments, it can be concluded that **BTT-5F** molecules do not pack tightly, leading to the rapid dynamics of monomer releasing and/or the easy penetration of water molecules into the polymers. Thus, the exchange of the amide hydrogen atoms to deuterium atoms is fast.

CryoTEM images of **BTT** (Figure 9D) show that the molecules assemble into longer supramolecular polymers than **BTT-5F**. According to MD simulations, the self-assembly of **BTT** is dominated by directional hydrogen bonding between the amides of the bezotrithiophene cores which provides a better force for self-assembly than the hydrophobic interactions in **BTT-5F**.[13] These cooperative interactions make the assemblies of **BTT** more ordered, resulting in a slower exchange as compared to **BTT-5F**. Interestingly, the H/D exchange of the amides of **BTT** is fast and significantly driven by solvent penetration as inferred from the high percentages of BTT4D, BTT5D, BTT6D, BTT7D and BTT8D. This fast exchange and solvent penetration may be explained by the lack of a secondary structure in **BTT** assemblies, which do not seem to show the double helix structure as found for **BTA**.

3.5 Comparison of the HDX dynamics of different supramolecular polymers

The exchange profiles of the HDX-MS experiments of the three cooperatively formed supramolecular polymers can now be compared. To minimize the effects of the different exchange mechanisms and intermediates, only the percentage of molecules with all hydrogen atoms exchanged are compared for the first 24 hours of H/D exchange in Figure 10. Although the initial increase in BTA6D is fast, the rate of increase levels off after a few hours and only 59.4% of the BTAs are fully deuterated after 24 hours. The percentage of BU6D initially increases less rapidly than that of BTA6D, but the fast exchange is maintained longer, resulting in 78.6% of BU6D after 24 hours. The percentage of BTT9D is already 22% after 3 minutes but shows the most constant increase of all supramolecular assemblies and after 23.5 hours the percentage of fully deuterated molecules is 94.2%, thereby surpassing the percentage of BTA6D and BU6D obtained after 24 hours.

Interestingly, the increase in the percentage of fully deuterated molecules of all supramolecular polymers can be described with a bi-exponential growth function with

a fast and a slow contribution. The rate of exchange can be quantified by a rate constant, k, and a relative contribution (see section 3.9.4). BTT9D has the highest rate constants in both regimes, whereas BU6D has the lowest rate constants. The large contribution of the fast exchange of BU6D results in more exchange in assemblies of **BU** than in assemblies of **BTA** over time. The fast exchange of BTT9D only has a small contribution and therefore the percentage of completely deuterated molecules is lowest for BTT9D in the first 10 h. From the bi-exponential fit it can be concluded that **BTA** will never have all its hydrogen atoms replaced for deuterium atoms, resembling very stable amyloid fibrils.[41,42] This very stable component of the assemblies of **BTA** might be caused by the double helix structure.[48]
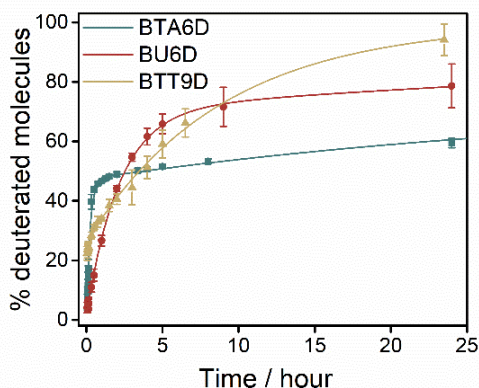
Figure 10. The percentage of fully deuterated **BTA**, **BU** and **BTT** as a function of time. All HDX-MS experiments were started with a 500 µM sample in H_2O. The samples for **BTA** and **BU** were diluted 100x into D_2O and the samples of **BTT** were diluted 10x into D_2O (T = room temperature). The symbols represent the average and the error bars the standard deviation calculated from three independent measurements. The lines represent a bi-exponential growth function.

3.6 The impact of the hydrophobic chain length on the HDX dynamics

The new method for the analysis of the HDX-MS experiments described in this chapter, prompted us to revisit some of our old results on water-compatible BTAs with the hydrophobic chain length increasing from C_{10} to C_{13} (Figure 11A).[27] The **BTA-C$_{12}$-EG$_4$** molecule in this study corresponds to **BTA** in Figure 1. Previous HDX-MS experiments showed that all labile hydrogen atoms of **BTA-C$_{10}$-EG$_4$** are immediately deuterated upon dilution into D_2O (Figure 11B). CryoTEM experiments in Chapter 2 revealed that this molecule assembles into short stacks of BTAs. These structures are ill-defined with weak hydrogen bonds,[53] which results in their immediate H/D exchange. In contrast, the H/D exchange of the amide hydrogen atoms of the other BTAs increases with time and the longer the hydrophobic chain, the lower the percentage of BTA6D is at the end of the experiments. CryoTEM experiments with those molecules

revealed that these BTAs assemble into supramolecular polymers with a double helix structure that increases in diameter and half helical pitch with increasing hydrophobic chain length.
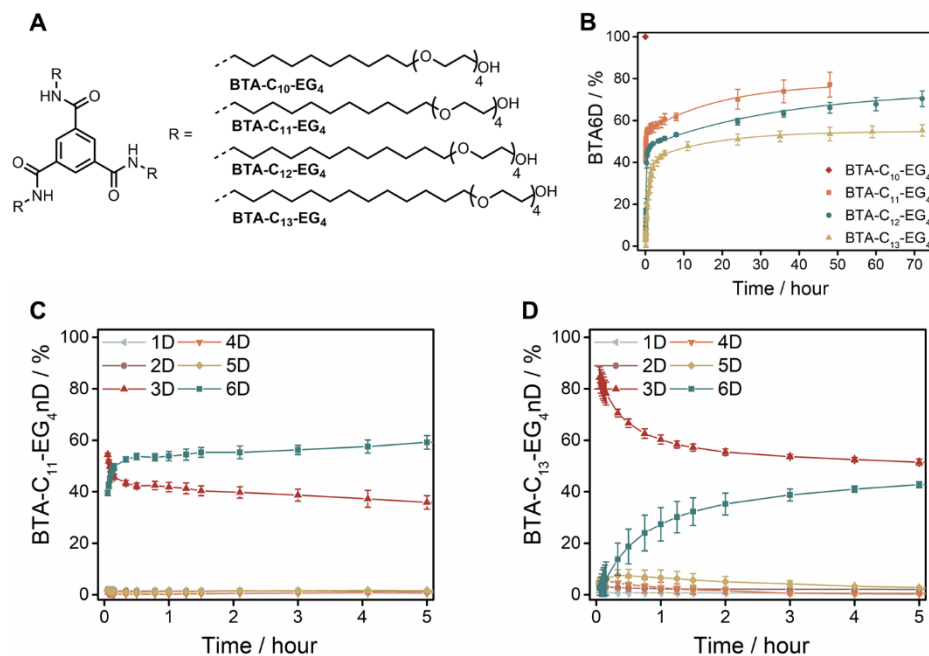
Figure 11. (A) Chemical structure of water-compatible BTAs with different hydrophobic chain lengths. **BTA-C$_{12}$-EG$_4$** corresponds to **BTA** in Figure 1. (B) The percentage of fully deuterated BTAs as a function of time after the 100x dilution of 500 μM samples into D$_2$O (T = room temperature). (C-D) The percentage of different deuterated analogues of (C) **BTA-C$_{11}$-EG$_4$** and (D) **BTA-C$_{13}$-EG$_4$** as a function of time after the 100x dilution of an aqueous 500 μM sample into D$_2$O (T = room temperature). The symbols represent the average and the error bars the standard deviation calculated from three independent measurements. The lines are added to guide the eye.

Interestingly, the slopes of the lines in Figure 11B are similar at long timescales and more pronounced differences are observed within the first 5 hours. A closer inspection of the first hours of the HDX-MS experiments therefore provides some additional insights into the degree of order within the samples. At the first measurement, that is 3 minutes after the dilution, already 40% of the **BTA-C$_{11}$-EG$_4$** molecules is fully deuterated (Figure 11C). In contrast, **BTA-C$_{12}$-EG$_4$** and **BTA-C$_{13}$-EG$_4$** have 6% and 3% of their BTAs fully deuterated at the first measurement point, respectively (Figure 4B & 11D). We hypothesize that this high starting percentage of BTA6D is because the sample of **BTA-C$_{11}$-EG$_4$** contains a mixture of supramolecular polymers and small ill-defined aggregates that resemble **BTA-C$_{10}$-EG$_4$**. Less of these assemblies are present in the samples with BTAs that have longer hydrophobic chains.

All lines in Figure 11B show a sharp transition point from an initially fast H/D exchange to a slow H/D exchange. For **BTA-C$_{11}$-EG$_4$** this transition point occurs after 20 minutes at 52% of BTA6D, for **BTA-C$_{12}$-EG$_4$** the transition point is found after 45 minutes at 46% of BTA6D and for **BTA-C$_{13}$-EG$_4$** this transition occurs after 5 hours at 43% of BTA6D. These timescales overlap with the times at which solvent penetration is observed, as is evidenced by the presence of BTA4D and BTA5D. We hypothesize that the H/D exchange until this transition point is due to less-ordered regions in the assemblies, either due to small aggregates or defects within the polymers, or both. The longer the hydrophobic chains, the fewer of these less-ordered regions are observed and the longer it takes for them to be exchanged.

Finally, the last part of the HDX curves shows a gradual increase of the percentage of BTA6D. As described in section 3.4, we attribute the slow H/D exchange at longer timescales to the presence of bundled polymers, wherein the hydrogen bonds are well-structured. We propose that exchange in this part arises from monomers exchanging into the surrounding solvent, which is a slow process.

3.7 HDX-MS as a tool to study the dynamics of supramolecular copolymers

HDX-MS not only provides valuable information about homopolymers but it also allows to study the dynamics of supramolecular co-assemblies. When the exact mass of the components within the solution differs HDX-MS can be used to track the dynamics of the individual components over time to determine the influence of co-assembly on their dynamics. To illustrate the insights that can be obtained with HDX-MS on supramolecular copolymers we have mixed **BTT-5F** and **BTT** in 3:1, 1:1 and 1:3 ratio. CryoTEM confirmed that all mixtures studied here contain supramolecular polymers of several tens of nanometers. UV-Vis spectroscopy showed that the co-assemblies of different ratios are altered upon 100x dilution of 500 μM samples, especially when **BTT-5F** is the main component, so a 10x diluted was selected for the HDX-MS experiments.

Immediately after dilution of the mixtures into D$_2$O several less deuterated analogs of **BTT-5F** can be observed, in contrast to the homo-assemblies of **BTT-5F** which showed mainly BTT-5F9D after dilution into D$_2$O. The detection of less deuterated analogs in the mixtures indicates that the molecules are no longer in their unstable homo-assembly but have an interaction with **BTT** which results in the protection of the amide hydrogen atoms of **BTT-5F**. Similarly, more fully deuterated molecules of **BTT** can be observed 3 minutes after dilution of the mixtures compared to the homopolymers. The first ESI-MS spectrum after dilution can already be used to confirm that two molecules are co-assembled to some extent, which is information that is difficult to obtain with other techniques such as spectroscopy and microscopy.

The HDX-MS spectra of mixtures can also be measured over a longer period of time and the percentage of deuterated molecules can be calculated individually for each component to study their exchange dynamics within the copolymers. The maximum percentage of BTT-5F9D is reached after 1.5 hours, 2 hours and 5 hours for the 3:1, 1:1 and 1:3 **BTT-5F:BTT** mixtures, respectively (Figure 12A). This indicates that **BTT-5F** is stabilized by the addition of more **BTT**. The opposite can be observed for **BTT** which shows faster exchange dynamics when more **BTT-5F** is present in the mixtures (Figure 12B). For **BTT** 1.5 hours, 5 hours and 6.5 hours are required to reach the maximum percentage of BTT9D for the 3:1, 1:1 and 1:3 mixtures with **BTT-5F**, respectively. By mixing the two components in different ratios the dynamics of the supramolecular system can be controlled and matched to a specific application. Such a stabilization of one component and destabilization of the other component has previously also been observed for BTAs,[54] although there are also reports in which both components were stabilized.[46]
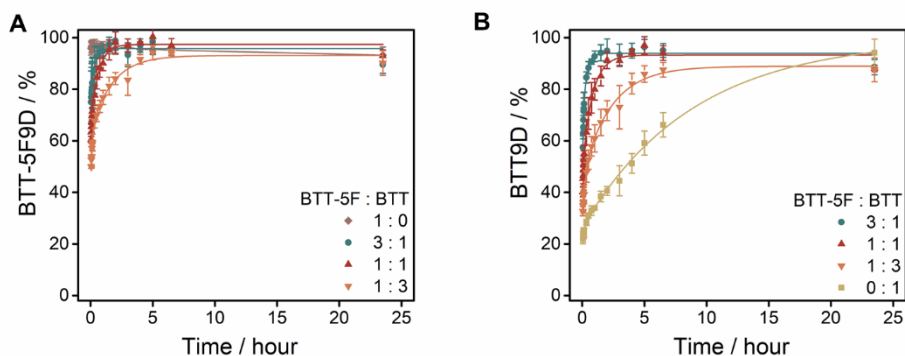
Figure 12. The percentage of fully deuterated (A) **BTT-5F** and (B) **BTT** as a function of time after the 10x dilution of 500 µM samples of different mixtures into D_2O (T = room temperature). The symbols represent the average and the error bars the standard deviation calculated from three independent measurements. The bi-exponential fits are added to guide the eye.

3.8 Conclusions

HDX-MS is a very attractive method for the characterization of dynamic supramolecular polymers in water as it only requires a minimal perturbation of the molecular structure of interest. We first confirmed some experimental aspects to obtain the most reliable results. No considerable differences in the polymer dynamics were observed whether the sample was diluted 100 times or 10 times into D_2O if the trace amount of H_2O was taken into account. Additionally, we confirmed that the start and end concentration are not of influence as long as both are above the CAC of the supramolecular building blocks.

The usefulness of HDX-MS is further demonstrated by applying this technique to different types of supramolecular polymers with different assembly mechanisms, one BTA-based, one BU-based and two BTT-based. These HDX-MS experiments not only

monitored the movement of monomers between assemblies, but also revealed that solvent molecules can penetrate the supramolecular polymers because of imperfect stacking of the molecules. This solvent penetration allowed us to extract information about the internal structure of the supramolecular assemblies that was otherwise hidden. **BTA** undergoes the least amount of solvent penetration, whereas **BTT** suffers from the most. Mixing of components is a well-known strategy in the design of new functional supramolecular materials and HDX-MS could provide valuable information in this field. The technique can be used as a tool to confirm supramolecular copolymerization and it provides the unique possibility to track the exchange dynamics of the individual components over time if they differ in mass.

HDX-MS is an important complement to many techniques widely used for the characterization of supramolecular systems in water. Instead of providing information about the global polymer structure, HDX-MS allows insights into the internal order of structurally diverse samples. Furthermore, HDX-MS can also be extremely useful to assist in the rational design of building blocks able to form supramolecular polymers in water. These results demonstrate that the structure, self-assembly mechanism and dynamics of supramolecular polymers are not independent variables and should be evaluated simultaneously.

3.9 Experimental section
3.9.1 Materials and Methods
All solvents used were of reagent grade quality or better and purchased from Biosolve or Sigma-Aldrich at the highest purity available and used without further purification unless otherwise noted. **BTA**,[47] **BU**,[55] **BTT-5F** and **BTT**[13] were synthesized according to literature procedures. Water for aqueous samples was purified on an EMD Millipore Milli-Q Integral Water Purification System.

Sample preparation of BTA and BTA-C$_{11}$-EG$_4$: the solid material was weighed into a glass vial equipped with a magnetic stirring bar. MQ-water was added to obtain the desired concentration in H$_2$O. The sample was subsequently stirred at 80 °C for 15 minutes and the hot and hazy sample was vortexed immediately afterwards for 15 seconds. The sample was left to equilibrate overnight at room temperature.

Sample preparation of BU: the solid material was weighed into a glass vial and was subsequently dissolved in a small volume of chloroform. The solvent was allowed to evaporate overnight and the remaining solid was re-dissolved in MQ-water to a concentration of 20 mg/mL. Ultrasonication was used to assist with the dissolution of the material at this concentration. The sample was left to equilibrate at this concentration for at least 2 days at room temperature before diluting the sample to the desired concentration with MQ-water. The sample was left to equilibrate overnight at room temperature.

Sample preparation of BTT-5F and BTT: the solid material was weighed into a glass vial and DMSO was added to obtain a concentration of 10 mM. This stock solution was vortexed to get a homogeneously mixed solution. A small aliquot of this stock solution was injected into MQ-water to obtain the desired concentration. The sample was left to equilibrate overnight at room temperature.

Sample preparation of BTA-C$_{13}$-EG$_4$: roughly 2 mg the solid material was weighed into a 15 mL glass vial with a magnetic stirring bar. Approximately 300 µL CHCl$_3$ was added and the sample was vortexed for 15 seconds. The solvent was evaporated by blowing a constant stream of N$_2$ (g) above the solvent. 15 mL MQ-water was added and the sample was stirred at 80 °C for 15 minutes. Subsequently, the hot and hazy mixture was vortexed for 15 seconds and was left to equilibrate at room temperature overnight. The next day the sample was filtered with a 0.2 µm syringe filter. Water was evaporated by blowing a stream of N$_2$ (g) over the sample, while stirring, thereby increasing the concentration. UV spectroscopy was used to determine the concentration using a calibration curve based on the absorbance of **BTA-C$_{12}$-EG$_4$** at 250 nm: conc = (0.00434 + A$_{250}$)/0.001615. The concentration was increased to 500 µM.

Sample preparation of mixtures of BTF-5F and BTT: 10 mM stock solution of **BTT-5F** and **BTT** in DMSO were combined in a vial in the desired ratio. MQ-water was added to obtain the desired concentration. The sample was left to equilibrate overnight at room temperature.

Samples for HDX-MS: 500 µM samples were diluted 100 or 10 times with D$_2$O (including 0.5 mM sodium acetate to facilitate detection) using a balance or volumetric pipette, resulting in a final concentration of 5 or 50 µM, respectively. The samples were stored at room temperature during the experiment. Aliquots of the samples with D$_2$O were taken at specific time points and were subjected to ESI-MS to record the MS spectra. ACN was added to a sample diluted into D$_2$O in a roughly 1:1 ratio to study the MS spectra of disassembled supramolecular systems. MS spectra of supramolecular assemblies in water were recorded after diluting a 500 µM sample to 5 µM or 50 µM with MQ-water.

3.9.2 Instrumentation

Hydrogen deuterium exchange experiments with electrospray ionization were carried out using a Xevo™ G2 QTof mass spectrometer (Waters) with a capillary voltage of 2.7 kV, a cone voltage of 80 V and an extraction cone voltage of 4.0 V. The source temperature was set at 100 °C, the desolvation temperature at 400 °C, and the cone gas flow at 10 L/h and the desolvation gas flow at 500 L/h. The sample solutions subjected to H/D exchange were introduced into the mass spectrometer using a Harvard syringe pump (11 Plus, Harvard Apparatus) at a flow rate of 50 µL/min. The signal was left to equilibrate for 1 measurement before starting the measurement and each measurement was averaged over 1 minute to account for instabilities in the signal. Spectra were recorded in centroid mode and the intensity of the peaks is used for the calculations as described in section 3.9.3. Before each measurement, the system was calibrated with a 0.05% H$_3$PO$_4$ solution in 1:1 H$_2$O:ACN. Isotope patterns for calculation were determined with IsoPro software.

Ultraviolet-visible (UV-vis) absorbance spectra were recorded on a Jasco V-650 UV-Vis spectrometer equipped with a Jasco ETCT-762 temperature controller or on a Jasco V-750 UV-Vis spectrometer equipped with a PAC-743 multi-cuvette holder and Jasco ETCT-762 temperature controller. Measurements were performed using Quartz cuvettes (Hellma) with a pathlength of 1 mm (500 µM samples), 1 cm (25 and 50 µM samples) or 5 cm (5 and 10 µM samples). First, a baseline of the corresponding solvent was measured. All measurements were performed with a bandwidth of 1.0 nm, a scan speed of 100 nm/min and a data interval of 0.1 nm, spanning the UV-Vis range from 350 nm to 190 nm. All spectra were averaged over three measurements.

Cryogenic transmission electron microscopy images were obtained with the instrument as described in Chapter 2.

3.9.3 Analysis of the HDX-MS measurements

All HDX-MS experiments were performed under similar conditions to eliminate influences from the environment, for example temperature. The measurements were performed by diluting a sample of self-assembled supramolecular building-blocks in H_2O 100x or 10x into D_2O. 0.5 mM sodium acetate was added to the D_2O prior to the dilution to facilitate the detection. In all cases the distributions with two sodium ions were used for the calculations. In general, the calculations consist of two parts:

1. Correction for the presence of isotopes that overlap with more deuterated molecules.
2. Correction for D/H exchange due to the presence of H_2O which results in less deuterated molecules.
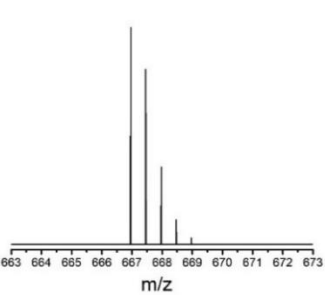
The calculations will first be fully explained for **BTA** and this method can then be translated to **BU**, **BTT-5F**, **BTT**, **BTA-C$_{11}$-EG$_4$** and **BTA-C$_{13}$-EG$_4$**.

a. Correction for the isotopes of BTA:

For **BTA**, peaks corresponding to BTA1D, BTA2D, BTA3D, BTA4D, BTA5D and BTA6D can be distinguished after dilution into D_2O. A peak corresponding to BTA0D could not be observed. All peaks observed have isotopes that overlap with more deuterated BTAs. For example, BTA3D has its first isotope at the same m/z as BTA4D, its second isotope at the same m/z as BTA5D and its third isotope at the same m/z as BTA6D. The distribution of the isotopes can be calculated with Isopro Software (Table 1).

Table 1: Theoretical isotope distribution of the undeuterated **BTA** as calculated with IsoPro Software, including a graphical representation. This would be the isotope distribution without the presence of D_2O.

[BTA+2Na]$^{2+}$	
m/z	*Relative abundance*
666.96	1
667.46	0.80
667.96	0.36
668.47	0.11
668.97	0.03
669.47	0.01

Although BTA3D and BTA6D are the most abundant distributions in case of **BTA** in D_2O, also the isotopes of BTA1D, BTA2D, BTA4D and BTA5D should be taken into account for the correct calculation of the intermediate deuterated states at the beginning of the experiment. With the distribution given in Table 1 we could calculate the intensity of the isotopes and subtract this from the measured intensities at each m/z value. For example, to get the intensity of BTA3D without the influence of isotopes, we would have to subtract the first isotope of BTA2D and the second isotope of BTA1D from the measured intensity at the m/z of BTA3D. We assume that the

deuterated BTAs have the same isotope distribution as the undeuterated BTA as described in Table 1. The corrected intensity (I_{BTAnD_c}) of the peaks without the influence of the isotopes can be calculated with the constants in the table above and the following set of equations:

$I_{BTA1D\_c} = I_{667.46}$

$I_{BTA2D\_c} = I_{667.96} - 0.80 I_{BTA1D\_c}$

$I_{BTA3D\_c} = I_{668.47} - 0.80 I_{BTA2D\_c} - 0.36 I_{BTA1D\_c}$

$I_{BTA4D\_c} = I_{668.97} - 0.80 I_{BTA3D\_c} - 0.36 I_{BTA2D\_c} - 0.11 I_{BTA1D\_c}$

$I_{BTA5D\_c} = I_{669.47} - 0.80 I_{BTA4D\_c} - 0.36 I_{BTA3D\_c} - 0.11 I_{BTA2D\_c} - 0.03 I_{BTA1D\_c}$

$I_{BTA6D\_c} = I_{669.97} - 0.80 I_{BTA5D\_c} - 0.36 I_{BTA4D\_c} - 0.11 I_{BTA3D\_c} - 0.03 I_{BTA2D\_c} - 0.01 I_{BTA1D\_c}$

with $I_{667.46}$, $I_{667.96}$, $I_{668.47}$, $I_{668.97}$, $I_{669.47}$ and $I_{669.97}$ the intensity at m/z = 667.46, 667.96, 668.47, 668.97, 669.47 and 669.97, respectively.

b. Correction for the presence of H₂O after dilution of BTA:

The presence of H_2O in the sample might lead to the exchange of deuterium atoms back to hydrogen atoms, which would result in an overestimation of the percentage of less deuterated molecules if not corrected for. Even if all labile hydrogen atoms are in contact with the solvent, there will be some BTA5D, BTA4D formed from BTA6D as illustrated in Figure 2B and 2D (top spectra). To correct for the presence of water the molar percentage of H_2O should be calculated first:

$$mol\%H_2O = \frac{V_{H_2O} \times \rho_{H_2O} \times M_{H_2O}}{V_{H_2O} \times \rho_{H_2O} \times M_{H_2O} + V_{D_2O} \times \rho_{D_2O} \times M_{D_2O}} \times 100\%$$

with V_{H_2O} and V_{D_2O} the volume of the aqueous sample and the volume of D_2O used to induce the H/D exchange, respectively, ρ_{H_2O} and ρ_{D_2O} the density of H_2O and D_2O, respectively, and M_{H_2O} and M_{D_2O} the molar mass of H_2O and D_2O, respectively. We have used the following constants: $\rho_{H_2O} = 1.0$, $\rho_{D_2O} = 1.1$, $M_{H_2O} = 18.01$ and $M_{D_2O} = 20.02$.

The statistical chance to have D/H exchange of m deuterium atoms of BTA6D can be calculated using a binomial coefficient with:

$$\binom{6}{m} \times \left(\frac{mol\%H_2O}{100}\right)^m \times \left(1 - \left(\frac{mol\%H_2O}{100}\right)\right)^{6-m}$$

The following distributions can be calculated for the formation of BTA0D to BTA5D from BTA6D in a BTA sample that was hundredfold (1.0 mol% of H_2O) or tenfold (10.0 mol% of H_2O) diluted:

Table 2: Relative occurrence of BTAs with m of the possible 6 deuterium atoms exchanged for hydrogen atoms for 1.0 mol% or 10.0 mol% of H_2O in the sample after dilution into D_2O.

m	Corresponding m/z	Corresponding BTA	Relative occurrence for 1.0 mol% H₂O	Relative occurrence for 10.0 mol% H₂O
0	669.47	BTA6D	1	1
1	668.97	BTA5D	6.06×10^{-2}	6.67×10^{-1}
2	668.47	BTA4D	1.53×10^{-3}	1.85×10^{-1}
3	667.96	BTA3D	2.06×10^{-5}	2.74×10^{-2}
4	667.46	BTA2D	1.56×10^{-7}	2.29×10^{-3}
5	666.96	BTA1D	6.31×10^{-10}	1.02×10^{-4}
6	666.46	BTA0D	1.06×10^{-12}	1.88×10^{-6}

Similarly, the statistical chance to have D/H exchange of n deuterium atoms of BTA3D can be calculated with:

$$\binom{3}{n} \times \left(\frac{mol\%H_2O}{100}\right)^n \times \left(1 - \left(\frac{mol\%H_2O}{100}\right)\right)^{3-n}$$

The following distributions can be calculated for BTA0D to BTA2D from BTA3D:

Table 3: Relative occurrence of BTAs with n of the possible 3 deuterium atoms exchanged for hydrogen atoms for 1.0 mol% or 10.0 mol% of H_2O in the sample after dilution into D_2O.

n	Corresponding m/z	Corresponding BTA	Relative occurrence for 1.0 mol% H_2O	Relative occurrence for 10.0 mol% H_2O
0	667.96	BTA3D	1	1
1	667.46	BTA2D	3.03×10^{-2}	3.33×10^{-1}
2	666.96	BTA1D	3.06×10^{-4}	3.70×10^{-2}
3	666.46	BTA0D	1.03×10^{-6}	1.37×10^{-3}

With those relative occurrences we can calculate the intensity that is expected to be present because of H_2O. Next, we subtract these calculated intensities from the contribution of BTA6D (Table 2) from the measured intensities of BTA5D, BTA4D, BTA3D, BTA2D and BTA1D and add those intensities to BTA6D to correct for the loss of BTA6D. Similarly, we subtract the calculated intensities from the contribution of BTA3D (Table 3) from the measured intensities of BTA2D and BTA1D and add those to the intensity of BTA3D. In this way we can calculate the intensity that only describes the H/D exchange and does not contain any artefacts. For a hundredfold dilution the following intensities can be calculated:

$I_{BTA1D} = I_{BTA1D\_c} - 6.31 \times 10^{-10} I_{BTA6D\_c} - 3.06 \times 10^{-4} I_{BTA3D\_c}$

$I_{BTA2D} = I_{BTA2D\_c} - 1.56 \times 10^{-7} I_{BTA6D\_c} - 3.03 \times 10^{-2} I_{BTA3D\_c}$

$I_{BTA3D} = I_{BTA3D\_c} - 2.06 \times 10^{-5} I_{BTA6D\_c} + \left(3.06 \times 10^{-4} + 3.03 \times 10^{-2}\right) I_{BTA3D\_c}$

$I_{BTA4D} = I_{BTA4D\_c} - 1.53 \times 10^{-3} I_{BTA6D\_c}$

$I_{BTA5D} = I_{BTA5D\_c} - 6.06 \times 10^{-2} I_{BTA6D\_c}$

$I_{BTA6D} = I_{BTA6D\_c} + \left(6.31 \times 10^{-10} + 1.56 \times 10^{-7} + 2.06 \times 10^{-5} + 1.53 \times 10^{-3} + 6.06 \times 10^{-2}\right) I_{BTA6D\_c}$

c. Calculation of the percentage of deuterated analogues of BTA:
Now that the influence of isotopes and of a trace amount of H_2O in the D_2O has been calculated and has been deducted from the measured intensities, the percentage of the deuterated analogues can be calculated:

$$\%BTAnD = \frac{I_{BTAnD}}{\sum_{k=1}^{6} I_{BTAkD}} \times 100\%$$

with $\sum_{k=1}^{6} I_{BTAkD}$ the sum of all intensities. The percentage of deuterated analogues was calculated for several time points and plotted as a function of time in this chapter.

d. Calculation of the percentage of deuterated analogues of BU:
The formulas described for **BTA** can easily be adapted to be used for **BU**. First of all, the isotope distribution of **BU** was corrected for:

$I_{BU1D\_c} = I_{698.92}$

$I_{BU2D\_c} = I_{699.42} - 0.80I_{BU1D\_c}$

$I_{BU3D\_c} = I_{699.92} - 0.80I_{BU2D\_c} - 0.36I_{BU1D\_c}$

$I_{BU4D\_c} = I_{700.42} - 0.80I_{BU3D\_c} - 0.36I_{BU2D\_c} - 0.12I_{BU1D\_c}$

$I_{BU5D\_c} = I_{700.92} - 0.80I_{BU4D\_c} - 0.36I_{BU3D\_c} - 0.12I_{BU2D\_c} - 0.03I_{BU1D\_c}$

$I_{BU6D\_c} = I_{701.42} - 0.80I_{BU5D\_c} - 0.36I_{BU4D\_c} - 0.12I_{BU3D\_c} - 0.03I_{BU2D\_c} - 0.01I_{BU1D\_c}$

BU has a maximum of 6 labile hydrogen atoms, similar to **BTA**. The influence of H_2O in the calculations given in Table 2 are therefore also applicable for BU6D. However, the influence of H_2O on BU2D still has to be calculated:

$$\binom{2}{p} \times \left(\frac{mol\%H_2O}{100}\right)^p \times \left(1 - \left(\frac{mol\%H_2O}{100}\right)\right)^{2-p}$$

The following distributions can be calculated for the contribution from BU2D:

Table 4: Relative occurrence of BUs with p of the possible 2 deuterium atoms exchanged for hydrogen atoms for 1.0 mol% or 10.0 mol% of H_2O in the sample after dilution into D_2O.

p	Corresponding m/z	Corresponding BU	Relative occurrence for 1.0 mol% H_2O	Relative occurrence for 10.0 mol% H_2O
0	699.42	BU2D	1	1
1	699.92	BU1D	2.03×10^{-2}	2.22×10^{-1}
2	700.42	BU0D	1.03×10^{-4}	1.23×10^{-2}

The intensity without artefacts can then be calculated with:

$I_{BU1D} = I_{BU1D\_c} - 6.31 \times 10^{-10} I_{BU6D\_c} - 2.03 \times 10^{-2} I_{BU2D\_c}$

$I_{BU2D} = I_{BU2D\_c} - 1.56 \times 10^{-7} I_{BU6D\_c} + 2.03 \times 10^{-2} I_{BU2D\_c}$

$I_{BU3D} = I_{BU3D\_c} - 2.06 \times 10^{-5} I_{BU6D\_c}$

$I_{BU4D} = I_{BU4D\_c} - 1.53 \times 10^{-3} I_{BU6D\_c}$

$I_{BU5D} = I_{BU5D\_c} - 6.06 \times 10^{-2} I_{BU6D\_c}$

$I_{BU6D} = I_{BU6D\_c} + \left(6.31 \times 10^{-10} + 1.56 \times 10^{-7} + 2.06 \times 10^{-5} + 1.53 \times 10^{-3} + 6.06 \times 10^{-2}\right) I_{BU6D\_c}$

From which the percentage of deuterated analogues can be calculated:

$$\%BUnD = \frac{I_{BUnD}}{\sum_{k=1}^{6} I_{BUkD}} \times 100\%$$

e. Calculation of the percentage of deuterated analogues of BTT-5F and BTT:

Next, the equations were adapted for **BTT-5F** and **BTT**. Below only the equations for **BTT** are given but the same equations can be adapted for **BTT-5F**.

$I_{BTT1D\_c} = I_{959.91}$

$I_{BTT2D\_c} = I_{960.41} - 1.08I_{BTT1D\_c}$

$I_{BTT3D\_c} = I_{960.91} - 1.08I_{BTT2D\_c} - 0.77I_{BTT1D\_c}$

$I_{BTT4D\_c} = I_{961.41} - 1.08I_{BTT3D\_c} - 0.77I_{BTT2D\_c} - 0.41I_{BTT1D\_c}$

$I_{BTT5D\_c} = I_{961.91} - 1.08I_{BTT4D\_c} - 0.77I_{BTT3D\_c} - 0.41I_{BTT2D\_c} - 0.18I_{BTT1D\_c}$

$I_{BTT6D\_c} = I_{962.42} - 1.08I_{BTT5D\_c} - 0.77I_{BTT4D\_c} - 0.41I_{BTT3D\_c} - 0.18I_{BTT2D\_c} - 0.07I_{BTT1D\_c}$

$I_{BTT7D\_c} = I_{962.92} - 1.08I_{BTT6D\_c} - 0.77I_{BTT5D\_c} - 0.41I_{BTT4D\_c} - 0.18I_{BTT3D\_c} - 0.07I_{BTT2D\_c} - 0.02I_{BTT1D\_c}$

$I_{BTT8D\_c} = I_{963.42} - 1.08I_{BTT7D\_c} - 0.77I_{BTT6D\_c} - 0.41I_{BTT5D\_c} - 0.18I_{BTT4D\_c} - 0.07I_{BTT3D\_c}$

- $0.02I_{BTT2D\_c} - 0.006I_{BTT1D\_c}$

$I_{BTT9D\_c} = I_{963.92} - 1.08I_{BTT8D\_c} - 0.77I_{BTT7D\_c} - 0.41I_{BTT6D\_c} - 0.18I_{BTT5D\_c} - 0.07I_{BTT4D\_c}$
$- 0.02I_{BTT3D\_c} - 0.006I_{BTT2D\_c} - 0.001I_{BTT1D\_c}$

For **BTT-5F**, the following changes should be made to the formula: $I_{959.91} = I_{1094.84}$, $I_{960.41} = I_{1095.34}$, $I_{960.91} = I_{1095.85}$, $I_{961.41} = I_{1096.35}$, $I_{961.91} = I_{1096.85}$, $I_{962.42} = I_{1097.35}$, $I_{962.91} = I_{1097.85}$, $I_{963.42} = I_{1098.35}$ and $I_{963.82} = I_{1098.86}$.

The BTT derivatives have 9 labile hydrogen atoms in total that can undergo H/D exchange. The relative contribution of a BTT molecule with r of the maximum 9 deuterium atoms exchanged to hydrogen atoms can be calculated with:

$$\binom{9}{r} \times \left(\frac{\text{mol\%H}_2\text{O}}{100}\right)^r \times \left(1 - \left(\frac{\text{mol\%H}_2\text{O}}{100}\right)\right)^{9-r}$$

The following distributions can be calculated for BTT9D in both BTT samples that was hundredfold (1.0 mol% of H_2O) or tenfold (10.0 mol% of H_2O) diluted:

Table 5: Relative occurrence of BTTs with r of the possible 9 deuterium atoms exchanged for hydrogen atoms for 1.0 mol% or 10.0 mol% of H_2O in the sample after dilution into D_2O.

r	Corresponding BTT	Relative occurrence for 1.0 mol% H_2O	Relative occurrence for 10.0 mol% H_2O
0	BTT9D	1	1
1	BTT8D	9.09×10^{-2}	1.00
2	BTT7D	3.67×10^{-3}	4.44×10^{-1}
3	BTT6D	8.66×10^{-5}	1.15×10^{-1}
4	BTT5D	1.31×10^{-6}	1.92×10^{-2}
5	BTT4D	1.32×10^{-8}	2.13×10^{-3}
6	BTT3D	8.92×10^{-11}	1.58×10^{-4}
7	BTT2D	3.86×10^{-13}	7.53×10^{-6}
8	BTT1D	9.75×10^{-16}	2.09×10^{-7}
9	BTT0D	1.09×10^{-18}	2.58×10^{-9}

The distributions as given in Table 3 can be used to calculate the D/H exchange from BTT3D. The BTT samples were diluted only tenfold with D_2O, so the molar percentage of H_2O is calculated to be 10.0%. The intensity without artefacts can then be calculated with:

$I_{BTT1D} = I_{BTT1D\_c} - 1.01 \times 10^{-7}I_{BTT9D\_c} - 3.06 \times 10^{-2}I_{BTT3D\_c}$

$I_{BTT2D} = I_{BTT2D\_c} - 4.02 \times 10^{-6}I_{BTT9D\_c} - 3.03 \times 10^{-2}I_{BTT3D\_c}$

$I_{BTT3D} = I_{BTT3D\_c} - 1.61 \times 10^{-4}I_{BTT9D\_c} + \left(3.06 \times 10^{-4} + 3.03 \times 10^{-2}\right)I_{BTT3D\_c}$

$I_{BTT4D} = I_{BTT4D\_c} - 2.17 \times 10^{-3}I_{BTT9D\_c}$

$I_{BTT5D} = I_{BTT5D\_c} - 1.95 \times 10^{-2}I_{BTT9D\_c}$

$I_{BTT6D} = I_{BTT6D\_c} - 1.15 \times 10^{-1}I_{BTT9D\_c}$

$I_{BTT7D} = I_{BTT7D\_c} - 4.47 \times 10^{-1}I_{BTT9D\_c}$

$I_{BTT8D} = I_{BTT8D\_c} - 1.00I_{BTT9D\_c}$

$I_{BTT9D} = I_{BTT9D\_c} + (1.01 \times 10^{-7} + 4.02 \times 10^{-6} + 1.61 \times 10^{-4} + 2.17 \times 10^{-3} + 1.95 \times 10^{-2}$
$+ 1.15 \ 10^{-1} + 4.47 \times 10^{-1} + 1.00) I_{BTT9D\_c}$

From which the percentage of deuterated analogues can be calculated:

$$\%BTTnD = \frac{I_{BTTnD}}{\sum_{k=1}^{6} I_{BTTkD}} \times 100\%$$

f. Calculation of the percentage of deuterated analogues of BTA-C$_{11}$-EG$_4$ and BTA-C$_{13}$-EG$_4$:
The calculation for **BTA-C$_{11}$-EG$_4$** and **BTA-C$_{13}$-EG$_4$** only differ from the calculation of **BTA** in their isotope corrections. The following set of equations was used for the isotope correction of **BTA-C$_{11}$-EG$_4$**:

$I_{BTA1D\_c} = I_{646.44}$
$I_{BTA2D\_c} = I_{646.94} - 0.77 I_{BTA1D\_c}$
$I_{BTA3D\_c} = I_{647.44} - 0.77 I_{BTA2D\_c} - 0.33 I_{BTA1D\_c}$
$I_{BTA4D\_c} = I_{647.94} - 0.77 I_{BTA3D\_c} - 0.33 I_{BTA2D\_c} - 0.10 I_{BTA1D\_c}$
$I_{BTA5D\_c} = I_{648.45} - 0.77 I_{BTA4D\_c} - 0.33 I_{BTA3D\_c} - 0.10 I_{BTA2D\_c} - 0.02 I_{BTA1D\_c}$
$I_{BTA6D\_c} = I_{648.95} - 0.77 I_{BTA5D\_c} - 0.33 I_{BTA4D\_c} - 0.10 I_{BTA3D\_c} - 0.02 I_{BTA2D\_c} - 0.005 I_{BTA1D\_c}$
With $I_{646.44}$, $I_{646.94}$, $I_{647.44}$, $I_{647.94}$, $I_{648.45}$ and $I_{648.95}$ the intensity at m/z = 646.44, 646.94, 647.44, 647.94, 648.45 and 648.95, respectively.

Isotope correction for **BTA-C$_{13}$-EG$_4$** is based on the following set of equations:
$I_{BTA1D\_c} = I_{688.49}$
$I_{BTA2D\_c} = I_{688.99} - 0.84 I_{BTA1D\_c}$
$I_{BTA3D\_c} = I_{689.49} - 0.84 I_{BTA2D\_c} - 0.38 I_{BTA1D\_c}$
$I_{BTA4D\_c} = I_{689.99} - 0.84 I_{BTA3D\_c} - 0.38 I_{BTA2D\_c} - 0.12 I_{BTA1D\_c}$
$I_{BTA5D\_c} = I_{690.49} - 0.84 I_{BTA4D\_c} - 0.38 I_{BTA3D\_c} - 0.12 I_{BTA2D\_c} - 0.03 I_{BTA1D\_c}$
$I_{BTA6D\_c} = I_{690.99} - 0.84 I_{BTA5D\_c} - 0.38 I_{BTA4D\_c} - 0.12 I_{BTA3D\_c} - 0.03 I_{BTA2D\_c} - 0.01 I_{BTA1D\_c}$
with $I_{688.49}$, $I_{688.99}$, $I_{689.49}$, $I_{689.99}$, $I_{690.49}$ and $I_{690.99}$ the intensity at m/z = 688.49, 688.99, 689.49, 689.99, 690.49 and 690.99, respectively.

The equations described in section 3.9.3.b and 3.9.3.c can be used for the correction for the presence of water after 100x dilution and the calculation of the percentage of deuterated analogs.

3.9.4 Details on the bi-exponential fits
The data for the fully deuterated **BTA**, **BU** and **BTT** was plotted as a function of time (Figure 10) and the data was fitted with a bi-exponential growth function with Origin 2015. The percentage of BTA6D was fitted over 72 hours although only 24 hours are shown in Figure 10. The pre-defined function 'ExpGro2' was used for the fit:

$$y = y0 + A_{fast} \exp\left(\frac{x}{t_{fast}}\right) + A_{slow} \exp\left(\frac{x}{t_{slow}}\right)$$

with y the dependent variable (percentage of deuterated molecules), x the independent variable (time) and y0, A_{fast}, A_{slow}, t_{fast}, and t_{slow} the variables that were varied during the fitting. The offset, y0, can be related to the maximum percentage of deuterated molecules that can be reached, A_{fast} and A_{slow} describe the contribution of the fast and slow component and t_{fast} and t_{slow} describe the

time constants of the fast and slow component. The rate constants, k, were calculated from the time constants with:

$k_{fast} = 1/t_{fast}$ and $k_{slow} = 1/t_{slow}$

The pre-defined bi-exponential growth function was modified to include the following constraints:

$y0 \leq 100$

$y0 \geq A1 + A2$

Statistical F-tests were used to confirm that the bi-exponential growth function was a better fit than a mono-exponential or tri-exponential growth function. The fits were compared pairwise (mono-exponential vs bi-exponential and bi-exponential vs tri-exponential) with the null-hypothesis being that the fit with the lowest number of parameters was the best fit. The f-statistic was calculated with:

$$F = \left(\frac{SS_1 - SS_2}{df_1 - df_2}\right) / \left(\frac{SS_2}{df_2}\right)$$

with SS_1 the residual sum of squares of the fit with the lowest number of parameters, SS_2 the residual sum of squares of the fit with the highest number of parameters, df_1 the degrees of freedom of the fit with the lowest number of parameters and df_2 the degrees of freedom of the fit with the highest number of parameters. All these variables were obtained from Origin 2015. The corresponding p-value for $\alpha = 0.05$ was obtained from the software package Rcmdr. The null-hypothesis was rejected when $p < \alpha$. From this it was concluded that all data was best described with a bi-exponential growth function.

With the bi-exponential function and constraints the following fits were found:

$BTA6D = 74.5 - 47.3e^{\frac{t}{-0.24}} - 27.3e^{\frac{t}{-35.7}}$ with ($R^2_{adj} = 0.976$)

$BU6D = 100.0 - 68.9e^{\frac{t}{-2.16}} - 29.6e^{\frac{t}{-75.7}}$ with ($R^2_{adj} = 0.999$)

$BTT9D = 99.7 - 6.35e^{\frac{t}{-0.16}} - 73.4e^{\frac{t}{-8.91}}$ with ($R^2_{adj} = 0.996$)
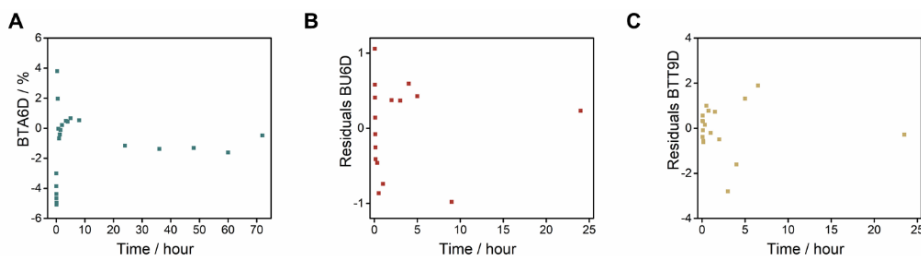
Figure 13. Residuals of the bi-exponential fits used to fit the data for BTA6D (A), BU6D (B) and BTT9D (C). All fits and residuals plots were generated with Origin 2015.

The results of the bi-exponential fit are summarized in Table 6:

Table 6. Rate constants, k, contributions and maximum percentage of deuteration of the H/D exchange processes obtained after fitting the percentage of molecules with all hydrogen atoms exchanged for deuterium atoms with a bi-exponential growth function.

	Rate constants (h^{-1})		Contributions (%)		Maximum percentage of deuteration (%)
	k_{fast}	k_{slow}	Fast	Slow	
BTA6D	4.22	0.028	47.3	27.3	74.5
BU6D	0.46	0.013	68.9	29.6	100.0
BTT9D	6.21	0.11	6.35	73.4	99.7

3.10 References

1　B. N. S. Thota, L. H. Urner and R. Haag, *Chem. Rev.*, 2016, **116**, 2079–2102.
2　H. L. K. Fu, C. Po, S. Y. L. Leung and V. W. W. Yam, *ACS Appl. Mater. Interfaces*, 2017, **9**, 2786–2795.
3　Y. Loo, S. Zhang and C. A. E. Hauser, *Biotechnol. Adv.*, 2012, **30**, 593–603.
4　E. Krieg, M. M. C. Bastings, P. Besenius and B. Rybtchinski, *Chem. Rev.*, 2016, **116**, 2414–2477.
5　K. Petkau-Milroy, M. H. Sonntag and L. Brunsveld, *Chem. - A Eur. J.*, 2013, **19**, 10786–10793.
6　M. H. Bakker, R. E. Kieltyka, L. Albertazzi and P. Y. W. Dankers, *RSC Adv.*, 2016, **6**, 110600–110603.
7　G. A. Silva, C. Czeisler, K. L. Niece, E. Beniash, D. A. Harrington, J. A. Kessler and S. I. Stupp, *Science (80-.).*, 2004, **303**, 1352–1355.
8　W. E. M. Noteborn, V. Saez Talens and R. E. Kieltyka, *ChemBioChem*, 2017, **18**, 1995–1999.
9　S. I. Stupp, *Nano Lett.*, 2010, **10**, 4783–4786.
10　B. Rybtchinski, in *Hierarchical Macromolecular Structures: 60 Years after the Staudinger Nobel Prize II*, ed. V. Percec, Springer International Publishing, Cham, 2013, pp. 363–387.
11　J. Boekhoven and S. I. Stupp, *Adv. Mater.*, 2014, **26**, 1642–1659.
12　R. Dong, Y. Zhou, X. Huang, X. Zhu, Y. Lu and J. Shen, *Adv. Mater.*, 2015, **27**, 498–526.
13　N. M. Casellas, S. Pujals, D. Bochicchio, G. M. Pavan, T. Torres, L. Albertazzi and M. García-Iglesias, *Chem. Commun.*, 2018, **54**, 4112–4115.
14　C. Rest, M. J. Mayoral, K. Fucke, J. Schellheimer, V. Stepanenko and G. Fernández, *Angew. Chemie - Int. Ed.*, 2014, **53**, 700–705.
15　F. García and L. Sánchez, *Chem. - A Eur. J.*, 2010, **16**, 3138–3146.
16　D. Straßburger, N. Stergiou, M. Urschbach, H. Yurugi, D. Spitzer, D. Schollmeyer, E. Schmitt and P. Besenius, *ChemBioChem*, 2018, **19**, 912–916.
17　S. S. Lee, T. Fyrner, F. Chen, Z. Álvarez, E. Sleep, D. S. Chun, J. A. Weiner, R. W. Cook, R. D. Freshman, M. S. Schallmo, K. M. Katchko, A. D. Schneider, J. T. Smith, C. Yun, G. Singh, S. Z. Hashmi, M. T. McClendon, Z. Yu, S. R. Stock, W. K. Hsu, E. L. Hsu and S. I. Stupp, *Nat. Nanotechnol.*, 2017, **12**, 821–829.
18　K. Petkau-Milroy, M. H. Sonntag, A. H. A. M. Van Onzen and L. Brunsveld, *J. Am. Chem. Soc.*, 2012, **134**, 8086–8089.
19　J. P. Patterson, Y. Xu, M. A. Moradi, N. A. J. M. Sommerdijk and H. Friedrich, *Acc. Chem. Res.*, 2017, **50**, 1495–1501.
20　H. Weissman and B. Rybtchinski, *Curr. Opin. Colloid Interface Sci.*, 2012, **17**, 330–342.
21　T. F. A. De Greef, M. M. J. Smulders, M. Wolffs, A. P. H. J. Schenning, R. P. Sijbesma and E. W. Meijer, *Chem. Rev.*, 2009, **109**, 5687–5754.
22　J. H. Ortony, C. J. Newcomb, J. B. Matson, L. C. Palmer, P. E. Doan, B. M. Hoffman and S. I. Stupp, *Nat. Mater.*, 2014, **13**, 812–816.
23　L. Albertazzi, D. van der Zwaag, C. M. A. Leenders, R. Fitzner, R. W. van der Hofstad and E. W. Meijer, *Science*, 2014, **344**, 491–495.
24　L. Albertazzi, F. J. Martinez-Veracoechea, C. M. A. Leenders, I. K. Voets, D. Frenkel and E. W. Meijer, *Proc. Natl. Acad. Sci.*, 2013, **110**, 12203–12208.
25　K. Petkau-Milroy, D. A. Uhlenheuer, A. J. H. Spiering, J. A. J. M. Vekemans and L. Brunsveld, *Chem. Sci.*, 2013, **4**, 2886.
26　S. I. S. Hendrikse, S. P. W. Wijnands, R. P. M. Lafleur, M. J. Pouderoijen, H. M. Janssen, P. Y. W. Dankers and E. W. Meijer, *Chem. Commun.*, 2017, **53**, 2279–2282.
27　X. Lou, R. P. M. Lafleur, C. M. A. Leenders, S. M. C. Schoenmakers, N. M. Matsumoto, M. B. Baker, J. L. J. van Dongen, A. R. A. Palmans and E. W. Meijer, *Nat. Commun.*, 2017, **8**, 15420.

28   T. E. Wales and J. R. Engen, *Mass Spectrom. Rev.*, 2006, **25**, 158–170.
29   L. Konermann and D. A. Simmons, *Mass Spectrom. Rev.*, 2003, **22**, 1–26.
30   S. W. Englander, *J. Am. Soc. Mass Spectrom.*, 2006, **17**, 1481–1489.
31   L. Konermann, J. Pan and Y.-H. Liu, *Chem. Soc. Rev.*, 2011, **40**, 1224–1234.
32   A. J. Percy, M. Rey, K. M. Burns and D. C. Schriemer, *Anal. Chim. Acta*, 2012, **721**, 7–21.
33   J. R. Engen and T. E. Wales, *Annu. Rev. Anal. Chem.*, 2015, **8**, 127–148.
34   S. W. Englander, *Annu. Rev. Biophys. Biomol. Struct.*, 2000, **29**, 213–238.
35   A. N. Hoofnagle, K. A. Resing and N. G. Ahn, *Annu. Rev. Biophys. Biomol. Struct.*, 2003, **32**, 1–25.
36   V. Katta and B. T. Chait, *Rapid Commun Mass Spectrom*, 1991, **5**, 214–217.
37   L. Konermann, S. Vahidi and M. A. Sowole, *Anal. Chem.*, 2014, **86**, 213–232.
38   W. Hu, B. T. Walters, Z. Y. Kan, L. Mayne, L. E. Rosen, S. Marqusee and S. W. Englander, *Proc. Natl. Acad. Sci. U. S. A.*, 2013, **110**, 7684–7689.
39   R. E. Iacob and J. R. Engen, *J. Am. Soc. Mass Spectrom.*, 2012, **23**, 1003–1010.
40   D. L. Smith, Y. Deng and Z. Zhang, *J. mass Spectrom.*, 1997, **32**, 135–146.
41   N. Carulla, M. Zhou, M. Arimon, M. Gairi, E. Giralt, C. V. Robinson and C. M. Dobson, *Proc. Natl. Acad. Sci.*, 2009, **106**, 7828–7833.
42   N. Carulla, G. L. Caddy, D. R. Hall, J. Zurdo, M. Gairí, M. Feliz, E. Giralt, C. V. Robinson and C. M. Dobson, *Nature*, 2005, **436**, 554–558.
43   H. D. F. Winkler, E. V. Dzyuba and C. A. Schalley, *New J. Chem.*, 2011, **35**, 529.
44   Z. Qi, C. Schlaich and C. A. Schalley, *Chem. - A Eur. J.*, 2013, **19**, 14867–14875.
45   L. Cera and C. A. Schalley, *Chem. Soc. Rev.*, 2014, **43**, 1800.
46   B. N. S. Thota, X. Lou, D. Bochicchio, T. F. E. Paffen, R. P. M. Lafleur, J. L. J. van Dongen, S. Ehrmann, R. Haag, G. M. Pavan, A. R. A. Palmans and E. W. Meijer, *Angew. Chemie - Int. Ed.*, 2018, **57**, 6843–6847.
47   C. M. A. Leenders, L. Albertazzi, T. Mes, M. M. E. Koenigs, A. R. A. Palmans and E. W. Meijer, *Chem. Commun.*, 2013, **49**, 1963–1965.
48   R. P. M. Lafleur, S. Herziger, S. M. C. Schoenmakers, A. D. A. Keizer, J. Jahzerah, B. N. S. Thota, L. Su, P. H. H. Bomans, N. A. J. M. Sommerdijk, A. R. A. Palmans, R. Haag, H. Friedrich, C. Böttcher and E. W. Meijer, *J. Am. Chem. Soc.*, 2020, **142**, 17644–17652.
49   M. Fernandez-Castano Romera, R. P. M. Lafleur, C. Guibert, I. K. Voets, C. Storm and R. P. Sijbesma, *Angew. Chemie - Int. Ed.*, 2017, **56**, 8771–8775.
50   R. P. M. Lafleur, X. Lou, G. M. Pavan, A. R. A. Palmans and E. W. Meijer, *Chem. Sci.*, 2018, **9**, 6199–6209.
51   N. Chebotareva, P. H. H. Bomans, P. M. Frederik, N. A. J. M. Sommerdijk and R. P. Sijbesma, *Chem. Commun.*, 2005, 4967.
52   M. Fernández-Castaño Romera, X. Lou, J. Schill, G. Ter Huurne, P. P. K. H. Fransen, I. K. Voets, C. Storm and R. P. Sijbesma, *J. Am. Chem. Soc.*, 2018, **140**, 17547–17555.
53   R. P. M. Lafleur, S. M. C. Schoenmakers, P. Madhikar, D. Bochicchio, B. Baumeier, A. R. A. Palmans, G. M. Pavan and E. W. Meijer, *Macromolecules*, 2019, **52**, 3049–3055.
54   S. I. S. Hendrikse, L. Su, T. P. Hogervorst, R. P. M. Lafleur, X. Lou, G. A. van der Marel, J. D. C. Codee and E. W. Meijer, *J. Am. Chem. Soc.*, 2019, **141**, 13877–13886.
55   X. Lou, S. M. C. Schoenmakers, J. L. J. van Dongen, M. Garcia-Iglesias, N. M. Casellas, M. Fernández-Castaño Romera, R. P. Sijbesma, E. W. Meijer and A. R. A. Palmans, *J. Polym. Sci.*, 2021, **59**, 1151–1161.

Chapter 4

Consequences of Chirality on the Structure and Dynamics of Supramolecular Polymers

Abstract: The introduction of stereogenic centers in supramolecular building blocks is a common strategy to obtain information about their aggregation into supramolecular polymers. In this chapter, two chiral, non-racemic benzene-1,3,5-tricarboxamides (BTAs) will be studied to elucidate the effect of stereogenic centers on the morphology and dynamics of supramolecular polymers in water using the techniques described in Chapters 2 and 3. Three stereogenic centers based on deuterium atoms were introduced in the first BTA, resulting in a supramolecular polymer that at first glance has a structure and dynamics identical to its achiral counterpart. However, an increase in circular dichroism (CD) is observed over 4 weeks as well as a decrease in the helical pitch and monomer exchange dynamics. These results indicate that the order within the assemblies increases over time, an effect that is enhanced by the isotopic chirality. The second BTA has three stereogenic centers based on methyl groups. These stereocenters change the packing of the molecules such that a strong CD signal is found that originates from a supramolecular polymer that consists of a single stack of molecules with different exchange dynamics. Neither of the chiral BTAs display a strong sergeants-and-soldiers effect when mixed with an achiral BTA. Instead, morphological transitions from single stacks to double helices with opposite helicity are observed. The results presented here demonstrate that the introduction of stereogenic centrers increases the stability of the supramolecular assemblies. As a result, care should be taken when introducing chemical modifications to the monomers as this could drastically change their packing within an assembly.
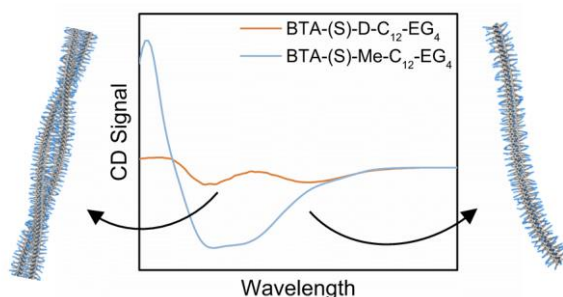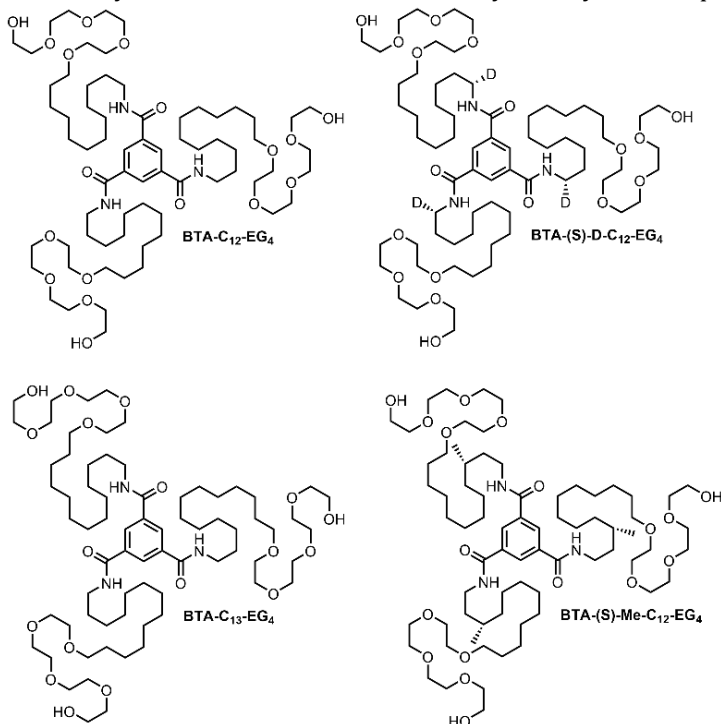
4.1 Introduction

Natural supramolecular assemblies exhibit a wide range of structures and dynamics, sometimes even within one assembly. Amino acid sequences that lack a secondary structure show more fluctuations in space than amino acids contained in α-helices or β-sheets.[1–3] Additionally, a tighter packing of phospholipids limits their lateral diffusion, for example when they are assembled into lipid rafts with a specialized function.[4–6] In general, it can be observed that the structure, dynamics and function of those assemblies are influenced by the order within the assemblies: the tighter the packing of the molecules, the less dynamic they are.

Synthetic supramolecular polymers in water are promising candidates for the formation of synthetic biomaterials since they share a lot of similarities in their structure and dynamics to living tissue.[7–10] Several types of supramolecular polymers have been designed for this purpose, based on various motifs such as peptide amphiphiles,[11–13] ureidopyrimidinones[14,15] or discotics.[16–18] Supramolecular monomers can easily be modified to create supramolecular assemblies with new properties. However, a major challenge in the field of supramolecular chemistry lies in the ability to understand how minor changes in the chemical structure of the monomers influence their molecular packing and the overall structure and dynamics of the resulting supramolecular polymers. These effects are generally studied over a short time period as these supramolecular polymers are expected to be in thermodynamic equilibrium.[18] Surprisingly, the hydrogen/deuterium exchange experiments with water-compatible benzene-1,3,5-tricarboxamides (BTAs) presented in Chapter 3 indicate that some molecular exchange processes occur over very long timescales in the range of several weeks. Additionally, the detailed microscopy studies in Chapter 2 revealed the presence of a secondary structure within those assemblies which was previously overlooked. An understanding of the packing at the molecular level is therefore essential to understand the properties of the systems at the supramolecular level.[19]

One dimensional supramolecular polymers assembled from discotic building blocks such as BTAs are characterized by their helical arrangement which can be biased by the introduction of stereogenic centers.[20–22] This has led to several new revelations about the supramolecular self-assembly of BTAs in organic solvents. The introduction of one deuterium atoms at the α-position next to the amides was already enough to induce a preference in the helical conformation of the BTAs.[23] Moreover, conformational changes due to solvent and temperature effects could be elucidated in those chiral assemblies.[24,25] However, no amplification of asymmetry was observed when those motifs were mixed with achiral BTAs in sergeant-and-soldier experiments, which was proposed to be due to the small difference between an hydrogen and deuterium atom resulting in a low mismatch energy.[26] BTAs with a more bulky methyl group could amplify asymmetry to various degrees in organic solvents depending on temperature[27,28] and the position and number of stereogenic centers.[29]

In this chapter, we study water-compatible BTAs in which stereogenic centers were introduced to gain a better understanding of the packing within supramolecular polymers and the influence of stereogenic centers on their structure and dynamics. The chemical structure of a BTA with dodecyl chains and tetra(ethylene glycol) periphery (**BTA-C$_{12}$-EG$_4$**, Figure 1) was modified to contain a deuterium atom at the α-position (**BTA-(S)-D-C$_{12}$-EG$_4$**, Figure 1) or a methyl group at the γ-position (**BTA-(S)-Me-C$_{12}$-EG$_4$**, Figure 1). Preliminary studies on both molecules with UV and circular dichroism (CD) spectroscopy were performed previously by Janus Leenders.[30–32] The spectroscopy experiments will be repeated here after which the structure and dynamics of the assemblies will be elucidated in detail. **BTA-(S)-D-C$_{12}$-EG$_4$** was previously shown to assemble into supramolecular polymers with a packing that is similar to **BTA-C$_{12}$-EG$_4$** but with a Cotton effect that increases over time.[32] Here, the effect of this increase in order on the structure and dynamics will be followed over time. **BTA-(S)-Me-C$_{12}$-EG$_4$** on the other hand assembles into supramolecular polymers with spectra that resemble helical polymers based on BTAs in organic solvents.[30] Its self-assembly will be compared to **BTA-C$_{13}$-EG$_4$** (Figure 1) which has the same number of carbon atoms in its hydrophobic chain. Based on these experiments, a proposal for the different packing of the molecules will be presented. Finally, mixing experiments will be performed to study if the BTAs can transfer their asymmetry to other polymers.


Figure 1. Chemical structure of **BTA-C$_{12}$-EG$_4$**, **BTA-(S)-D-C$_{12}$-EG$_4$**, **BTA-C$_{13}$-EG$_4$** and **BTA-(S)-Me-C$_{12}$-EG$_4$**.

4.2 The self-assembly of a BTA with stereogenic centers due to the introduction of deuterium atoms

The self-assembly protocol for **BTA-(S)-D-C$_{12}$-EG$_4$** was previously based on injection of the molecules from an organic stock solution into water. Since then, it has been shown that cosolvents influence both the structure and dynamics of supramolecular polymers[33] and that more reproducible results can be obtained with a controlled heating-cooling protocol.[32] Previous spectroscopy experiments were therefore repeated with samples prepared with this new protocol (see section 4.7.1).

The UV spectrum of **BTA-(S)-D-C$_{12}$-EG$_4$** contains maxima at 211 nm and 229 nm (Figure 2A), resembling the spectrum of the achiral **BTA-C$_{12}$-EG$_4$**. Already after 1 day a negative Cotton effect is observed in the CD spectrum with a positive band around 196 nm and negative bands at 213 and 250 nm (Figure 2B). In between these last two bands the CD signal becomes slightly positive at 230 nm. The occurrence of a CD signal indicates that an ordered packing with a preferred helicity is adopted. Additionally, a negative linear dichroism (LD) signal is observed around 229 nm (Figure 2C). It has been reported that a CD signal that overlaps with an opposite LD signal does originate from macroscopic alignment of assemblies rather than a helical preference.[34] Only the small positive CD signal at 230 nm is influenced by this artefact. Interestingly, the UV spectrum is unaffected by time whereas both the CD and LD signal change over time. The extremes in the CD spectrum at 196, 213 and 250 nm double in intensity over 4 weeks, with the most prominent changes observable in the first 2 weeks (Figure 2B). The LD signal decreases over time until it is barely observable after 4 weeks, resulting in a decrease of the CD signal at that same position. The time-dependent increase in CD signal indicates a slow increase of order.

The presence of intermolecular hydrogen bonds between the amides of **BTA-(S)-D-C$_{12}$-EG$_4$** in solution was probed with Fourier transform infrared (FT-IR) spectroscopy. Samples were prepared in deuterated solvents to prevent overlap of the O-H vibrations from the solvent with the amide I vibration of the BTA.[35] The amide I vibration of **BTA-(S)-D-C$_{12}$-EG$_4$** is positioned at 1647 cm^{-1} in MeOD (Figure 2D), indicative for a molecularly dissolved state without hydrogen bonds. After self-assembly in D$_2$O the amide I vibration is observed at 1633 cm^{-1}. This shift to lower wavenumbers compared to the molecularly dissolved state is indicative for the formation of hydrogen bonds and is identical to the one observed for **BTA-C$_{12}$-EG$_4$**,[36] revealing that both molecules assemble with the same hydrogen bond pattern. The resemblance of the UV and FT-IR spectra of **BTA-(S)-D-C$_{12}$-EG$_4$** and **BTA-C$_{12}$-EG$_4$** suggests that both molecules assemble with the same molecular packing.
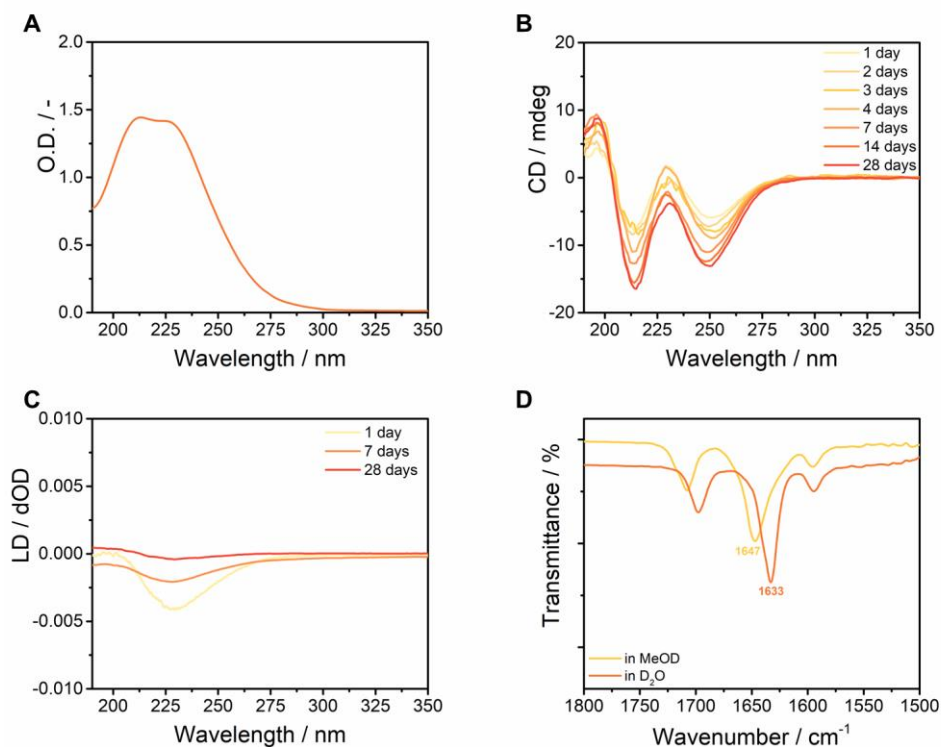
Figure 2. (A) UV spectrum of **BTA-(S)-D-C₁₂-EG₄** in water after 1 day of equilibration (c = 50 μM, l = 1 cm, T = 20 °C). (B) CD spectra of **BTA-(S)-D-C₁₂-EG₄** in water after different equilibration times (c = 50 μM, l = 1 cm, T = 20 °C). (C) LD spectrum of **BTA-(S)-D-C₁₂-EG₄** in water after different equilibration times (c = 50 μM, l = 1 cm, T = 20 °C). (D) Zoom of the FT-IR spectrum of the amide I vibration of **BTA-(S)-D-C₁₂-EG₄** in MeOD and D_2O (c = 20 mg/mL, l = 0.05 mm, T = room temperature). The vibrations at 1708 cm^{-1} in MeOD[37] and 1697 cm^{-1} in D_2O[38] originate from the C=O vibration of acetone which was used to clean the cuvette.

The morphology of the polymers of **BTA-(S)-D-C₁₂-EG₄** after 1 day of aging was studied with cryogenic transmission electron microscopy (cryoTEM). Micrometer long one-dimensional assemblies are observed with a diameter around 7 nm (Figure 3A). Next, the image processing technique described in Chapter 2 was applied in collaboration with dr. Svenja Herziger and dr. Christoph Böttcher to obtain information about a possible secondary structure. A double helix structure with a half pitch of 19.9 ± 0.4 nm (Figure 3B) and 18.6 ± 0.4 nm (Figure 3C) is found after 1 day and 4 weeks of equilibration, respectively. The decrease of the pitch after 4 weeks is indicative for a tighter packing of molecules, related to the increase in order as observed with CD spectroscopy. The half pitch after 1 day matches with the half pitch of 19.9 ± 0.4 nm as measured for **BTA-C₁₂-EG₄** after 1 day (Chapter 2). These experiments were not repeated for **BTA-C₁₂-EG₄** over time.
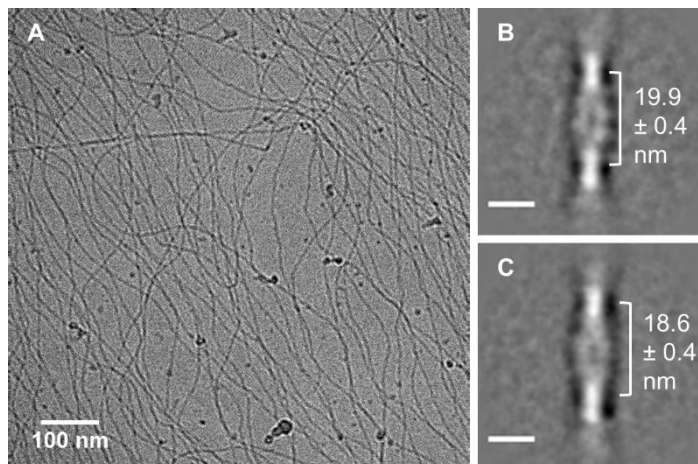
Figure 3. (A) CryoTEM image of **BTA-(S)-D-C₁₂-EG₄** in water after 1 day of equilibration (c = 500 µM). Dark spherical objects are crystalline ice particles. (B-C) Class sum images of aligned image extracts of a sample of **BTA-(S)-D-C₁₂-EG₄** in water after (B) 1 day and (C) 4 weeks of equilibration (c = 500 µM). The scale bars are 10 nm.

Finally, hydrogen/deuterium exchange followed by mass spectrometry (HDX-MS) experiments were performed to study the dynamics of the polymers. Aqueous samples of self-assembled BTAs are diluted into D₂O to study the exchange of labile hydrogen atoms. The three peripheral hydroxyl hydrogen atoms are exchanged immediately for deuterium atoms, whereas the exchange of the amide hydrogen atoms is delayed since they are protected from contact with the solvent by the hydrophobic pocket. The H/D exchange of those amide hydrogen atoms is therefore a good measure for the exchange of monomers between supramolecular assemblies (see Chapter 3).

An aqueous sample of **BTA-(S)-D-C₁₂-EG₄** was equilibrated for 1 day in water before 100x dilution into D₂O. The H/D exchange of the amides was found to be a slow process (Figure 4A). The initial exchange occurs fast and some BTA4D and BTA5D, that is BTAs with only 1 or 2 of the amide hydrogen atoms exchanged for deuterium atoms, can be observed in the first hour. This indicates that there are some less-ordered assemblies that undergo fast H/D exchange. The process slows down when 43% of the molecules is deuterated and 70.0% of the BTAs have all their labile hydrogen atoms exchanged after 72 hours in D₂O. This is comparable to the degree and rate of deuteration of a sample of **BTA-C₁₂-EG₄** (Figure 4D).

The HDX-MS experiments were repeated with a sample that was equilibrated for 4 weeks in water before dilution into D₂O. The H/D exchange of the 4-weeks equilibrated sample follows a similar trend as the 1-day equilibrated sample, with an initial fast exchange and a slow exchange after a few hours (Figure 4B). However, the percentage of BTA4D and BTA5D is lower in this sample. Additionally, after 72 hours the percentage of fully deuterated BTAs is only 59.5% compared to 70.0% for the 1-day

equilibrated sample. Especially the last part of the H/D exchange is slower after aging, which indicates that the double helices becomes less dynamic over time. Such a difference in the percentage of BTA6D is not found for a 4-week equilibrated sample of **BTA-C$_{12}$-EG$_4$** (Figure 4C-D). Taking all measurements together, it can be concluded that the introduction of isotopic chirality initially does not influence the structure and dynamics but over time the order in the assemblies increases which results in a tighter packing of molecules and slower dynamics. A proposal for the packing of **BTA-(S)-D-C$_{12}$-EG$_4$** molecules will be presented in section 4.4.
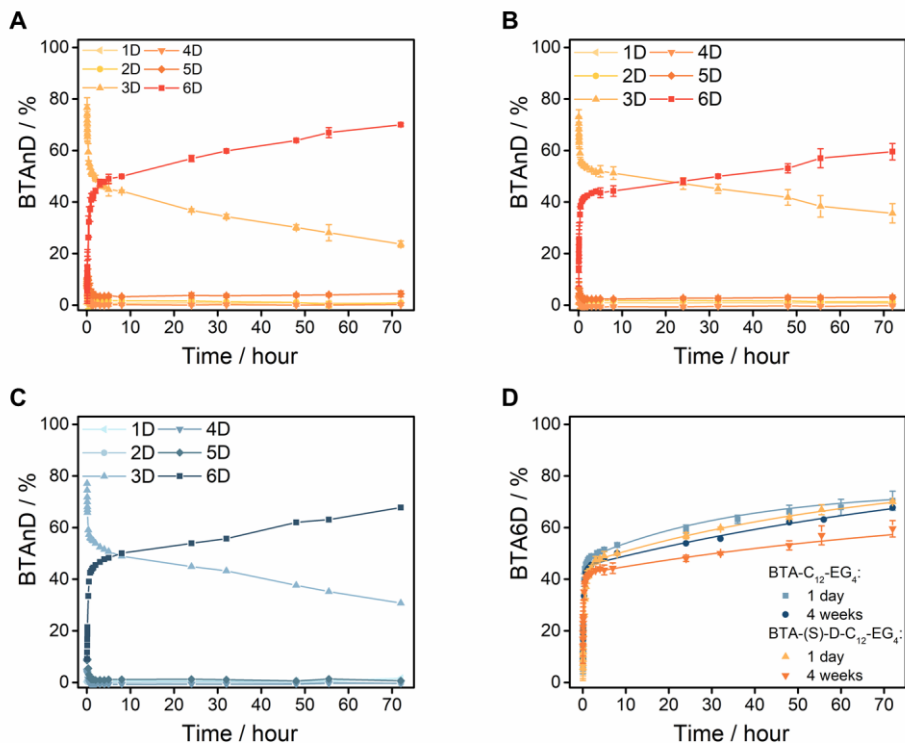
Figure 4. (A-B) The percentage of different deuterated analogues of **BTA-(S)-D-C$_{12}$-EG$_4$** as a function of time after the 100x dilution of an aqueous 500 μM sample into D$_2$O (T = room temperature). The sample was diluted after (A) 1 day or (B) 4 weeks of equilibration in H$_2$O. (C) The percentage of different deuterated analogues of **BTA-C$_{12}$-EG$_4$** as a function of time after the 100x dilution of an aqueous 4-weeks equilibrated 500 μM sample into D$_2$O (T = room temperature). (D) The percentage of fully deuterated **BTA-C$_{12}$-EG$_4$** and **BTA-(S)-D-C$_{12}$-EG$_4$** as a function of time after the 100x dilution of aqueous 500 μM samples into D$_2$O (T = room temperature). Samples were diluted after 1 day or 4 weeks of equilibration in H$_2$O. The symbols represent the average and the error bars the standard deviation calculated from three independent measurements (except for **BTA-C$_{12}$-EG$_4$** after 4 weeks). The lines in B represent a bi-exponential growth function. All lines are added to guide the eye.

4.3 The self-assembly of a BTA with stereogenic centers due to the introduction of methyl groups

Next, the self-assembly of **BTA-(S)-Me-C$_{12}$-EG$_4$** in water was studied. The introduction of additional methyl groups in the aliphatic chains changes the hydrophilic/hydrophobic balance, which influences the self-assembly. This was previously observed for **BTA-C$_{13}$-EG$_4$** which initially assemblies into a mixture of complex structures from which the supramolecular polymers were isolated.[32] **BTA-(S)-Me-C$_{12}$-EG$_4$** on the other hand could not be dissolved with the heating-cooling protocol used for **BTA-C$_{12}$-EG$_4$**, **BTA-C$_{13}$-EG$_4$** and **BTA-(S)-D-C$_{12}$-EG$_4$**. Instead, the molecules had to be injected into water from a stock solution in acetonitrile (ACN) before being subjected to the controlled heating-cooling protocol. All samples were prepared with a final ACN concentration of 2% as this was found to be the minimal amount needed to make reproducible samples.

The UV spectrum of **BTA-(S)-Me-C$_{12}$-EG$_4$** contains a maximum at 194 nm and a shoulder around 240 nm (Figure 5A) and does not resemble the UV spectra of the other three molecules under investigation here. Additionally, the spectrum does not match with the molecularly dissolved state in ACN, which is characterized by a maximum at 207 nm. The UV spectrum is however very similar to those observed for aggregated lipophilic BTAs in alkane solvents.[20] It can therefore be concluded that **BTA-(S)-Me-C$_{12}$-EG$_4$** aggregates in water. The CD spectrum is characterized by a negative Cotton effect with a positive band at 193 nm and negative bands at 213 and 228 nm (Figure 5B). A positive LD signal is found at 194 nm and around 240 nm (Figure 5C), which indicates that the CD signals at higher wavelengths are not artefacts. The CD spectrum differs from the spectrum of **BTA-(S)-D-C$_{12}$-EG$_4$**, both in shape and in intensity, suggesting a different type of packing. All spectra were measured again after weeks of equilibration, but no influence of time was found. Interestingly, the CD spectrum of **BTA-(S)-Me-C$_{12}$-EG$_4$** closely resembles the spectrum of a lipophilic BTA with stereogenic centers based on methyl groups that is assembled into columnar helical assemblies in organic solvents.[20,39]

The ability of **BTA-(S)-Me-C$_{12}$-EG$_4$** to form intermolecular hydrogen bonds in solution was studied with FT-IR spectroscopy. In MeOD the amide I vibration is found at 1648 cm^{-1} (Figure 5D), which resembles other BTAs in a molecularly dissolved state. The amide I vibration is split into two peaks at 1635 and 1618 cm^{-1} upon self-assembly in D$_2$O. The shift towards lower wavenumbers is indicative for hydrogen bonding. This specific split pattern has not been observed for BTAs in water before, but a similar pattern was found for chiral BTAs in organic media.[39]
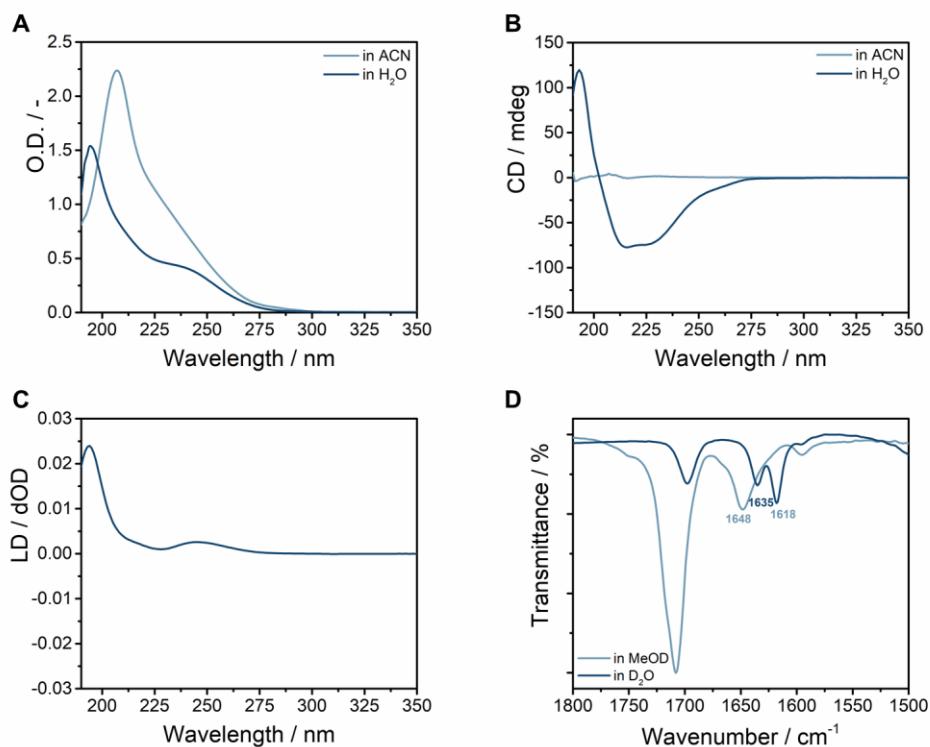
Figure 5. (A) UV spectra of **BTA-(S)-Me-C₁₂-EG₄** in ACN and water with 2% ACN (c = 50 μM, l = 1 cm, T = 20 °C). (B) CD spectra of **BTA-(S)-Me-C₁₂-EG₄** in ACN and water with 2% ACN (c = 50 μM, l = 1 cm, T = 20 °C). (C) LD spectrum of **BTA-(S)-Me-C₁₂-EG₄** in water with 2% ACN (c = 50 μM, l = 1 cm, T = 20 °C). (D) Zoom of the FT-IR spectrum of the amide I vibration of **BTA-(S)-Me-C₁₂-EG₄** in MeOD and D₂O (c = 20 mg/mL, l = 0.05 mm, T = room temperature). The vibrations at 1708 cm⁻¹ in MeOD[37] and 1697 cm⁻¹ in D₂O[38] originate from the C=O vibration of acetone which was used to clean the cuvette.

The assemblies of **BTA-(S)-Me-C₁₂-EG₄** were visualized with cryoTEM. Micrometer long fibrillar supramolecular assemblies were found (Figure 6A), which appear to be thinner than the fibers of the other BTAs. Image processing reveals that **BTA-(S)-Me-C₁₂-EG₄** assembles into a straight fiber with a diameter of 3.7 ± 0.4 nm (Figure 6B), corresponding to a single stack of molecules. Such a single fiber structure has not been observed before. The absence of a secondary double helix structure is not a result of the increase in hydrophobicity of the monomers, since **BTA-C₁₃-EG₄** does form assemblies based on two strands of BTAs (Chapter 2). The additional methyl groups should therefore be responsible for this new supramolecular structure.
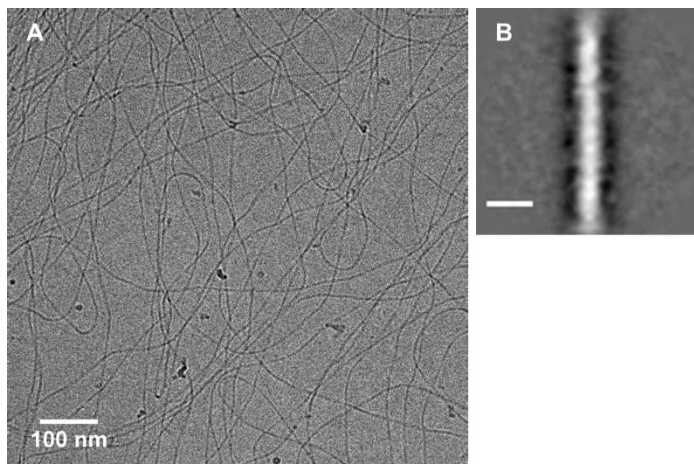
Figure 6. (A) CryoTEM image of **BTA-(S)-Me-C$_{12}$-EG$_4$** in water with 2% ACN (c = 500 μM). Dark spherical objects are crystalline ice particles. (B) Class sum image of aligned image extracts of a sample of **BTA-(S)-Me-C$_{12}$-EG$_4$** in water with 2% ACN (c = 500 μM). The scale bar is 10 nm.

The molecular exchange dynamics of the **BTA-(S)-Me-C$_{12}$-EG$_4$** polymers were evaluated with HDX-MS by diluting a 500 μM aqueous sample 100x into D$_2$O. The fastest H/D exchange occurs in the first 20 minutes when the percentage of fully deuterated molecules increases from 9.3% to 13.8% (Figure 7A). BTA4D and BTA5D are barely observed in this experiment, suggesting that there is almost no penetration of D$_2$O into ill-defined structures. The H/D exchange slows down after 20 minutes and 63.8% of the molecules is fully deuterated after one week.

The percentage of BTA6D is lower for **BTA-(S)-Me-C$_{12}$-EG$_4$** than for **BTA-C$_{12}$-EG$_4$** during most of the experiment (Figure 7B). The most prominent differences are observed in the first hour in which the percentage of BTA6D increases to 15% for the chiral BTA and to 47% for the achiral BTA. The small increase observed for **BTA-(S)-Me-C$_{12}$-EG$_4$** might indicate that there are less ill-defined aggregates in the sample of this BTA. The second part of the H/D exchange curve is probably due to the long supramolecular polymers in solution and the H/D exchange on this timescale is faster for **BTA-(S)-Me-C$_{12}$-EG$_4$** than for **BTA-C$_{12}$-EG$_4$**. This might suggest that the single fibers of the chiral BTA are more dynamic than the double helix. The HDX-MS experiments of **BTA-C$_{13}$-EG$_4$**, with the same number of carbon atoms in its hydrophobic chain as **BTA-(S)-Me-C$_{12}$-EG$_4$**, has a H/D exchange that resembles that of **BTA-C$_{12}$-EG$_4$** but lower (Figure 7B). Based on the different profile of **BTA-(S)-Me-C$_{12}$-EG$_4$** it be concluded that the changes in the H/D exchange of this molecule mainly originate from the change in supramolecular structure and not solely from an increase in hydrophobic chain length.
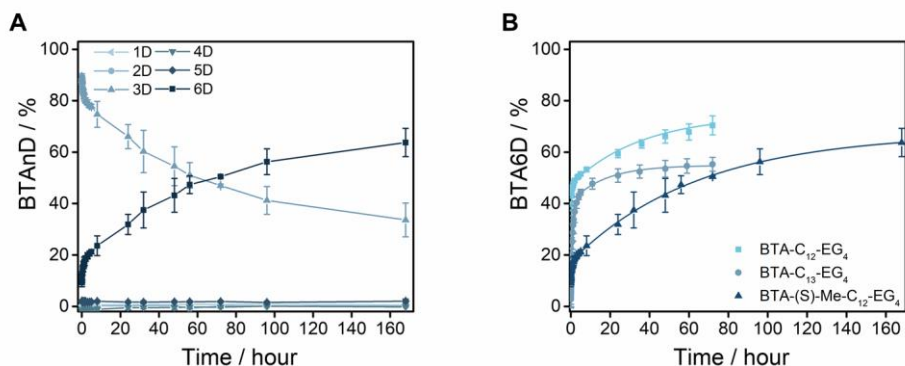
Figure 7. (A) The percentage of different deuterated analogues of **BTA-(S)-Me-C$_{12}$-EG$_4$** as a function of time after the 100x dilution of an aqueous 500 µM sample with 2% ACN into D$_2$O (T = room temperature). (B) The percentage of fully deuterated **BTA-C$_{12}$-EG$_4$**, **BTA-C$_{13}$-EG$_4$** and **BTA-(S)-Me-C$_{12}$-EG$_4$** as a function of time after the 100x dilution of aqueous 500 µM samples into D$_2$O (T = room temperature). The symbols represent the average and the error bars the standard deviation calculated from three independent measurements. The lines in B represent a bi-exponential growth function. All lines are added to guide the eye.

4.4 Proposed molecular packing for the BTAs

Previous sections described notable differences between the structure and dynamics of **BTA-(S)-D-C$_{12}$-EG$_4$** and **BTA-(S)-Me-C$_{12}$-EG$_4$**. **BTA-(S)-D-C$_{12}$-EG$_4$** resembles **BTA-C$_{12}$-EG$_4$** assemblies both in the double helix structure and the dynamic exchange of monomers. The order within those assemblies increases over time resulting in a decrease in helical pitch and dynamics. **BTA-(S)-Me-C$_{12}$-EG$_4$** assembles in a single fiber with a different mechanism of exchange. The differences in dynamics between achiral **BTA-C$_{12}$-EG$_4$** and chiral **BTA-(S)-Me-C$_{12}$-EG$_4$** have previously been observed with other techniques than HDX-MS.[31] It was attempted to explain the differences with molecular dynamics simulations based on an identical packing of the two molecules into a single stack, as it was then unknown that **BTA-C$_{12}$-EG$_4$** assembles into a double helix. Based on the results obtained in this chapter an improved proposal for the molecular packing of both chiral BTAs will be presented here.

The UV and CD spectra of **BTA-(S)-D-C$_{12}$-EG$_4$** do not resemble the spectra of BTAs in organic solvents, suggesting that they do not stack on each other with a threefold helical hydrogen bond pattern.[25,39] Additionally, it is known that two stacks rotate around each other as a double helix, which we propose to be due to hydrophobic interactions between the side chains. A simplified model of a double helix structure formed by two strands of BTAs was constructed by dr. Tobias Schnitzer (Figure 8A). Only one side chain is depicted per monomer and the hydrophilic periphery is omitted for clarity. The hydrophobic parts of two sidechains interact such that the two strands are connected. The pitch of about 40 nm found for the double helix structure dictates that there should not be too much rotation between consecutive amides such that the

hydrophobic chains stay relatively close together. A helical hydrogen bond pattern in which all amides have the same orientation would therefore not suffice. A conformation is proposed here in which one amide per monomer is flipped (see zoom-in in Figure 8A). This results in a zig-zag hydrogen bond pattern in which the hydrogen bonds change direction between monomers (see top left of the zoom-out in Figure 8A). This does reduce the rotation of molecules although there is still enough rotation for the helical pitch as is seen in the top view (Figure 8B). The hydrophilic periphery of all side chains was omitted but we expect that those chains fold around the hydrophobic parts to create a water-compatible layer. Computational studies are currently being conducted to validate this proposed molecular packing.

A similar packing is probably adopted by other BTAs that assemble into a double helix, such as **BTA-C$_{12}$-EG$_4$**. HDX-MS experiments show a slight stabilization of the assemblies after equilibration over several weeks. However, much larger increases in stability are observed for its chiral counterpart, **BTA-(S)-D-C$_{12}$-EG$_4$**. The achiral BTA assembles into equal amounts of P and M helices, whereas a preference for either of those helicities exists in the assemblies of **BTA-(S)-D-C$_{12}$-EG$_4$**. It is likely that not all monomers immediately adopt this preferred helicity due to the low mismatch energy.[26] The assemblies remain optimizing their arrangement over several weeks which is a slow process due to strong hydrophobic interactions. However, a large gain in stability is observed over time.

A secondary structure is absent in the assemblies of **BTA-(S)-Me-C$_{12}$-EG$_4$** which is shown to assemble into a one-dimensional supramolecular polymer with a diameter that matches with the diameter of a single molecule. The FT-IR spectra in solution suggest a different type of hydrogen bonds compared to the double helix. Additionally, the CD spectrum matches with helical columnar assemblies of BTAs found in organic solvents. It is therefore proposed that **BTA-(S)-Me-C$_{12}$-EG$_4$** assembles with a similar helical hydrogen bond pattern in which all amides have the same orientation (Figure 8C). Based on the CD spectra a dihedral angle of 45° is proposed.[39] This change in molecular packing does not solely originate from an increase in hydrophobicity since **BTA-C$_{13}$-EG$_4$** does assemble into two interacting stacks. Instead, it is proposed that the branching of the methyl group influences the packing of the hydrophobic chain and alters the special arrangement of the hydrophobic pocket such that the formation of a single stack is more favorable.
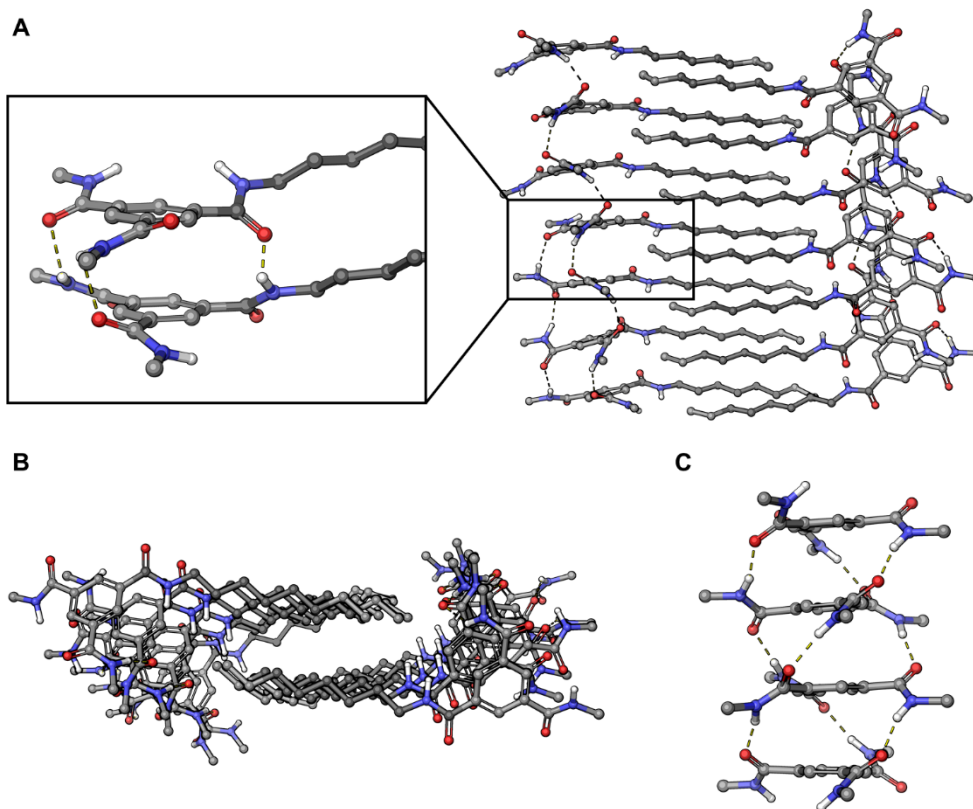
Figure 8. (A) Side view of a model of short stacks of BTAs that illustrates the proposed molecular packing of a double helix. The two side chains on the outside of each BTA are completely omitted and only a small part of the interacting hydrophobic side chains is depicted for clarity. Hydrogen bonds are indicated with dashed lines. The zoom-in shows the three hydrogen bonds between two consecutive monomers. Since the model is not completely optimized, some hydrogen bonds are missing from the zoom-out. However, this increases the visibility of the zig-zag hydrogen bond pattern on the top left. (B) Top view of the model from A to show the rotation of the stacks around each other into a double helix. (C) Model of a single stack of BTAs that assemble via a helical hydrogen bond pattern.

4.5 Copolymers containing chiral BTAs

The mixing of chiral and achiral BTAs is often used as a strategy to amplify the asymmetry of supramolecular assemblies.[28,29,40] In sergeant-and-soldier experiments a small number of chiral molecules dictates the helical preference of the supramolecular assemblies without a helical preference. This could be useful to increase the order within functional assemblies in water such that their structure and dynamics can be controlled. Spectroscopy techniques will therefore be used to study if the

copolymerization of **BTA-C$_{12}$-EG$_4$** with **BTA-(S)-D-C$_{12}$-EG$_4$** or **BTA-(S)-Me-C$_{12}$-EG$_4$** leads to an amplification of asymmetry and thereby an increase in order.

First, **BTA-C$_{12}$-EG$_4$** and **BTA-(S)-D-C$_{12}$-EG$_4$** were mixed in different ratios and their UV and CD spectra were measured after 1 day and 4 weeks of equilibration. Both BTAs show absorption maxima at 211 and 229 nm, which did not change upon co-assembly. No CD signal is observed in samples that contained 10% of **BTA-(S)-D-C$_{12}$-EG$_4$** or less (Figure 9A-B). Samples with at least 25% of chiral BTAs exhibit a CD signal that resembles the sample of pure **BTA-(S)-D-C$_{12}$-EG$_4$**, indicating the formation of assemblies with a helical preference. The sample with 25% of **BTA-(S)-D-C$_{12}$-EG$_4$** shows a stronger CD signal than expected, but this is an artefact from a large LD effect. A linear trend can be observed in the CD signal at 215 nm as a function of concentration of chiral BTA (Figure 9C), indicating that **BTA-(S)-D-C$_{12}$-EG$_4$** does not act as a strong sergeant since there is no amplification of asymmetry. Additionally, copolymers do not undergo as much of an increase in order over time as the homopolymers of **BTA-(S)-D-C$_{12}$-EG$_4$**. Similar findings were reported in organic solvents, in which BTAs with isotopic chirality also did not act as sergeants due to the small mismatch penalty.[24–26] Previous reports also pointed out that the transfer of asymmetry is a slow process in water due to the presence of strong non-directional hydrophobic interactions.[41,42]
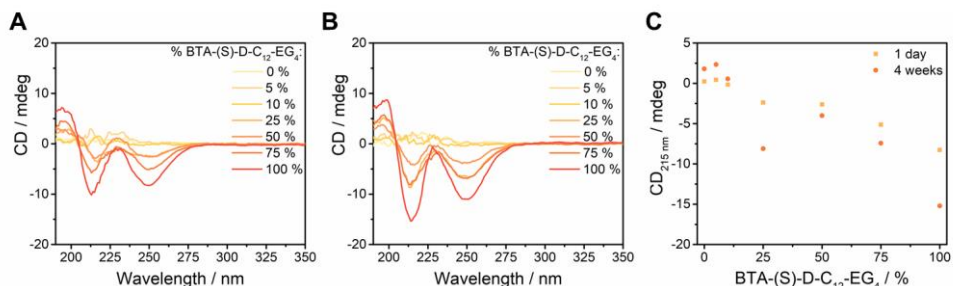
Figure 9. (A-B) CD spectra of mixtures of **BTA-C$_{12}$-EG$_4$** with **BTA-(S)-D-C$_{12}$-EG$_4$** in water after (A) 1 day and (B) 4 weeks of equilibration (c_{total} = 50 μM, l = 1 cm, T = 20°C). (C) CD signal at 215 nm for the mixtures of **BTA-C$_{12}$-EG$_4$** with **BTA-(S)-D-C$_{12}$-EG$_4$** in water as a function of concentration of chiral BTA.

Next, **BTA-C$_{12}$-EG$_4$** was copolymerized with different amounts of **BTA-(S)-Me-C$_{12}$-EG$_4$**. Samples with 5% **BTA-(S)-Me-C$_{12}$-EG$_4$** have a UV spectrum that resembles that of **BTA-C$_{12}$-EG$_4$**, samples with 10 or 25% of **BTA-(S)-Me-C$_{12}$-EG$_4$** mainly resemble the spectrum of the chiral BTA but with a deviation in the shoulder at 230 nm and the spectrum of **BTA-(S)-Me-C$_{12}$-EG$_4$** is adopted at higher percentages of this chiral BTA (Figure 10A). The CD spectrum of a sample of only **BTA-C$_{12}$-EG$_4$** shows a positive cotton effect at 228 nm (Figure 10B), which is an artefact that sometimes occurs due to macroscopic alignment of the fibers as is proven by LD spectroscopy.[34] Interestingly, the mirror image CD spectrum of **BTA-(S)-D-C$_{12}$-EG$_4$** was observed when 5% of **BTA-(S)-Me-C$_{12}$-EG$_4$** was added to the achiral BTA, suggesting the formation of a double

helix with opposite helicity. Spectra with a higher percentage of **BTA-(S)-Me-C$_{12}$-EG$_4$** show the same bands as the homopolymers of **BTA-(S)-Me-C$_{12}$-EG$_4$** but with increasing intensity. These mixing experiments are more complex than general sergeant-and-soldier experiments. Below 5% of **BTA-(S)-Me-C$_{12}$-EG$_4$** this molecule dictates the chirality as if it is a sergeant but at higher percentages a switch in the supramolecular structure is observed from a double helix to a single fiber. The maximum CD signal for a single fiber is observed with a large excess of 75% of **BTA-(S)-Me-C$_{12}$-EG$_4$** (Figure 10C).
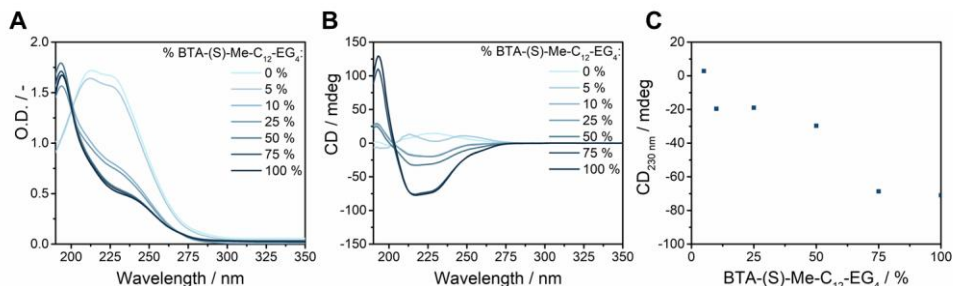
Figure 10. (A) UV spectra of mixtures of **BTA-C$_{12}$-EG$_4$** with **BTA-(S)-Me-C$_{12}$-EG$_4$** in water with 2% ACN (c$_{total}$ = 50 μM, l = 1 cm, T = 20°C). (B) CD spectra of mixtures of **BTA-C$_{12}$-EG$_4$** with **BTA-(S)-Me-C$_{12}$-EG$_4$** in water with 2% ACN (c$_{total}$ = 50 μM, l = 1 cm, T = 20°C). (C) CD signal at 230 nm for the mixtures of **BTA-C$_{12}$-EG$_4$** with **BTA-(S)-Me-C$_{12}$-EG$_4$** in water with 2% ACN as a function of concentration of chiral BTA.

Intrigued by this inversed helicity and change in supramolecular structure, we explored the effect of the mixing of the two chiral BTAs. **BTA-(S)-D-C$_{12}$-EG$_4$** was therefore co-assembled with increasing amounts of **BTA-(S)-Me-C$_{12}$-EG$_4$**. Three regimes can be observed for the samples that were equilibrated for 1 day. First of all, the UV and CD spectra of a sample with 10% of **BTA-(S)-Me-C$_{12}$-EG$_4$** resemble that of **BTA-(S)-D-C$_{12}$-EG$_4$** but with opposite helicity (Figure 11A-B). Secondly, the sample with 25% of **BTA-(S)-Me-C$_{12}$-EG$_4$** shows a non-linear combination of the spectra of both molecules, indicating that the molecules have copolymerized but that multiple aggregation states are present. Thirdly, samples with more **BTA-(S)-Me-C$_{12}$-EG$_4$** only contain features of this chiral BTA and the maximum helical preference is reached at 75% of **BTA-(S)-Me-C$_{12}$-EG$_4$** (Figure 11C). In these experiments, small amounts of **BTA-(S)-Me-C$_{12}$-EG$_4$** are able to direct the helicity of the double helix structure and to overrule the helical preference of the other chiral BTA. At high concentrations this BTA dictates the supramolecular structure.
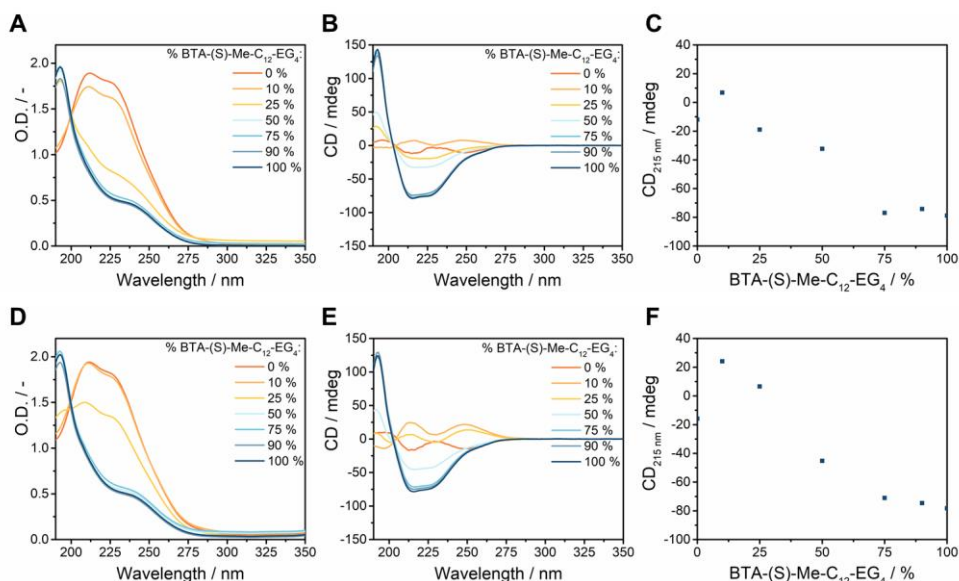
Figure 11. (A, D) UV spectra of mixtures of **BTA-(S)-D-C₁₂-EG₄** with **BTA-(S)-Me-C₁₂-EG₄** in water with 2% ACN after (A) 1 day and (D) 4 weeks of equilibration (c_{total} = 50 µM, l = 1 cm, T = 20°C). (B, E) CD spectra of mixtures of **BTA-(S)-D-C₁₂-EG₄** with **BTA-(S)-Me-C₁₂-EG₄** in water with 2% ACN after (B) 1 day and (E) equilibration (c_{total} = 50 µM, l = 1 cm, T = 20°C). (C, F) CD signal at 215 nm for the mixtures of **BTA-(S)-D-C₁₂-EG₄** with **BTA-(S)-Me-C₁₂-EG₄** in water with 2% ACN after (C) 1 day and (F) 4 weeks equilibration as a function of concentration of **BTA-(S)-Me-C₁₂-EG₄**.

An equilibration time of 4 weeks did not change the spectra of the samples with a large excess of **BTA-(S)-Me-C₁₂-EG₄** (Figure 11D-F). All samples with less **BTA-(S)-Me-C₁₂-EG₄** show an increase in CD signal and thereby an increase in order. Remarkably, the spectra of the sample with 25% of **BTA-(S)-Me-C₁₂-EG₄** now resembles the spectrum of a double helix with opposite helicity compared to **BTA-(S)-D-C₁₂-EG₄**, whereas it previously resembled the spectrum of a single fiber. **BTA-(S)-Me-C₁₂-EG₄** thus overrules the helicity of **BTA-(S)-D-C₁₂-EG₄** at this ratio but the structure is dictated by **BTA-(S)-D-C₁₂-EG₄**.

4.6 Conclusions

Two water-compatible chiral BTAs were studied to reveal the influence of stereogenic centers on the structure and dynamics of supramolecular polymers in water. The stereogenic centers in **BTA-(S)-D-C₁₂-EG₄** come from the introduction of deuterium atoms, which results in supramolecular polymers that initially resemble the achiral BTAs in their double helix structure and dynamics. However, spectroscopy studies reveal an increase in order over time, which results in a decrease of the double helix pitch and dynamics. These experiments demonstrate for the first time that

supramolecular polymers, previously believed to be in thermodynamic equilibrium, undergo changes in their molecular packing over several weeks to reach a more stable state. It is proposed that chiral **BTA-(S)-D-C$_{12}$-EG$_4$** prefers to assemble in either P or M helices but due to the small difference between deuterium and hydrogen atoms a mixture of both is initially formed. The alignment of all helices is a slow process due to the strong hydrophobic interactions that hold the double helix together. Such a stabilization of the supramolecular assemblies was not observed for the achiral **BTA-C$_{12}$-EG$_4$** as it polymerizes with equal amounts of P and M helices.

The introduction of methyl groups as stereogenic centers in **BTA-(S)-Me-C$_{12}$-EG$_4$** leads to a stronger CD signal than in the assemblies of **BTA-(S)-D-C$_{12}$-EG$_4$**. However, the branching of the side chains drastically changes the packing of the molecules such that they assemble into a single stack of helical assemblies, similar to the ones found in organic solvents. The single fibers have a different monomer exchange pattern with a more gradual increase in the first hours comparted to the BTAs with a double helix structure and a faster exchange after a few hours that surpasses the exchange of the other molecules. These results indicate that minor changes in the chemical structure can result in major differences on the level of the supramolecular polymer.

Finally, the impact of stereogenic centers on BTA copolymers was studied. **BTA-(S)-D-C$_{12}$-EG$_4$** does not show a sergeants-and-soldiers effect when mixed with achiral **BTA-C$_{12}$-EG$_4$** due to the small mismatch penalty. More complex behavior was observed in mixtures with **BTA-(S)-Me-C$_{12}$-EG$_4$** as these not only involve the transfer of asymmetry by this stronger chiral sergeant, but also a structural transition from double helices with opposite chirality to single fibers. When **BTA-(S)-Me-C$_{12}$-EG$_4$** was copolymerized with **BTA-(S)-D-C$_{12}$-EG$_4$** it could even be observed that one of the copolmers switched from a single fiber to a double helix over time. It can therefore by suggested that the double helix structure is more stable than the single stacks, which could explain the presence of a secondary structure in most BTA assemblies in water. The introduction of stereogenic centers is a well-known strategy to obtain information about supramolecular self-assembly in organic solvents but it is barely used in water. The new insights in the molecular packing, structure and dynamics of the supramolecular polymers in this chapter could be a motivation for others to also explore this strategy.

4.7 Experimental section

4.7.1 Materials and Methods

All solvents and chemicals used were of reagent grade quality or better and purchased from Biosolve or Sigma-Aldrich at the highest purity available and used without further purification unless otherwise noted. **BTA-C$_{12}$-EG$_4$**,[30] **BTA-(S)-D-C$_{12}$-EG$_4$**,[32] **BTA-C$_{13}$-EG$_4$**[32] and **BTA-(S)-Me-C$_{12}$-EG$_4$**[30] were synthesized according to literature procedure. Water for aqueous samples was purified on an EMD Millipore Milli-Q Integral Water Purification System.

Sample preparation of BTA-C$_{12}$-EG$_4$ and BTA-(S)-D-C$_{12}$-EG$_4$: the solid material was weighed into a glass vial equipped with a magnetic stirring bar. MQ-water was added to obtain the desired

concentration. The sample was subsequently stirred at 80 °C for 15 minutes and the hot and hazy sample was vortexed immediately afterwards for 15 seconds. All samples were left to equilibrate at room temperature. Samples in ACN were prepared by directly dissolving the solid material at the desired concentration in ACN.

Sample preparation of BTA-C$_{13}$-EG$_4$: roughly 2 mg the solid material was weighed into a 15 mL glass vial with a magnetic stirring bar. Approximately 300 μL CHCl$_3$ was added and the sample was vortexed for 15 seconds. The solvent was evaporated by blowing a constant stream of N$_2$ (g) above the solvent. 15 mL MQ-water was added and the sample was stirred at 80 °C for 15 minutes. Subsequently, the hot and hazy mixture was vortexed for 15 seconds and was left to equilibrate at room temperature overnight. The next day the sample was filtered with a 0.2 μm syringe filter. Water was evaporated by blowing a stream of N$_2$ (g) over the sample, while stirring, thereby increasing the concentration. UV spectroscopy was used to determine the concentration using a calibration curve based on the absorbance of **BTA-C$_{12}$-EG$_4$** at 250 nm: conc = (0.00434 + A$_{250}$)/0.001615. The concentration was increased to 500 μM.

Sample preparation of BTA-(S)-Me-C$_{12}$-EG$_4$: the solid material was weighed into a glass vial equipped with a magnetic stirring bar. ACN was added to obtain stock solutions with a concentration of 2.5 mM (for a 50 μM aqueous sample) or 25 mM (for a 500 μM aqueous sample). Stock solutions were vortexed for 1 minute and left to equilibrate at room temperature for at least 2 hours. A small aliquot of such a stock solution was injected into a separate vial with MQ-water and a magnetic stirring bar to obtain the desired concentration. The sample was subsequently stirred at 80 °C for 15 minutes and the hot and hazy sample was vortexed immediately afterwards for 15 seconds. All samples were left to equilibrate at room temperature.

Sample preparation of mixtures: 2.5 mM stock solutions of all three BTAs were prepared in ACN. Stock solutions were mixed in the desired ratio in a separate vial with magnetic stirring bar. ACN was only evaporated with a stream of N$_2$ (g) in samples without **BTA-(S)-Me-C$_{12}$-EG$_4$**. MQ-water was added to obtain the desired concentration. The sample was subsequently stirred at 80 °C for 15 minutes and the hot and hazy sample was vortexed immediately afterwards for 15 seconds. All samples were left to equilibrate at room temperature.

4.7.2 Instrumentation

Ultraviolet-visible (UV-Vis) absorbance spectra were recorded with the instruments described in Chapter 3.

Circular dichroism (CD) and linear dichroism (LD) spectra were measured on a JASCO J-815 CD spectrometer with either a JASCO Peltier MPTC-490S temperature controller with a range of 278 – 373 K or a JASCO Peltier PFD-425S/15 with a range of 263 – 383 K. Measurements were done in Quartz cuvettes (Hellma) with a pathlength of 1 mm (500 μM) or 1 cm (50 μM). A standard sensitivity, a D.I.T of 0.5 seconds, a bandwidth of 1.0 nm, a data pitch of 0.2 nm and a scanning speed of 100 nm/min were used. The spectra were recorded from 350 nm to 190 nm. A baseline of the corresponding solvent was recorded before the measurement.

Fourier-Transform infrared (FT-IR) spectra in solution were recorded on a Perkin Elmer Spectrum Two FT-IR spectrometer. Liquid FT-IR measurements were performed using a CaF2 Liquid Cell with an optical path length of 0.05 mm. Samples for FT-IR in solution were prepared at a concentration of 20 mg/mL to facilitate dissolution. BTA material was weighed and added to a clean vial. All samples were dried overnight with approximately 5 grams of P$_2$O5 in a separate beaker in the vacuum oven at 40 °C. Samples in MeOD were prepared by adding MeOD to the vials

to obtain the desired concentration. The sample of **BTA-(S)-D-C$_{12}$-EG$_4$** in D$_2$O was prepared by addition of the solvent at the desired concentration, followed by stirring at 80 °C for 15 minutes. The hot and hazy samples were subsequently vortexed for 15 seconds and this procedure was repeated again if the sample still looked hazy. The sample of **BTA-(S)-Me-C$_{12}$-EG$_4$** in D$_2$O was first dissolved in ACN-d$_3$ before D$_2$O was added (final ACN concentration = 2%) and the heating-cooling protocol was used. All samples were left to equilibrate at room temperature overnight and samples in D$_2$O were viscous the next day. First a background of the appropriate solvent was measured. All spectra were measured at room temperature from 400 cm^{-1} to 4000 cm^{-1}, averaged over 64 scans.

Cryogenic transmission electron microscopy (cryoTEM) images were obtained with the instrument described in Chapter 2.

2D image reconstruction was performed in Berlin with the instruments described in Chapter 2. The Volta phase plate was only used for the characterization of **BTA-(S)-Me-C$_{12}$-EG$_4$**.

Hydrogen deuterium exchange experiments with electrospray ionization were carried out with the instruments described in Chapter 3.

The **computational modeling** of the BTA assemblies was obtained using the Schrödinger Suite 2021-1. A respective number of BTA monomers were oriented in the expected assembly arrangement and optimized using Macromodel. The geometry optimization was performed using molecular modeling with the OPLS-4 force field and a solvent model for water.

4.7.3 Analysis of the HDX-MS measurements

All HDX-MS experiments were performed under similar conditions to eliminate influences from the environment, for example temperature. The measurements were performed by diluting a sample of self-assembled supramolecular building-blocks in H$_2$O 100x into D$_2$O. 0.5 mM sodium acetate was added to the D$_2$O prior to the dilution to facilitate the detection. In all cases the distributions with two sodium ions were used for the calculations. All calculations are based on the method presented in Chapter 3. The equations used for samples of **BTA-C$_{12}$-EG$_4$** and **BTA-C$_{13}$-EG$_4$** are given in section 3.9.3. The equations described for **BTA-C$_{13}$-EG$_4$** were also applied to **BTA-(S)-Me-C$_{12}$-EG$_4$**.

Isotope correction for **BTA-(S)-D-C$_{12}$-EG$_4$** is based on the following set of equations:

$I_{BTA1D\_c} = I_{668.97}$

$I_{BTA2D\_c} = I_{669.47} - 0.80 I_{BTA1D\_c}$

$I_{BTA3D\_c} = I_{669.97} - 0.80 I_{BTA2D\_c} - 0.36 I_{BTA1D\_c}$

$I_{BTA4D\_c} = I_{670.48} - 0.80 I_{BTA3D\_c} - 0.36 I_{BTA2D\_c} - 0.11 I_{BTA1D\_c}$

$I_{BTA5D\_c} = I_{670.98} - 0.80 I_{BTA4D\_c} - 0.36 I_{BTA3D\_c} - 0.11 I_{BTA2D\_c} - 0.03 I_{BTA1D\_c}$

$I_{BTA6D\_c} = I_{671.48} - 0.80 I_{BTA5D\_c} - 0.36 I_{BTA4D\_c} - 0.11 I_{BTA3D\_c} - 0.03 I_{BTA2D\_c} - 0.01 I_{BTA1D\_c}$

with $I_{668.97}$, $I_{669.47}$, $I_{669.97}$, $I_{670.48}$, $I_{670.98}$ and $I_{671.48}$ the intensity at m/z = 668.97, 669.47, 669.97, 670.48, 670.98 and 671.48, respectively.

The correction for the presence of 1 vol% H$_2$O can be calculated with the following set of equations:

$I_{BTA1D} = I_{BTA1D\_c} - 6.31 \times 10^{-10} I_{BTA6D\_c} - 3.06 \times 10^{-4} I_{BTA3D\_c}$

$I_{BTA2D} = I_{BTA2D\_c} - 1.56 \times 10^{-7} I_{BTA6D\_c} - 3.03 \times 10^{-2} I_{BTA3D\_c}$

$$I_{BTA3D} = I_{BTA3D\_c} - 2.06 \times 10^{-5} I_{BTA6D\_c} + (3.06 \times 10^{-4} + 3.03 \times 10^{-2}) I_{BTA3D\_c}$$

$$I_{BTA4D} = I_{BTA4D\_c} - 1.53 \times 10^{-3} I_{BTA6D\_c}$$

$$I_{BTA5D} = I_{BTA5D\_c} - 6.06 \times 10^{-2} I_{BTA6D\_c}$$

$$I_{BTA6D} = I_{BTA6D\_c} + (6.31 \times 10^{-10} + 1.56 \times 10^{-7} + 2.06 \times 10^{-5} + 1.53 \times 10^{-3} + 6.06 \times 10^{-2}) I_{BTA6D\_c}$$

The percentage of the deuterated analogues can be calculated:

$$\%BTAnD = \frac{I_{BTAnD}}{\sum_{k=1}^{6} I_{BTAkD}} \times 100\%$$

with $\sum_{k=1}^{6} I_{BTAkD}$ the sum of all intensities. The percentage of deuterated analogues was calculated for several time points and plotted as a function of time in this chapter.

4.8 References

1   D. E. Shaw, P. Maragakis, K. Lindorff-larsen, R. O. Dror, M. P. Eastwood, J. A. Bank, J. M. Jumper, S. J. K., S. Piana, Y. Shan and W. Wriggers, *Science*, 2010, **330**, 341–347.
2   W. Hu, B. T. Walters, Z. Y. Kan, L. Mayne, L. E. Rosen, S. Marqusee and S. W. Englander, *Proc. Natl. Acad. Sci.*, 2013, **110**, 7684–7689.
3   T. E. Wales and J. R. Engen, *Mass Spectrom. Rev.*, 2006, **25**, 158–170.
4   G. L. Nicolson, *Biochim. Biophys. Acta - Biomembr.*, 2014, **1838**, 1451–1466.
5   D. Lingwood and K. Simons, *Science*, 2010, **327**, 46–50.
6   F. R. Maxfield, *Curr. Opin. Cell Biol.*, 2002, **14**, 483–487.
7   T. Aida, E. W. Meijer and S. I. Stupp, *Science*, 2012, **335**, 813–817.
8   O. J. G. M. Goor, S. I. S. Hendrikse, P. Y. W. Dankers and E. W. Meijer, *Chem. Soc. Rev.*, 2017, **46**, 6621–6637.
9   J. Boekhoven and S. I. Stupp, *Adv. Mater.*, 2014, **26**, 1642–1659.
10   S. I. Stupp, *Nano Lett.*, 2010, **10**, 4783–4786.
11   J. D. Hartgerink, E. Beniash and S. I. Stupp, *Science*, 2001, **294**, 1684–1688.
12   J. D. Hartgerink, E. Beniash and S. I. Stupp, *Proc. Natl. Acad. Sci.*, 2002, **99**, 5133–5138.
13   H. Jiang, M. O. Guler and S. I. Stupp, *Soft Matter*, 2007, **3**, 454-462.
14   M. M. L. Nieuwenhuizen, T. F. A. De Greef, R. L. J. Van Der Bruggen, J. M. J. Paulusse, W. P. J. Appel, M. M. J. Smulders, R. P. Sijbesma and E. W. Meijer, *Chem. - A Eur. J.*, 2010, **16**, 1601–1612.
15   M. M. C. Bastings, S. Koudstaal, R. E. Kieltyka, Y. Nakano, A. C. H. Pape, D. A. M. Feyen, F. J. van Slochteren, P. A. Doevendans, J. P. G. Sluijter, E. W. Meijer, S. A. J. Chamuleau and P. Y. W. Dankers, *Adv. Healthc. Mater.*, 2014, **3**, 70–78.
16   D. Straßburger, N. Stergiou, M. Urschbach, H. Yurugi, D. Spitzer, D. Schollmeyer, E. Schmitt and P. Besenius, *ChemBioChem*, 2018, **19**, 912–916.
17   K. Petkau-Milroy, M. H. Sonntag and L. Brunsveld, *Chem. - A Eur. J.*, 2013, **19**, 10786–10793.
18   E. Krieg, M. M. C. Bastings, P. Besenius and B. Rybtchinski, *Chem. Rev.*, 2016, **116**, 2414–2477.
19   J. H. Ortony, C. J. Newcomb, J. B. Matson, L. C. Palmer, P. E. Doan, B. M. Hoffman and S. I. Stupp, *Nat. Mater.*, 2014, **13**, 812–816.
20   L. Brunsveld, A. P. H. J. Schenning, M. A. C. Broeren, H. M. Janssen, J. A. J. M. Vekemans and E. W. Meijer, *Chem. Lett.*, 2000, 292–293.
21   L. N. J. De Windt, C. Kulkarni, H. M. M. Ten Eikelder, A. J. Markvoort, E. W. Meijer and A. R. A. Palmans, *Macromolecules*, 2019, **52**, 7430–7438.
22   N. J. Van Zee, M. F. J. Mabesoone, B. Adelizzi, A. R. A. Palmans and E. W. Meijer, *J. Am. Chem. Soc.*, 2020, **142**, 20191–20200.
23   S. Cantekin, D. W. R. Balkenende, M. M. J. Smulders, A. R. A. Palmans and E. W. Meijer, *Nat. Chem.*, 2011, **3**, 42–46.
24   Y. Nakano, A. J. Markvoort, S. Cantekin, I. A. W. Filot, H. M. M. Ten Eikelder, E. W. Meijer and A. R. A. Palmans, *J. Am. Chem. Soc.*, 2013, **135**, 16497–16506.
25   S. Cantekin, Y. Nakano, J. C. Everts, P. Van der Schoot, E. W. Meijer and A. R. A. Palmans, *Chem. Commun.*, 2012, **48**, 3803–3805.
26   I. A. W. Filot, A. R. A. Palmans, P. A. J. Hilbers, E. J. M. Hensen, T. F. A. De Greef and E. A. Pidko, *Phys. Chem. Chem. Phys.*, 2012, **14**, 13997–14002.

27   M. M. J. Smulders, I. A. W. Filot, J. M. A. Leenders, P. Van Der Schoot, A. R. A. Palmans, A. P. H. J. Schenning and E. W. Meijer, *J. Am. Chem. Soc.*, 2010, **132**, 611–619.

28   M. M. J. Smulders, A. P. H. J. Schenning and E. W. Meijer, *J. Am. Chem. Soc.*, 2008, **130**, 606–611.

29   M. M. J. Smulders, P. J. M. Stals, T. Mes, T. F. E. Paffen, A. P. H. J. Schenning, A. R. A. Palmans and E. W. Meijer, *J. Am. Chem. Soc.*, 2010, **132**, 620–626.

30   C. M. A. Leenders, L. Albertazzi, T. Mes, M. M. E. Koenigs, A. R. A. Palmans and E. W. Meijer, *Chem. Commun.*, 2013, **49**, 1963–1965.

31   M. B. Baker, L. Albertazzi, I. K. Voets, C. M. A. Leenders, A. R. A. Palmans, G. M. Pavan and E. W. Meijer, *Nat. Commun.*, 2015, **6**, 6234.

32   X. Lou, R. P. M. Lafleur, C. M. A. Leenders, S. M. C. Schoenmakers, N. M. Matsumoto, M. B. Baker, J. L. J. van Dongen, A. R. A. Palmans and E. W. Meijer, *Nat. Commun.*, 2017, **8**, 15420.

33   R. P. M. Lafleur, X. Lou, G. M. Pavan, A. R. A. Palmans and E. W. Meijer, *Chem. Sci.*, 2018, **9**, 6199–6209.

34   M. Wolffs, S. J. George, Ž. Tomović, S. C. J. Meskers, A. P. H. J. Schenning and E. W. Meijer, *Angew. Chemie - Int. Ed.*, 2007, **46**, 8203–8205.

35   J. J. Max and C. Chapados, *J. Chem. Phys.*, 2009, **131**, 184505.

36   C. M. A. Leenders, M. B. Baker, I. A. B. Pijpers, R. P. M. Lafleur, L. Albertazzi, A. R. A. Palmans and E. W. Meijer, *Soft Matter*, 2016, **12**, 2887–2893.

37   J. J. Max and C. Chapados, *J. Chem. Phys.*, 2005, **122**, 014504.

38   J. J. Max and C. Chapados, *J. Chem. Phys.*, 2003, **119**, 5632–5643.

39   Y. Nakano, T. Hirose, P. J. M. Stals, E. W. Meijer and A. R. A. Palmans, *Chem. Sci.*, 2012, **3**, 148–155.

40   A. R. A. Palmans, E. W. Meijer and S. E. Denmark, *J. Polym. Sci.*, 2021, **59**, 1171–1174.

41   L. Brunsveld, B. G. G. Lohmeijer, J. A. J. M. Vekemans and E. W. Meijer, *Chem. Commun.*, 2000, 2305–2306.

42   L. Brunsveld, H. Zhang, M. Glasbeek, J. A. J. M. Vekemans and E. W. Meijer, *J. Am. Chem. Soc.*, 2000, **122**, 6175–6182.

Chapter 5

Saccharides as a Water-compatible Periphery: their Impact on the Structure and Dynamics of Supramolecular Polymers

Abstract: Saccharides are ubiquitous in nature and are important as recognition motifs for saccharide-binding proteins. Additionally, saccharides are known for their excellent water-solubility. In this chapter, monosaccharides will be explored as alternative solubilizing units for water-compatible benzene-1,3,5-tricarboxamides (BTAs) and the impact of this chemical modification on the structure and dynamics of the supramolecular polymers will be studied. Bundled supramolecular polymers with increased monomer exchange dynamics were found when β-D-glucose or α-D-mannose replaced the previously used tetra(ethylene glycol) as solubilizing motif. However, the hydrophilic/hydrophobic balance is distorted when the hydrophilic periphery comprises saccharides covalently attached to the tetra(ethylene glycol) chains and small BTA micelles are formed instead. Molecular dynamics simulations reveal the presence of numerous hydrogen bonds between the saccharides on the BTAs, explaining their increased dynamics and bundling. Additionally, a systematic study of the co-assembly of saccharide-functionalized BTAs will be presented. Saccharide-decorated BTAs that assemble into micelles on their own can copolymerize with BTAs with an tetra(ethylene glycol) or β-D-glucose periphery. Copolymerization is the most efficient when a BTA with tetra(ethylene glycol) periphery is used. Moreover, it will be revealed that the molecular linker used for the attachment of the saccharides could limit the copolymerization although it also helps to overcome solubility problems. The results presented in this chapter are useful in the design of new multivalent supramolecular polymers for the interaction with saccharide-binding proteins.
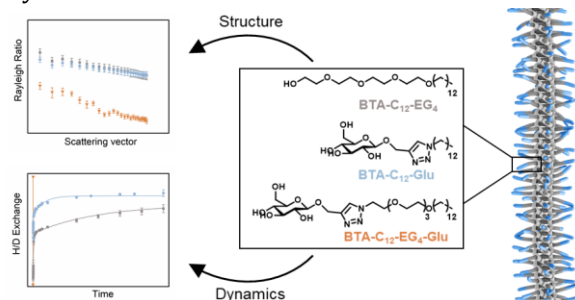
5.1 Introduction

Saccharides and saccharide-conjugates are abundant in nature and fulfil important regulatory, recognition and signal transduction functions.[1] Polysaccharides are for example present in the glycocalyx on the cell surface[2] and as glycosaminoglycans in the extracellular matrix.[3] The glycosaminoglycans are known to bind water molecules to create a hydration shell around the biopolymers.[4] Variations in anomeric linkage, ring size, linkage position, branching and side specific substituents allow for the creating of a great amount of structurally divers compounds.[5]

In chemistry, saccharides have been attached to covalent polymers, fatty acids, peptides, dendrimers, and a variety of nanoparticles with the aim to achieve selective and efficient interactions with saccharide-binding proteins.[6–17] Different properties can be introduced depending on the type of saccharide used. Glucose, without charge and with a large hydrophilicity, has for example been used as antifouling saccharide in order to reduce aspecific cell interactions during cell experiments.[18] Mannose on the other hand is a well-known binding ligand for Con A lectins and bacteria and was therefore used in antimicrobial materials.[19–21] In addition, saccharides attached to water-incompatible moieties impart excellent water compatibility, affording biocompatible hydrogels and surfaces.[22–24]

Since molecular interactions involving saccharides are generally weak, multivalency plays an important role to increase their interaction strength. Supramolecular polymers are excellent candidates for this task as their modularity makes it possible to combine different building blocks while maintaining control over the number of functional groups presented on their surface.[25,26] In addition, supramolecular polymers exhibiting water compatibility attract increasing attention due to their potential as biomaterials.[27] Recently, self-assembling scaffolds with peripheral saccharides have been investigated as an alternative method to create multivalent systems.[26] Such systems have the advantage of remaining responsive, guarantee easy accessibility, and permit to combine different ligands through mixing of building blocks. The responsive nature of self-assembled systems is directly linked to the dynamic exchange of monomers between different aggregates. The rate of exchange and stability of the system strongly depend on the molecular interactions encoded in the chemical structure of the monomers[28–31] and on the interactions with the solvent.[32–34] The exchange of molecules between aggregates has previously been tracked by attaching bulky probe molecules to the molecule of interest,[28,29,35] but recently hydrogen-deuterium exchange (HDX) followed by mass spectrometry (MS) emerged as a powerful tool to study the exchange processes in supramolecular systems (Chapter 3).[36,37]

The self-assembly of amphiphilic, discotic compounds based on the benzene-1,3,5-tricaboxamide (BTA) unit comprising tetra(ethylene glycol) chains (**BTA-C$_{12}$-EG$_4$**) has been studied in great detail in our group.[38] Research elucidated the importance of a sufficiently large hydrophobic spacer on the ability of the BTAs to form supramolecular

polymers,[38] and with the help of HDX-MS the dynamic exchange of monomers between aggregates in water was measured.[36,37] Additionally, it was shown that **BTA-C$_{12}$-EG$_4$** is able to copolymerize with BTAs with a disturbed hydrophilic/hydrophobic balance.[39] However, reports of hypersensitivity to, and early degradation of ethylene glycol-based materials stimulated us to explore alternative water-solubilizing units.[40] The tetra(ethylene glycol) chains were therefore replaced by various monosaccharides, functioning as both a water-compatible periphery and as a biological recognition motif.[41] Initially, all saccharides were attached via Cu(I)-catalyzed azide-alkyne cycloaddition but later reports focused on the attachment of saccharides via direct glycosylation.[42]

In this chapter, a systematic comparison of the (co-)assemblies of saccharide-functionalized BTAs with **BTA-C$_{12}$-EG$_4$** is presented. The influence of the water-compatible periphery on the structure of the assemblies is investigated in detail as well as its impact on the exchange dynamics. In the first section, different saccharides were introduced into the side chains of the BTAs at different positions to study the effect of the saccharides on the homo-assembly of BTAs. A combination of spectroscopy techniques, cryogenic transmission electron microscopy (cryoTEM, Chapter 2), HDX-MS and molecular dynamics simulations will be used to reveal structural and dynamic diversities between the assemblies. In the final section, the co-assembly of saccharide-decorated BTAs will be studied. Not only the position and number of saccharides will be taken into account, but also the type of linkage used to attach the saccharides to the BTA. These results provide some fundamental insights on the (co-)assembly of saccharide-decorated BTAs that could be useful in the design of new biomaterials.

5.2 The impact of a saccharide periphery on the self-assembly of BTAs

First, the self-assembly of three saccharide-functionalized BTAs in water will be compared to the self-assembly of **BTA-C$_{12}$-EG$_4$**. In this section, all saccharides were coupled to azide-functionalized BTAs via Cu(I)-catalyzed azide-alkyne cycloaddition. This inevitably results in the introduction of a triazole moiety in the side chains of the BTAs. In case of **BTA-C$_{12}$-tri-Glu** (Figure 1) β-D-glucose was attached to the aliphatic chain as reported in literature.[41] **BTA-C$_{12}$-tri-Man** with its α-D-mannose moiety will be used to study the impact of a different type of saccharide and anomeric linkage on the self-assembly. Finally, a new BTA was designed with β-D-glucose attached to the tetra(ethylene glycol) chains (**BTA-C$_{12}$-EG$_4$-tri-Glu**) to study the effect of the saccharide position.
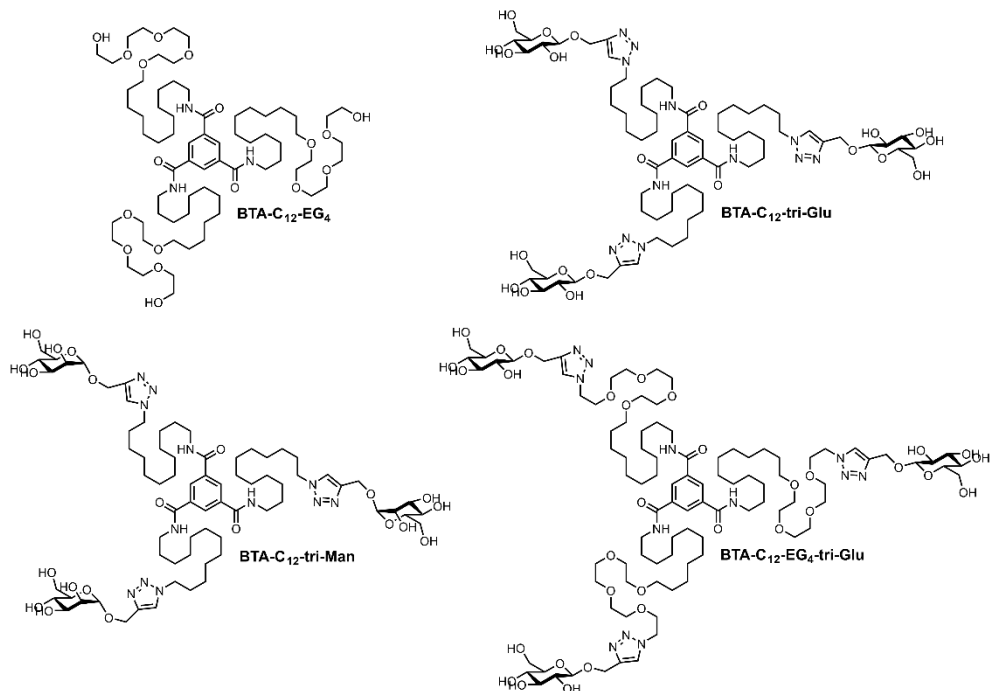
Figure 1. Chemical structure of **BTA-C$_{12}$-EG$_4$**, **BTA-C$_{12}$-tri-Glu**, **BTA-C$_{12}$-tri-Man** and **BTA-C$_{12}$-EG$_4$-tri-Glu**.

BTA-C$_{12}$-EG$_4$-tri-Glu was synthesized by Jolanda Spiering starting from a BTA with terminal azide groups on the three tetra(ethylene glycol) chains (**BTA-C$_{12}$-EG$_4$-N$_3$**). Acetyl protected β-D-glucose was coupled via Cu(I)-catalyzed azide-alkyne cycloaddition, yielding intermediate **1** in high yield (Scheme 1). Deprotection of the acetyl groups with sodium hydroxide resulted in pure **BTA-C$_{12}$-EG$_4$-tri-Glu** as was confirmed by ^{1}H NMR, ^{13}C NMR, FT-IR and mass spectrometry.
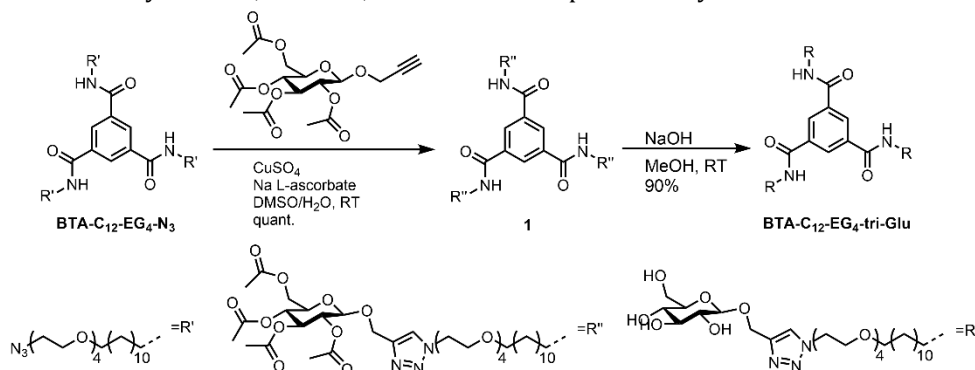
Scheme 1. Synthesis of **BTA-C$_{12}$-EG$_4$-tri-Glu**.

All molecules were assembled in water with a standard protocol involving controlled heating to 80 °C, followed by equilibration at room temperature overnight. The formation of micrometer long supramolecular polymers by **BTA-C$_{12}$-EG$_4$** is characterized by a maximum UV absorbance at 211 and 229 nm (Figure 2A). **BTA-C$_{12}$-tri-Glu** and **BTA-C$_{12}$-tri-Man** both have a more pronounced maximum in their absorbance spectrum at 213 nm and a small shoulder around 229 nm. The UV spectrum of **BTA-C$_{12}$-EG$_4$-tri-Glu** contains a maximum at 196 nm and a shoulder at 213 nm. The increased absorbance at 213 nm as observed for all saccharide-functionalized BTAs is attributed to the presence of the triazole moieties, which were introduced with the Cu(I)-catalyzed azide-alkyne cycloaddition and absorb around this wavelength (Figure 2A). The UV spectra of **BTA-C$_{12}$-tri-Glu** and **BTA-C$_{12}$-tri-Man** overlap, showing no influence of the saccharide type. Although they absorb in the same region as **BTA-C$_{12}$-EG$_4$** it cannot be confirmed that they have the same aggregation type due to the overlapping triazole absorbance. **BTA-C$_{12}$-EG$_4$-tri-Glu** comprises a different UV spectrum, indicating a change in the type of aggregation.

Static light scattering (SLS) showed that **BTA-C$_{12}$-EG$_4$**, **BTA-C$_{12}$-tri-Glu** and **BTA-C$_{12}$-tri-Man** all have the same angular dependence of the Rayleigh ratio that is typical for large, elongated assemblies (Figure 2B). **BTA-C$_{12}$-EG$_4$-tri-Glu** on the other hand comprises a lower Rayleigh ratio with a steeper slope. The angle dependence indicates the formation of non-spherical aggregates. These results suggest that **BTA-C$_{12}$-EG$_4$-tri-Glu** assembles into a different morphology than the other BTAs.

The presence of intermolecular hydrogen bonds between the saccharide-functionalized BTAs in solution was probed with Fourier-transform infrared (FT-IR) spectroscopy. The BTAs were assembled in deuterated methanol and D$_2$O to prevent overlap of the O-H vibration of the solvent with the amide I vibration of the BTAs.[43] The resulting hydrogen to deuterium exchange does not influence the ability of the molecules to self-assemble.[44] **BTA-C$_{12}$-EG$_4$** shows an amide I vibration at 1648 cm^{-1} in its molecularly dissolved state in MeOD and at 1635 cm^{-1} upon supramolecular polymerization in D$_2$O.[44] All saccharide-functionalized BTAs show an amide I vibration at 1648 cm^{-1} in MeOD, indicative for the absence of hydrogen bonds (Figure 2C-E). The amide I vibration of **BTA-C$_{12}$-tri-Glu** and **BTA-C$_{12}$-tri-Man** is positioned at 1634 cm^{-1} in D$_2$O (Figure 2C-D). This shift of the amide I vibration upon aggregation is indicative for the formation of intermolecular hydrogen bonds, similar to **BTA-C$_{12}$-EG$_4$**. The amide I vibration of **BTA-C$_{12}$-EG$_4$-tri-Glu** in D$_2$O is split into vibrations at 1637 and 1621 cm^{-1}. The shift to lower wavenumbers compared to the molecularly dissolved state, indicates the formation of some hydrogen bonds, although not as well-defined as observed for the other BTAs.
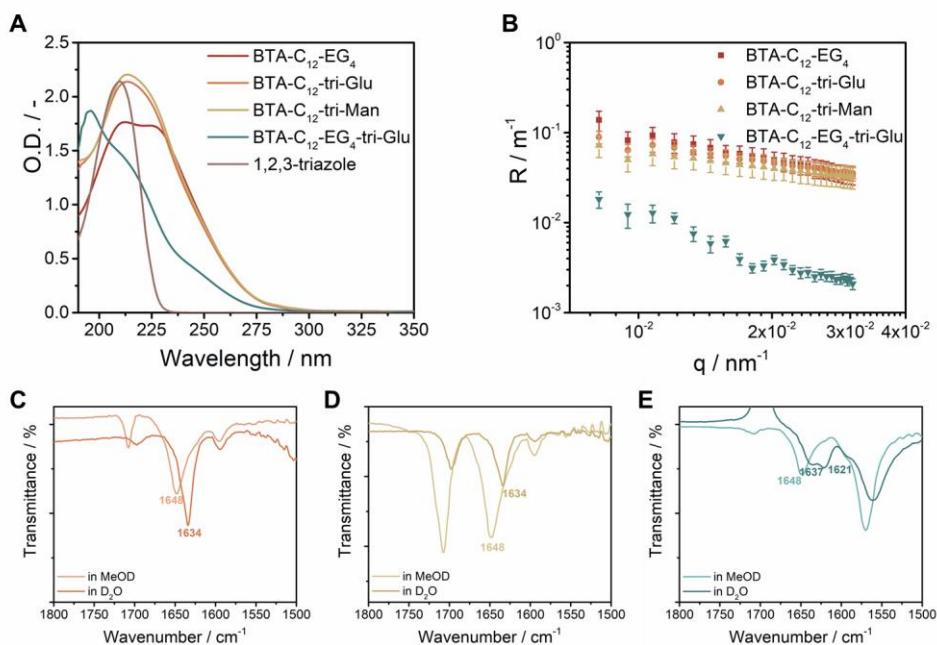
Figure 2. (A) UV spectrum of **BTA-C$_{12}$-EG$_4$**, **BTA-C$_{12}$-tri-Glu**, **BTA-C$_{12}$-tri-Man**, **BTA-C$_{12}$-EG$_4$-tri-Glu** (c = 500 μM, l = 1 mm, T = 20 °C) and 1,2,3-triazole (c = 100 μM, l = 1 cm, T = 20 °C) in water. (B) Rayleigh ratio of **BTA-C$_{12}$-EG$_4$**, **BTA-C$_{12}$-tri-Glu**, **BTA-C$_{12}$-tri-Man** and **BTA-C$_{12}$-EG$_4$-tri-Glu** as a function of the scattering vector in water (c = 500 μM, l = 1 cm, λ = 532 nm, T = 20 °C). (C-E) Zoom of the FT-IR spectrum of the amide I vibration of (C) **BTA-C$_{12}$-tri-Glu**, (D) **BTA-C$_{12}$-tri-Man** and (E) **BTA-C$_{12}$-EG$_4$-tri-Glu** in MeOD and D$_2$O (c = 20 mg/mL, l = 0.05 mm, T= room temperature). The vibrations at 1708 cm^{-1} in MeOD[45] and 1697 cm^{-1} in D$_2$O[46] originate from the C=O vibration of acetone which was used to clean the cuvette.

CryoTEM images show that **BTA-C$_{12}$-tri-Glu** and **BTA-C$_{12}$-tri-Man** assemble into bundles of micrometer long fibers (Figure 3). This bundling is likely a result of interactions between the saccharides which will be further explored in section 5.3. The fibers appear to be tighter packed in the image of **BTA-C$_{12}$-tri-Glu** but for both molecules also regions with less crowded areas with unbundled fibers in between could be observed. The structure of **BTA-C$_{12}$-tri-Glu** was analyzed in more detail with the image reconstruction method presented in Chapter 2 in collaboration with dr. Svenja Herziger and dr. Christoph Böttcher. Only unbundled fibers were used for this analysis. The clear strand separation of the double helix of **BTA-C$_{12}$-EG$_4$** could not be distinguished, but the diameter of 8.6 nm suggest that the fibers consist of two stacks of BTAs (Figure 3A). Less ordered regions were observed every 16.8 nm, which could be an indication of some separation of the two stacks. Although it was not investigated, a similar morphology is expected for **BTA-C$_{12}$-tri-Man**.
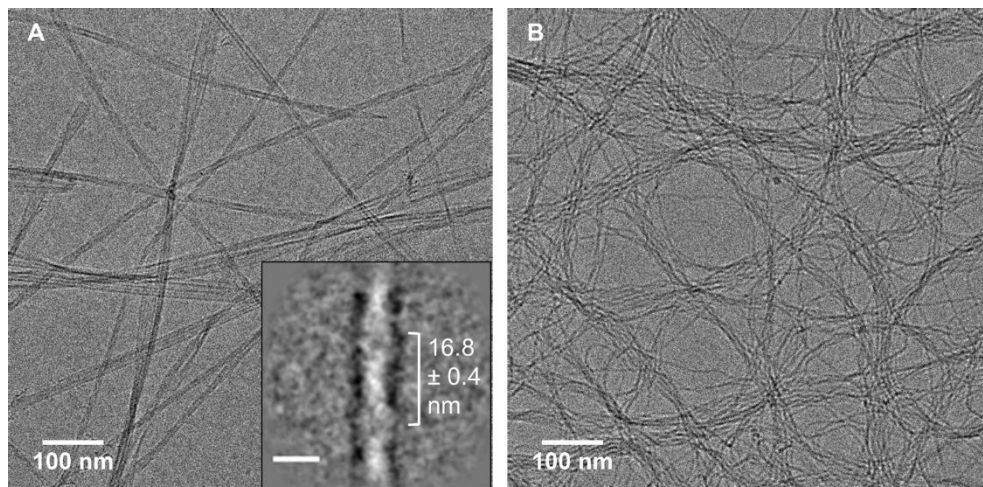
Figure 3. (A) CryoTEM image of **BTA-C$_{12}$-tri-Glu** in water (c = 500 µM). The inset shows the class sum image of aligned image extracts. The scale bar is 10 nm. (B) CryoTEM image of **BTA-C$_{12}$-tri-Man** in water (c = 500 µM).

Whereas the type of saccharide, β-D-glucose or α-D-mannose, did not influence the structure of the assemblies it seems that their position in the side chain is of influence as no long assemblies were found for **BTA-C$_{12}$-EG$_4$-tri-Glu**. Its absorbance, angular dependent Rayleigh ratio and amide I vibration match with those of a BTA with a dendritic periphery.[39] This molecule was shown to assemble into short stacks of BTAs, referred to as BTA micelles, due to its larger hydrophilic periphery compared to a BTA with linear ethylene glycol. It is hypothesized that **BTA-C$_{12}$-EG$_4$-tri-Glu** adopts the same micellar morphology. The tetra(ethylene glycol) chains and the glucose moieties individually give the correct hydrophilic/hydrophobic balance with a dodecyl chain to promote the elongation of the stacks into supramolecular polymers. However, the combination of those two hydrophilic moieties disrupts this balance and changes the morphology of the assemblies. The better exposure of this hydrophilic periphery to water in the micellar morphology is expected to be the cause of this change in packing.

Next, the influence of the saccharides on the dynamics of the supramolecular assemblies is studied with HDX-MS. Aqueous samples of assembled BTAs are diluted into D$_2$O for those experiments to track the exchange of labile hydrogen atoms to deuterium atoms with MS. The saccharide-functionalized BTAs all have 15 labile hydrogen atoms: 12 on the hydroxyl groups of the saccharides and 3 amide hydrogen atoms of the BTA core. It is hypothesized that the 12 hydroxyl groups are in direct contact with the solvent and will exchange immediately for deuterium atoms upon dilution into D$_2$O. The 3 amide hydrogen atoms are contained in the hydrophobic pocket and their exchange to deuterium atoms is therefore delayed and can be used as a

measure for the exchange of monomers between assemblies as was explained for **BTA-C$_{12}$-EG$_4$** in Chapter 3.

All aqueous samples were diluted 100x times into D$_2$O and the percentage of BTAs with at least 10 deuterium atoms was followed over time, since less deuterated BTAs were barely observable. The exchange of **BTA-C$_{12}$-tri-Glu** (Figure 4A) and **BTA-C$_{12}$-tri-Man** (Figure 4B) is almost identical with an initial fast exchange of the amide hydrogen atoms. Around 42% of the molecules is fully deuterated at the first measurement point, which indicates the presence of some ill-defined structures. The exchange slows down after 45 minutes around 62% BTA15D but the percentage of fully deuterated molecules keeps increasing to 84.7% for **BTA-C$_{12}$-tri-Glu** and 82.8% for **BTA-C$_{12}$-tri-Man** after 72 hours. Both molecules have roughly 5% BTA13D and 8% BTA14D immediately after dilution into D$_2$O, which both decrease to a stable value within 1 hour. This indicates that part of the H/D exchange occurs via a solvent penetration mechanism, although not as much as in case of **BTA-C$_{12}$-EG$_4$** (see Chapter 3).
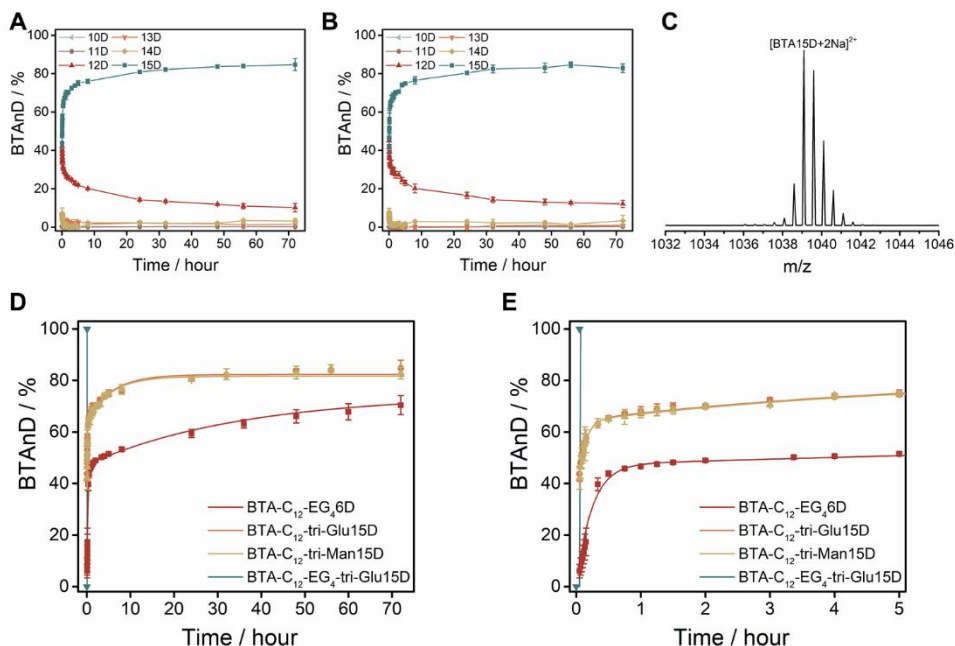
Figure 4. (A-B) The percentage of different deuterated analogues of (A) **BTA-C$_{12}$-tri-Glu** and (B) **BTA-C$_{12}$-tri-Man** as a function of time after the 100x dilution of an aqueous 500 μM sample into D$_2$O (T = room temperature). (C) The ESI-MS spectrum of **BTA-C$_{12}$-EG$_4$-tri-Glu** 3 minutes after the 100x dilution of an aqueous 500 μM sample into D$_2$O (T = room temperature). (D) The percentage of fully deuterated **BTA-C$_{12}$-EG$_4$**, **BTA-C$_{12}$-tri-Glu**, **BTA-C$_{12}$-tri-Man** and **BTA-C$_{12}$-EG$_4$-tri-Glu** as a function of time after the 100x dilution of aqueous 500 μM samples into D$_2$O (T = room temperature). (E) Zoom-in on the first 5 hours. The symbols represent the average and the error bars the standard deviation calculated from three independent measurements. The lines in D and E represent a bi-exponential growth function.

In contrast, the ESI-MS spectrum of **BTA-C$_{12}$-EG$_4$-tri-Glu** after the 100x dilution of an aqueous sample into D$_2$O only contains the isotopic distribution of a BTA with all labile hydrogen atoms exchanged for deuterium atoms (Figure 4C). The peaks at higher m/z represent its isotopes and the peaks at lower m/z originate from a small percentage of D/H exchange due to the presence of 1 vol% H$_2$O after dilution. The immediate exchange of all amide hydrogen atoms indicates that these atoms are not as well protected from the solvent in the micellar assemblies.

The exchange dynamics of all BTAs are compared in Figure 4D-E. The increase in the percentage of fully deuterated BTAs overlaps for **BTA-C$_{12}$-tri-Glu** and **BTA-C$_{12}$-tri-Man**. The exchange of those molecules is higher than the exchange of **BTA-C$_{12}$-EG$_4$** over the whole period measured. It can be concluded from those results that the introduction of saccharides in the periphery of the BTAs increases their exchange dynamics. Additionally, the higher start percentage and the higher transition point in the graphs suggest that there are more ill-defined regions in the samples of **BTA-C$_{12}$-tri-Glu** and **BTA-C$_{12}$-tri-Man**. The type of saccharide does not have an influence on the dynamics, but its position in the side chain does. **BTA-C$_{12}$-EG$_4$-tri-Glu** with its glucose moiety attached to the tetra(ethylene glycol) chain shows immediate exchange of all labile hydrogen atoms. This increase in dynamics is likely related to the less-ordered micellar morphology that those BTAs adopt.

All BTAs with monosaccharides in this chapter were prepared via Cu(I)-catalyzed azide-alkyne cycloadditions, resulting in the introduction of a triazole linker. Recently, saccharide-functionalized BTAs were synthesized via acid-catalyzed glycosylation, thereby omitting the introduction the triazole linker.[42] These BTAs with β-D-glucose or α-D-mannose directly attached to the dodecyl chain suffer from some solubility problems, especially at high concentrations, and therefore require the presence of a cosolvent. These molecules assemble into supramolecular polymers that are shorter than the ones observed for **BTA-C$_{12}$-tri-Glu** and **BTA-C$_{12}$-tri-Man**. Only the BTA with α-D-mannose showed some bundling, although to a less extent than observed for **BTA-C$_{12}$-tri-Glu** and **BTA-C$_{12}$-tri-Man**. A circular dichroism (CD) signal similar to **BTA-(S)-D-C$_{12}$-EG$_4$** (Chapter 4) was reported for the assemblies of the BTAs without a triazole linker, indicating the formation of ordered assemblies with a preferred helicity. Such a signal was absent in the assemblies of **BTA-C$_{12}$-tri-Glu** and **BTA-C$_{12}$-tri-Glu**, which could be due to the increased distance between the BTA core and the stereogenic monosaccharides due to the presence of the triazole. Additionally, the exchange dynamics of the assemblies without the triazole linkers are slower, which could be an effect of the increased order within the assemblies. It can be concluded that the triazole linker influences the solubility, structure and dynamics of the supramolecular assemblies when present between the dodecyl chain and the saccharide. However, BTAs with α-D-mannose moieties directly attached to the tetra(ethylene glycol) chains assemble into the same micellar structures as **BTA-C$_{12}$-EG$_4$-tri-Glu**, indicating that the triazole is not of influence at this position.

5.3 Molecular dynamics simulations to study the interactions between saccharide functionalized BTAs

To gain a molecular insight into the structural and dynamic differences between saccharide-functionalized BTAs and **BTA-C$_{12}$-EG$_4$**, the group of prof. dr. Giovanni Pavan performed all atom molecular dynamics (MD) simulations on supramolecular polymers of **BTA-C$_{12}$-tri-Glu** using the same procedure as they applied for **BTA-C$_{12}$-EG$_4$** fibers.[47] The interaction of the two strands in the double helix formation, as evidenced by cryoTEM and subsequent image analysis, was not taken into account, as that was not evident at the time of these simulations. Nevertheless, these models still provide insightful information about the intermolecular interactions as well as the interactions of the saccharides with the solvent. Simulations were started from a model of an ideal fiber composed of 48 pre-stacked and initially extended **BTA-C$_{12}$-tri-Glu** units. The atomistic model for the **BTA-C$_{12}$-tri-Glu** fiber was built and parameterized following the same procedure used for **BTA-C$_{12}$-EG$_4$** (see section 5.6.6 for details on the simulations).[47] The initial extended configuration for the atomistic **BTA-C$_{12}$-tri-Glu** fiber model replicates along the main axis of a simulation box filled with explicit water molecules by means of periodic boundary conditions, effectively modelling the bulk of an infinitely long fiber (Figure 5A). The starting geometry of the **BTA-C$_{12}$-tri-Glu** fiber is thus identical to that of the previously studied **BTA-C$_{12}$-EG$_4$**. This fiber was then equilibrated in water through 400 ns of MD simulation at 20 °C. During this time the **BTA-C$_{12}$-tri-Glu** fiber model reached the equilibrium in the atomistic MD regime.

During the simulations, the initially extended **BTA-C$_{12}$-tri-Glu** fiber structurally reorganizes to optimize the interactions between the monomers and with the solvent.[47] After equilibration, the side chains of **BTA-C$_{12}$-tri-Glu** appear to be more extended than those of **BTA-C$_{12}$-EG$_4$** (Figure 5A-B). Previous MD simulations of **BTA-C$_{12}$-EG$_4$** fibers revealed that the flexible EG-C$_{12}$ side chains collapse around the core of the fiber to reduce the hydrophobic area exposed to the solvent, which is referred to as the primary folding process. After this phase significant hydrophobic regions along the fiber were still in contact with water. Consequently, the **BTA-C$_{12}$-EG$_4$** fiber was seen to undergo a secondary folding process along the main fiber axis to further reduce the exposed hydrophobic area.[47] Such a secondary folding process is not observed along the MD run in case of the **BTA-C$_{12}$-tri-Glu** fibers. This is reflected into a higher persistence or order of the core-core stacking in the equilibrated **BTA-C$_{12}$-tri-Glu** fiber when compared to **BTA-C$_{12}$-EG$_4$**. The radial distribution functions (Figure 5C) demonstrate higher g(r) peaks at stacking distances c (= 3.4 Å), 2c, 3c, etc. The higher the g(r) peaks, the higher the stacking persistence, indicating a higher probability for finding cores at stacking distance in case of **BTA-C$_{12}$-tri-Glu**.[47] In general, the **BTA-C$_{12}$-tri-Glu** fiber deviates less from the extended fiber configuration during the MD simulation compared to the **BTA-C$_{12}$-EG$_4$** fiber. This could explain the absence of strand separation in the reconstructed cryoTEM images of the fibers.
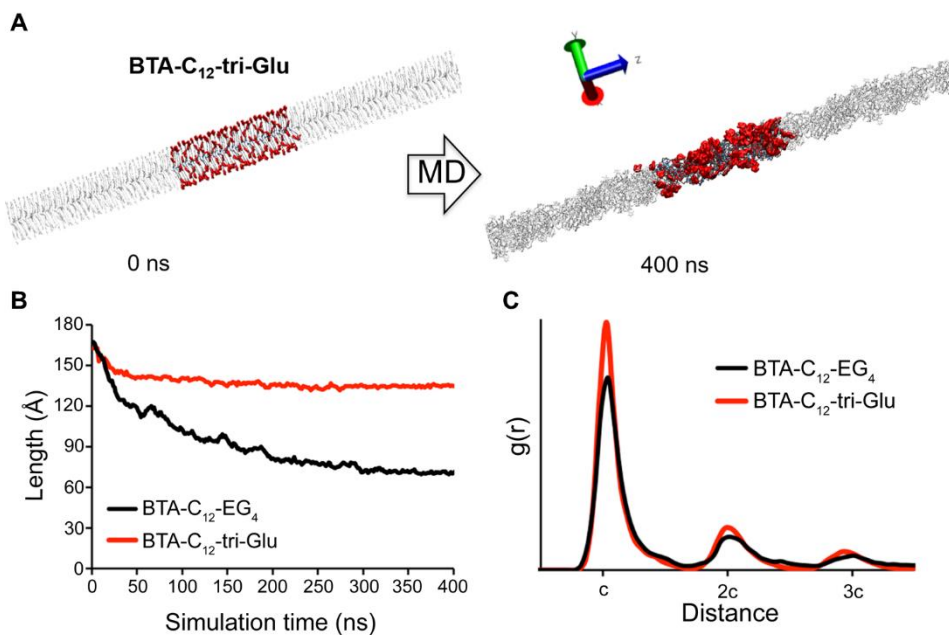
Figure 5. (A) Starting and equilibrated (400 ns) configuration during MD simulation of the **BTA-C$_{12}$-tri-Glu** fiber. In the periodic simulation box, the saccharides are colored red (grey in the periodic box images). (B) Fiber length (z-direction) during the MD simulations of the **BTA-C$_{12}$-EG$_4$**[48] and **BTA-C$_{12}$-tri-Glu** fibers. (C) Radial distribution functions (g(r)) of the cores in equilibrated (last 100 ns of MD) **BTA-C$_{12}$-EG$_4$**[48] and **BTA-C$_{12}$-tri-Glu** fibers. The distance c corresponds to the intercore distance (3.4 Å).

When analyzing the organization of the glucose moieties on the surface of the fibers in more detail, numerous hydrogen bond interactions between the glucose moieties are observed. Closer inspection of the MD trajectories shows that these hydrogen bonds can be direct (saccharide-saccharide) or even indirect, involving bridging by water molecules (saccharide-water-saccharide). Quantitative analysis of the hydrogen bonding in these fibers demonstrates that the hydrogen bonds involving glucose residues in **BTA-C$_{12}$-tri-Glu** (either direct or indirect) are way more numerous than those between the core amides. In the case of the **BTA-C$_{12}$-tri-Glu** fiber, the average number of hydrogen bonds between the core amides (Figure 6, green) is found to be roughly 2.1 per monomer, which is in the same range as found for the **BTA-C$_{12}$-EG$_4$** fibers.[47] However, the average number of hydrogen bonds between the saccharides in **BTA-C$_{12}$-tri-Glu** (Figure 6, pink) are about twice in number (see Table 1). Moreover, the indirect hydrogen bonds involving bridging by water molecules in **BTA-C$_{12}$-tri-Glu** (Figure 6, "wet" hydrogen bonds, cyan) are one order of magnitude more numerous than the core ones (Table 1). In this simulation only a single polymer is considered, but

it is expected that the "wet" hydrogen bonds can also connect the glucose moieties of two stacks, resulting in the bundled structure as observed with cryoTEM.
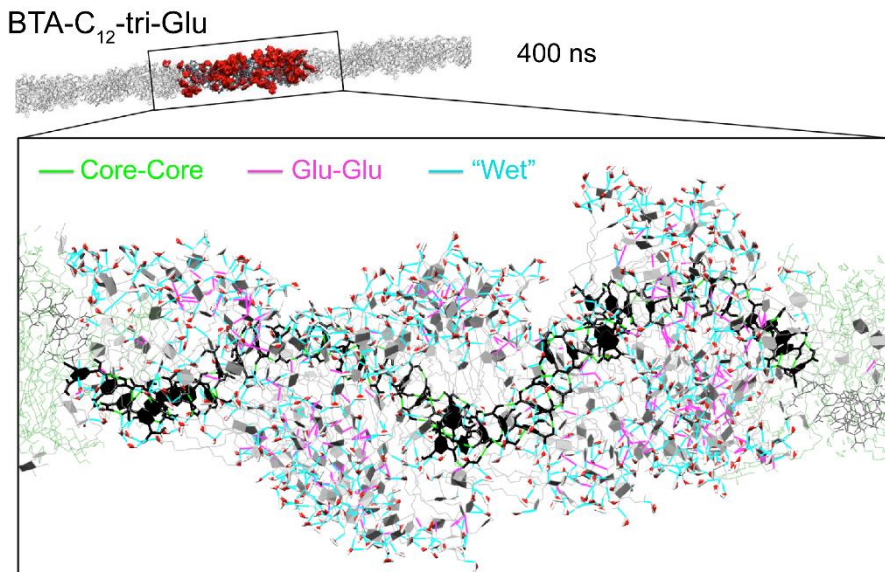
Figure 6. Details of the hydrogen bond interactions in the equilibrated **BTA-C$_{12}$-tri-Glu** fiber. At the MD equilibrium (400 ns), the saccharides form clusters (in red in the top image) on the fiber surface. **BTA-C$_{12}$-tri-Glu** cores are colored in black, side chains in grey and saccharides are shown as grey filled rings (in green in the periodic image). Water molecules are shown as red and white triangles. Core-core hydrogen bonds through the amides are colored in green, direct saccharide-saccharide hydrogen bonds in pink and indirect hydrogen bonds involving water molecules in cyan.

The surface of the **BTA-C$_{12}$-tri-Glu** fiber thus appears as a hydrogel-like structure, in which water molecules can be involved in hydrogen bonds and become immobilized by the glucose residues (Figure 6). In general, the MD simulations indicate that the additional hydrogen bond interactions between the surface glucose residues make the periphery of the fiber more hydrated compared to **BTA-C$_{12}$-EG$_4$**. This increased hydration of the periphery and core in **BTA-C$_{12}$-tri-Glu** could explain the increased exchange dynamics as observed with HDX-MS, as more solvated molecules are more likely to migrate into the solvent to exchange between polymers.

Table 1. Average number of hydrogen bonds per monomer calculated from the equilibrated phase MD simulations (last 100 ns).

	Hydrogen bond type		
	Core-core	Glu-Glu	"Wet
BTA-C$_{12}$-EG$_4$	2.2	-	8.0
BTA-C$_{12}$-tri-Glu	2.1	3.8	21.1

5.4 The influence of saccharides on supramolecular copolymerization

The co-assembly of functional monomers with unfunctional monomers is a well-known strategy to control the number of biological motifs presented on a supramolecular polymer.[25,26,42,49] Mixing of such monomers with a supramolecular polymer yields multivalent platforms.[39,42] Additionally, co-assembly can be used as a strategy to create supramolecular polymers with monomers that cannot form supramolecular polymers on their own due to an unbalanced hydrophilic/hydrophobic ratio. Examples of such monomers are **BTA-C$_{12}$-EG$_4$-tri-Man** and **BTA-C$_{12}$-EG$_4$-Man** (Figure 7) which were designed as binders to Con A lectins but cannot polymerize on their own. Here, a combination of UV spectroscopy and SLS will be used to study if these mannose-functionalized BTAs can copolymerize with **BTA-C$_{12}$-EG$_4$**, **BTA-C$_{12}$-tri-Glu** and **BTA-C$_{12}$-Glu**. Additionally, the impact of copolymerization on the structure and dynamics will be elucidated for some mixtures.
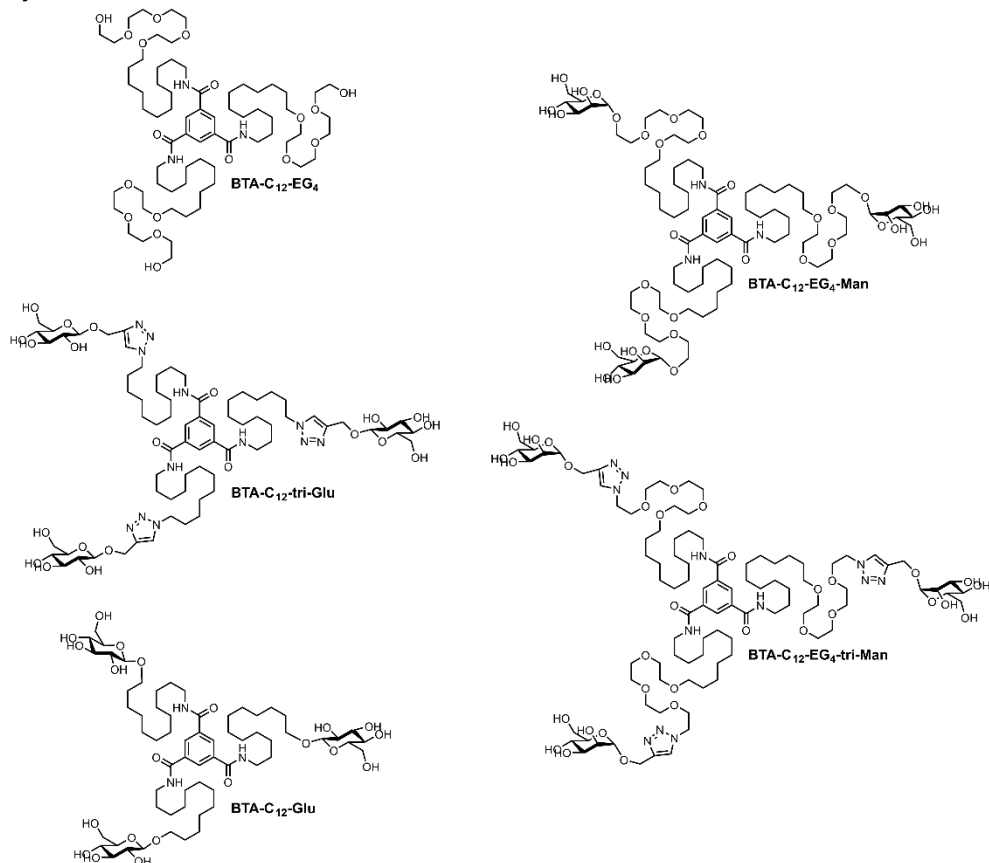
Figure 7. Chemical structure of **BTA-C$_{12}$-EG$_4$**, **BTA-C$_{12}$-tri-Glu**, **BTA-C$_{12}$-Glu**, **BTA-C$_{12}$-EG$_4$-Man** and **BTA-C$_{12}$-EG$_4$-tri-Man**.

5.4.1 The copolymerization of BTA-C₁₂-EG₄ with mannose-functionalized BTAs

The different BTAs were co-assembled by mixing equilibrated homo-assemblies in the desired ratio. First, the co-assemblies of **BTA-C₁₂-EG₄** with **BTA-C₁₂-EG₄-Man** were studied. **BTA-C₁₂-EG₄-Man** is characterized by a UV spectrum with maximum absorbance at 196 nm, indicative for the formation of BTA micelles. This peak disappears when the BTA is co-assembled with **BTA-C₁₂-EG₄** in different ratios and the resulting spectra have the same maxima as **BTA-C₁₂-EG₄** (Figure 8A). None of the measured spectra match with the calculated spectra for the self-sorted state, that is the weighted average of the spectra of the homo-assemblies, indicating that the two BTAs are interacting.
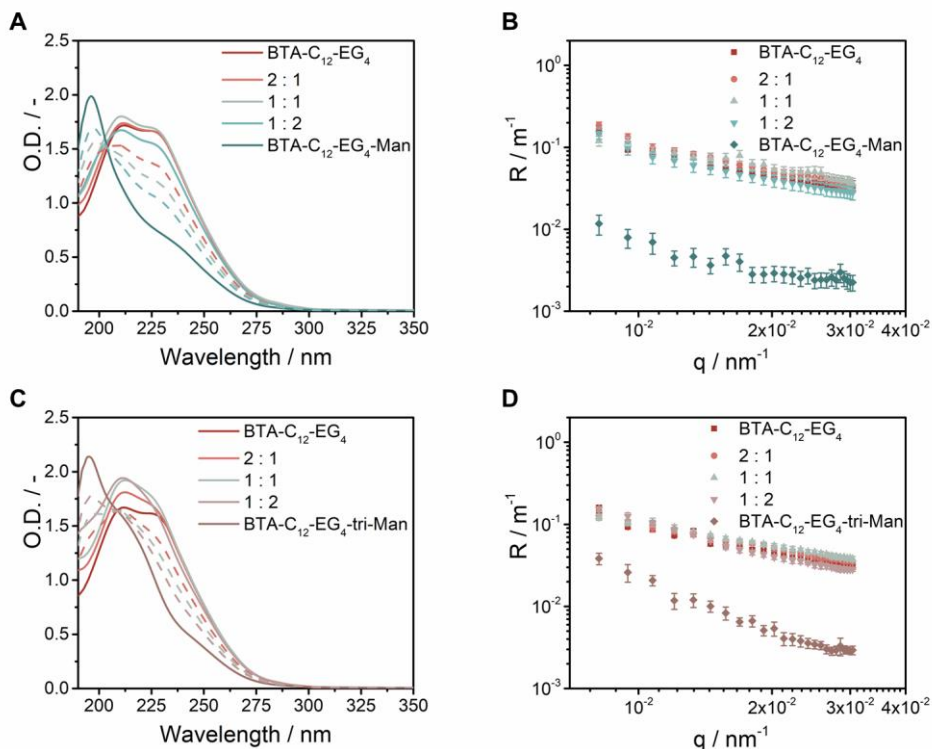
Figure 8. (A) UV spectra of mixtures of **BTA-C₁₂-EG₄** and **BTA-C₁₂-EG₄-Man** in water (c = 50 μM, l = 1 cm, T = 20 °C). Dashed lines represent calculated spectra of the self-sorted state. (B) Rayleigh ratio of mixtures of **BTA-C₁₂-EG₄** and **BTA-C₁₂-EG₄-Man** as a function of the scattering vector in water (c = 500 μM, l = 1 cm, λ = 532 nm, T = 20 °C). (C) UV spectra of mixtures of **BTA-C₁₂-EG₄** and **BTA-C₁₂-EG₄-tri-Man** in water (c = 50 μM, l = 1 cm, T = 20 °C). Dashed lines represent calculated spectra of the self-sorted state. (D) Rayleigh ratio of mixtures of **BTA-C₁₂-EG₄** and **BTA-C₁₂-EG₄-tri-Man** as a function of the scattering vector in water (c = 500 μM, l = 1 cm, λ = 532 nm, T = 20 °C).

SLS measurements show that all mixtures have an angle-dependent Rayleigh ratio that closely resembles the Rayleigh ratio of **BTA-C$_{12}$-EG$_4$** (Figure 8B). It can be concluded from those results that **BTA-C$_{12}$-EG$_4$** and **BTA-C$_{12}$-EG$_4$-Man** can copolymerize into supramolecular polymers with dimensions that resemble the polymers of **BTA-C$_{12}$-EG$_4$**. Dr. Svenja Herziger confirmed with cryoTEM that there is no bundling or uncontrolled aggregation of the supramolecular copolymers due to saccharide-saccharide interactions after mixing.[50] Image analysis of samples with a 1:1 ratio or with an excess of **BTA-C$_{12}$-EG$_4$** revealed the presence of a double helix structure, whereas strand separation was absent with an excess of **BTA-C$_{12}$-EG$_4$-Man**.

Mixtures of **BTA-C$_{12}$-EG$_4$** and **BTA-C$_{12}$-EG$_4$-tri-Man** were prepared with the same ratios to study the impact of the triazole linker. All mixtures have a maximum at 211 nm and a shoulder around 225 nm (Figure 8C), which does again not match with the calculated spectra of self-sorted assemblies, thereby confirming co-assembly. The Rayleigh ratio obtained of all mixtures overlaps with that of **BTA-C$_{12}$-EG$_4$** (Figure 8D), indicating the formation of micrometer long supramolecular polymers upon co-assembly. Supramolecular copolymerization of **BTA-C$_{12}$-EG$_4$** with mannose-functionalized BTAs is therefore not hindered by the presence of a triazole moiety at a long distance from the core.

The measurements presented here show that supramolecular copolymers can be obtained when **BTA-C$_{12}$-EG$_4$** is mixed with **BTA-C$_{12}$-EG$_4$-Man** or **BTA-C$_{12}$-EG$_4$-tri-Man**. Surprisingly, copolymers are also formed with an excess of the mannose-decorated BTAs, suggesting that a small amount of BTAs with the ability to form polymers is enough to drive the formation of supramolecular polymers.

5.4.2 The copolymerization of BTA-C$_{12}$-tri-Glu with mannose-functionalized BTAs

Having confirmed that **BTA-C$_{12}$-tri-Glu** is able to form supramolecular polymers, it was tested if this BTA could be used for copolymerization with **BTA-C$_{12}$-EG$_4$-Man**. The UV spectrum of the 2:1 sample resembles the spectrum of **BTA-C$_{12}$-tri-Glu** (Figure 9A), suggesting the presence of supramolecular copolymers. When the amount of mannose-functionalized BTA is increased a peak starts to appear around 196 nm, suggesting a mixture of supramolecular polymers and small micelles. This is corroborated by the SLS measurements which show a slightly lower Rayleigh ratio for the 1:1 and 1:2 samples compared to the 2:1 and **BTA-C$_{12}$-tri-Glu** samples (Figure 9B).

Next, the influence of the triazole linker between the tetra(ethylene glycol) and the α-D-mannose moiety was studied with mixtures of **BTA-C$_{12}$-tri-Glu** and **BTA-C$_{12}$-EG$_4$-tri-Man**. The peak in the UV spectrum indicative for the coexistence of micelles becomes more prominent in those samples (Figure 9C), especially in the 1:2 sample which completely overlaps with the spectrum of **BTA-C$_{12}$-EG$_4$-tri-Man**. The SLS spectra also show a drastic decrease in the Rayleigh ratio of all mixtures, indicating that there are more small micelles present (Figure 9D). It can therefore be concluded that the

triazole moiety between tetra(ethylene glycol) and α-D-mannose limits the copolymerization. It even seems that the supramolecular polymers of **BTA-C$_{12}$-tri-Glu** are disrupted in the 1:2 sample and that these molecules form small micelles with **BTA-C$_{12}$-EG$_4$-tri-Man** instead.
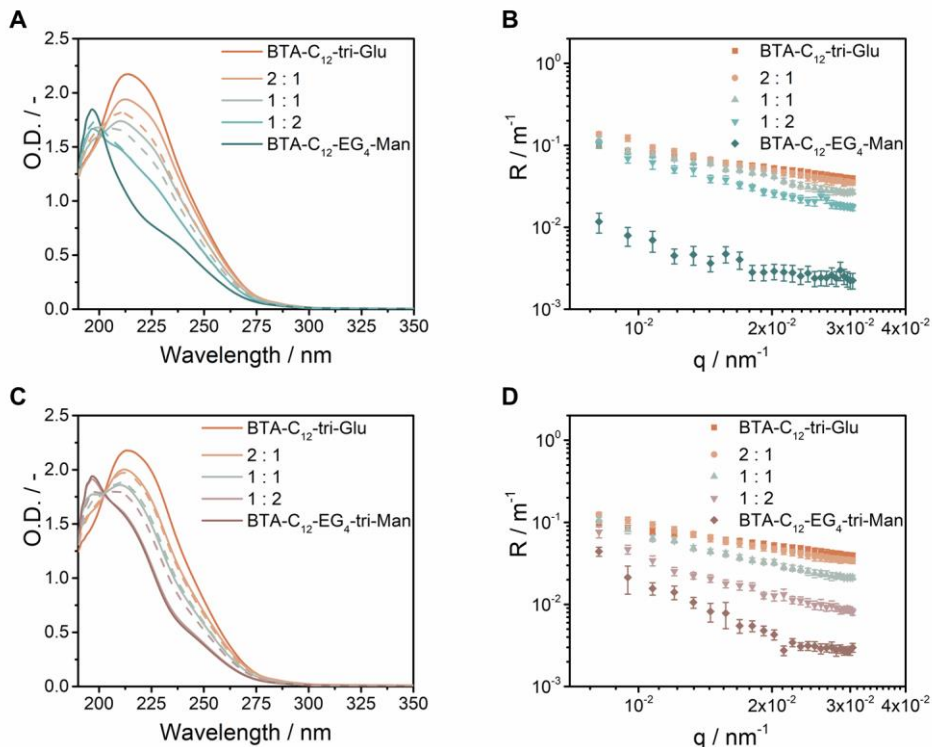
Figure 9. (A) UV spectra of mixtures of **BTA-C$_{12}$-tri-Glu** and **BTA-C$_{12}$-EG$_4$-Man** in water (c = 50 µM, l = 1 cm, T = 20 °C). Dashed lines represent calculated spectra of the self-sorted state. (B) Rayleigh ratio of mixtures of **BTA-C$_{12}$-tri-Glu** and **BTA-C$_{12}$-EG$_4$-Man** as a function of the scattering vector in water (c = 500 µM, l = 1 cm, λ = 532 nm, T = 20 °C). (C) UV spectra of mixtures of **BTA-C$_{12}$-tri-Glu** and **BTA-C$_{12}$-EG$_4$-tri-Man** in water (c = 50 µM, l = 1 cm, T = 20 °C). Dashed lines represent calculated spectra of the self-sorted state. (D) Rayleigh ratio of mixtures of **BTA-C$_{12}$-tri-Glu** and **BTA-C$_{12}$-EG$_4$-tri-Man** as a function of the scattering vector in water (c = 500 µM, l = 1 cm, λ = 532 nm, T = 20 °C).

The effect of copolymerization on the supramolecular structure was studied with a 1:1 mixture of **BTA-C$_{12}$-tri-Glu** and **BTA-C$_{12}$-EG$_4$-Man**. CryoTEM images reveal the presence of many supramolecular polymers of micrometer length (Figure 10A). However, a few ends can be observed, indicating that the copolymers are slightly shortened compared to **BTA-C$_{12}$-tri-Glu** by the addition of **BTA-C$_{12}$-EG$_4$-Man**. Remarkably, the bundling previously observed for the homopolymers of **BTA-C$_{12}$-tri-Glu** is completely absent. A closer inspection of the supramolecular polymers by image

reconstruction techniques shows that there is no separation of strands and thus is indicative for the absence of a double helix structure (Figure 10B). However, the diameter of 5.6 nm could be an indication that there are two strands in these polymers.
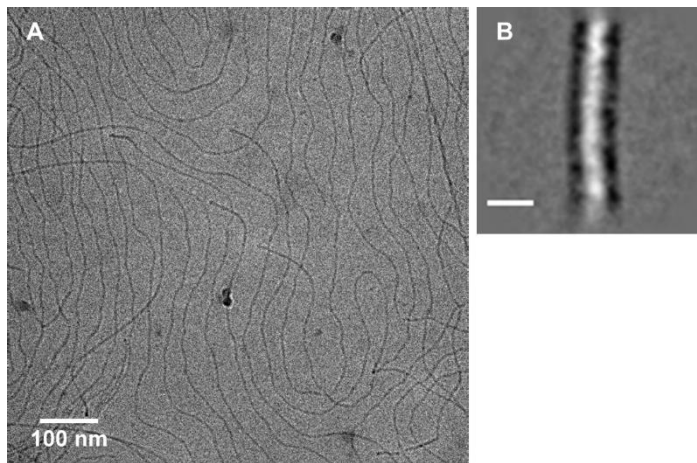
Figure 10. (A) CryoTEM image of the 1:1 mixture of **BTA-C$_{12}$-tri-Glu** and **BTA-C$_{12}$-EG$_4$-Man** in water (c = 500 μM). Dark spherical particles are crystalline ice particles. (B) The class sum image of aligned image extracts. The scalebar is 10 nm.

It can be concluded from those results that **BTA-C$_{12}$-tri-Glu** is not as efficient in copolymerizing mannose-functionalized BTAs as **BTA-C$_{12}$-EG$_4$**. The UV spectra of all equimolar mixtures or of mixtures with an excess of mannose-decorated BTAs contain a peak at 196 nm, indicating the presence of BTA micelles. CryoTEM images revealed that the bundling due to saccharide-saccharide interactions previously observed for **BTA-C$_{12}$-tri-Glu** is absent in the copolymers. The presence of the extended side chains of **BTA-C$_{12}$-EG$_4$-Man** might limit the interactions between the glucose moieties, thereby preventing bundling.

5.4.3 The copolymerization of BTA-C$_{12}$-Glu with a mannose-functionalized BTA

The triazole moiety between tetra(ethylene glycol) and α-D-mannose was found to slightly hinder the supramolecular copolymerization. It was therefore investigated if the triazole moiety attached to the dodecyl chain also influences copolymerization by mixing **BTA-C$_{12}$-Glu** with **BTA-C$_{12}$-EG$_4$-Man**. The self-assembly of **BTA-C$_{12}$-Glu** in water is complicated by the solubility issues of this molecule, resulting in scattering in the UV spectrum at higher wavelengths (Figure 11A), even in the presence of MeOH as a cosolvent.[42] The scattering disappears upon mixing of **BTA-C$_{12}$-Glu** with **BTA-C$_{12}$-EG$_4$-Man** (Figure 11A) which is a first indication for co-assembly. The 2:1 and 1:1 sample both have a higher UV absorbance than **BTA-C$_{12}$-Glu** but with the same maxima. The increase in absorbance and the significant differences with the calculated spectra indicate that those molecules likely co-assemble into supramolecular polymers. Only

the sample with an excess of mannose-functionalized BTA has a small peak at 196 nm that indicates the presence of some micelles. CD measurements indicate that the internal order of the supramolecular polymers is altered by the co-assembly as a smaller Cotton effect at lower wavelengths is found (Figure 11B). The copolymerization with **BTA-C$_{12}$-EG$_4$-Man** thus limits the ability of the molecules to adapt a preferred helicity.
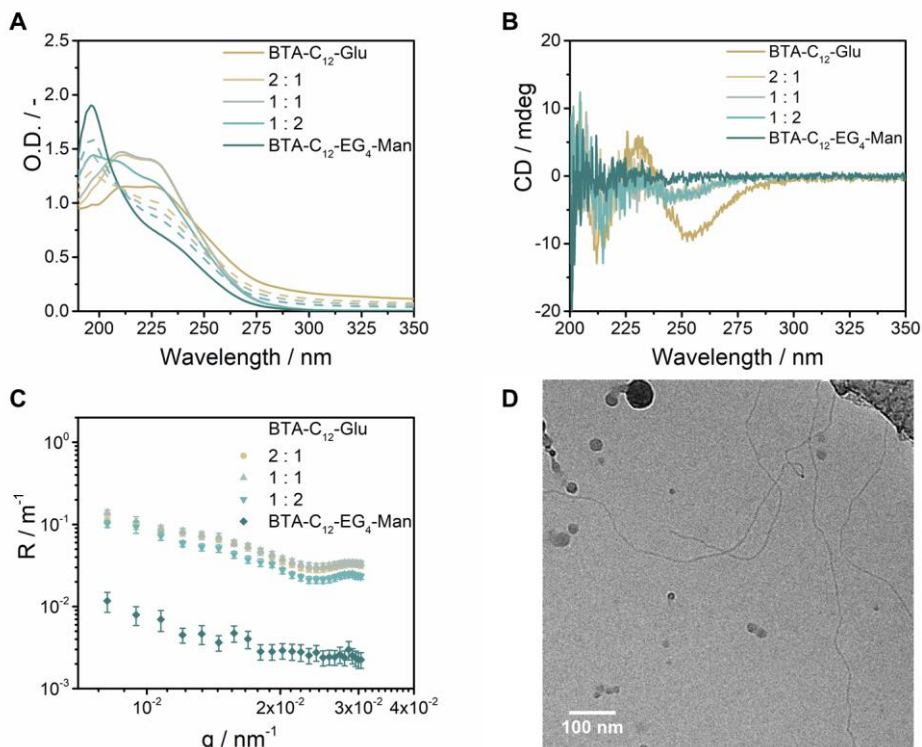
Figure 11. (A) UV spectra of mixtures of **BTA-C$_{12}$-Glu** and **BTA-C$_{12}$-EG$_4$-Man** in water (c = 50 μM, l = 1 cm, T = 20 °C). Dashed lines represent calculated spectra of the self-sorted state. (B) CD spectra of mixtures of **BTA-C$_{12}$-Glu** and **BTA-C$_{12}$-EG$_4$-Man** in water (c = 50 μM, l = 1 cm, T = 20 °C). (C) Rayleigh ratio of mixtures of **BTA-C$_{12}$-Glu** and **BTA-C$_{12}$-EG$_4$-Man** as a function of the scattering vector in water (c = 500 μM, l = 1 cm, λ = 532 nm, T = 20 °C). (D) CryoTEM image of the 1:1 mixture of **BTA-C$_{12}$-tri-Glu** and **BTA-C$_{12}$-EG$_4$-Man** in water (c = 500 μM). Dark spherical particles are crystalline ice particles. All samples with MeOH contain a small volume of MeOH for solubility (≤4%).

SLS could not be measured of a sample containing only **BTA-C$_{12}$-Glu** since all samples were turbid at high concentrations. However, all mixtures of **BTA-C$_{12}$-Glu** were clear solutions and SLS measurements showed a higher Rayleigh ratio than for **BTA-C$_{12}$-EG$_4$-Man** (Figure 11C). The bump at higher q values could indicate the presence of several morphologies. The slope and height of the graphs is in the same

range as measured for **BTA-C$_{12}$-EG$_4$** and **BTA-C$_{12}$-EG$_4$-Man**, indicating the formation of supramolecular copolymers. The 1:2 sample shows a slightly lower Rayleigh ratio, which matches with a combination of supramolecular polymers and BTA micelles as suggested from UV spectroscopy. CryoTEM images of the equimolar sample confirm the presence of supramolecular copolymers with a length of roughly 1 µm (Figure 11D).

It can be concluded from those measurements that **BTA-C$_{12}$-Glu** can copolymerize with **BTA-C$_{12}$-EG$_4$-Man**, although some micelles are formed at the 1:2 ratio. The copolymerization even solves the solubility issues of **BTA-C$_{12}$-Glu**. However, some of the preferred helicity dictated by the β-D-glucose moieties is lost after copolymerization. When these results are compared to the copolymerization of **BTA-C$_{12}$-tri-Glu** (Figure 9C-D) it can be concluded that the triazole linker close to the BTA core significantly lowers the copolymerization ability.

5.4.4 The dynamics of saccharide-functionalized copolymers

Finally, the effect of copolymerization on the exchange dynamics of the polymers was studied with HDX-MS. Copolymerization of **BTA-C$_{12}$-EG$_4$** and **BTA-C$_{12}$-EG$_4$-Man** was shown to have a stabilizing effect on both components.[42] In this section, the 1:1 mixtures of **BTA-C$_{12}$-tri-Glu** or **BTA-C$_{12}$-Glu** with **BTA-C$_{12}$-EG$_4$-Man** were diluted 100x into D$_2$O to follow the percentage of different deuterated analogs. In case of the mixture with **BTA-C$_{12}$-tri-Glu**, a fast increase in the percentage of fully deuterated **BTA-C$_{12}$-tri-Glu** (Figure 12A) and **BTA-C$_{12}$-EG$_4$-Man** (Figure 12B) can be observed in the first hour. The percentage of BTA15D stabilizes around 88% for **BTA-C$_{12}$-tri-Glu** and around 90% for **BTA-C$_{12}$-EG$_4$-Man**. The percentage of less deuterated analogs decreases the first hour, indicating some solvent penetration into the assemblies. However, there remains a large contribution of less deuterated analogs afterwards. Comparison with the measurements in Figure 4 reveals that the dynamics of **BTA-C$_{12}$-tri-Glu** have increased after copolymerization with **BTA-C$_{12}$-EG$_4$-Man**.

In case of the 1:1 mixture with **BTA-C$_{12}$-Glu**, a gradual increase in the percentage of fully deuterated **BTA-C$_{12}$-Glu** (Figure 12C) and **BTA-C$_{12}$-EG$_4$-Man** (Figure 12D) can be observed, which slows down after 2 hours. After 72 hours, 80.0% of **BTA-C$_{12}$-Glu** and 86.8% of **BTA-C$_{12}$-EG$_4$-Man** is fully deuterated. The percentage of BTA14D of both molecules decreases in the first hour and is negligible afterwards. The percentage of **BTA-C$_{12}$-Glu** does not increase smoothly, indicating that the polymer is not stable under the measurement conditions, probably because of its solubility issues and need for a cosolvent.

The two mixtures have in common they both some a time-dependent exchange of the **BTA-C$_{12}$-EG$_4$-Man** amide hydrogen atoms, indicating the copolymerization of at least a fraction of this material. Additionally, the exchange of **BTA-C$_{12}$-EG$_4$-Man** is slightly faster than the exchange of the BTAs decorated with β-D-glucose. None of the BTAs reach 100% deuteration, indicating that there are some very stable components within the sample, which could be related to the strand association as discussed in

Chapter 3. However, the HDX-MS experiments also show many differences. The H/D exchange is faster in reaching the maximum percentage of fully deuterated BTAs in the mixtures with **BTA-C$_{12}$-tri-Glu** than in the mixtures with **BTA-C$_{12}$-Glu**. The percentage of BTA15D 3 minutes after dilution, that is the first measurement, is already higher in mixtures with **BTA-C$_{12}$-tri-Glu** than in mixtures with **BTA-C$_{12}$-Glu**. This could be because there are less-structured assemblies present in the mixtures with **BTA-C$_{12}$-tri-Glu**, such as micelles. Additionally, it could be that the supramolecular copolymers in the solution are less stable. Overall, it can be concluded that the triazole linker between the dodecyl chain and β-D-glucose seems to increase the dynamics of the co-assemblies.
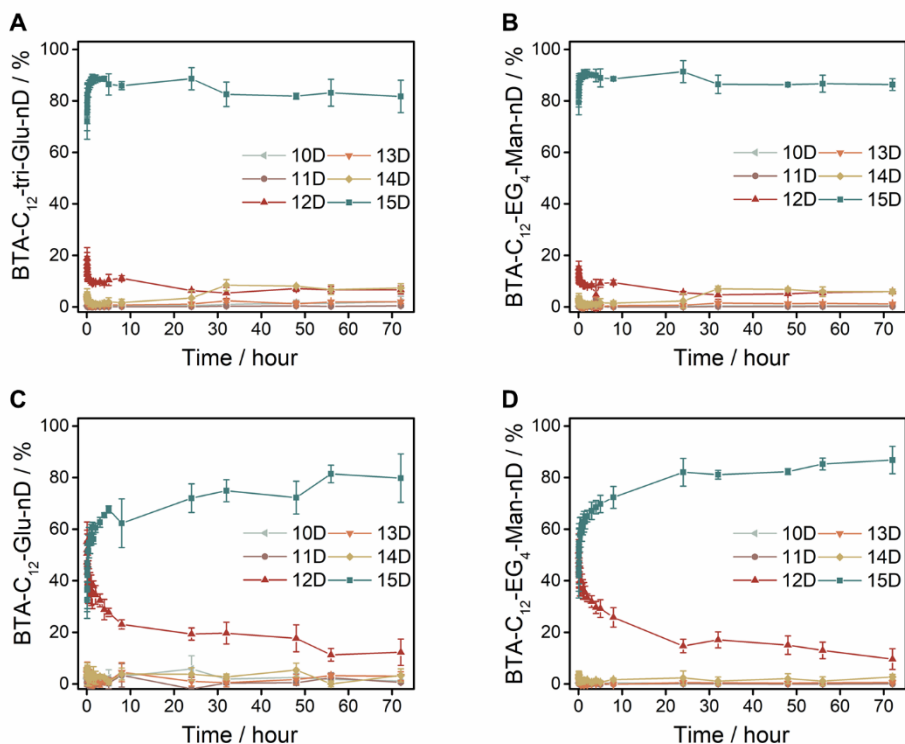
Figure 12. (A-B) The percentage of different deuterated analogues in a 1:1 mixture of (A) **BTA-C$_{12}$-tri-Glu** and (B) **BTA-C$_{12}$-EG$_4$-Man** as a function of time after the 100x dilution of an aqueous 500 μM sample into D$_2$O (T = room temperature). (C-D) The percentage of different deuterated analogues in a 1:1 mixture of (C) **BTA-C$_{12}$-Glu** and (D) **BTA-C$_{12}$-EG$_4$-Man** as a function of time after the 100x dilution of an aqueous 500 μM sample into D$_2$O (T = room temperature).

5.5 Conclusions

In this chapter, monosaccharides were explored as alternative water-solubilizing groups for BTAs. When the tetra(ethylene glycol) periphery was replaced with β-D-glucose or α-D-mannose bundled supramolecular polymers were obtained with faster exchange dynamics. MD-simulations revealed that this is due to the surface saccharides

being more exposed on the fiber surface and the presence of numerous hydrogen bond interactions between the saccharides, both direct and through bridging by water molecules. When the monosaccharides were attached to the tetra(ethylene glycol) the periphery becomes too hydrophilic and the morphology of the assemblies changed to less-ordered non-spherical micelles. This is a more favorable packing of molecules as this allows for a better exposure of the periphery to the water.

Next, copolymerization was explored as a strategy to create multivalent supramolecular polymers. **BTA-C₁₂-EG₄-Man** and **BTA-C₁₂-EG₄-tri-Man** assemble into small micelles on their own, but mixing with a BTA with tetra(ethylene glycol) or glucose periphery resulted in the formation of supramolecular copolymers. Copolymerization was the most efficient when a BTA with tetra(ethylene glycol) periphery was used as in this case supramolecular polymers were formed even in case of an excess of mannose-decorated BTAs. This is most likely because the chemical structure of **BTA-C₁₂-EG₄** shows the most resemblance to the BTAs with terminal mannose motifs, thereby resulting in a better packing of molecules. BTAs with a glucose periphery were not able to copolymerize all of the **BTA-C₁₂-EG₄-Man** and **BTA-C₁₂-EG₄-tri-Man** and instead mixtures of polymers and BTA micelles were observed. Copolymerization prevents the bundling of the polymers and increases their exchange dynamics. It is proposed that this is because the tetra(ethylene glycol) chains extend beyond the glucose moieties, thereby sterically hindering the saccharide-saccharide interactions.

In this chapter, special attention was paid to the linkage of the monosaccharides to the BTA, either direct or via a triazole linker. In case of the homopolymers the direct attachment results in solubility issues, the need for a cosolvent and shorter unbundled polymers. The triazole moiety overcomes these problems but also prohibit the saccharides from directing the helicity of the assemblies. Additionally, the triazole motif can seriously limit the copolymerization depending on its position in the side chains. The triazole linker in **BTA-C₁₂-tri-Man** has no effect on copolymerization with **BTA-C₁₂-EG₄** but when mixed with **BTA-C₁₂-tri-Glu** it results in the formation of micelles instead of polymers when it is present in excess. All mixtures with **BTA-C₁₂-tri-Glu** contain a combination of supramolecular polymers and BTA micelles, whereas mixtures with **BTA-C₁₂-Glu** contain mainly supramolecular polymers. This indicates that the triazole linker directly after the dodecyl chain limits the supramolecular copolymerization. It remains to be studied if this is due to a disrupted packing or due to triazole-triazole interactions. This research not only emphasizes the importance of a careful consideration when designing the periphery of a supramolecular motif, but it also opens the door to multivalent, water-compatible supramolecular polymers for biological recognition. Future work should focus on the interaction of those supramolecular materials with saccharide-binding proteins.

5.6 Experimental section

5.6.1 Materials and Methods

All solvents and chemicals used were of reagent grade quality or better and purchased from Biosolve or Sigma-Aldrich at the highest purity available and used without further purification unless otherwise noted. **BTA-C$_{12}$-EG$_4$**,[38] **BTA-C$_{12}$-tri-Glu**,[41] **BTA-C$_{12}$-tri-Man**,[41] and **BTA-C$_{12}$-EG$_4$-N$_3$**[51] were synthesized by Jolanda Spiering according to literature procedures. **BTA-C$_{12}$-Glu** was synthesized by Tim Hogervorst according to literature procedure.[42] **BTA-C$_{12}$-EG$_4$-Man** was synthesized by Lu Su according to literature procedure.[42] Water for aqueous samples was purified on an EMD Millipore Milli-Q Integral Water Purification System.

Sample preparation of BTA-C$_{12}$-EG$_4$, BTA-C$_{12}$-tri-Glu, **BTA-C$_{12}$-tri-Man**, **BTA-C$_{12}$-EG$_4$-tri-Glu BTA-C$_{12}$-EG$_4$-tri-Man, BTA-C$_{12}$-EG$_4$-Man:** the solid material was weighed into a glass vial equipped with a magnetic stirring bar. MQ-water was added to obtain the desired concentration in H$_2$O. The sample was subsequently stirred at 80 °C for 15 minutes and the hot and hazy sample was vortexed immediately afterwards for 15 seconds. All samples were left to equilibrate at room temperature.

Sample preparation for BTA-C$_{12}$-Glu: the molecule suffers from solubility issues and therefore requires the presence of a cosolvent. The solid material was weighed into a glass vial. MeOH was added to obtain a concentration of 12.5 mM. After 2 hours of equilibration, the stock solution was injected into a clean glass vial with MQ-water and stirring bar to obtain a BTA concentration of 50 or 500 µM. The sample was subsequently stirred at 80 °C for 15 minutes and the hot and hazy sample was vortexed immediately afterwards for 15 seconds. All samples were left to equilibrate at room temperature.

Sample preparation for mixtures: the overnight equilibrated homo-assemblies were mixed in the desired ratio in a clean glass vial with stirring bar. Samples with **BTA-C$_{12}$-Glu** were turbid after overnight equilibration so co-assemblies were instead prepared by adding the **BTA-C$_{12}$-Glu** solution 8 minutes after the heating of the sample. The sample was subsequently stirred at 80 °C for 15 minutes and the hot and hazy sample was vortexed immediately afterwards for 15 seconds. All samples were left to equilibrate at room temperature.

5.6.2 Instrumentation

Newly synthesis molecules were characterized with nuclear magnetic resonance (NMR), solid-state Fourier-transform infrared (FT-IR), liquid chromatography mass spectroscopy (LC-MS) and matrix assisted laser absorption/ionization mass time of flight mass spectroscopy (MALDI-TOF-MS) using the instruments described in Chapter 2.

Column chromatography was performed with the instruments described in Chapter 2. Reactions were followed by thin-layer chromatography (TLC) using 60-F$_{254}$ silica gel plates from Merck and visualized by UV light at 254 nm and/or staining (ninhydrin, bromocresol green, potassium permanganate, iodine chamber).

Ultraviolet-visible (UV-visible) absorbance spectra were recorded with the instruments described in Chapter 3.

Static light scattering (SLS) measurements were recorded on an ALV/CGS-3 MD-4 compact goniometer system equipped with a multiple tau digital real time correlator (ALV-7004) and a solid-state laser (λ = 532 nm; 40 mW). Scattering intensity was detected over an angular range of 30° to 150° with steps of 5° and averaged over at least 4 runs of 10 seconds per angle. As a reference, samples of water and toluene were measured. Water was filtered with a 0.2 µm syringe

filter (Supor membrane, PALL Corporation) and toluene were filtered with a 0.2 µm syringe filter (PTFE membrane, Whatman). The measurements were analyzed to remove measurements showing obvious scattering from dust. The Rayleigh ratio as a function of the angle was computed with $R_θ=((I_{sample}-I_{water})/I_{toluene})*R_{toluene}*n^2_{water}/n^2_{toluene}$ with I_{sample} the count rate of the sample solution, I_{water} the count rate of water and $I_{toluene}$ the count rate for toluene. $R_{toluene}$ is the known Rayleigh ratio of toluene (2.1×10^{-2} m^{-1} at 532 nm), n_{water} is the refractive index of water (1.333) and $n_{toluene}$ is the refractive index of toluene (1.497).

Fourier-Transform infrared (FT-IR) spectra in solution were recorded with the instruments and methods described in Chapter 4.

Cryogenic transmission electron microscopy (cryoTEM) images were obtained with the instrument described in Chapter 2.

2D image reconstruction was performed in Berlin with the instruments described in Chapter 2. The Volta phase plate was only used for all characterization.

Hydrogen deuterium exchange experiments with electrospray ionization were carried out with the instruments described in Chapter 3.

5.6.3 Synthetic procedures

Acetyl protected N^1,N^3,N^5-tris(1-(4-((((2R,3R,4S,5S,6R)-3,4,5-trihydroxy-6-(hydroxymethyl)tetrahydro-2H-pyran-2-yl)oxy)methyl)-1H-1,2,3-triazol-1-yl)-3,6,9,12-tetraoxatetracosan-24-yl)benzene-1,3,5-tricarboxamide (1)

BTA-C$_{12}$-EG$_4$-N$_3$ (535 mg, 0.390 mmol) was dissolved in 18 mL DMSO in a 50 mL round bottom flask. 2-propynyl-tetra-O-acetal-β-D-glucopyranoside (500 mg, 1.30 mmol) was added and the solution was stirred. When the solution was clear, sodium-L-ascorbate (70 mg, 0.350 mmol) and CuSO$_4$ (50 mg, 0.310 mmol) were added from 2 mL of water. The reaction mixture turned yellow and precipitation was observed. The reaction mixture became clear and green after 2 hours of stirring at room temperature. 150 mL of CHCl$_3$ was added and the solution was washed with EDTA (0.1M, 2x150 mL), citric acid (10%, 3x100 mL), NH$_4$Cl (sat., 150 mL) and water (150 mL). The organic phase was dried with MgSO$_4$ and the solvent was evaporated. The crude was purified by column chromatography (55 g SiO$_2$, 5% MeOH in CHCl$_3$), yielding **1** (1.0 g, 102% due to a small fraction of water). ^{1}H NMR (400 MHz, CDCl$_3$ δ): 8.35 (s, 3H, Ar), 7.72 (s, 3H, triazole), 6.58 (t, 3H, amides), 5.19 (m, 3H, glucose C$\underline{H}$), 5.09 (m, 3H, glucose C$\underline{H}$), 5.00 (m, 3H, glucose C$\underline{H}$), 4.86 (m, 6H, triazole-C$\underline{H_2}$O), 4.59-4.47 (m, 6H, CH$_2$C$\underline{H_2}$-triazole), 4.22 (m, 6H, glucose C$\underline{H_2}$), 3.92-3.81 (m, 6H, C$\underline{H_2}$CH$_2$-triazole), 3.77-3.69 (m, 3H, glucose C$\underline{H}$CH$_2$), 3.68-3.52 (m, 36H, OC$\underline{H_2}$C$\underline{H_2}$O), 3.51-3.38 (m, 12H, NHC$\underline{H_2}$CH$_2$, CH$_2$C$\underline{H_2}$O), 2.12-1.92 (m, 36H, acetyl C$\underline{H_3}$), 1.67-1.49 (m, 12H, NHCH$_2$C$\underline{H_2}$, C$\underline{H_2}$CH$_2$O), 1.44-1.18 (m, 48H, aliphatic). ^{13}C NMR (100 MHz, CDCl$_3$ δ): 170.67, 170.19, 169.43, 169.34, 165.62, 143.83, 135.30, 127.98, 124.06, 99.68, 72.82, 71.88, 71.55, 71.21, 70.64, 70.59, 70.56, 70.48, 70.04, 69.42, 68.33, 62.76, 61.86, 50.30, 40.37, 29.62, 29.56, 29.53, 29.48, 29.46, 29.26, 26.97, 26.08, 20.77, 20.63, 20.61. MALDI-TOF-MS: *m/z* calculated for C$_{120}$H$_{192}$N$_{12}$O$_{45}$+Na$^+$: 2544.30 [M+Na]$^+$; observed 2545.34.

BTA-C$_{12}$-EG$_4$-tri-Glu

A 50 mL round bottom flask was charged with **1** (980 mg, 0.388 mmol) in 20 mL MeOH. NaOH (256 mg, 6.40 mmol) was added and the reaction was stirred overnight at room temperature. The progress was monitored by TLC and the reaction was quenched with Dowex® 50WX8 hydrogen form resin. The resin was removed by filtration and the solvent in the filtrate was evaporated,

yielding **BTA-C₁₂-EG₄-tri-Glu** (710 mg, 90.2%). ¹H NMR (400 MHz, DMSO-d₆ δ): 8.86 (t, 3H, amides), 8.43 (s, 3H, Ar), 8.08 (s, 3H, triazole), 4.73 (m, 6H, triazole-C$\underline{H}_2$O), 4.51 (t, 6H, CH₂C$\underline{H}_2$-triazole), 4.24 (d, 3H, glucose C$\underline{H}$), 3.81 (t, 6H, C$\underline{H}_2$CH₂-triazole), 3.72-3.66 (m, 3H, glucose C$\underline{H}$CH₂), 3.55-3.40 (m, 39H, OC$\underline{H}_2$C$\underline{H}_2$O, glucose C$\underline{H}$), 3.38-3.21 (m, 12H, NHC$\underline{H}_2$CH₂, CH₂C$\underline{H}_2$O), 3.18-3.01 (m, 9H, glucose C$\underline{H}$, glucose C$\underline{H}_2$), 2.97 (t, 3H, glucose C$\underline{H}$), 1.81-1.60 (s, 4H, glucose O$\underline{H}$), 1.59-1.40 (m, 12H, NHCH₂C$\underline{H}_2$, C$\underline{H}_2$CH₂O), 1.36-1.16 (m, 48H, aliphatic). ¹³C NMR (100 MHz, DMSO-d₆ δ): 165.83, 144.10, 135.51, 128.83, 125.01, 102.64, 77.53, 77.20, 73.87, 70.79, 70.58, 70.24, 70.09, 70.01, 69.93, 69.19, 61.91, 61.63, 49.78, 29.67, 29.51, 29.37, 29.29, 26.98, 26.13. FT-IR (ATR) ν (cm^{-1}): 3254, 2922, 2853, 1642, 1560, 1410, 1350, 1292, 1102, 1077, 1044, 929, 829, 788, 706, 690, 650, 625, 574, 530, 468, 428, 418, 408. LC-MS: *m/z* calculated for $C_{96}H_{168}N_{12}O_{33}+3H^+$: 673.40 [M+3H]$^{3+}$; observed 673.67.
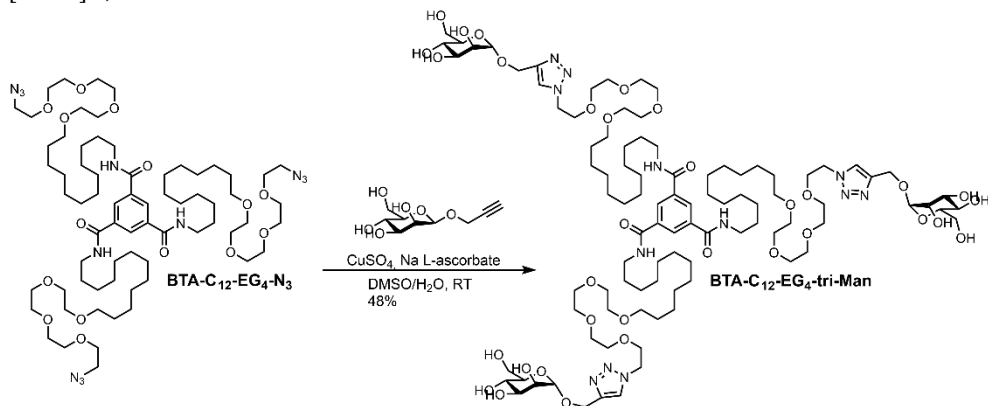
BTA-C₁₂-tri-Man

BTA-C₁₂-EG₄-N₃ (140 mg, 0.103 mmol) was dissolved in 7 mL DMSO in a 25 mL round bottom flask. Propynyl-α-D-mannopyranoside (75 mg, 0.330 mmol) was added and the solution was stirred. Sodium-ʟ-ascorbate (10.2 mg, 0.051 mmol) and CuSO₄ (8.2 mg, 0.051 mmol) were added with 4 drops of water. The reaction mixture turned from brown to yellow-green. The reaction was stirred overnight at room temperature but the conversion was not complete yet. Additional Propynyl-α-D-mannopyranoside, sodium-ʟ-ascorbate and CuSO₄ were added and the reaction was complete after overnight stirring. The DMSO was evaporated *in vacuo*. The crude was dissolved in 3.5 mL water and was purified by reverse phase column chromatography (KP-C₁₈-HS column, 60 g, H₂O/ACN 90/10 – 20/80 v/v). Lyophilization of the pure fractions yielded **BTA-C₁₂-EG₄-tri-Man** as a fluffy white solid (100 mg, 48%). ¹H NMR (400 MHz, DMSO-d₆ δ): 8.82 (t, 3H, amides), 8.35 (s, 3H, Ar), 8.07 (s, 3H, triazole), 4.72 (m, 6H, triazole-C$\underline{H}_2$O), 4.69 (m, 6H, t, 6H, CH₂C$\underline{H}_2$-triazole), 4.56-4.44 (m, 15H, mannose C$\underline{H}$, C$\underline{H}_2$) 3.81 (t, 6H, C$\underline{H}_2$CH₂-triazole), 3.72-3.63 (m, 3H, mannose C$\underline{H}$CH₂), 3.58-3.20 (m, 48H, OC$\underline{H}_2$C$\underline{H}_2$O, NHC$\underline{H}_2$CH₂, CH₂C$\underline{H}_2$O), 1.58-1.40 (m, 12H, NHCH₂C$\underline{H}_2$, C$\underline{H}_2$CH₂O), 1.36-1.18 (m, 48H, aliphatic). ¹³C NMR (100 MHz, DMSO-d₆ δ): 165.87, 143.82, 135.59, 124.88, 99.47, 74.61, 71.39, 70.79, 70.66, 70.24, 70.21, 70.09, 70.00, 69.92, 69.13, 67.45, 61.74, 59.53, 49.78, 29.67, 29.50, 29.36, 29.27, 26.97, 26.12. FT-IR (ATR) ν (cm^{-1}): 3343, 2922, 2853, 1641, 1556, 1456, 1436, 1350, 1295, 1250, 1228, 1099, 1056, 1030, 879, 811, 690, 580, 511. LC-MS: *m/z* calculated for $C_{96}H_{168}N_{12}O_{33}+3H^+$: 673.40 [M+3H]$^{3+}$; observed 673.75.

5.6.4 Additional notes on the purity and sample preparation of BTA-C₁₂-tri-Glu

Supramolecular self-assembly is very sensitive to small impurities and subtle changes in sample preparation. In this section, examples will be presented to show the influence of a small impurity and a different sample preparation method on structure and dynamics of supramolecular polymers of **BTA-C₁₂-tri-Glu**. Although drastic changes are revealed with cryoTEM, all samples shown here are characterized by the same UV spectrum with a single maximum at 213 nm and a shoulder at 229 nm (see Figure 2A).
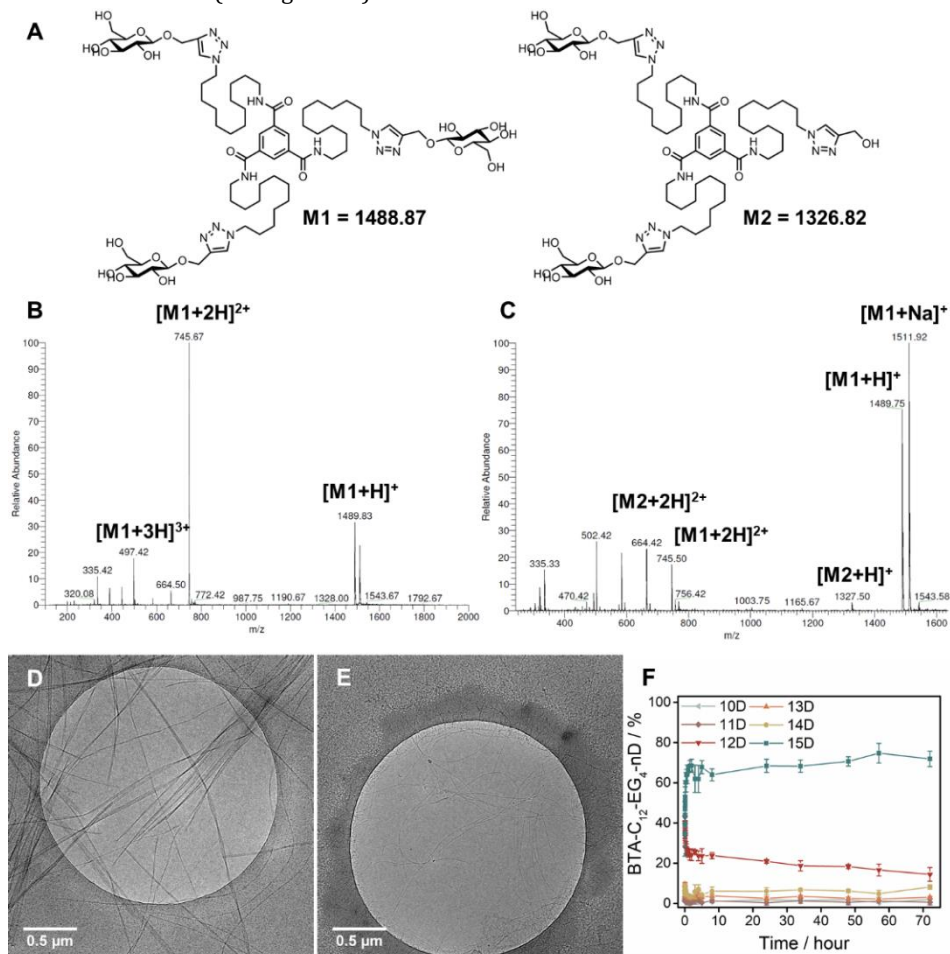
Figure 13. (A) Chemical structure of **BTA-C₁₂-tri-Glu** and its derivative with one of the β-D-glucose motifs missing. Their exact mass of each structure is indicated. (B) ESI-MS spectrum of the batch of **BTA-C₁₂-tri-Glu** used for the measurements in this chapter. (C) ESI-MS spectrum of an old batch of **BTA-C₁₂-tri-Glu** that contains some clear peaks of BTAs with only 2 β-D-glucose motifs. (D) CryoTEM image of the batch of **BTA-C₁₂-tri-Glu** used for the measurements in this chapter (c = 500 µM). (E) CryoTEM image of an old batch of **BTA-C₁₂-tri-Glu** that contains some BTAs with only 2 β-D-glucose motifs (c = 500 µM). (F) The percentage of different deuterated analogues in the impure sample of **BTA-C₁₂-tri-Glu** as a function of time after the 100x dilution of an aqueous 500 µM sample into D₂O (T = room temperature).

Previous publications of **BTA-C$_{12}$-tri-Glu** reported that this molecule assembles into unbundled supramolecular polymers.[41] However, a new batch of material was synthesized for the measurements in this chapter, which assembles into bundles of supramolecular polymers. Comparison of the LC-MS spectra of the two batches reveals that the old batch contained an impurity coming from the cleavage of one of the β-D-glucose motifs (Figure 13A, C). The new batch was purified by reverse phase chromatography to remove most of this impurity (Figure 13A, B). CryoTEM images show that the new batch assembles into bundled polymers (Figure 13D), whereas the batch with some BTAs with 2 glucose moieties assembles into unbundled fibers (Figure 13E). It seems that the absence of some of the β-D-glucose motifs reduces the saccharide-saccharide interactions and limits the bundling of the assemblies. HDX-MS experiments reveal that 71.9% of the **BTA-C$_{12}$-tri-Glu** molecules (only taking the molecules with a mass of 1488.87 Da into account) are completely deuterated after 72 hours when the impurity is present (Figure 13F). Surprisingly, this is a slower exchange than found for the bundled pure **BTA-C$_{12}$-tri-Glu** and the reason for this is still under investigation.

The first published experiments with **BTA-C$_{12}$-tri-Glu** were based on a different sample preparation protocol as described here. Although the same UV spectrum was obtained, cryoTEM images reveal drastic differences. When **BTA-C$_{12}$-tri-Glu** (the new batch) was directly dissolved in water without applying the heating-cooling protocol, short bundled polymers were found (Figure 14A). Longer supramolecular polymers were observed when the BTA was injected into water from a concentrated stock solution in MeOH (Figure 14B). However, the bundles are not as thick as the ones found with the sample preparation protocol that involved dissolving the molecules in water and subsequent heating-cooling. These experiments highlight the importance of a reproducible sample preparation method and show that evaluation of a sample preparation protocol should involve multiple techniques since the UV spectra did not reveal those structural differences.
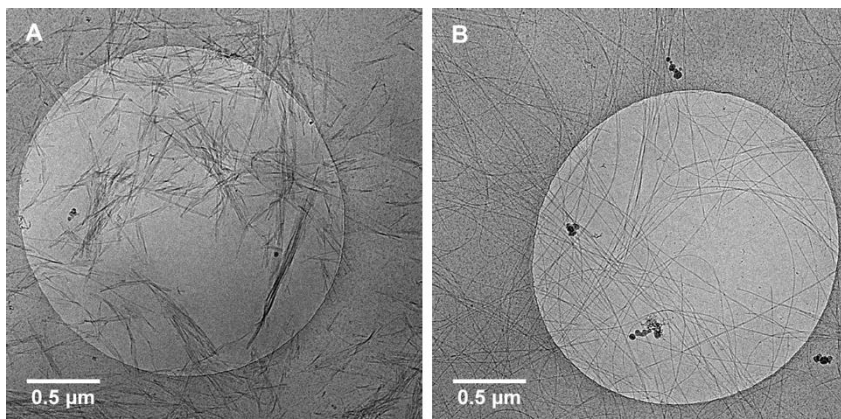
Figure 14. (A) CryoTEM image of a sample of **BTA-C$_{12}$-tri-Glu** that was directly dissolved in water (c = 500 µM). (B) CryoTEM image of a sample of **BTA-C$_{12}$-tri-Glu** that was injected into water from a stock solution in MeOH (c = 500 µM).

5.6.5 Analysis of the HDX-MS measurements

All HDX-MS experiments were performed under similar conditions to eliminate influences from the environment, for example temperature. The measurements were performed by diluting a

sample of self-assembled supramolecular building-blocks in H_2O 100x into D_2O. 0.5 mM sodium acetate was added to the D_2O prior to the dilution to facilitate the detection. The distribution with one sodium ion was used for **BTA-C$_{12}$-Glu** and in all other cases the distributions with two sodium ions were used for the calculations. All calculations are based on the method presented in Chapter 3. The equations used for samples of **BTA-C$_{12}$-EG$_4$** are given in section 3.9.3.

Isotope correction for **BTA-C$_{12}$-tri-Glu** and **BTA-C$_{12}$-tri-Man** is based on the following set of equations:

$I_{BTA10D\_c} = I_{772.46}$

$I_{BTA11D\_c} = I_{772.96} - 0.87I_{BTA10D\_c}$

$I_{BTA12D\_c} = I_{773.46} - 0.87I_{BTA11D\_c} - 0.42I_{BTA10D\_c}$

$I_{BTA13D\_c} = I_{773.97} - 0.87I_{BTA12D\_c} - 0.42I_{BTA11D\_c} - 0.14I_{BTA10D\_c}$

$I_{BTA14D\_c} = I_{774.47} - 0.87I_{BTA13D\_c} - 0.42I_{BTA12D\_c} - 0.14I_{BTA11D\_c} - 0.04I_{BTA10D\_c}$

$I_{BTA15D\_c} = I_{774.97} - 0.87I_{BTA14D\_c} - 0.42I_{BTA13D\_c} - 0.14I_{BTA12D\_c} - 0.04I_{BTA11D\_c} - 0.01I_{BTA10D\_c}$

with $I_{772.46}$, $I_{772.96}$, $I_{773.46}$, $I_{773.97}$, $I_{774.47}$ and $I_{774.97}$ the intensity at m/z = 772.46, 772.96, 773.46, 773.97, 774.47 and 774.97, respectively.

Isotope correction for **BTA-C$_{12}$-Glu** is based on the following set of equations:

$I_{BTA10D\_c} = I_{1278.83}$

$I_{BTA11D\_c} = I_{1279.83} - 0.74I_{BTA10D\_c}$

$I_{BTA12D\_c} = I_{1280.84} - 0.74I_{BTA11D\_c} - 0.31I_{BTA10D\_c}$

$I_{BTA13D\_c} = I_{1281.84} - 0.74I_{BTA12D\_c} - 0.31I_{BTA11D\_c} - 0.09I_{BTA10D\_c}$

$I_{BTA14D\_c} = I_{1282.85} - 0.74I_{BTA13D\_c} - 0.31I_{BTA12D\_c} - 0.09I_{BTA11D\_c} - 0.02I_{BTA10D\_c}$

$I_{BTA15D\_c} = I_{1283.86} - 0.74I_{BTA14D\_c} - 0.31I_{BTA13D\_c} - 0.09I_{BTA12D\_c} - 0.02I_{BTA11D\_c} - 0.005I_{BTA10D\_c}$

with $I_{1278.83}$, $I_{1279.83}$, $I_{1280.84}$, $I_{1281.84}$, $I_{1282.85}$ and $I_{1283.86}$ the intensity at m/z = 1278.83, 1279.83, 1280.84, 1281.84, 1282.85 and 1283.86 respectively.

Isotope correction for **BTA-C$_{12}$-EG$_4$-Man** is based on the following set of equations:

$I_{BTA10D\_c} = I_{915.07}$

$I_{BTA11D\_c} = I_{915.57} - 1.02_{BTA10D\_c}$

$I_{BTA12D\_c} = I_{916.07} - 1.02I_{BTA11D\_c} - 0.58I_{BTA10D\_c}$

$I_{BTA13D\_c} = I_{916.57} - 1.02I_{BTA12D\_c} - 0.58I_{BTA11D\_c} - 0.24I_{BTA10D\_c}$

$I_{BTA14D\_c} = I_{917.08} - 1.02I_{BTA13D\_c} - 0.58I_{BTA12D\_c} - 0.24I_{BTA11D\_c} - 0.08I_{BTA10D\_c}$

$I_{BTA15D\_c} = I_{917.58} - 1.02I_{BTA14D\_c} - 0.58I_{BTA13D\_c} - 0.24I_{BTA12D\_c} - 0.08I_{BTA11D\_c} - 0.02I_{BTA10D\_c}$

with $I_{915.07}$, $I_{915.57}$, $I_{916.07}$, $I_{916.57}$, $I_{917.08}$ and $I_{917.58}$ the intensity at m/z = 915.07, 915.57, 916.07, 916.57, 917.08 and 917.58 respectively.

The correction for the presence of 1 vol% H_2O can be calculated with the following set of equations for **BTA-C$_{12}$-tri-Glu**, **BTA-C$_{12}$-tri-Man**, **BTA-C$_{12}$-Glu** and **BTA-C$_{12}$-EG$_4$-Man**:

$I_{BTA10D} = I_{BTA10D\_c} - 3.21 \times 10^{-7} I_{BTA15D\_c} - 6.71 \times 10^{-3} I_{BTA12D\_c}$

$I_{BTA11D} = I_{BTA11D\_c} - 1.44 \times 10^{-5} I_{BTA15D\_c} - 1.22 \times 10^{-1} I_{BTA12D\_c}$

$I_{BTA12D} = I_{BTA12D\_c} - 4.74 \times 10^{-4} I_{BTA15D\_c} + (6.71 \times 10^{-3} + 1.22 \times 10^{-1}) I_{BTA12D\_c}$

$I_{BTA13D} = I_{BTA13D\_c} - 1.08 \times 10^{-2} I_{BTA15D\_c}$

$I_{BTA14D} = I_{BTA14D\_c} - 1.52 \times 10^{-1} I_{BTA15D\_c}$

$$I_{BTA15D} = I_{BTA15D\_c} + \left(3.21{\times}10^{-7} + 1.44{\times}10^{-5} + 4.74{\times}10^{-4} + 1.08{\times}10^{-2} + 1.52{\times}10^{-1}\right)I_{BTA15D\_c}$$

The percentage of the deuterated analogues can be calculated:

$$\%BTAnD = \frac{I_{BTAnD}}{\sum_{k=1}^{6} I_{BTAkD}} \times 100\%$$

with $\sum_{k=1}^{6} I_{BTAkD}$ the sum of all intensities. The percentage of deuterated analogues was calculated for several time points and plotted as a function of time in this chapter.

5.6.6 Details of the MD simulations

The entire simulation work was conducted using the AMBER 12 software.[52] The atomistic model for the **BTA-C$_{12}$-tri-Glu** fiber was built according to the same procedure used in works on **BTA-C$_{12}$-EG$_4$** ones.[47,48,53] The **BTA-C$_{12}$-tri-Glu** monomer was parameterized with the "general AMBER force field (GAFF)" (*gaff.dat*).[54] The initial **BTA-C$_{12}$-tri-Glu** fiber model was build starting from 48 self-assembled pre-stacked cores (configuration obtained replicating along the main fiber axis BTA core stacks previously optimized by density functional theory (DFT) calculations: intercore distance of 3.4 Å),[55] on which we mounted the extended C$_{12}$-triazole-glucose chains. The molecular model for the **BTA-C$_{12}$-tri-Glu** fiber was immersed in a periodic simulation box containing explicit TIP3P water molecules,[56] built in such a way that the **BTA-C$_{12}$-tri-Glu** fiber replicates to the infinite along the *z*-axis (main axis of the fiber) via periodic boundary conditions. As such, the molecular model replicated in space is representative of a section of the bulk of an ideal (monodisperse) **BTA-C$_{12}$-tri-Glu** fiber of infinite length in water. This initial configuration for the **BTA-C$_{12}$-tri-Glu** fiber is identical to that of **BTA-C$_{12}$-EG$_4$** fibers we simulated recently,[47,48] with the unique difference of the saccharide-functionalized side chains.

After initial minimization, the systems initially underwent 50 ps of heating MD simulation in NVT conditions (constant N: number of atoms, V: volume, and T: temperature in the system) to reach the experimental temperature of 20 °C (293 K), during which the solute was kept fixed. Following to the same simulation protocol reported recently for **BTA-C$_{12}$-EG$_4$** fibers,[48] the restraints were removed from the lateral chains, and the **BTA-C$_{12}$-tri-Glu** fiber was pre-equilibrated for other 2 ns of MD simulation in NPT conditions (constant N: number of atoms, P: pressure, and T: temperature in the system) at room temperature (T = 20 °C) and 1 atm of pressure. This phase allowed the lateral chains to pre-relax around the fiber core. Finally, all restraints were removed and the systems underwent 400 ns of MD simulation in NPT conditions at room temperature (T = 20 °C) and 1 atm of pressure. Due to the anisotropic (1D) nature of the simulated fiber models, anisotropic pressure scaling was adopted in order to allow the fiber to rearrange and fold during the MD run. In the MD, a time step of 2 femtoseconds, the Langevin thermostat, and a 10 Å cutoff were used.[47,48] The particle mesh Ewald[57] approach (PME) was used to treat the long-range electrostatics. All bonds involving hydrogen atoms were treated with the SHAKE algorithm.[58] The fiber length, the root mean square displacement (RMSD) and the fiber energy data were used to assess the equilibration of the simulated systems in the MD regime. The fiber was observed to reach the equilibrium after ~250 ns of MD (see Figure 5B). The last 100 ns of MD were considered as representative of the equilibrated **BTA-C$_{12}$-tri-Glu** fiber and were used for the analysis. The structural and hydrogen bonding analyses were conducted with the *ptraj* module of AMBER 12. The length of the fiber model was monitored directly from the box size in *z*-direction (main fiber axis).[47,48]

5.7 References

1   V. M. Dembitsky, *Chem. Biodivers.*, 2004, **1**, 673–781.
2   S. Reitsma, D. W. Slaaf, H. Vink, M. A. M. J. Van Zandvoort and M. G. A. Oude Egbrink, *Pflugers Arch. Eur. J. Physiol.*, 2007, **454**, 345–359.
3   A. Köwitsch, G. Zhou and T. Groth, *J. Tissue Eng. Regen. Med.*, 2018, **12**, 23–41.
4   J. K. Mouw, G. Ou and V. M. Weaver, *Nat. Rev. Mol. Cell Biol.*, 2014, **15**, 771–785.
5   H. J. Gabius and J. Roth, *Histochem. Cell Biol.*, 2017, **147**, 111–117.
6   M. Delbianco, P. Bharate, S. Varela-Aramburu and P. H. Seeberger, *Chem. Rev.*, 2016, **116**, 1693–1752.
7   I. Papp, J. Dernedde, S. Enders, S. B. Riese, T. C. Shiao, R. Roy and R. Haag, *ChemBioChem*, 2011, **12**, 1075–1083.
8   S. S. Lee, T. Fyrner, F. Chen, Z. Álvarez, E. Sleep, D. S. Chun, J. A. Weiner, R. W. Cook, R. D. Freshman, M. S. Schallmo, K. M. Katchko, A. D. Schneider, J. T. Smith, C. Yun, G. Singh, S. Z. Hashmi, M. T. McClendon, Z. Yu, S. R. Stock, W. K. Hsu, E. L. Hsu and S. I. Stupp, *Nat. Nanotechnol.*, 2017, **12**, 821–829.
9   M. Dong, M. G. Wessels, J. Y. Lee, L. Su, H. Wang, R. A. Letteri, Y. Song, Y. N. Lin, Y. Chen, R. Li, D. J. Pochan, A. Jayaraman and K. L. Wooley, *ACS Nano*, 2019, **13**, 5147–5162.
10   C. R. Becer, M. I. Gibson, J. Geng, R. Ilyas, R. Wallis, D. A. Mitchell and D. M. Haddleton, *J. Am. Chem. Soc.*, 2010, **132**, 15130–15132.
11   M. J. Joralemon, K. S. Murthy, E. E. Remsen, M. L. Becker and K. L. Wooley, *Biomacromolecules*, 2004, **5**, 903–913.
12   B. Bondurant, J. A. Last, T. A. Waggoner, A. Slade and D. Y. Sasaki, *Langmuir*, 2003, **19**, 1829–1837.
13   N. Nagahori, R. T. Lee, S. I. Nishimura, D. Pagé, R. Roy and Y. C. Lee, *ChemBioChem*, 2002, **3**, 836–844.
14   D. Grünstein, M. Maglinao, R. Kikkeri, M. Collot, K. Barylyuk, B. Lepenies, F. Kamena, R. Zenobi and P. H. Seeberger, *J. Am. Chem. Soc.*, 2011, **133**, 13957–13966.
15   D. Ponader, F. Wojcik, F. Beceren-Braun, J. Dernedde and L. Hartmann, *Biomacromolecules*, 2012, **13**, 1845–1852.
16   J. E. Gestwicki, C. W. Cairo, L. E. Strong, K. A. Oetjen and L. L. Kiessling, *J. Am. Chem. Soc.*, 2002, **124**, 14922–14933.
17   Y. B. Lim, S. Park, E. Lee, H. Jeong, J. H. Ryu, M. S. Lee and M. Lee, *Biomacromolecules*, 2007, **8**, 1404–1408.
18   H. O. Ham, S. H. Park, J. W. Kurutz, I. G. Szleifer and P. B. Messersmith, *J. Am. Chem. Soc.*, 2013, **135**, 13015–13022.
19   M. K. Müller and L. Brunsveld, *Angew. Chemie - Int. Ed.*, 2009, **48**, 2921–2924.
20   D. Straßburger, N. Stergiou, M. Urschbach, H. Yurugi, D. Spitzer, D. Schollmeyer, E. Schmitt and P. Besenius, *ChemBioChem*, 2018, **19**, 912–916.
21   B. S. Kim, W. Y. Yang, J. H. Ryu, Y. S. Yoo and M. Lee, *Chem. Commun.*, 2005, 2035–2037.
22   M. J. Clemente, P. Romero, J. L. Serrano, J. Fitremann and L. Oriol, *Chem. Mater.*, 2012, **24**, 3847–3858.
23   Z. Yang, G. Liang, M. Ma, A. S. Abbah, W. W. Lu and B. Xu, *Chem. Commun.*, 2007, 843–845.
24   Y. Ogawa, C. Yoshiyama and T. Kitaoka, *Langmuir*, 2012, **28**, 4404–4412.
25   P. Y. W. Dankers, M. C. Harmsen, L. A. Brouwer, M. J. A. Van Luyn and E. W. Meijer, *Nat. Mater.*, 2005, **4**, 568–574.
26   K. Petkau-Milroy, M. H. Sonntag and L. Brunsveld, *Chem. - A Eur. J.*, 2013, **19**, 10786–10793.
27   E. Krieg, M. M. C. Bastings, P. Besenius and B. Rybtchinski, *Chem. Rev.*, 2016, **116**, 2414–2477.
28   J. H. Ortony, C. J. Newcomb, J. B. Matson, L. C. Palmer, P. E. Doan, B. M. Hoffman and S. I. Stupp, *Nat. Mater.*, 2014, **13**, 812–816.
29   L. H. Beun, L. Albertazzi, D. Van Der Zwaag, R. De Vries and M. A. Cohen Stuart, *ACS Nano*, 2016, **10**, 4973–4980.
30   S. Swaminathan, C. Fowley, B. McCaughan, J. Cusido, J. F. Callan and F. M. Raymo, *J. Am. Chem. Soc.*, 2014, **136**, 7907–7913.
31   N. M. Casellas, S. Pujals, D. Bochicchio, G. M. Pavan, T. Torres, L. Albertazzi and M. García-Iglesias, *Chem. Commun.*, 2018, **54**, 4112–4115.
32   N. Zweep, A. Hopkinson, A. Meetsma, W. R. Browne, B. L. Feringa and J. H. Van Esch, *Langmuir*, 2009, **25**, 8802–8809.
33   K. Venkata Rao, D. Miyajima, A. Nihonyanagi and T. Aida, *Nat. Chem.*, 2017, **9**, 1133–1139.
34   F. Aparicio, F. García and L. Sánchez, *Chem. - A Eur. J.*, 2013, **19**, 3239–3248.

35   K. Petkau-Milroy, D. A. Uhlenheuer, A. J. H. Spiering, J. A. J. M. Vekemans and L. Brunsveld, *Chem. Sci.*, 2013, **4**, 2886.

36   X. Lou, R. P. M. Lafleur, C. M. A. Leenders, S. M. C. Schoenmakers, N. M. Matsumoto, M. B. Baker, J. L. J. van Dongen, A. R. A. Palmans and E. W. Meijer, *Nat. Commun.*, 2017, **8**, 15420.

37   X. Lou, S. M. C. Schoenmakers, J. L. J. van Dongen, M. Garcia-Iglesias, N. M. Casellas, M. Fernández-Castaño Romera, R. P. Sijbesma, E. W. Meijer and A. R. A. Palmans, *J. Polym. Sci.*, 2021, **59**, 1151–1161.

38   C. M. A. Leenders, L. Albertazzi, T. Mes, M. M. E. Koenigs, A. R. A. Palmans and E. W. Meijer, *Chem. Commun.*, 2013, **49**, 1963–1965.

39   B. N. S. Thota, X. Lou, D. Bochicchio, T. F. E. Paffen, R. P. M. Lafleur, J. L. J. van Dongen, S. Ehrmann, R. Haag, G. M. Pavan, A. R. A. Palmans and E. W. Meijer, *Angew. Chemie - Int. Ed.*, 2018, **57**, 6843–6847.

40   K. Knop, R. Hoogenboom, D. Fischer and U. S. Schubert, *Angew. Chemie - Int. Ed.*, 2010, **49**, 6288–6308.

41   C. M. A. Leenders, G. Jansen, M. M. M. Frissen, R. P. M. Lafleur, I. K. Voets, A. R. A. Palmans and E. W. Meijer, *Chem. - A Eur. J.*, 2016, **22**, 4608–4615.

42   S. I. S. Hendrikse, L. Su, T. P. Hogervorst, R. P. M. Lafleur, X. Lou, G. A. van der Marel, J. D. C. Codee and E. W. Meijer, *J. Am. Chem. Soc.*, 2019, **141**, 13877–13886.

43   J. J. Max and C. Chapados, *J. Chem. Phys.*, 2009, **131**, 184505.

44   C. M. A. Leenders, M. B. Baker, I. A. B. Pijpers, R. P. M. Lafleur, L. Albertazzi, A. R. A. Palmans and E. W. Meijer, *Soft Matter*, 2016, **12**, 2887–2893.

45   J. J. Max and C. Chapados, *J. Chem. Phys.*, 2005, **122**, 014504.

46   J. J. Max and C. Chapados, *J. Chem. Phys.*, 2003, **119**, 5632–5643.

47   M. Garzoni, M. B. Baker, C. M. A. Leenders, I. K. Voets, L. Albertazzi, A. R. A. Palmans, E. W. Meijer and G. M. Pavan, *J. Am. Chem. Soc.*, 2016, **138**, 13985–13995.

48   M. B. Baker, L. Albertazzi, I. K. Voets, C. M. A. Leenders, A. R. A. Palmans, G. M. Pavan and E. W. Meijer, *Nat. Commun.*, 2015, **6**, 6234.

49   G. Morgese, B. F. M. Waal, S. Varela-Aramburu, A. R. A. Palmans, L. Albertazzi and E. W. Meijer, *Angew. Chemie*, 2020, **132**, 17382–17386.

50   S. Ehrmann, 2019.

51   L. Albertazzi, F. J. Martinez-Veracoechea, C. M. A. Leenders, I. K. Voets, D. Frenkel and E. W. Meijer, *Proc. Natl. Acad. Sci.*, 2013, **110**, 12203–12208.

52   R. D.A. Case, T.A. Darden, T.E. Cheatham, III, C.L. Simmerling, J. Wang, R.E. Duke, G. S. Luo, R.C. Walker, W. Zhang, K.M. Merz, B. Roberts, S. Hayik, A. Roitberg, J. L. J. Swails, A.W. Götz, I. Kolossváry, K.F. Wong, F. Paesani, J. Vanicek, R.M. Wolf, G. X. Wu, S.R. Brozell, T. Steinbrecher, H. Gohlke, Q. Cai, X. Ye, J. Wang, M.-J. Hsieh and P. A. K. Cui, D.R. Roe, D.H. Mathews, M.G. Seetin, R. Salomon-Ferrer, C. Sagui, V. Babin, T. Luchko, S. Gusarov, A. Kovalenko, *AMBER 12*, 2012, University of California, San Francisco.

53   D. Bochicchio, M. Salvalaglio and G. M. Pavan, *Nat. Commun.*, 2017, **8**, 147.

54   J. M. Wang, R. M. Wolf, J. W. Caldwell, P. a Kollman and D. a Case, *J. Comput. Chem.*, 2004, **25**, 1157–1174.

55   I. A. W. Filot, A. R. A. Palmans, P. A. J. Hilbers, R. A. Van Santen, E. A. Pidko and T. F. A. De Greef, *J. Phys. Chem. B*, 2010, **114**, 13667–13674.

56   W. L. Jorgensen, J. Chandrasekhar, J. D. Madura, R. W. Impey, M. L. Klein, *J. Chem. Phys.,* 1983, **79**, 926-935.

57   T. Darden, D. York and L. Pedersen, *J. Chem. Phys.*, 1993, **98**, 10089–10092.

58   V. Kräutler, W. F. Van Gunsteren and P. H. Hünenberger, *J. Comput. Chem.*, 2001, **22**, 501–508.

Chapter 6

Facilitating Functionalization of Benzene-1,3,5-Tricarboxamides by Switching Amide Connectivity

Abstract: Synthetic water-compatible supramolecular polymers based on benzene-1,3,5-tricarboxamides (BTAs) have attracted a lot of interest in recent years, as they are uniquely suited to generate functional multicomponent biomaterials. Their morphology and intrinsic dynamic behavior mimic fibrous structures found in nature. Moreover, their modularity allows to control the density of functionalities presented on the surface of the fibers when using functionalized BTA monomers. However, such moieties generally comprise a functionality on only one of three side chains, resulting in lengthy synthetic protocols and limited yields. In this work, we avert the need for desymmetrization of the core by starting from commercially available 5-aminoisophthalic acid. This approach eliminates the statistical reactions and reduces the number of synthetic steps. It also leads to the inversion of the connectivity of one of the amides to the benzene core. It is confirmed that the inversed amide BTAs (iBTAs) form intermolecular hydrogen bonds and assemble into supramolecular polymers, like previously used symmetrical BTAs, albeit with a slight decrease in water-solubility. Solubility problems were overcome by incorporating iBTAs into conventional BTA-based supramolecular polymers. These two-component mixtures formed supramolecular fibers with a morphology and dynamic behavior identical to BTA-homopolymers. Finally, iBTAs were decorated with a fluorescent dye to demonstrate the synthesis of functional monomers, and to visualize their co-assembly with BTAs. Our results show that functionality can be introduced into supramolecular polymers with monomers that slightly differ in their core structure while maintaining the structure and dynamics of the fibers.
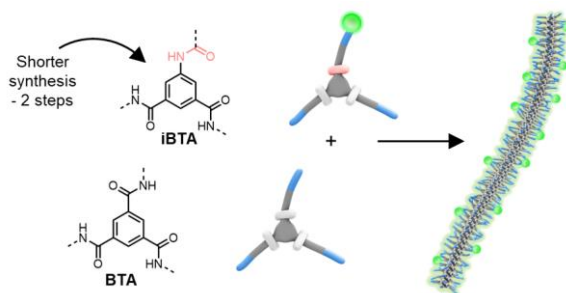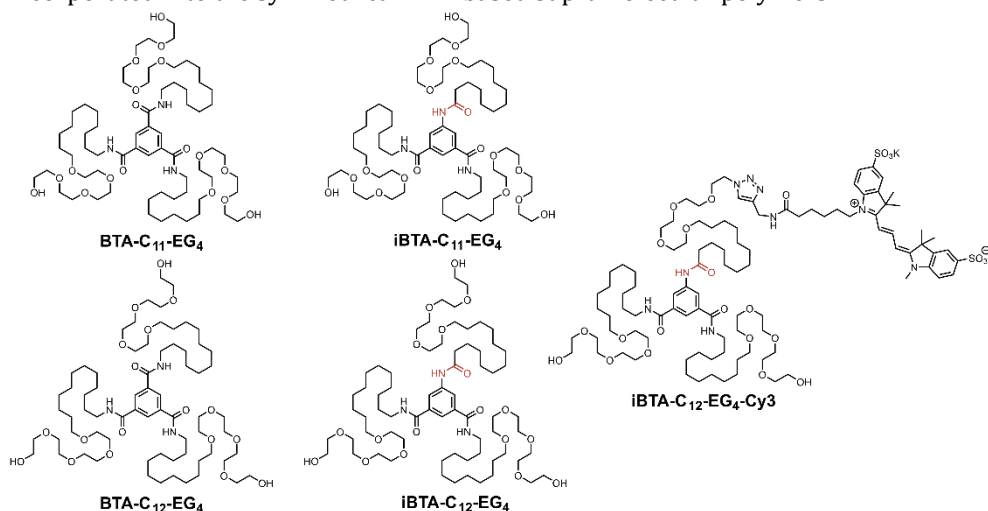
6.1 Introduction

Synthetic water-compatible supramolecular polymers have recently emerged as potential biomaterials since they can easily be decorated with functional moieties.[1,2] The use of non-covalent interactions allows to control the number of biological recognition motifs presented on the supramolecular structures by mixing in different functional monomers in the desired ratio.[3,4] This modular approach has been applied in, for example, supramolecular polymers formed by peptide amphiphiles to create scaffolds for cartilage[5] and bone regeneration,[6] for targeted therapy for atherosclerosis[7] and for the promotion of angiogenesis.[8] The dynamics of multicomponent supramolecular polymers based on ureidopyrimidinones (UPys) can be tuned by mixing mono- and bivalent variants.[9] Both types of monomers have been functionalized with charged end groups for the intracellular delivery of siRNA[10] and with peptides to make the polymers suitable for cell adhesion.[11] Additionally, the periphery of various columnar structures formed by discotic molecules were decorated with carbohydrates to trigger cellular uptake[12,13] and with biotin to create a fibrous scaffold for protein binding.[14,15]

The self-assembly of discotic benzene-1,3,5-tricarboxamides (BTAs) into supramolecular polymers has been studied extensively in recent years.[16] The amides can be connected to the benzene ring *via* the carbonyl group or *via* the nitrogen atom, yielding *C*-centered and *N*-centered BTAs, respectively. Although both variants self-assemble in organic media, the aggregation and hydrogen bonding was weaker in case of *N*-centered BTAs.[17,18] *C*-Centered BTAs have been modified to be water-compatible by decorating the core amides with a hydrophobic chain of at least eleven carbon atoms to protect the intermolecular hydrogen bonds from interaction with the solvent.[19,20] Water-solubility was ensured by a tetra(ethylene glycol) periphery (see **BTA-C$_{11}$-EG$_4$** and **BTA-C$_{12}$-EG$_4$**, Figure 1).[19,20] The micrometer long supramolecular fibers that were formed in water were found to be highly dynamic[21,22] and the dynamic exchange of monomers between supramolecular polymers could be tuned by modification of the hydrophilic/hydrophobic balance of the monomers[21] or by co-assembling structurally different monomers.[23] Recently, these BTA-based supramolecular polymers have been functionalized with benzoxaborole to interact with red blood cells,[24] with charged groups for the intracellular delivery of siRNA,[25] with carbohydrates for binding to lectins[26] and with DNA for protein recruitment.[27] These examples illustrate the potential use of BTA-based polymers to access sophisticated biomaterials.

Linear peptide amphiphiles and UPy monomers generally contain only one side that is suitable for functionalization, whereas the discotic molecules comprise a *C$_3$*-symmetrical core containing three equally reactive sites for the attachment of functional groups. As it is often favorable to use monovalent monomers to prevent solubility issues and unfavorable steric effects,[24,28] this inherently introduces lengthy synthesis protocols for the desymmetrization of the monomers, often affording limited

yields. For *C*-centered BTAs, this involves the statistical deprotection of a trimethyl 1,3,5-benzenecarboxylate core, creating multiple products which limits the yield.[29] A strategy to circumvent statistical reactions and to introduce only one different side chain onto the core is to start from a C_2-symmetrical core.[30–37] The group of Bouteiller synthesized *N*-substituted benzene-1-urea-3,5-biscarboxamide (BUBA) monomers with a significantly enhanced yield, starting from a commercially available dimethyl 5-aminoisophthalate core.[38] The BUBA molecules showed cooperative self-assembly into long helices in organic media, similar to BTAs. Despite the altered hydrogen-bonding ability of the urea moieties compared to the amides, the BUBA molecules were readily incorporated into the symmetrical BTA-based supramolecular polymers.

Figure 1. Chemical structures of **BTA-C$_{11}$-EG$_4$**, **iBTA-C$_{11}$-EG$_4$**, **BTA-C$_{12}$-EG$_4$**, **iBTA-C$_{12}$-EG$_4$** and **iBTA-C$_{12}$-EG$_4$-Cy3**. The inversed amide bonds are indicated in red.

Inspired by the work of Bouteiller *et al*,[38] we here selectively introduce function onto water-compatible BTAs by starting from a C_2-symmetrical 5-aminoisophthalic acid or dimethyl 5-aminoisophthalate core. This affords a BTA core with the connectivity of one of the amides inverted from *C*-centered to *N*-centered, which we refer to as iBTA. First, we evaluate if this single inversion of the amide connectivity affects the supramolecular self-assembly behavior by synthesizing two unfunctionalized iBTAs that are atomically identical to their C_3-symmetrical counterparts. The aqueous self-assembly of iBTAs with undecyl (**iBTA-C$_{11}$-EG$_4$**, Figure 1) and dodecyl aliphatic chains (**iBTA-C$_{12}$-EG$_4$**, Figure 1) is compared to their *C*-centered counterparts using spectroscopy, static light scattering (SLS), cryogenic transmission electron microscopy (cryoTEM) and hydrogen/deuterium exchange followed by mass spectrometry (HDX-MS). Furthermore, we explore the incorporation of iBTAs into supramolecular polymers of BTAs. Finally, we report the synthesis of iBTA functionalized with a cyanine dye (**iBTA-C$_{12}$-E$_4$-Cy3**, Figure 1) and visualize its co-assembly with a completely *C*-centered BTA

using stochastic optical reconstruction microscopy (STORM).[39–43] High resolution microscopy images show that the synthetically easily accessible iBTAs can indeed be used for the introduction of function into BTA-based supramolecular polymers.

6.2 Design and synthesis of iBTAs

The synthesis of the iBTAs, performed by ir. Bart van den Bersselaar, requires side chains comprising either an amine or a carboxylic acid group for coupling to the core. Amine-terminated side chains were synthesized based on optimized literature procedures.[19] For the carboxylic acid-terminated chains a new synthetic procedure was developed (see section 6.7.3). Herein, a carboxylic acid is protected with a *tert*-butyl group to limit transesterification reactions. A subsequent Williamson ether synthesis with tetra(ethylene glycol) and deprotection of the carboxylic acid yields the desired side chain. The desired iBTAs can be obtained *via* two pathways, which are demonstrated in the synthesis of both **iBTA-C$_{11}$-EG$_4$** and **iBTA-C$_{12}$-EG$_4$**. **iBTA-C$_{11}$-EG$_4$** was synthesized by first attaching the carboxylic acid terminated side chain to dimethyl 5-aminobenzene-1,3-dicarboxylate (see section 6.7.3). After hydrolysis of the methyl esters, the diacid was reacted with the amine terminated side chains, yielding pure **iBTA-C$_{11}$-EG$_4$** as confirmed by ^{1}H and ^{13}C NMR, FT-IR and LC-MS. In the second pathway for the synthesis of **iBTA-C$_{12}$-EG$_4$** (Scheme 1), the amine terminated side chains were attached first to 5-aminobenzene-1,3-dicarboxylic acid after activation of the carboxylic acids using thionyl chloride. The resulting intermediate **1** was stable under argon atmosphere in the fridge. For **iBTA-C$_{12}$-EG$_4$** the synthesis was continued by coupling of the carboxylic acid terminated side chain to **1** resulted in a benzyl protected iBTA **2** which, after hydrogenation, yielded **iBTA-C$_{12}$-EG$_4$** in high purity as confirmed by ^{1}H and ^{13}C NMR, FT-IR and LC-MS.

We selected a peripheral azide moiety to introduce a functional group onto the iBTA scaffold, as this allows to directly attach different types of functionalities *via* Cu(I)-catalyzed azide-alkyne cycloaddition or *via* a Staudinger reduction of the azide to yield a reactive primary amine. The carboxylic acid-terminated side chain was therefore equipped with an azide-derivative of tetra(ethylene glycol) that was synthesized according to a literature procedure.[44] The azide group in the periphery required a minor adaptation of the synthetic route, since azides are known to form side products in a catalytic hydrogenation due to imine formation.[45] Although ammonia can be added to prevent the formation of the intermediate, the catalytic hydrogenation is also effectively hindered by this addition.[46] Therefore, **1** was catalytically hydrogenated to **3** prior to the introduction of the azide-decorated side chain (Scheme 1). The azide-decorated **iBTA-C$_{12}$-EG$_4$-N$_3$** (**4**) was obtained in high purity as confirmed by ^{1}H and ^{13}C NMR, FT-IR and LC-MS. Finally, **iBTA-C$_{12}$-EG$_4$-N$_3$** was reacted with an alkyne functionalized Sulfo-Cy3-dye in a Cu(I)-catalyzed azide-alkyne cycloaddition reaction to yield **iBTA-C$_{12}$-EG$_4$-Cy3** as confirmed by LC-MS.
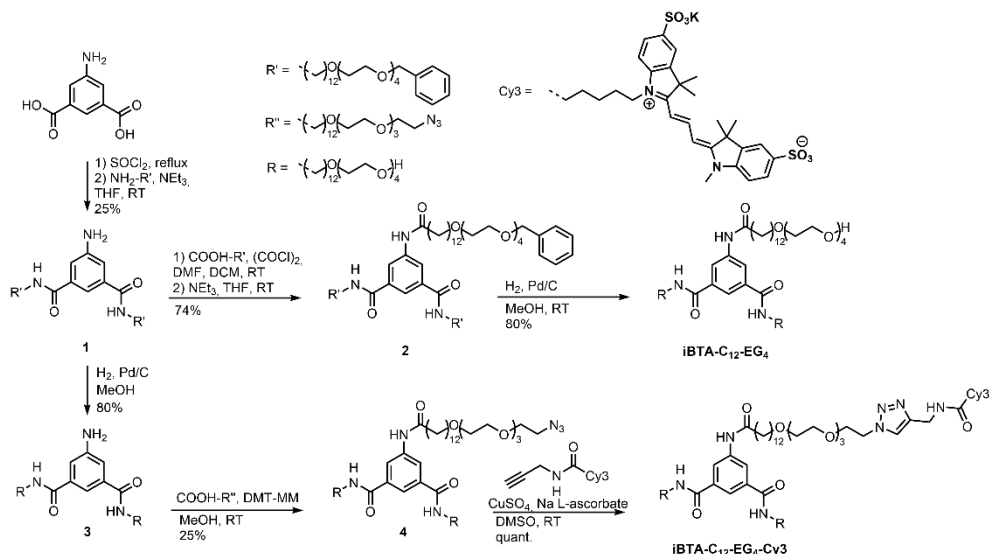
Scheme 1. Synthesis of **iBTA-C₁₂-EG₄** and **iBTA-C₁₂-EG₄-Cy3**.

6.3 Supramolecular polymerization of BTAs with inversed amides

We applied a previously optimized sample preparation protocol to assess the self-assembly of the newly synthesized iBTA monomers into supramolecular polymers.[21] Using this protocol, a clear solution was obtained for **iBTA-C₁₁-EG₄** after overnight equilibration but the sample with **iBTA-C₁₂-EG₄** was turbid, indicating that the material did not completely dissolve. To compensate for the decreased water-solubility of **iBTA-C₁₂-EG₄**, the compound was injected into water from a concentrated stock solution in acetonitrile (ACN), followed by controlled heating and cooling of the sample as described before. A final concentration of 10 vol% of ACN in water was required to obtain samples that did not show any scattering. This mixture of water with 10% ACN is hereafter denoted as water*.

The self-assembly of the iBTAs in aqueous media was first studied with UV spectroscopy. We previously established that **BTA-C₁₁-EG₄** and **BTA-C₁₂-EG₄** form micrometer long supramolecular polymers in water, with characteristic absorbance bands at 211 and 226 nm (Figure 2A-B). In contrast, the UV spectra of iBTAs are red shifted, with **iBTA-C₁₁-EG₄** showing a maximum at 237 nm and **iBTA-C₁₂-EG₄** at 230 nm. Both spectra also contain a shoulder around 268 nm and a broad band of low intensity between 290-310 nm. The spectra of both iBTA in aqueous media differ significantly compared to those in pure ACN, a solvent in which they are molecularly dissolved. This indicates that **iBTA-C₁₁-EG₄** and **iBTA-C₁₂-EG₄** self-assemble in water and water*, respectively. The small difference in the position of the maximum between **iBTA-C₁₁-EG₄** and **iBTA-C₁₂-EG₄** probably results from the presence of 10% ACN in the

latter, which may affect the propensity to form intermolecular hydrogen bonds.[47] The broad band between 290-310 nm has previously been observed for symmetrical *N*-centered BTAs in organic media[17] and is connected to the switch in connectivity of one amide bond. The spectra of the iBTAs differ both in shape and intensity compared to their symmetrical BTA counterparts, which suggests that the inversion of one of the amides may affect the packing of the hydrogen bonds.
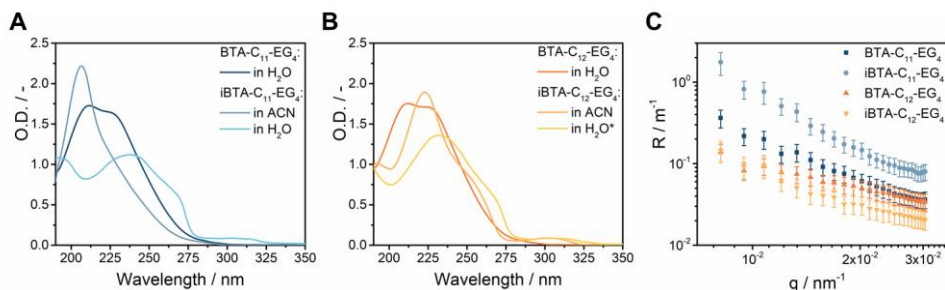
Figure 2. (A) UV spectra of **BTA-C$_{11}$-EG$_4$** in water and **iBTA-C$_{11}$-EG$_4$** in ACN and water (c = 500 µM, l = 1 mm, T = 20°C). (B) UV spectra of **BTA-C$_{12}$-EG$_4$** in water and **iBTA-C$_{12}$-EG$_4$** in ACN and water* (c = 500 µM, l = 1 mm, T = 20°C). (C) Rayleigh ratio as a function of the scattering vector for **BTA-C$_{11}$-EG$_4$**, **iBTA-C$_{11}$-EG$_4$** and **BTA-C$_{12}$-EG$_4$** in water and of **iBTA-C$_{12}$-EG$_4$** in water* (c = 500 µM, l = 1 cm, λ = 532 nm, T = 20 °C).

To study the morphologies formed by **iBTA-C$_{11}$-EG$_4$** and **iBTA-C$_{12}$-EG$_4$** in water and water*, respectively, SLS and cryoTEM measurements were performed and compared to those of the symmetrical counterparts. Like **BTA-C$_{11}$-EG$_4$** and **BTA-C$_{12}$-EG$_4$**, **iBTA-C$_{11}$-EG$_4$** and **iBTA-C$_{12}$-EG$_4$** show an angular dependence of the Rayleigh ratio, that is typical for the presence of long, elongated structures (Figure 2C). Although there slopes are similar, the Rayleigh ratio was slightly increased for **iBTA-C$_{11}$-EG$_4$** compared to **iBTA-C$_{12}$-EG$_4$**. These findings suggest that iBTAs form elongated structures with a similar anisotropy as their symmetrical counterparts, but they differ in size. CryoTEM was therefore used to visualize the morphologies of the iBTAs. The cryoTEM image of **iBTA-C$_{11}$-EG$_4$** shows fibers of several micrometers in length (Figure 3A) whereas the image of **iBTA-C$_{12}$-EG$_4$** shows fibers of various lengths, mainly below one micrometer (Figure 3C). There are, however, subtle differences compared to the morphologies formed by symmetrical BTAs. Both *C*-centered BTAs assemble into micrometer long supramolecular polymers and for **BTA-C$_{12}$-EG$_4$** a double helix structure was recently revealed with high magnification cryoTEM and image reconstruction,[48] whereas such a strand separation is absent in **BTA-C$_{11}$-EG$_4$** (Chapter 2). **iBTA-C$_{11}$-EG$_4$** also lacks the strand separation of a double helix structure (Figure 3B) whereas in the case of **iBTA-C$_{12}$-EG$_4$** only a fraction of the fibers shows strand separation that may indicate the presence of a double helix (Figure 3D). From these results, we conclude that **iBTA-C$_{11}$-EG$_4$** forms fibers of similar morphology as **BTA-C$_{11}$-EG$_4$**, and **iBTA-C$_{12}$-EG$_4$** forms fibers that are slightly altered in length and secondary structure compared to **BTA-C$_{12}$-EG$_4$**.

Previous result indicate that the decrease in length does not originate from the presence of ACN[47] and is therefore a result of the amide bond inversion.
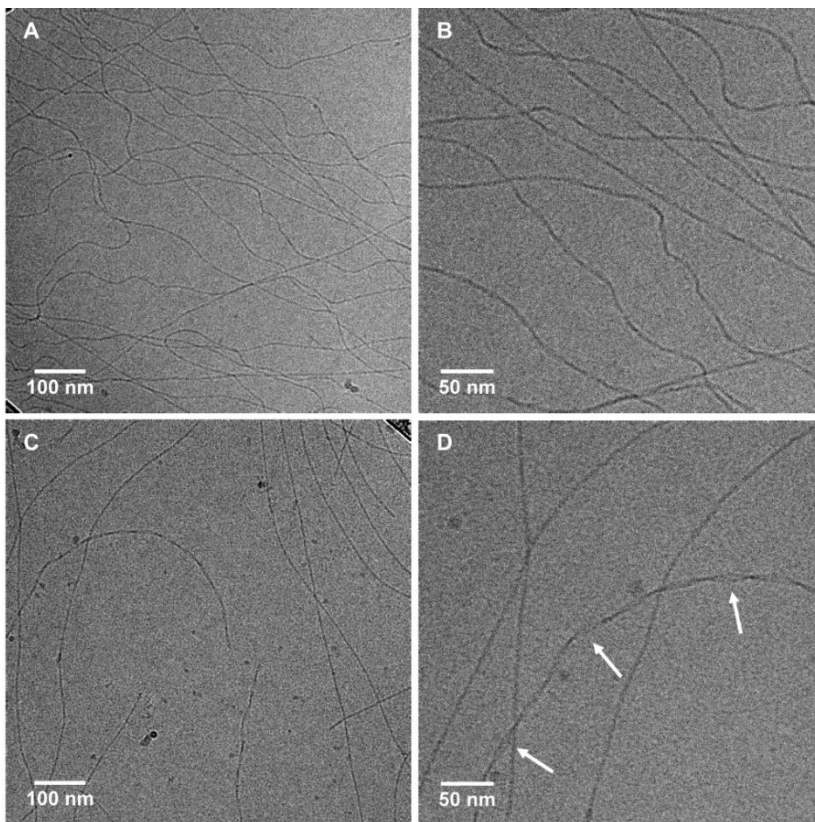
Figure 3. (A-B) CryoTEM images of **iBTA-C$_{11}$-EG$_4$** in water at different magnifications (c = 500 μM). (C-D) CryoTEM images of **iBTA-C$_{12}$-EG$_4$** in water* at different magnifications. (c = 500 μM). Strand separation is indicated with white arrows. Dark objects are spherical ice particles.

The presence of intermolecular hydrogen bonds in solution was studied with FT-IR spectroscopy. Deuterated solvents were used to prevent overlap of the O-H vibrations from the solvent with the amide vibrations of the BTAs.[49] The C_3-symmetrical BTAs show an amide I vibration (C=O stretch) at 1648 cm^{-1} in the molecularly dissolved state and a vibration at 1635 cm^{-1} when intermolecular hydrogen bonds are present.[20] In the molecularly dissolved state, the amide I vibration of **iBTA-C$_{11}$-EG$_4$** and **iBTA-C$_{12}$-EG$_4$** is positioned at 1642 cm^{-1} and 1643 cm^{-1}, respectively, with a shoulder around 1670 cm^{-1}. The amide I vibration of both iBTAs is found at 1628 cm^{-1} after self-assembly and the shoulder shifted to 1667 cm^{-1} (Figure 4). This shift of the amide I vibration to lower wavenumbers after self-assembly is indicative for the formation of intermolecular hydrogen bonds. The split of the amide I vibration in case of the iBTAs could arise from the different connectivity of one of the amides in the iBTAs. Although the FT-IR spectra

of iBTAs are similar, they are shifted towards lower wavenumbers compared to the BTAs, suggesting a different hydrogen bond pattern and strength.
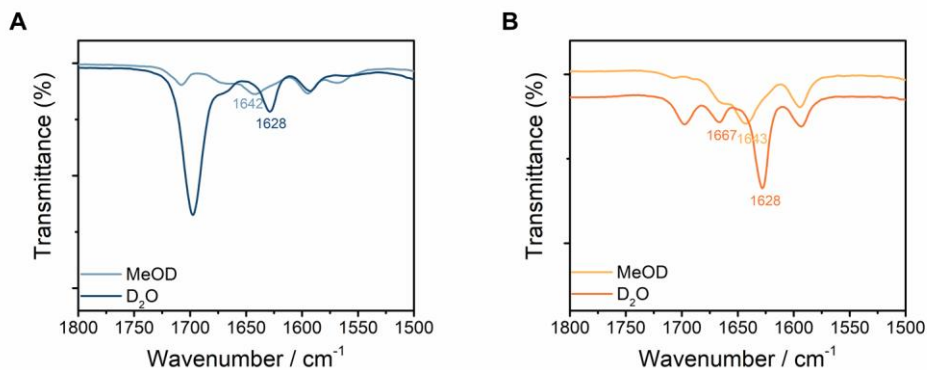
Figure 4. Zoom of the FT-IR spectrum of the amide I vibration of (A) **iBTA-C₁₁-EG₄** and (B) **iBTA-C₁₂-EG₄** in MeOD and D₂O (c = 20 mg/mL, l = 0.05 mm, T = room temperature, 10% of ACN-d₃ was present in the sample of **iBTA-C₁₂-EG₄**). The vibrations at 1708 cm⁻¹ in MeOD[50] and 1697 cm⁻¹ in D₂O[51] originate from the C=O vibration of acetone which was used to clean the cuvette.

Taken all together, the above results show that iBTAs form a primary supramolecular structure that is similar to that formed by symmetrical BTAs. Long, elongated fibers stabilized by intermolecular hydrogen bonds are formed in aqueous media. The morphologies of iBTAs differ in secondary structure from the well-studied **BTA-C₁₂-EG₄** in the sense that strand separation due to a double helix structure are absent in **iBTA-C₁₁-EG₄** and less pronounced in **iBTA-C₁₂-EG₄**. This may affect the exchange dynamics of monomers between polymers.

To assess the exchange dynamics of iBTAs, HDX-MS was measured. With this technique, the exchange of labile hydrogen atoms to deuterium atoms is followed over time after dilution of aqueous samples into D₂O (see Chapter 3).[21,22] The three outer hydroxyl hydrogen atoms of BTAs and iBTAs are in direct contact with the solvent and will exchange immediately to deuterium atoms. The three amide hydrogen atoms are contained in the hydrophobic pocket and form hydrogen bonds. As a result, their H/D exchange will mainly occur when the monomers move between polymers and are released into the surrounding D₂O. HDX-MS is therefore a powerful tool to elucidate the rate of monomer exchange between polymers and permits to evaluate if the change in amide connectivity affects the exchange dynamics of the supramolecular polymers.

After confirming that the nature of the supramolecular polymers does not change upon dilution, all samples were 100-fold diluted into D₂O without ACN and the percentage of deuterated analogues was followed over time. The H/D exchange of **BTA-C₁₂-EG₄** is described in Chapter 3. The decrease of the aliphatic chain length in case of **BTA-C₁₁-EG₄** results in more H/D exchange of the amide hydrogen atoms and no indications of partly deuteration due to solvent penetration is observed (Figure 5A).

Likewise, solvent penetration seems to be absent in case of **iBTA-C$_{11}$-EG$_4$** (Figure 5B). The H/D exchange of the amide hydrogen atoms is fast in the first hours, but significantly slows down. For **iBTA-C$_{12}$-EG$_4$** a similar fast H/D exchange is observed (Figure 5C), but the H/D exchange in the first hour is slightly governed by a solvent penetration mechanism, similar to **BTA-C$_{12}$-EG$_4$**.
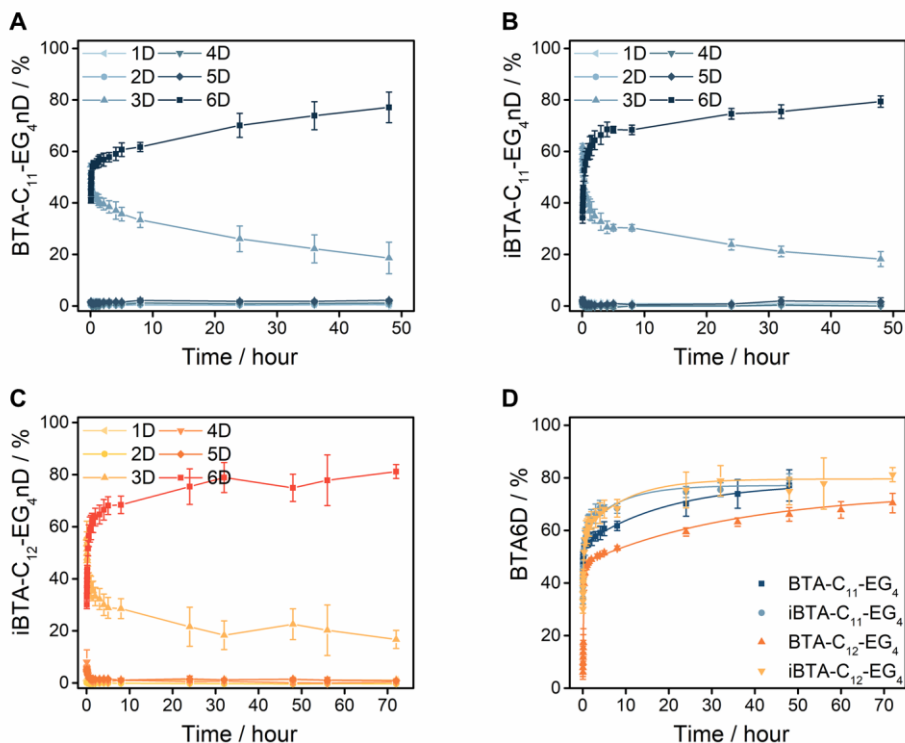
Figure 5. (A-C) The percentage of different deuterated analogues of (A) **BTA-C$_{11}$-EG$_4$**, (B) **iBTA-C$_{11}$-EG$_4$** and (C) **iBTA-C$_{12}$-EG$_4$** as a function of time after the 100x dilution of an aqueous 500 µM sample into D$_2$O (T = room temperature, 10% ACN was present in the sample of **iBTA-C$_{12}$-EG$_4$** before dilution). (D) The percentage of fully deuterated **BTA-C$_{11}$-EG$_4$**, **iBTA-C$_{11}$-EG$_4$**, **BTA-C$_{12}$-EG$_4$** and **iBTA-C$_{12}$-EG$_4$** as a function of time after the 100x dilution of 500 µM aqueous samples into D$_2$O (T = room temperature, 10% ACN was present in the sample of **iBTA-C$_{12}$-EG$_4$**). The symbols represent the average and the error bars the standard deviation calculated from three independent measurements. The lines in D represent a bi-exponential growth function.

The percentage of fully deuterated molecules can be used to compare the exchange dynamics between the different BTAs and iBTAs. In all cases, a fast increase of deuteration to BTA6D is observed in the first hour, followed by a more gradual increase (Figure 5D). At the first measurement point, 34% of **iBTA-C$_{11}$-EG$_4$** is fully deuterated, whereas this is 41% for **BTA-C$_{12}$-EG$_4$**. This indicates the presence of less ill-defined structure in the sample of the iBTA. **iBTA-C$_{11}$-EG$_4$** shows more exchange than **BTA-C$_{11}$-EG$_4$** in the first hour, but the percentage of fully deuterated molecules is almost the same

after 24 hours. After 48 hours, 77% of the **BTA-C₁₁-EG₄** polymers is fully deuterated and 79% of the **iBTA-C₁₁-EG₄** molecules. For **iBTA-C₁₂-EG₄** 31% of the molecules is fully deuterated after 3 minutes, whereas this is almost negligible for the BTA. This indicates that there are more defects in the sample of **iBTA-C₁₂-EG₄**. The exchange of the molecules with dodecyl chains was followed for 72 hours such that 70% of **BTA-C₁₂-EG₄** and 81% of **iBTA-C₁₂-EG₄** is fully deuterated. The percentage of fully deuterated molecules is higher for **iBTA-C₁₂-EG₄** than for **BTA-C₁₂-EG₄** over the whole period measured. This could indicate that the inversion of the amide bond increases the exchange dynamics, but it could also be an effect of the small percentage of ACN still present after the preparation of the sample.[47]

6.4 Supramolecular copolymerization of BTAs and iBTAs

The iBTAs have been designed to incorporate functional monomers into supramolecular polymers of BTAs, which requires the co-assembly of BTAs and iBTAs. To evaluate the ability of the molecules to copolymerize, samples of **BTA-C₁₂-EG₄** with several percentages of **iBTA-C₁₂-EG₄** were prepared. **BTA-C₁₂-EG₄** and **iBTA-C₁₂-EG₄** were mixed in the solid state before dissolving in water and applying the heating-cooling protocol as described before. ACN was not required to obtain homogeneous samples, since **BTA-C₁₂-EG₄** helps to solubilize **iBTA-C₁₂-EG₄**, indicating their possible copolymerization. UV spectra of mixtures at a concentration of 500 µM do not show any changes in the absorption bands up to 10% of **iBTA-C₁₂-EG₄** (Figure 6A). At higher percentages of iBTA, a change in the absorption spectra is observed but the spectra never overlap with those of self-sorted systems, suggesting an interaction between **BTA-C₁₂-EG₄** and **iBTA-C₁₂-EG₄**. The formation of supramolecular copolymers of **BTA-C₁₂-EG₄** and **iBTA-C₁₂-EG₄** was further corroborated with SLS (Figure 6B), which reveals the presence of structures of similar dimensions as **BTA-C₁₂-EG₄** polymers.
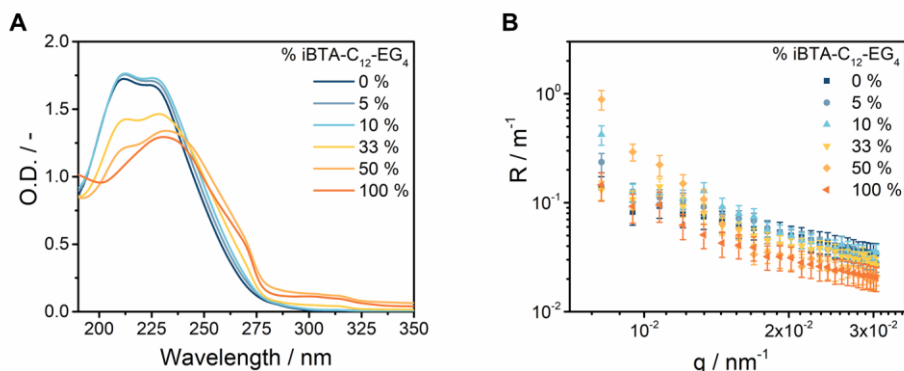
Figure 6. UV spectra of mixtures of **BTA-C₁₂-EG₄** and **iBTA-C₁₂-EG₄** in different ratios in water (c = 500 µM, l = 1 mm, T = 20 °C). (B) Rayleigh ratio of mixtures of **BTA-C₁₂-EG₄** and **iBTA-C₁₂-EG₄** in different ratios as a function of the scattering vector in water (c = 500 µM, l = 1 cm, λ = 532 nm, T = 20 °C).

Biomedical applications generally require only a fraction of the monomers within the supramolecular polymers to be functionalized.[24,28] We therefore focus on the supramolecular copolymers containing a maximum of 10% of **iBTA-C$_{12}$-EG$_4$**. CryoTEM images verified the formation of the supramolecular copolymers upon mixing **BTA-C$_{12}$-EG$_4$** with 10% **iBTA-C$_{12}$-EG$_4$** (Figure 7). The copolymers are micrometers long and contain the double helix secondary structure as previously observed for **BTA-C$_{12}$-EG$_4$**.[48]
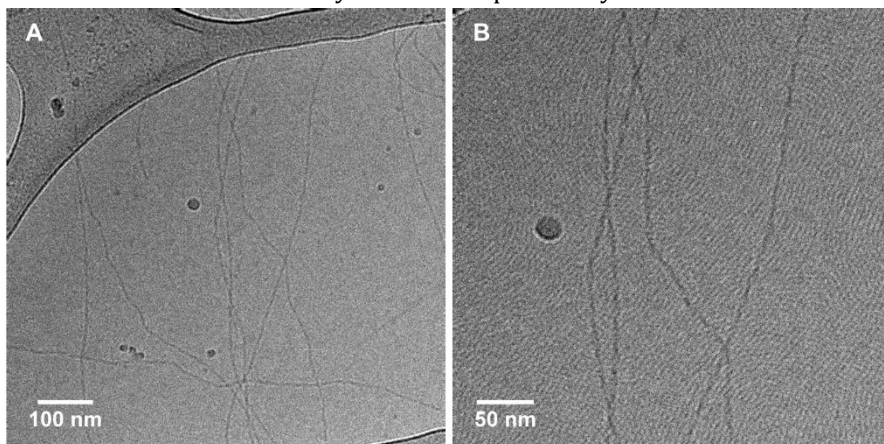
Figure 7. CryoTEM images at different magnifications of the mixture of **BTA-C$_{12}$-EG$_4$** with 10% **iBTA-C$_{12}$-EG$_4$** in water (c = 500 µM). The dark spherical objects are crystalline ice particles.

HDX-MS could not be used to characterize the dynamics of the individual components in the **BTA-C$_{12}$-EG$_4$** mixture with 10% **iBTA-C$_{12}$-EG$_4$** since they comprise the same molecular mass. Nevertheless, the percentage of the deuterated analogs combined still provides information on the monomer exchange dynamics of the copolymers (Figure 8A). The faster exchange of the homopolymers of **iBTA-C$_{12}$-EG$_4$** cannot be observed anymore, indicating that **BTA-C$_{12}$-EG$_4$** and **iBTA-C$_{12}$-EG$_4$** are indeed interacting. Instead, a H/D exchange profile that resembles the features of **BTA-C$_{12}$-EG$_4$** can be observed. In addition, these experiments revealed that the exchange dynamics of the copolymer match with those of the homopolymer of **BTA-C$_{12}$-EG$_4$** (Figure 8B). From these results, we conclude that the structure and dynamics of **BTA-C$_{12}$-EG$_4$** supramolecular polymers are not altered by the incorporation of a small percentage of **iBTA-C$_{12}$-EG$_4$**.
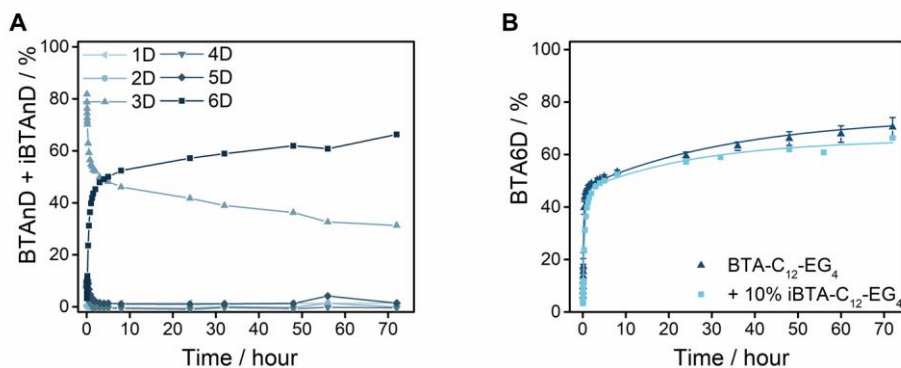
Figure 8. (A) The percentage of different deuterated analogous of the mixture of **BTA-C$_{12}$-EG$_4$** with 10% **iBTA-C$_{12}$-EG$_4$** as a function of time after the 100x dilution of an aqueous 500 µM sample into D$_2$O (T = room temperature). (B). The percentage of fully deuterated molecules for the homopolymer of **BTA-C$_{12}$-EG$_4$** and its mixture with 10% **iBTA-C$_{12}$-EG$_4$**. The symbols represent the measured value from one experiment. The lines in B represent a bi-exponential growth function.

6.5 Introducing functionalized iBTAs into BTA-based supramolecular polymers

The aforementioned spectroscopic and microscopic experiments confirmed the insignificant changes in structure and monomeric packing upon mixing of BTAs and iBTAs. Although these experiments suggest copolymerization, STORM was used by dr. Shikha Dhiman to obtain visual evidence for the incorporation of iBTA monomers into **BTA-C$_{12}$-EG$_4$** fibers. For this, an iBTA was functionalized with the fluorescent dye sulfo-Cy3 (**iBTA-C$_{12}$-EG$_4$-Cy3**). A sample was prepared of supramolecular copolymers based on **BTA-C$_{12}$-EG$_4$** with 10% **iBTA-C$_{12}$-EG$_4$-Cy3** incorporated. Additionally, 5% **BTA-C$_{12}$-EG$_4$-Cy5** was added for visualization of the polymers of **BTA-C$_{12}$-EG$_4$** to confirm that the dye-labelled iBTAs co-assemble with **BTA-C$_{12}$-EG$_4$** polymers and to rule out self-sorting of the iBTAs (see Figure 9A chemical structures relevant to this experiment). The sample was equilibrated for several days, diluted into phosphate buffered saline (PBS) and adsorbed on a coverslip. Dual channel imaging was performed by simultaneous excitation of Cy3 (green) and Cy5 (red). Super resolution STORM imaging reveals micrometer long supramolecular polymers that contain both Cy3- and Cy5-labeled monomers (Figure 9B), thereby confirming that the functionalized iBTA is present within the supramolecular polymers of **BTA-C$_{12}$-EG$_4$**. **iBTA-C$_{12}$-Cy3** can be observed throughout the whole length of the supramolecular polymer, indicating that there is no preference for the incorporation of iBTAs to the end of the polymers. However, the copolymers appear to have a blocky structure. Future experiments are required to elucidate the type of copolymer formed by **BTA-C$_{12}$-EG$_4$** and **iBTA-C$_{12}$-EG$_4$**.
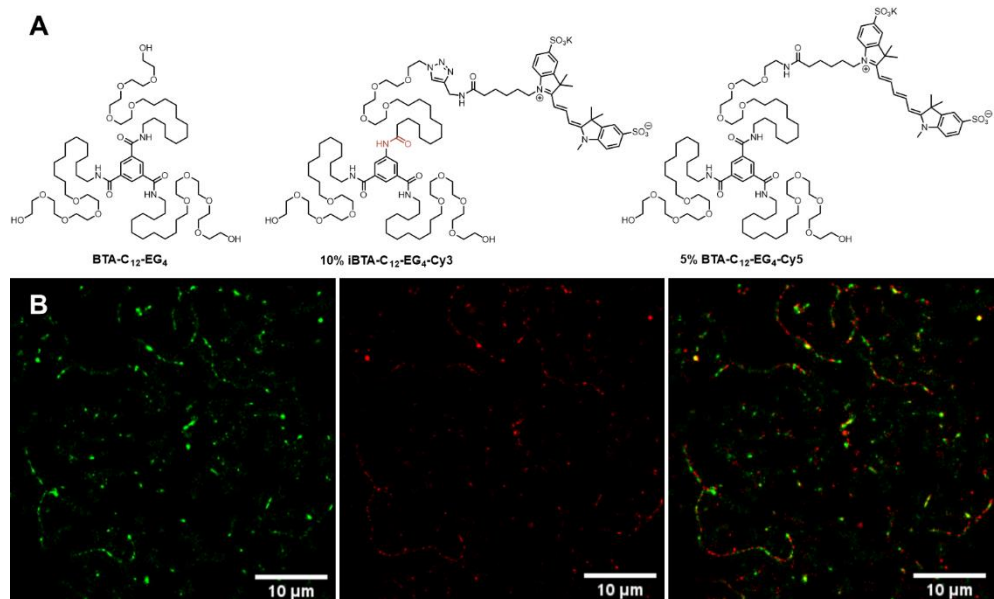
Figure 9. STORM experiment of a BTA polymer functionalized with iBTA. (A) Chemical structures of the components used in this experiment. A polymer of **BTA-C$_{12}$-EG$_4$** was mixed with 10% **iBTA-C$_{12}$-EG$_4$-Cy3** and 5% **BTA-C$_{12}$-EG$_4$-Cy5**. (B) STORM image of **BTA-C$_{12}$-EG$_4$** mixed with dye-functionalized iBTA and BTA. The separate Cy3 (λ_{ex} = 561 nm, green colour) and Cy5 (λ_{ex} = 647 nm, red colour) channels and the merged image are presented.

6.6 Conclusions

In conclusion, we demonstrated the synthesis of iBTAs by starting from a C_2-symmetrical core to facilitate access to BTA-based supramolecular polymers that can be easily appended with a tunable amount of functional groups. Hereto, we changed the terminal group of one the side chains from an amine to a carboxylic acid, which required the same amount of synthetic steps and thus did not affect the synthetic effort. Furthermore, an azide moiety —acting as a handle for further functionalization— was introduced in a three step synthesis similar to the procedure for an amine terminated side chain. By using a carboxylic acid terminated side chain in combination with C_2-symmetrical 5-aminoisophthalic acid, the statistical deprotection of trimethyl benzene-1,3,5-tricarboxylate was circumvented. The synthetic effort to obtain the desired core molecule was hereby reduced from 5 steps to 3 steps. Although the overall yield of the novel route is slightly lower than that of the previously reported method, we expect these yields to be improved upon further optimization of the reaction conditions.

Since this newly developed synthesis protocol results in the inversion of the connectivity of one of the amide bonds, we first studied if this mutation would hamper the self-assembly of the iBTAs with unfunctional monomers. **iBTA-C$_{11}$-EG$_4$** forms supramolecular polymers of similar morphology and dynamics as its completely C-

centered counterpart. **iBTA-C$_{12}$-EG$_4$**, on the other hand, shows a reduced water solubility compared to **BTA-C$_{12}$-EG$_4$**, although they are atomically identical. By adding ACN as a cosolvent, the solubility is enhanced while the formation of supramolecular polymers is retained. The difference in solubility between **iBTA-C$_{11}$-EG$_4$** and **iBTA-C$_{12}$-EG$_4$**, which differ by one methylene unit only, illustrates once more the importance of the delicate balance between hydrophobic and hydrophilic interactions that should be taken into consideration in the design of new supramolecular building blocks.

Despite their different amide bond orientation, iBTAs are fully compatible with symmetrical BTAs and the molecules were copolymerized in several ratios without the need for a cosolvent. Especially at lower percentages of iBTA, which is desired for the introduction of biological motifs, the copolymers adopt a morphology and exchange dynamics identical to homopolymers of the BTA. Visual proof of the copolymerization was provided by STORM microscopy of a dye-functionalized **iBTA-C$_{12}$-EG$_4$**.

Our results exemplify that iBTAs are a versatile platform for the functionalization of BTA-based polymers without altering the properties of the polymers. We envision that the introduction of function via building blocks with a small mismatch in core structure is not restricted to the BTA-based system presented here and this strategy should be applied to other building blocks used in the quest towards multipurpose synthetic biomaterials. Our future work will focus on the interaction of functional iBTAs embedded in BTA-based systems with biological material.

6.7 Experimental section

6.7.1 Materials and Methods

All solvents and chemicals used were of reagent grade quality or better and purchased from Biosolve, Sigma-Aldrich or Lumiprobe at the highest purity available and used without further purification unless otherwise noted. **BTA-C$_{11}$-EG$_4$**,[20] **BTA-C$_{12}$-EG$_4$**[19] and **BTA-C$_{12}$-EG$_4$-Cy5**[41] were synthesized according to literature procedures. Water for aqueous samples was purified on an EMD Millipore Milli-Q Integral Water Purification System.

Sample preparation of BTA-C$_{11}$-EG$_4$, BTA-C$_{12}$-EG$_4$ and iBTA-C$_{11}$-EG$_4$: the solid material was weighed into a glass vial equipped with stirring bean. MQ-water was added to obtain the desired concentration and the samples were subsequently stirred at a temperature of 80 °C for 15 minutes. The hot and hazy samples were vortexed for 15 seconds and then left to equilibrate at room temperature overnight. Samples in ACN were prepared by weighing the solid material into a glass vial and adding ACN to reach the desired concentration.

Sample preparation of iBTA-C$_{12}$-EG$_4$: the solid material was weighed into a glass vial and dissolved in ACN to prepare a concentrated stock solution (0.5 mM for 50 μM in water or 5 mM for 500 μM in water). A small aliquot of this stock solution was then added to a glass vail equipped with MQ-water and a stirring bar to reach the desired concentration. The samples were stirred at a temperature of 80 °C for 15 minutes. The hot and hazy samples were vortexed for 15 seconds and then left to equilibrate at room temperature overnight. Samples in ACN were prepared by weighing the solid material into a glass vial and adding ACN to reach the desired concentration.

Sample preparation for mixtures of BTA-C$_{12}$-EG$_4$ and iBTA-C$_{12}$-EG$_4$: the solid **BTA-C$_{12}$-EG$_4$** was weighed into a glass vial. **iBTA-C$_{12}$-EG$_4$** was added from a concentrated stock solution in ACN in the desired concentration. ACN was evaporated with a stream of N$_2$ (g) before addition of a stirring bar and MQ-water to reach the desired final concentration. The samples were subsequently stirred at a temperature of 80 °C for 15 minutes. The hot and hazy samples were vortexed for 15 seconds and then left to equilibrate at room temperature overnight.

Sample preparation of dye-labelled BTA-C$_{12}$-EG$_4$ or iBTA-C$_{12}$-EG$_4$: samples of the homopolymers were prepared with the previously described protocol. The hot and hazy samples were vortexed for 15 seconds before **BTA-C$_{12}$-EG$_4$-Cy5** or **iBTA-C$_{12}$-EG$_4$-Cy3** were added from a 1 mM stock solution in MeOH in the desired concentration. The samples were equilibrated at a temperature of 45 °C for 30 minutes, without stirring. The samples were left to equilibrate at room temperature overnight and were further equilibrated in the fridge for one week until the measurement to prevent degradation of the dye.

Sample preparation for STORM measurements: the 50 µM BTA/iBTA samples were diluted to 2.5 µM with STORM buffer and were immediately imaged. STORM buffer contains 50 mM Tris pH 7, an oxygen scavenging system (0.5 mg/mL glucose oxidase, 40 µg/mL catalase), 10% (w/v) glucose and 10 mM 2-aminoethanethiol. A flow chamber was assembled by sticking a glass slide on a glass microscope coverslip (No. 1.5, 22*22 mm, thickness 0.17 mm) using double-sided tape. First, 20 µL of 0.1 mg/mL Poly-L-lysine (PLL) in MQ-water was flown through the chamber and incubated for 5 minutes. Next, the chamber was washed with 75 µL PBS. Finally, 20 µL solution of BTA/iBTA was flown through the chamber to immobilize them by adsorption on glass coverslip. Excess unbound fibers were removed by washing the chamber with 50 µL of STORM buffer.

6.7.2 Instrumentation

Newly synthesis molecules were characterized with nuclear magnetic resonance (NMR), solid-state Fourier-transform infrared (FT-IR), liquid chromatography mass spectroscopy (LC-MS) and matrix assisted laser absorption/ionization mass time of flight mass spectroscopy (MALDI-TOF-MS) using the instruments described in Chapter 2.

Column chromatography was performed with the instruments described in Chapter 2. Reactions were followed by thin-layer chromatography (TLC) using 60-F$_{254}$ silica gel plates from Merck and visualized by UV light at 254 nm and/or staining (ninhydrin, bromocresol green, potassium permanganate, iodine chamber).

Ultraviolet-visible (UV-visible) absorbance spectra were recorded with the instruments described in Chapter 3.

Static light scattering (SLS) measurements were performed on the instruments described in Chapter 5.

Cryogenic transmission electron microscopy (cryoTEM) images were obtained with the instrument described in Chapter 2.

Fourier-Transform infrared (FT-IR) spectra in solution were recorded with the instruments and methods described in Chapter 4. The sample of **iBTA-C$_{12}$-EG$_4$** in D$_2$O was first dissolved in ACN-d$_3$ before D$_2$O was added (final ACN concentration = 10%) and the heating-cooling protocol was used.

Hydrogen deuterium exchange experiments with electrospray ionization were carried out with the instruments described in Chapter 3.

STORM and TIRF images were acquired and analyzed using a Nikon N-STORM system configured for total internal reflection fluorescence (TIRF) imaging. **iBTA-C$_{12}$-EG$_4$-Cy3** and **BTA-C$_{12}$-EG$_4$-Cy5** labelled samples were irradiated with 561 and 647 nm laser lines built into the microscope. Fluorescence was collected by means of a Nikon 100x, 1.4NA oil immersion objective and passed through a quad-band pass dichroic filter (97335 Nikon). All time lapses for STORM were recorded onto a 256x256 pixel region (pixel size 0.17 μm) of a EMCCD camera (ixon3, Andor). For one-color measurements 7500 frames were acquired. For the mixing experiments 10000 frames for each channel were sequentially acquired. STORM movies were analyzed with the STORM module of the NIS element Nikon software.

6.7.3 Synthetic procedures

The synthesis of 1-Phenyl-2,5,8,11,14-pentaoxapentacosan-25-amine[20] and 1-Phenyl-2,5,8,11,14-pentaoxahexacosan-26-amine[19] were synthesized according to literature procedures but with optimized yields due to longer reaction times.

5a: n = 11, 47%
5b: n = 12, 55%

6a: n = 11, 31%
6b: n = 12, 31%

7a: n = 11, 81%
7b: n = 12, 68%
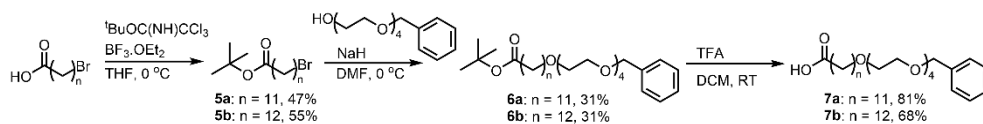
tert-Butyl-12-bromododecanoate (5a)

This procedure was adapted from literature.[52] A round-bottom flask was charged with 12-bromododecanoic acid (1.0609 g, 3.7996 mmol) in dry THF (10 mL) at 0 °C and *tert*-butyl imidate was added (2.0 mL, 11.1 mmol). Consequently, BF$_3$.OEt$_2$ (160.0 μL, 608.0 μmol) was added and the mixture was stirred overnight. The reaction mixture was quenched using saturated aqueous NaHCO$_3$. Ethyl acetate was added and the mixture was washed using saturated NaHCO$_3$ (3x) and brine (1x). The organic phase was dried over NaSO$_4$ and concentrated in vacuo. The crude oil was purified using column chromatography (SNAP-KI column 40 g, eluent hexane/ethyl acetate 4.5 CV: 25/1; 4 CV ramp to 4/1; 3.8 CV 4/1) to yield the product as a colorless oil (619.2 mg, 47%). ^{1}H NMR (400 MHz, DMSO-d$_6$ δ): 3.52 (t, J = 6.7 Hz, 2H, CH$_2$CH$_2$C$\underline{H}_2$Br), 2.16 (t, J = 7.3 Hz, 2H, *t*BuOOCC$\underline{H}_2$), 1.77 (p, J = 7.0 Hz, 2H, CH$_2$C$\underline{H}_2$CH$_2$Br), 1.48 (m, 2H,*t*BuOOCCH$_2$C$\underline{H}_2$), 1.39 (s, 9H, *t*$\underline{Bu}$OOC), 1.24 (s, 12H, aliphatic). ^{13}C NMR (100 MHz, DMSO-d$_6$ δ): 173.36, 79.90, 63.12, 35.63, 34.06, 32.84, 29.46, 29.42, 29.40, 29.28, 29.09, 28.76, 28.18, 28.13, 25.11. FT-IR (ATR) v (cm^{-1}): 3459, 3007, 2975, 2926, 2855, 1729, 1457, 1392 ,1366, 1255, 1151, 1043, 952, 919, 848, 755, 723, 645, 563, 462.

tert-Butyl-13-bromotridecanoate (5b)

The synthesis of **6b** was performed following the same procedure as described for **6a** using 13-bromotridecanoic acid[53], yielding **6b** as a colorless oil that solidified upon standing (1.9887 g, 55%). ^{1}H NMR (400 MHz, CDCl$_3$ δ): 3.42 – 3.39 (t, J = 6.9 Hz, 2H, CH$_2$C$\underline{H}_2$Br), 2.20 (t, J = 7.5 Hz, 2H, *t*BuOOCC$\underline{H}_2$CH$_2$), 1.85 (p, J = 7.0 Hz, 2H, C$\underline{H}_2$CH$_2$Br), 1.69 – 1.66 (m, 2H, *t*BuOOCCH$_2$C$\underline{H}_2$), 1.45 – 1.36 (m, 11H, *t*$\underline{Bu}$OOCCH$_2$, C$\underline{H}_2$CH$_2$CH$_2$Br), 1.36 – 1.21 (m, 14H, aliphatic). ^{13}C NMR (100 MHz, CDCl$_3$ δ): 173.36, 79.89, 60.40, 35.64, 34.06, 32.85, 29.54, 29.50, 29.45, 29.43, 29.29, 29.10, 28.77, 28.18, 28.13, 25.12. FT-IR (ATR) v (cm^{-1}): 3424, 2975, 2916, 2850, 1718, 1473, 1366, 1218, 1150, 1108, 847, 718.

tert-Butyl-1-phenyl-2,5,8,11,14-pentaoxaheptacosan-26-oate (6a)

A three-necked round bottom flask (250 mL, dried at 135 °C) was charged with monobenzyl tetraethylene glycol (0.8092 mg, 2.8458 mmol) in dry DMF (60 mL) and some 3 Å mole sieves to ensure dry conditions. The solution was cooled to 0 °C and NaH (0.1094 g, 2.7350 mmol) was added, upon which the mixture foamed vigorously. The ice bath was removed and after 30 minutes, **5a** (0.5978 g, 1.7827 mmol) was added in one portion and the mixture was stirred over the weekend. The mixture was subsequently quenched with H_2O (50 mL) and extracted with diethyl ether (3x 50 mL). Some saturated NaCl was added to improve phase separation. The organic layers were combined, dried with $MgSO_4$, filtered and concentrated *in vacuo*. The crude product was further purified using column chromatography (SNAP-KI column 24 g, eluent heptane/ethyl acetate 3 CV 80/20; 1 CV ramp to 70/30; 6 CV 70/30). The product was obtained as a colorless oil (295.0 mg, 31%). ^{1}H NMR (400 MHz, CDCl$_3$ δ): 7.35 – 7.29 (m, 5H, Ar), 4.57 (s, 2H, ArC$\underline{H}_2$), 3.66 – 3.64 (m, 14H, O(C$\underline{H}_2$)$_2$O), 3.58 – 3.56 (m, 2H, O(C$\underline{H}_2$)O), 3.44 (t, J = 6.8 Hz, 2H, CH$_2$CH$_2$C$\underline{H}_2$O), 2.20 (t, J = 7.5 Hz, 2H, *t*BuOOCC$\underline{H}_2$), 1.62 – 1.52 (m, 4H, *t*BuOOCCH$_2$C$\underline{H}_2$ & CH$_2$C$\underline{H}_2$CH$_2$O), 1.44 (s, 9H, *t*$\underline{Bu}$OOCCH$_2$), 1.35 – 1.20 (m, 14H, aliphatic). ^{13}C NMR (100 MHz, CDCl$_3$ δ): 173.37, 128.36, 127.75, 127.59, 79.89, 73.25, 71.56, 70.66, 70.62, 70.05, 69.44, 35.64, 31.89, 29.64, 29.59, 29.56, 29.50, 29.48, 29.32, 29.11, 28.13, 26.10, 25.13, 22.71, 14.13. FT-IR (ATR) ν (cm^{-1}): 2925, 2855, 1730, 1455, 1366, 1250, 1144, 1103, 1043, 946, 848, 736, 698, 464.

tert-Butyl-1-phenyl-2,5,8,11,14-pentaoxaheptacosan-27-oate (6b)

The synthesis of **6b** was performed following the same procedure as described for **6a** starting from **5b**, yielding **6b** as a colorless oil that solidified upon standing (535.0 mg, 31%).

^{1}H NMR (400 MHz, CDCl$_3$ δ): 7.35 – 7.29 (m, 5H, Ar), 4.57 (s, 2H, ArC$\underline{H}_2$), 3.66 – 3.64 (m, 14H, O(C$\underline{H}_2$)$_2$O), 3.58 – 3.56 (m, 2H, O(C$\underline{H}_2$)O), 3.44 (t, J = 6.8 Hz, 2H, CH$_2$CH$_2$C$\underline{H}_2$O), 2.20 (t, J = 7.5 Hz, 2H, *t*BuOOCC$\underline{H}_2$), 1.62 – 1.52 (m, 4H, *t*BuOOCCH$_2$C$\underline{H}_2$ & CH$_2$C$\underline{H}_2$CH$_2$O), 1.44 (s, 9H, *t*$\underline{Bu}$OOCCH$_2$), 1.35 – 1.20 (m, 16H, aliphatic). ^{13}C NMR (100 MHz, CDCl$_3$ δ): 138.29, 128.35, 127.74, 127.58, 79.88, 77.22, 73.25, 71.56, 70.66, 70.63, 70.06, 69.45, 35.65, 29.65, 29.60, 29.51, 29.32, 29.11, 28.14, 26.10, 25.14. FT-IR (ATR) ν (cm^{-1}): 2922, 2853, 1728, 1455, 1365, 1247, 1148, 1101, 845, 737, 698. LC-MS: *m/z* calculated for C$_{32}$H$_{56}$O$_7$+Na$^+$: 575.39 [M+Na]$^+$; observed 575.42; *m/z* calculated for C$_{28}$H$_{46}$O$_6$+NH$_4^+$: 496.70 [transesterification/elimination product + NH$_4$]$^+$; observed 496.25.

1-Phenyl-2,5,8,11,14-pentaoxahexacosan-26-oic acid (7a)

A round-bottom flask was charged with **6a** (0.2950 g, 0.5475 mmol) was dissolved in DCM (15 mL) and one equivalent TFA was added (15 mL). The mixture was stirred at room temperature overnight. After this, it was quenched at 0 °C with water. The aqueous phase was washed with DCM (3 x 20 mL). The combined organic phases were dried over $MgSO_4$ and concentrated *in vacuo*. The product was purified using column chromatography to remove amongst others the alkene side product (SNAP-KI column 24 g eluent heptane/ethyl acetate 80/20 - 50/50). After this, the compound was fully dried under vacuum with P_2O_5 to yield the pure product as a colorless oil (123.7 mg, 81%). ^{1}H NMR (400 MHz, DMSO-d$_6$ δ): 11.96 (s, 1H, $\underline{H}$OOCCH$_2$), 7.31 (m, 5H, Ar), 4.49 (s, 2H, ArC$\underline{H}_2$), 3.60 – 3.40 (m, 16H, O(C$\underline{H}_2$)$_2$O), 3.33 (m, 2H, CH$_2$C$\underline{H}_2$O), 2.18 (t, J = 7.3 Hz, 2H, HOOCC$\underline{H}_2$CH$_2$), 1.47 (m, 4H, HOOCCH$_2$C$\underline{H}_2$ & C$\underline{H}_2$CH$_2$O), 1.33 – 1.15 (m, 14H, aliphatic). ^{13}C NMR (100 MHz, DMSO-d$_6$ δ): 174.95, 138.95, 128.66, 127.93, 127.81, 72.49, 70.77, 70.28, 69.95, 69.60, 34.15, 31.73, 29.68, 29.49, 29.43, 29.37, 29.22, 29.03, 28.85, 26.12, 24.97, 22.58,

14.43. FT-IR (ATR) ν (cm-1): 3584-2440, 2928, 2852, 1733, 1706, 1456, 1353, 1251, 1096, 938, 845, 735, 698. MALDI-TOF-MS: m/z calculated for $C_{27}H_{46}O_7+Na^+$: 505.31 [M+Na]$^+$; observed 505.35; m/z calculated for $C_{27}H_{46}O_7+K^+$: 521.42 [M+K]$^+$; observed 521.32.

1-Phenyl-2,5,8,11,14-pentaoxaheptacosan-27-oic acid (7b)

The synthesis of **7b** was performed following the same procedure as described for **7a**, yielding **7b** as a colorless oil (327.1 mg, 68%). ^{1}H NMR (400 MHz, DMSO-d$_6$ δ): 11.96 (s, 1H, $\underline{H}$OOCCH$_2$), 7.31 (m, 5H, Ar), 4.49 (s, 2H, ArC$\underline{H_2}$O), 3.60 – 3.40 (m, 16H, O(C$\underline{H_2}$)$_2$O), 3.33 (m, 2H, CH$_2$C$\underline{H_2}$O), 2.18 (t, J = 7.3 Hz, 2H, HOOCCH$_2$C$\underline{H_2}$), 1.47 (m, 4H, HOOCCH$_2$C$\underline{H_2}$ & C$\underline{H_2}$CH$_2$O), 1.33 – 1.15 (m, 16H, aliphatic). ^{13}C NMR (100 MHz, DMSO-d$_6$ δ): 174.95, 138.94, 128.65, 127.92, 127.81, 72.49, 70.76, 70.32, 70.28, 70.24, 69.94, 69.60, 34.12, 31.73, 29.67, 29.49, 29.45, 29.37, 29.33, 29.21, 29.01, 26.11, 24.96. FT-IR (ATR) ν (cm^{-1}): 3719-2365, 2921, 2856, 1737, 1703, 1454, 1349, 1242, 1101, 940, 739, 698. MALDI-TOF-MS: m/z calculated for $C_{28}H_{48}O_7+Na^+$: 519.33 [M+Na]$^+$; observed 519.33; m/z calculated for $C_{28}H_{48}O_7+K^+$: 535.44 [M+K]$^+$; observed 535.30.
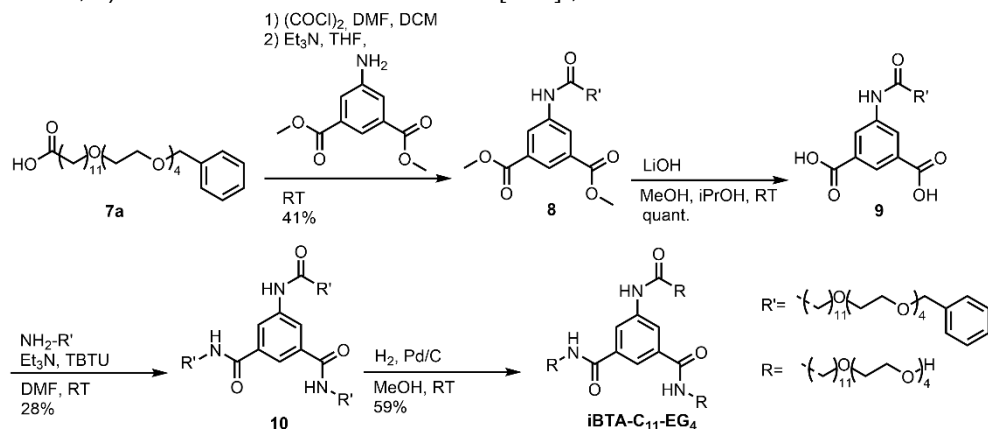
Dimethyl 5-(1-phenyl-2,5,8,11,14-pentaoxahexacosan-26-amido)isophthalate (8)

An oven-dried round-bottom flask (dried at 140 °C) was charged with **7a** (0.1214 g, 0.2515 mmol) in DCM (3 mL). Oxalyl chloride (120.0 µL, 1.3 mmol) was added to the stirring mixture. One droplet of DMF was added, after which vigorous bubbling was observed. After ten minutes, a bright yellow color was observed. The mixture was stirred for three hours, after which it was concentrated *in vacuo*. The purity of the activated acid was confirmed using ^{1}H NMR and it was used without further purification. Subsequently, a two-necked round bottom flask was dried at 140 °C and charged with dimethyl-5-aminoisophthalate (75.3 mg, 0.4 mmol) in dry THF (4 mL). Triethylamine (267.0 µL, 1.9 mmol) was added in one portion and the mixture was stirred for 15 min. The acid chloride was dissolved in dry THF (2 mL) and added dropwise. The mixture was stirred overnight, after which it was concentrated *in vacuo*. The solid was dissolved in chloroform and extracted with water (3 x 30 mL). After this, the water phase was washed with chloroform (3 x 30 mL) and the combined organic fractions were dried over MgSO$_4$. The mixture was filtered, concentrated *in vacuo* and purified using column chromatography (SNAP-KI column 24 g, eluent heptane/ethyl acetate 50/50) to yield the product as a colorless sticky oil (69.7 mg, 41%). ^{1}H NMR (400 MHz, DMSO-d$_6$ δ): 10.33 (s, 1H, ArN$\underline{H}$COCH$_2$), 8.50 (s, 2H, core next to amide), 8.15 (s, 1H, core between esters), 7.31 (m, 5H, Ar), 4.48 (s, 2H, ArC$\underline{H_2}$O), 3.89 (s, 6H, 2x ArCOOC$\underline{H_3}$), 3.49 (m, 16H, O(C$\underline{H_2}$)$_2$O), 3.34 (m, 2H, CH$_2$C$\underline{H_2}$O), 2.33 (t, J = 7.2 Hz, 2H, NHCOC$\underline{H_2}$CH$_2$), 1.59 (m, 2H,

NHCOCH$_2$C$\underline{H}_2$), 1.45 (m, 2H, C$\underline{H}_2$CH$_2$O), 1.27 (m, 14H, aliphatic). ^{13}C NMR (100 MHz, DMSO-d$_6$ δ): 172.42, 165.77, 140.69, 138.92, 131.08, 128.65, 127.92, 127.80, 124.22, 123.85, 72.47, 70.75, 70.31, 70.26, 70.22, 69.93, 69.58, 60.23, 52.99, 36.86, 31.73, 29.66, 29.47, 29.43, 29.34, 29.21, 29.03, 28.85, 26.11, 25.37, 22.58, 21.24, 14.56, 14.44. FT-IR (ATR) v (cm^{-1}): 3322, 2925, 2855, 1725, 1698, 1604, 1553, 1453, 1438, 1342, 1240, 1102, 1003, 949, 906, 873, 794, 759, 721, 698, 542, 464. LC-MS: *m/z* calculated for C$_{37}$H$_{55}$NO$_{10}$+H$^+$: 674.39 [M+H]$^+$; observed 674.25; *m/z* calculated for C$_{37}$H$_{55}$NO$_{10}$+NH$_4^+$: 691.41 [M+NH$_4$]$^+$; observed 691.17.

5-(1-Phenyl-2,5,8,11,14-pentaoxahexacosan-26-amido)isophthalic acid (9)

A round-bottom flask was charged with **8** (69.7 mg, 0.1 mmol) in methanol/isopropanol (2/1, 1.5 mL) and lithium hydroxide monohydrate (19.6 mg, 0.8 mmol) was added, followed by a few drops of water. The reaction mixture was stirred overnight at room temperature and subsequently concentrated *in vacuo*. Water was added to the solids (10 mL) and the mixture was acidified with HCl (1 M) followed by extraction with DCM (3 x 30 mL). The organic layers were combined, dried with MgSO$_4$, filtered and concentrated *in vacuo* yielding the product as a white waxy solid (67.6 mg, 100%). ^{1}H NMR (400 MHz, DMSO-d$_6$ δ): 8.22 (s, 2H, core next to amide), 8.12 (s, 1H, core between carboxylic acids), 7.34 – 7.27 (m, 5H, Ar), 6.31 (s, 2H, 2x COO$\underline{H}$), 4.57 (s, 2H, ArC$\underline{H}_2$O), 3.69 – 3.56 (m, 16H, O(C$\underline{H}_2$)$_2$O), 3.45 – 3.38 (m, 2H, CH$_2$CH$_2$C$\underline{H}_2$O), 2.30 – 2.27 (t, J =7.3 Hz, 2H, ArNHCOC$\underline{H}_2$CH$_2$), 1.58 – 1.47 (m, 2H, CH$_2$C$\underline{H}_2$CH$_2$O), 1.47 – 1.44 (m, 2H, ArNHCOCH$_2$C$\underline{H}_2$), 1.27 (m, 14H, aliphatic). ^{13}C NMR (100 MHz, DMSO-d$_6$ δ): 181.91, 128.66, 127.93, 72.47, 70.76, 70.26, 69.59, 36.86, 33.68, 32.83, 29.66, 29.49, 26.34, 26.12, 23.06. FT-IR (ATR) v (cm-1): 3500 – 2500, 2917, 2855, 1625, 1559, 1435, 1358, 1095, 949, 779, 719, 697. MALDI-TOF-MS: *m/z* calculated for C$_{35}$H$_{51}$NO$_{10}$+Li$^+$: 652.29 [M+Li]$^+$; observed 652.39; *m/z* calculated for C$_{35}$H$_{51}$NO$_{10}$+Na$^+$: 668.34 [M+Na]$^+$; observed 668.37.

5-(1-Phenyl-2,5,8,11,14-pentaoxahexacosan-26-amido)-N^1,N^3-bis(1-phenyl-2,5,8,11,14-pentaoxapentacosan-25-yl)isophthalamide (10)

An oven-dried round-bottom flask (dried at 135 °C) and charged with **9** (67.6 mg, 0.1 mmol) in dry DMF (1 mL). Triethylamine (72.0 µL, 0.5 mmol) and 1-Phenyl-2,5,8,11,14-pentaoxapentacosan-25-amine[20] (113.0 mg, 0.2 mmol) were added to the mixture and it was cooled to 0 °C. Subsequently, TBTU (99.2 mg, 0.3 mmol) was added and the mixture was stirred overnight at room temperature. The mixture was quenched with water, upon which it turned milky-white. The mixture was extracted with ethyl acetate (3 x 30 mL) and the combined organic phases were extracted with water and brine. The compound was purified using column chromatography (SNAP-KI column 12 g, eluent isopropanol/DCM, 0/100 – 5/95 – 10/90) which yielded the pure product as a slightly yellow solid (43.8 mg, 28%). ^{1}H NMR (400 MHz, CDCl$_3$ δ): 8.27 (m, 1H, ArN$\underline{H}$COCH$_2$), 8.24 (s, 2H, core protons), 7.98 (s, 1H, core proton between regular amides), 7.34 – 7.27 (m, 15H, Ar), 6.52 (m, 2H, 2x ArCON$\underline{H}$CH$_2$), 4.57 (s, 6H, 3x ArC$\underline{H}_2$O), 3.69 – 3.54 (m, 48H, O(C$\underline{H}_2$)$_2$O), 3.47 – 3.38 (m, 10H, 3x CH$_2$CH$_2$C$\underline{H}_2$O, 2x CONHC$\underline{H}_2$CH$_2$), 2.43 - 2.39 (t, J = 7.5 Hz, 2H, ArNHOCC$\underline{H}_2$CH$_2$) 1.73 – 1.68 (m, 2H, 1.85 ArNHOCCH$_2$C$\underline{H}_2$), 1.60 – 1.53 (m, 10H, 3x CH$_2$C$\underline{H}_2$CH$_2$O, 2x ArCONHCH$_2$C$\underline{H}_2$), 1.36 – 1.21 (m, 42H, aliphatic). ^{13}C NMR (100 MHz, CDCl$_3$ δ): 128.36, 127.77, 127.61, 77.23, 73.25, 71.55, 70.60, 70.05, 69.42, 64.47, 38.63, 29.60, 29.58, 29.51, 29.43, 29.36, 29.24, 26.94, 26.06, 25.38. FT-IR (ATR) v (cm^{-1}): 3320, 2926, 2853, 1648, 1536, 1425, 1349, 1096, 734, 697. LC-MS: *m/z* calculated for C$_{87}$H$_{141}$N$_3$O$_{18}$+NH$_4^+$: 1534.05 [M+NH$_4$]$^+$; observed 1534.50; *m/z* calculated for C$_{80}$H$_{135}$N$_3$O$_{18}$+H$^+$: 1426.98 [M-benzyl+H]$^+$; observed

1426.58; *m/z* calculated for $C_{73}H_{129}N_3O_{18}+H^+$: 1336.94 [M-2benzyl+H]$^+$; observed 1336.58; *m/z* calculated for $C_{66}H_{123}N_3O_{18}+H^+$: 1246.89 [M-3benzyl+H]$^+$; observed 1246.58;

iBTA-C$_{11}$-EG$_4$

A round-bottom flask was charged with **10** (42.2 mg, 0.027 mmol) in MeOH (10 mL) and flushed with N_2 gas for 10 minutes. 10% Pd/C (6.3 mg) was subsequently added, followed by H_2 exchange facilitated with a balloon. The mixture was left stirring overnight under H_2 atmosphere. Afterwards, a small amount of the reaction mixture was taken and filtered over celite in a Pasteur pipette to check conversion using ^{1}H NMR. After confirmation of full deprotection, the rest of the mixture was filtered through celite which was washed with MeOH until TLC did not show any UV-active spots. The combined organic phases were concentrated *in vacuo* and the material was obtained as a brown waxy solid (19.877 mg, 59%). ^{1}H NMR (400 MHz, CDCl$_3$ δ): 9.32 (m, 1H, ArNHCOCH$_2$), 8.24 (s, 2H, core protons), 7.98 (s, 1H, core proton between regular amides), 7.12 (m, 2H, 2x ArCONHCH$_2$), 3.69 – 3.62 (m, 48H, O(CH$_2$)$_2$O), 3.47 – 3.38 (m, 10H, 3x CH$_2$CH$_2$CH$_2$O, 2x CONHCH$_2$CH$_2$), 2.43 – 2.39 (t, J = 7.5 Hz, ArNHOCCH$_2$CH$_2$) 1.73 – 1.68 (m, 2H, ArNHOCCH$_2$CH$_2$), 1.60 – 1.53 (m, 10H, 3x CH$_2$CH$_2$CH$_2$O, 2x ArCONHCH$_2$CH$_2$), 1.36 – 1.21 (m, 42H, aliphatic). ^{13}C NMR (100 MHz, CDCl$_3$ δ): 73.00, 166.78, 139.34, 135.45, 120.89, 72.55, 71.54, 70.49, 70.45, 70.37, 70.34, 70.10, 69.82, 61.46, 40.30, 37.34, 29.62, 29.44, 29.40, 29.36, 29.33, 29.19, 26.92, 25.96, 25.47. FT-IR (ATR) ν (cm^{-1}): 3460, 3346, 3074, 2927, 2853, 1729, 1656, 1595, 1546, 1460, 1428, 1346, 1286, 1244, 1106, 943, 882, 837, 707, 697. MALDI-TOF-MS: *m/z* calculated for $C_{66}H_{123}N_3O_{18}+Na^+$: 1268.87 [M+Na]$^+$; observed 1268.69; *m/z* calculated for $C_{66}H_{123}N_3O_{18}+K^+$: 1284.98 [M+K]$^+$; observed 1284.85.

5-Amino-N^1,N^3-bis(1-phenyl-2,5,8,11,14-pentaoxahexacosan-26-yl)isophthalamide (1)

A round-bottom flask was charged with 5-aminoisophthalic acid (0.1994 g, 1.1007 mmol) in thionyl chloride (15 mL). The mixture was stirred at room temperature for one hour, after which it was left to reflux for two hours. Conversion was checked using FT-IR and after two hours, no broad peak corresponding to a carboxylic acid could be seen anymore. The mixture was concentrated *in vacuo*, co-evaporated with toluene once and used without further purification. Subsequently, a two-necked round bottom flask was dried at 140 °C and charged with 1-Phenyl-2,5,8,11,14-pentaoxahexacosan-26-amine[19] (1.08 g, 2.30 mmol) in dry THF (15 mL). Triethylamine (420.0 μL, 3.0 mmol) was added in one portion and the mixture was stirred for 20 min. The flask was cooled to 0 °C and the acid-chloride was dissolved in dry THF (10 mL) and added dropwise. The mixture was stirred overnight at RT, after which it was concentrated *in vacuo*. The mixture was dissolved in chloroform and extracted with water (3 x 20 mL). The combined aqueous phases were washed with chloroform (3 x 50 mL) and the combined organic phases were dried over MgSO$_4$ and concentrated *in vacuo*. The mixture was purified using column chromatography (SNAP-KI column 12 g, eluent DCM/methanol 95/5) and obtained as a dark yellow oil. Hereafter, it was determined that impurities were still present using LC-MS. Therefore, reversed phase column was used to obtain the pure product (C$_{18}$ column 30 g, eluent acetonitrile/water 3 CV ramp 1/9 – 5/5; 4 CV 5/5; 1 CV ramp to 6/4; 1 CV 6/4; 1 CV ramp to 7/3; 5 CV 7/3; 1 CV ramp to 8/2; 14 CV 8/2). After freeze-drying, the material was obtained as an off-white flaky solid (290.3 mg, 25%). ^{1}H NMR (400 MHz, CDCl$_3$ δ): 7.45 (s, 1H, core), 7.34 – 7.27 (m, 10H, Ar), 7.22 (s, 2H, core), 6.30 (s, 2H, 2x ArCONHCH$_2$), 4.57 (s, 4H, ArCH$_2$O), 3.68 – 3.62 (m, 28H, O(CH$_2$)$_2$O), 3.58 – 3.56 (m, 4H, O(CH$_2$)$_2$O), 3.45 – 3.38 (m, 8H, CH$_2$CH$_2$CH$_2$O, ArCONHCH$_2$CH$_2$CH$_2$),

1.60 – 1.54 (m, 8H, CH$_2$C$\underline{H}_2$CH$_2$O, ArCONHCH$_2$C$\underline{H}_2$CH$_2$), 1.38 - 1.26 (m, 32H, aliphatic). ^{13}C NMR (100 MHz, CDCl$_3$ δ): 128.36, 127.76, 127.60, 77.21, 73.26, 71.54, 70.63, 70.06, 29.60, 29.49, 29.44, 29.43, 29.42, 29.40, 29.23, 26.05. FT-IR (ATR) ν (cm^{-1}): 3322, 2924, 2854, 1619, 1593, 1524, 1454, 1348, 1291, 1100, 860, 732, 698. LC-MS: Calculated M_w: m/z calculated for C$_{62}$H$_{101}$N$_3$O$_{12}$+H$^+$: 1080.75 [M+H]$^+$; observed 1080.58; m/z calculated for C$_{62}$H$_{101}$N$_3$O$_{12}$+H$^+$+Na$^+$: 551.87 [M+H+Na]$^{2+}$; observed 551.75; m/z calculated for C$_{55}$H$_{95}$N$_3$O$_{12}$+H$^+$: 990.70 [M-benzyl+H]$^+$; observed 990.58.

5-(1-Phenyl-2,5,8,11,14-pentaoxaheptacosan-27-amido)-N^1,N^3-bis(1-phenyl-2,5,8,11,14-pentaoxahexacosan-26-yl)isophthalamide (2)

An oven-dried round-bottom flask (dried at 140 °C) was charged with **7b** (138.9 mg, 0.3 mmol) in DCM (5 mL). Oxalyl chloride (150.0 µL, 1.7 mmol) was added to the stirring mixture. One droplet DMF was added, after which vigorous bubbling was observed. After ten minutes, a bright yellow color was observed. The mixture was left to stir for three hours, after which it was concentrated *in vacuo*. The conversion of the carboxylic acid was confirmed using ^{1}H NMR and it was used without further purification. Subsequently, a two-necked round bottom flask (dried at 140 °C) was charged with **1** (190.2 mg, 0.2 mmol) in dry THF (15 mL). Triethylamine (200.0 µL, 1.6 mmol) was added in one portion and the mixture was stirred for 15 min. The acid chloride was dissolved in dry THF (10 mL) and added dropwise. The mixture was stirred overnight, after which it was concentrated *in vacuo*. The mixture was purified using column chromatography (SNAP-KI 12 g, eluent isopropanol/DCM 4/96). After this, LC-MS still showed impurities, so a reversed phase column was performed (C$_{18}$ column 30 g, eluent acetonitrile/water 2 CV ramp 1/9 – 5/5; 2 CV 5/5; 1 CV ramp to 7/3; 2 CV 7/3; 1 CV ramp to 8/2; 2.5 CV 8/2; 1 CV ramp to 9/1; 3.7 CV 9/1; 2 CV ramp to 10/0; 7.7 CV 10/0; 1 CV ramp to 1/9; 2.8 CV 1/9; 1 CV ramp to 10/0; 12.7 CV 10/0). The acetonitrile was removed *in vacuo* and the product was obtained after lyophilization as a white solid (205 mg, 74%). ^{1}H NMR (400 MHz, CDCl$_3$ δ): 8.19 (s, 2H, core protons), 7.93 (s, 1H, core proton), 7.73 (m, 1H, ArN$\underline{H}$COCH$_2$), 7.34 – 7.27 (m, 15H, Ar), 6.39 (m, 2H, 2x ArCONHCH$_2$), 4.56 (s, 6H, ArC$\underline{H}_2$O), 3.69 – 3.62 (m, 42H, O(C$\underline{H}_2$)$_2$O), 3.57 – 3.55 (m, 6H, O(C$\underline{H}_2$)$_2$O), 3.47 – 3.38 (m, 10H, 3x CH$_2$CH$_2$C$\underline{H}_2$O, 2x ArCONHC$\underline{H}_2$CH$_2$), 2.43 – 2.39 (t, J = 7.5 Hz, 2H, ArNHCOC$\underline{H}_2$CH$_2$) 1.73 – 1.67 (m, 2H, 1.85 ArNHCOCH$_2$C$\underline{H}_2$), 1.60 – 1.53 (m, 10H, 3x CH$_2$C$\underline{H}_2$CH$_2$O, 2x ArNHCOCH$_2$C$\underline{H}_2$), 1.36 – 1.21 (m, 48H, aliphatic). ^{13}C NMR (100 MHz, CDCl$_3$ δ): 128.36, 127.76, 127.60, 77.22, 73.25, 71.55, 70.66, 70.61, 70.05, 69.44, 64.45, 29.48, 29.23, 26.93, 26.07, 25.37. FT-IR (ATR) ν (cm^{-1}): 3315, 2924, 2854, 1642, 1536, 1451, 1349, 1293, 1247, 1104, 749, 698. LC-MS: m/z calculated for C$_{90}$H$_{147}$N$_3$O$_{18}$+H$^+$: 1559.08 [M+H]$^+$; observed 1558.83; m/z calculated for C$_{77}$H$_{137}$N$_3$O$_{18}$+H$^+$: 1393.00 [M-2benzyl+H]$^+$; observed 1378.75; m/z calculated for C$_{90}$H$_{147}$N$_3$O$_{18}$+2Na$^+$: 802.03 [M+2Na]$^{2+}$; observed 802.25; m/z calculated for C$_{90}$H$_{147}$N$_3$O$_{18}$+3Na$^+$: 542.35 [M+3Na]$^{3+}$; observed 542.75.

iBTA-C$_{12}$-EG$_4$

The synthesis of **iBTA-C$_{12}$-EG$_4$** was performed following the same procedure as described for **iBTA-C$_{11}$-EG$_4$**, yielding **iBTA-C$_{12}$-EG$_4$** as a white solid (134.1 mg, 80%). ^{1}H NMR (400 MHz, CDCl$_3$ δ): 8.28 (m, 1H, ArN$\underline{H}$COCH$_2$), 8.22 (s, 2H, core protons), 7.95 (s, 1H, core proton between regular amides), 6.61 (m, 2H, 2x ArCON$\underline{H}$CH$_2$), 3.69 – 3.62 (m, 48H, O(C$\underline{H}_2$)$_2$O), 3.47 – 3.38 (m, 10H, 3x CH$_2$CH$_2$C$\underline{H}_2$O, 2x ArCONHC$\underline{H}_2$CH$_2$), 2.43 – 2.39 (t, J = 7.5 Hz, 2H, 2x ArNHCOC$\underline{H}_2$CH$_2$), 1.73 – 1.68 (m, 2H, ArNHCOCH$_2$C$\underline{H}_2$), 1.60 – 1.53 (m, 10H, 3x CH$_2$C$\underline{H}_2$CH$_2$O, 2x ArCONHCH$_2$C$\underline{H}_2$), 1.36 – 1.21

(m, 48H, aliphatic). ^{13}C NMR (100 MHz, CDCl$_3$ δ): 172.60, 166.46, 139.23, 135.60, 120.62, 72.64, 71.57, 71.55, 70.62, 70.60, 70.56, 70.53, 70.27, 70.03, 61.69, 40.30, 37.49, 29.52, 29.46, 29.44, 29.40, 29.37, 29.35, 29.31, 29.22, 26.92, 26.04, 26.00, 25.43. FT-IR (ATR) v (cm^{-1}): 3608 – 3068, 2924, 2854, 1637, 1603, 1546, 1444, 1335, 1272, 1118, 935, 884, 721. LC-MS: m/z calculated for C$_{69}$H$_{129}$N$_3$O$_{18}$+H$^+$: 1288.84 [M+H]$^+$; observed 1288.67; m/z calculated for C$_{69}$H$_{129}$N$_3$O$_{18}$+2H$^+$: 644.98 [M+2H]$^{2+}$; observed 944.92; m/z calculated for C$_{69}$H$_{129}$N$_3$O$_{18}$+3H$^+$: 430.32 [M+3H]$^{3+}$; observed 430.58.
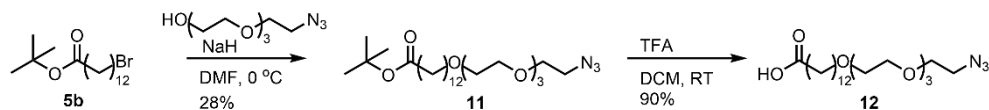
tert-Butyl-1-azido-3,6,9,12-tetraoxapentacosan-25-oate (11)

A three-necked round-bottom flask was dried at 135 °C and charged with 2-(2-(2-(2-azidoethoxy)ethoxy)ethoxy)ethan-1-ol[44] (0.5316 g, 0.0024 mol) and dry DMF (25 mL). The solution was cooled to 0 °C and sodium hydride (0.1195 g, 0.0029 mol) was added to the stirring solution. The reaction mixture was allowed to heat up to room temperature after 30 min and *tert*-butyl-13-bromotridecanoate **5b** (0.5573 g, 0.0016 mol) dissolved in 5 mL DMF was added in one go. The mixture was left to stir overnight and subsequently quenched with H$_2$O (20 mL) and extracted with diethyl ether (3 x 50 mL). A small amount of saturated NaCl was added to improve phase separation. The organic layers were combined, dried with MgSO$_4$, filtered and concentrated *in vacuo*. The crude product was further purified using column chromatography (SNAP-KI column 24 g, eluent heptane/ethyl acetate 80/20 - 70/30). The product was obtained as a colorless oil (221.6 mg, 28%). ^1H NMR (400 MHz, CDCl$_3$ δ): 3.66 (m, 12H, O(C$\underline{H_2}$)$_2$O), 3.58 (m, 2H, O(C$\underline{H_2}$)$_2$O), 3.45 (t, J = 6.8 Hz, 2H, CH$_2$CH$_2$C$\underline{H_2}$O), 3.39 (t, J = 5.1 Hz, 2H, N$_3$C$\underline{H_2}$), 2.20 (t, J = 7.5 Hz, 2H, *t*BuOOCC$\underline{H_2}$CH$_2$), 1.56 (m, 4H, *t*BuOOCCH$_2$C$\underline{H_2}$ & CH$_2$C$\underline{H_2}$CH$_2$O), 1.44 (s, 9H, *t*$\underline{Bu}$OOCH$_2$), 1.21 (m, 16H, aliphatic). ^{13}C NMR (100 MHz, CDCl$_3$ δ): 79.88, 77.21, 71.56, 70.71, 70.65, 70.06, 50.71, 35.65, 31.89, 29.65, 29.60, 29.49, 29.32, 29.11, 29.03, 28.13, 26.11, 25.13, 22.70, 14.12. FT-IR (ATR) v (cm^{-1}): 3455, 2922, 2853, 2104, 1729, 1460, 1367, 1247, 1147, 1102, 936, 851. LC-MS: m/z calculated for C$_{25}$H$_{49}$N$_3$O$_6$+Na$^+$: 510.35 [M+Na]$^+$; observed 510.25; m/z calculated for C$_{21}$H$_{39}$N$_3$O$_5$+Na$^+$: 436.28 [transesterification/elimination product + Na]$^+$; observed 436.17.

1-Azido-3,6,9,12-tetraoxapentacosan-25-oic acid (12)

A round-bottom flask was charged with **11** and DCM (15 mL) and one equivalent TFA was added (15 mL). The mixture was stirred at room temperature overnight. After this, it was quenched at 0 °C with water. The aqueous phase was washed with DCM three times. The combined organic phases were dried over MgSO$_4$ and concentrated *in vacuo*. The product was purified using column chromatography (SNAP-KI 24 g, eluent heptane/ethyl acetate 80/20 - 50/50). The product was obtained as a colorless oil (177.9 mg, 90%). ^1H NMR (400 MHz, DMSO-d$_6$ δ): 11.96 (s, 1H, HOOCC$\underline{H_2}$), 3.60 - 3.40 (m, 16H, O-(C$\underline{H_2}$)$_2$-O), 3.33 (m, 2H, CH$_2$C$\underline{H_2}$O), 2.18 (t, J = 7.3 Hz, 2H, HOOCC$\underline{H_2}$CH$_2$), 1.47 (m, 4H, HOOCCH$_2$C$\underline{H_2}$ & C$\underline{H_2}$CH$_2$O), 1.33 - 1.15 (m, 16H, aliphatic). ^{13}C NMR (100 MHz, DMSO-d$_6$ δ): 174.95, 70.77, 70.31, 70.27, 70.18, 69.95, 69.72, 60.22, 50.47, 34.12, 31.73, 29.67, 29.50, 29.45, 29.38, 29.33, 29.21, 29.02, 28.84, 26.12, 24.96, 22.57, 21.22, 14.55, 14.42. FT-IR (ATR) v (cm^{-1}): 3650 - 2450, 2924, 2854, 2098, 1731, 1708, 1454, 1349, 1284, 1243, 1102, 931, 837. MALDI-TOF-MS: m/z calculated for C$_{21}$H$_{41}$N$_3$O$_6$+Na$^+$: 454.29 [M+Na]$^+$; observed 454.27.

5-Amino-N1,N3-bis(1-hydroxy-3,6,9,12-tetraoxatetracosan-24-yl)isophthalamide (3)

A round bottom flask (50 ml, dried at 140 °C) was charged with methanol (10 ml) and **1** (28.0 mg, 0.026 mmol). The solution was purged with N_2 gas for 10 minutes to ensure all atmospheric oxen was removed. 10% Pd/C catalyst (10 mg) was added and a balloon filled with H_2 gas was attached. The solution was saturated with hydrogen gas and the mixture was left to stir overnight at room temperature. A small aliquot was taken and filtered over celite to check using TLC for conversion (Hept:EtAc 50:50). Hereafter, the mixture was filtered over celite and concentrated *in vacuo* to obtain the product as a white solid (18.6 mg, 80%). ^{1}H NMR (400 MHz, CDCl$_3$ δ): 7.51 (s, 1H, core), 7.20 (s, 2H, core), 6.71 (s, 2H, 2x ArCON$\underline{H}$CH$_2$), 3.72 – 3.57 (m, 32H, O(C$\underline{H}_2$)$_2$O), 3.44 – 3.36 (m, 8H, CH$_2$CH$_2$C$\underline{H}_2$O, ArCONHC$\underline{H}_2$CH$_2$CH$_2$), 1.58 – 1.54 (m, 8H, CH$_2$C$\underline{H}_2$CH$_2$O, ArCONHCH$_2$C$\underline{H}_2$CH$_2$), 1.38 - 1.24 (m, 32H, aliphatic). ^{13}C NMR (100 MHz, DMSO-d$_6$ δ): 79.79, 79.46, 79.13, 72.81, 70.80, 70.30, 70.28, 70.25, 69.95, 60.65, 29.69, 29.52, 29.50, 29.37, 29.24, 26.83, 26.13. FT-IR (ATR) v (cm^{-1}): 3298, 2925, 2855, 1640, 1555, 1462, 1348, 1312, 1250, 1208, 1102, 941, 884. MALDI-TOF-MS: *m/z* calculated for C$_{48}$H$_{89}$N$_3$O$_{12}$+Na$^+$: 922.63 [M+Na]$^+$; observed 922.66; *m/z* calculated for C$_{48}$H$_{89}$N$_3$O$_{12}$+K$^+$: 938.74 [M+K]$^+$; observed 938.62.

iBTA-C12-EG4-N3 (4)

A 10 mL round bottom flask was charged with **3** (crude mixture, 100 mg), **12** (44.8 mg, 0.103 mmol) and 3 mL MeOH. To this, DMT-MM (62.0 mg, 0.224 mmol) was added and the mixture was stirred overnight. Hereafter, the reaction was not complete hence more DMT-MM (43.3 mg, 0.156 mmol) was added and the mixture was stirred overnight again. The mixture was concentrated *in vacuo* and purified using reversed phase column (C$_{18}$ column 30 g, eluent acetonitrile/water 3 CV ramp 1/9 – 5/5; 2 CV 5/5; 1 CV ramp to 6/4; 2 CV 6/4; 1 CV ramp to 7/3; 2 CV 7/3; 1 CV ramp to 8/2; 2CV 8/2; 1 CV ramp to 9/1; 1 CV 9/1; 1 CV ramp to 9.5/0.5; 2 CV 9.5/0.5) to obtain the product as a white solid (33.8 mg, 23%). ^{1}H NMR (400 MHz, CDCl$_3$ δ): 8.20 (s, 2H, core protons), 8.14 (s, 1H, ArN$\underline{H}$COCH$_2$), 7.95 (s, 1H, core proton between regular amides), 6.59 (s, 2H, 2x ArCON$\underline{H}$CH$_2$), 3.72 - 3.57 (m, 48H, O(C$\underline{H}_2$)$_2$O), 3.44 - 3.37 (m, 12H, 3x CH$_2$CH$_2$C$\underline{H}_2$O, 2x ArCONHC$\underline{H}_2$CH$_2$, OCH$_2$C$\underline{H}_2$N$_3$), 2.41 (t, J = 8.0 Hz, 2H, NHCOC$\underline{H}_2$), 1.72 - 1.53 (water influence, m, 12H, 1x NHCOCH$_2$C$\underline{H}_2$CH$_2$, 2x CONHCH$_2$C$\underline{H}_2$CH$_2$, 3x C$\underline{H}_2$CH$_2$O(CH$_2$)$_2$O), 1.37 - 1.16 (m, 48H, aliphatic chain). ^{13}C NMR (100 MHz, CDCl$_3$ δ): 172.95, 168.32, 82.85, 77.34, 77.02, 76.70, 72.74, 71.65, 70.62, 70.05, 61.84, 50.46, 29.49, 26.09, 25.46. FT-IR (ATR) v (cm^{-1}): 3464, 3305, 2926, 2856, 2102, 1643, 1594, 1539, 1441, 1346, 1278, 1109, 942, 888. LC-MS: *m/z* calculated for C$_{69}$H$_{128}$N$_6$O$_{17}$+H$^+$: 1313.94 [M+H]$^+$; observed 1313.58; *m/z* calculated for C$_{69}$H$_{128}$N$_6$O$_{17}$+Na$^+$: 1335.92 [M+Na]$^+$; observed 1335.83; *m/z* calculated for C$_{69}$H$_{128}$N$_6$O$_{17}$+2H$^+$: 657.48 [M+2H]$^{2+}$; observed 657.33; *m/z* calculated for C$_{69}$H$_{128}$N$_6$O$_{17}$+H$^+$+Na$^+$: 668.47 [M+H+Na]$^{2+}$; observed 668.42; *m/z* calculated for C$_{69}$H$_{128}$N$_6$O$_{17}$+2Na$^+$: 679.46 [M+2Na]$^{2+}$; observed 679.50.

iBTA-C12-EG4-Cy3

A 5 mL round bottom flask was charged with **4** (4.6 mg, 0.0035 mmol) and alkyne-sulfo-Cy3 (5.0 mg, 0.0072 mmol) in 1 mL DMSO. To this mixture, CuSO$_4$ (1.117 mg, 0.0070 mmol) and Na-*L*-Ascorbate (1.370 mg, 0.0069 mmol) were added in a minimal amount of water. The mixture was stirred at RT overnight. LC-MS showed conversion of the starting material, thus the mixture was concentrated *in vacuo*. Subsequently the crude mixture was dissolved in CHCl$_3$ and extracted three times with water. The organic fraction was dried over MgSO$_4$ and concentrated *in vacuo* to obtain the product as a bright pink solid (4.0 mg, 58%). LC-MS: *m/z* calculated for

$C_{102}H_{166}N_9O_{24}S_2^-+H^++2Na^+$: 1005.57 $[M+H+2Na]^{2+}$; observed 1006.67; m/z calculated for $C_{102}H_{166}N_9O_{24}S_2^-+4H^+$: 656.40 $[M+4H]^{3+}$; observed 656.75.

6.7.4 Details on the HDX-MS analysis

All HDX-MS experiments were performed under similar conditions to eliminate influences from the environment, for example temperature. The measurements were performed by diluting a sample of self-assembled supramolecular building-blocks in H_2O 100x into D_2O. 0.5 mM sodium acetate was added to the D_2O prior to the dilution to facilitate the detection. In all cases the distributions with two sodium ions were used for the calculations. All calculations are based on the method presented in Chapter 3. The equations used for samples of **BTA-C₁₁-EG₄** and **BTA-C₁₂-EG₄** are given in section 3.9.3 and the same set of equations was used for **iBTA-C₁₁-EG₄**, **iBTA-C₁₂-EG₄** and the mixture of **BTA-C₁₂-EG₄** with **iBTA-C₁₂-EG₄**.

6.8 References

1   O. J. G. M. Goor, S. I. S. Hendrikse, P. Y. W. Dankers and E. W. Meijer, *Chem. Soc. Rev.*, 2017, **46**, 6621–6637.

2   E. Krieg, M. M. C. Bastings, P. Besenius and B. Rybtchinski, *Chem. Rev.*, 2016, **116**, 2414–2477.

3   P. Y. W. Dankers, M. C. Harmsen, L. A. Brouwer, M. J. A. Van Luyn and E. W. Meijer, *Nat. Mater.*, 2005, **4**, 568–574.

4   K. Petkau-Milroy, M. H. Sonntag and L. Brunsveld, *Chem. - A Eur. J.*, 2013, **19**, 10786–10793.

5   R. N. Shah, N. A. Shah, M. M. D. R. Lim, C. Hsieh, G. Nuber and S. I. Stupp, *Proc. Natl. Acad. Sci. U. S. A.*, 2010, **107**, 3293–3298.

6   A. Mata, Y. Geng, K. J. Henrikson, C. Aparicio, S. R. Stock, R. L. Satcher and S. I. Stupp, *Biomaterials*, 2010, **31**, 6004–6012.

7   N. A. Mansukhani, E. B. Peters, M. M. So, M. S. Albaghdadi, Z. Wang, M. R. Karver, T. D. Clemons, J. P. Laux, N. D. Tsihlis, S. I. Stupp and M. R. Kibbe, *Macromol. Biosci.*, 2019, **19**, 1900066.

8   R. Mammadov, B. Mammadov, S. Toksoz, B. Aydin, R. Yagci, A. B. Tekinay and M. O. Guler, *Biomacromolecules*, 2011, **12**, 3508–3519.

9   S. I. S. Hendrikse, S. P. W. Wijnands, R. P. M. Lafleur, M. J. Pouderoijen, H. M. Janssen, P. Y. W. Dankers and E. W. Meijer, *Chem. Commun.*, 2017, **53**, 2279–2282.

10   M. H. Bakker, R. E. Kieltyka, L. Albertazzi and P. Y. W. Dankers, *RSC Adv.*, 2016, **6**, 110600–110603.

11   R. C. van Gaal, B. D. Ippel, S. Spaans, M. I. Komil and P. Y. W. Dankers, *J. Polym. Sci.*, 2021, 1–14.

12   D. Straßburger, N. Stergiou, M. Urschbach, H. Yurugi, D. Spitzer, D. Schollmeyer, E. Schmitt and P. Besenius, *ChemBioChem*, 2018, **19**, 912–916.

13   K. Petkau-Milroy, M. H. Sonntag, A. H. A. M. Van Onzen and L. Brunsveld, *J. Am. Chem. Soc.*, 2012, **134**, 8086–8089.

14   K. Petkau-Milroy, M. H. Sonntag, A. Colditz and L. Brunsveld, *Int. J. Mol. Sci.*, 2013, **14**, 21189–21201.

15   M. K. Müller, K. Petkau and L. Brunsveld, *Chem. Commun.*, 2011, **47**, 310–312.

16   S. Cantekin, T. F. A. de Greef and A. R. A. Palmans, *Chem. Soc. Rev.*, 2012, **41**, 6125.

17   P. J. M. Stals, J. C. Everts, R. De Bruijn, I. A. W. Filot, M. M. J. Smulders, R. Martín-Rapún, E. A. Pidko, T. F. A. De Greef, A. R. A. Palmans and E. W. Meijer, *Chem. - A Eur. J.*, 2010, **16**, 810–821.

18   J. Van Herrikhuyzen, P. Jonkheijm, A. P. H. J. Schenning and E. W. Meijer, *Org. Biomol. Chem.*, 2006, **4**, 1539–1545.

19   C. M. A. Leenders, L. Albertazzi, T. Mes, M. M. E. Koenigs, A. R. A. Palmans and E. W. Meijer, *Chem. Commun.*, 2013, **49**, 1963–1965.

20   C. M. A. Leenders, M. B. Baker, I. A. B. Pijpers, R. P. M. Lafleur, L. Albertazzi, A. R. A. Palmans and E. W. Meijer, *Soft Matter*, 2016, **12**, 2887–2893.

21   X. Lou, R. P. M. Lafleur, C. M. A. Leenders, S. M. C. Schoenmakers, N. M. Matsumoto, M. B. Baker, J. L. J. van Dongen, A. R. A. Palmans and E. W. Meijer, *Nat. Commun.*, 2017, **8**, 15420.

22   X. Lou, S. M. C. Schoenmakers, J. L. J. van Dongen, M. Garcia-Iglesias, N. M. Casellas, M. Fernández-Castaño Romera, R. P. Sijbesma, E. W. Meijer and A. R. A. Palmans, *J. Polym. Sci.*, 2021, **59**, 1151–1161.

23   B. N. S. Thota, X. Lou, D. Bochicchio, T. F. E. Paffen, R. P. M. Lafleur, J. L. J. van Dongen, S. Ehrmann,

R. Haag, G. M. Pavan, A. R. A. Palmans and E. W. Meijer, *Angew. Chemie - Int. Ed.*, 2018, **57**, 6843–6847.

24 G. Morgese, B. F. M. Waal, S. Varela-Aramburu, A. R. A. Palmans, L. Albertazzi and E. W. Meijer, *Angew. Chemie*, 2020, **59**, 17382–17386.

25 M. H. Bakker, C. C. Lee, E. W. Meijer, P. Y. W. Dankers and L. Albertazzi, *ACS Nano*, 2016, **10**, 1845–1852.

26 S. I. S. Hendrikse, L. Su, T. P. Hogervorst, R. P. M. Lafleur, X. Lou, G. A. van der Marel, J. D. C. Codee and E. W. Meijer, *J. Am. Chem. Soc.*, 2019, **141**, 13877–13886.

27 S. P. W. Wijnands, W. Engelen, R. P. M. Lafleur, E. W. Meijer and M. Merkx, *Nat. Commun.*, 2018, **9**, 65.

28 K. Petkau-Milroy and L. Brunsveld, *European J. Org. Chem.*, 2013, 3470–3476.

29 J. Roosma, T. Mes, P. Leclère, A. R. A. Palmans and E. W. Meijer, *J. Am. Chem. Soc.*, 2008, **130**, 1120–1121.

30 J. J. Van Gorp, J. A. J. M. Vekemans and E. W. Meijer, *Mol. Cryst. Liq. Cryst.*, 2003, **397**, 191–205.

31 S. Bera, S. K. Maity and D. Haldar, *CrystEngComm*, 2014, **16**, 4834–4841.

32 N. San-José, A. Gómez-Valdemoro, S. Ibeas, F. C. García, F. Serna and J. M. García, *Supramol. Chem.*, 2010, **22**, 325–338.

33 S. Kumar, S. Bera, S. K. Nandi and D. Haldar, *Soft Matter*, 2021, **17**, 113–119.

34 M. U. Kassack, K. Braun, M. Ganso, H. Ullmann, P. Nickel, B. Böing, G. Müller and G. Lambrecht, *Eur. J. Med. Chem.*, 2004, **39**, 345–357.

35 M. Blomenhofer, S. Ganzleben, D. Hanft, H. W. Schmidt, M. Kristiansen, P. Smith, K. Stoll, D. Mäder and K. Hoffmann, *Macromolecules*, 2005, **38**, 3688–3695.

36 Y. Zhou, M. Xu, T. Yi, S. Xiao, Z. Zhou, F. Li and C. Huang, *Langmuir*, 2007, **23**, 202–208.

37 F. V. Gruschwitz, M. C. Fu, T. Klein, R. Takahashi, T. Higashihara, S. Hoeppener, I. Nischang, K. Sakurai and J. C. Brendel, *Macromolecules*, 2020, **53**, 7552–7560.

38 Y. Li, L. Dubreucq, B. G. Alvarenga, M. Raynal and L. Bouteiller, *Chem. - A Eur. J.*, 2019, **25**, 10650–10661.

39 M. J. Rust, M. Bates and X. Zhuang, *Nat. Methods*, 2006, **3**, 793–795.

40 B. Huang, M. Bates and X. Zhuang, *Annu. Rev. Biochem.*, 2009, **78**, 993–1016.

41 L. Albertazzi, D. van der Zwaag, C. M. A. Leenders, R. Fitzner, R. W. van der Hofstad and E. W. Meijer, *Science*, 2014, **344**, 491–495.

42 R. M. P. Da Silva, R. Van Der Zwaag, L. Albertazzi, S. S. Lee, E. W. Meijer and S. I. Stupp, *Nat. Commun.*, 2016, **7**, 1–10.

43 S. Pujals, N. Feiner-Gracia, P. Delcanale, I. Voets and L. Albertazzi, *Nat. Rev. Chem.*, 2019, **3**, 68–84.

44 L. Albertazzi, F. J. Martinez-Veracoechea, C. M. A. Leenders, I. K. Voets, D. Frenkel and E. W. Meijer, *Proc. Natl. Acad. Sci.*, 2013, **110**, 12203–12208.

45 M. Lange, A. L. Pettersen and K. Undheim, *Tetrahedron*, 1998, **54**, 5745–5752.

46 H. Sajiki, *Tetrahedron Lett.*, 1995, **36**, 3465–3468.

47 R. P. M. Lafleur, X. Lou, G. M. Pavan, A. R. A. Palmans and E. W. Meijer, *Chem. Sci.*, 2018, **9**, 6199–6209.

48 R. P. M. Lafleur, S. Herziger, S. M. C. Schoenmakers, A. D. A. Keizer, J. Jahzerah, B. N. S. Thota, L. Su, P. H. H. Bomans, N. A. J. M. Sommerdijk, A. R. A. Palmans, R. Haag, H. Friedrich, C. Böttcher and E. W. Meijer, *J. Am. Chem. Soc.*, 2020, **142**, 17644–17652.

49 J. J. Max and C. Chapados, *J. Chem. Phys.*, 2009, **131**, 184505.

50 J. J. Max and C. Chapados, *J. Chem. Phys.*, 2005, **122**, 014504.

51 J. J. Max and C. Chapados, *J. Chem. Phys.*, 2003, **119**, 5632–5643.

52 T. Aiba, M. Sato, D. Umegaki, T. Iwasaki, N. Kambe, K. Fukase and Y. Fujimoto, *Org. Biomol. Chem.*, 2016, **14**, 6672–6675.

53 S. Müller and R. Schmidt, *J. für Prakt. Chemie*, 2000, **342**, 779–784.

Chapter 7

The Interplay between Supramolecular Assemblies and Surfactants: from Disassembly to Co-assembly

Abstract: Nature has achieved a high level of functionality and adaptivity in its assemblies via the combination of structurally different building blocks. These properties are still lacking in synthetic supramolecular assemblies, limiting their application as biomaterials. Inspired by nature's approach, we investigate the possibility to combine two different self-assembling units: charged surfactants and benzene-1,3,5-tricarboxamides (BTAs). First, the influence of charged surfactants on supramolecular polymers based on BTAs with a tetra(ethylene glycol) periphery was explored. A detailed study on the interaction of the BTAs with cetyltrimethylammonium bromide (CTAB) revealed that the supramolecular polymers were disrupted by the intercalation of the surfactant but were reformed by dilution of the sample. This dilution-induced supramolecular polymerization phenomenon is not limited to CTAB as was evidenced with a library of surfactant molecules. In the second part, charged end groups were introduced onto C_3-symmetrical BTAs. The resulting BTAs only assemble into larger structures in the presence of surfactants with opposite charge. Finally, a C_2-symmetrical BTA was introduced, comprising one chiral hydrophobic and two charged side chains. These molecules assembled into small micelles in the absence of additives due to charge repulsion. In contrast, in the presence of salts, the hydrophobic interactions dominate such that the BTAs assembled into tubular structures as if they are surfactants. These surfactant interactions between the BTAs were turned off by the addition of a linear surfactant, resulting in the formation of supramolecular polymers via interactions of the BTA cores. With this, we show that biocompatible materials with unique morphologies and stimuli-responsiveness can be obtained using the various interactions between BTAs and surfactants and by influencing the balance between attractive non-covalent interactions and repulsive electrostatic interactions.
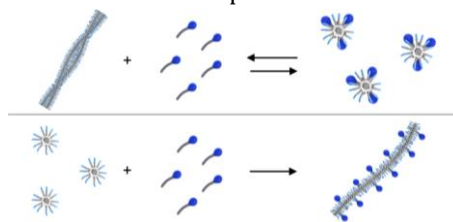
7.1 Introduction

Nature combines structurally different building blocks to create complex, multicomponent materials with tunable functions. The cell membrane is such a multicomponent system that contains phospholipids for the formation of the bilayer, cholesterol for the control of the fluidity and organization of the bilayer, and proteins for the introduction of biological functions.[1,2] All of these components cooperate via non-covalent interactions such that the cell membrane is a structure that is dynamic and functional. In contrast, synthetic multicomponent systems generally contain building blocks with identical core structures.[3–5] For example, functional supramolecular polymers were obtained from the co-assembly of covalently-functionalized peptide amphiphiles[6,7] or discotic molecules[8] with their unfunctional counterparts. Examples of multicomponent supramolecular polymers with structurally different building blocks still depend on identical directional interactions such as hydrogen bonds.[9–11] This limits the responsiveness of the supramolecular assemblies and does not match with the high level of complexity and functionality found in nature.

Inspired by nature, we therefore aim to create multicomponent systems using structurally different supramolecular self-assembly motifs that can be combined. We select surfactants as the first component since these assemble into larger structures above their critical aggregation concentration (CAC) via non-directional hydrophobic interactions. The morphology of those assemblies is dictated by the packing parameter of the surfactants (Chapter 1).[12] The second component, benzene-1,3,5-tricarboxamides (BTAs), assemble via directional hydrogen bonds. Although the two types of interactions differ, we envision that both types of molecules can interact via hydrophobic interactions. The use of charged surfactants thereby adds responsiveness to salt concentrations and pH[13] to the two-component systems and it stimulates the cellular uptake of the supramolecular materials.[14]

The introduction of charges adds new challenges to supramolecular self-assembly in water as it results in repulsive electrostatic interactions that act over longer distances. The concept of frustrated self-assembly explores the balance of attractive non-covalent interactions (e.g. hydrogen bonding, π-π stacking and hydrophobic interactions) with repulsive interactions (e.g. electrostatic or steric effects).[15] Supramolecular assemblies with controlled shape, size and stability were obtained by fine-tuning this delicate balance.[16–21] The screening of charges by the addition of salts is a well-known strategy to diminish repulsive electrostatic interactions, not only for supramolecular polymerization[22] but also for example for the assembly of surfactants[23–25] and the complexation of polyelectrolytes.[26] The Debye length, κ^{-1}, is a measure for the radius of the ionic atmosphere around an ion which is proportional to the concentration of counterions that can screen the central ion.[27] For a solution of 1-1 electrolytes, such as monovalent salts, this Debye length can be calculated with:

$$\kappa^{-1} = \frac{0.304 \text{ nm M}^{1/2}}{\sqrt{c_s}} \qquad (7.1)$$

with κ^{-1} the Debye length in nm and c_s the salt concentration in M. Increasing the concentration of screening salts therefore leads to a decrease of the Debye length, meaning that repulsive interactions act over a shorter distance. In order to promote the formation of larger supramolecular assemblies from charged moieties, the electrostatic screening should be sufficient such that the strength of the attractive interactions surpasses that of the repulsive interactions. Not only the concentration of salts influences electrostatic screening, but also the nature of the salts. The Hofmeister series organizes different salts based on their capability to stabilize a protein[28] and similar trends were later observed in other fields.[29–31] It is therefore expected that different salts can have different effects on supramolecular self-assembly.

In this chapter, several different examples of the mixing of BTAs with linear charged surfactants will be discussed. First, we investigate if surfactants can interact with supramolecular polymers of BTAs with a tetra(ethylene glycol) periphery. We demonstrate that this results in a surprising case of dilution-induced supramolecular polymerization. In the next part, the self-assembly of C_3-symmetrical charged BTAs is described in which surfactants play a crucial role in the formation of larger assemblies. Finally, the properties of BTAs and surfactants are combined in one molecule to reveal some interesting supramolecular morphologies, which can be achieved by switching between directional supramolecular interactions and surfactant interactions. The results presented here will provide new ways to create complex materials with tunable properties.

7.2 The interaction of charged surfactants with tetra(ethylene glycol)-based supramolecular polymers

Multicomponent supramolecular assemblies can be obtained from various building blocks as long as their interactions are compatible. Compatibility is often ensured when additives have identical core structures and interactions,[4,32] but examples exist of supramolecular co-assemblies with a small mismatch in core structure.[33,34] However, the molecular structure of BTAs and surfactants could not be more different and their compatibility should be studied in order to create multicomponent assemblies.

The mixing of discotic supramolecular building blocks and surfactants has only sparsely been studied. Previous experiments of 1,3,5-cyclohexyltricarboxamides with charged surfactants did not reveal any interaction and instead resulted in interpenetrating networks of supramolecular polymers and surfactant assemblies.[35–38] However, the structure of those 1,3,5-cyclohexyltricarboxamide building blocks lacks the linear hydrophobic chains that are present in our design of water-compatible BTA molecules. **BTA-C$_{12}$-EG$_4$** (Figure 1) is known to assemble into micrometer long fibers via intermolecular hydrogen bonds between the amides which are protected from the solvent by a hydrophobic pocket.[39] This hydrophobic pocket has been shown to accommodate other molecules via hydrophobic interactions, such as the

solvatochromic dye Nile Red.[40] Dr. Jesús Mosquera and Cyprien Muller provided the first proof that **BTA-C$_{12}$-EG$_4$** can interact with charged surfactants at a hydrogel concentration. Additional experiments in dilute conditions were performed by me in collaboration with dr. Lu Su and ir. Marle Vleugels and the most important results are presented here with the aim to gain a better understanding of the interactions between BTAs and surfactants. The surfactant cetyltrimethylammonium bromide (CTAB, Figure 1) was selected for those experiments as it is hypothesized that its hexadecyl chain is long enough to intercalate in the hydrophobic pocket of the BTA assemblies such that interactions can be studied.
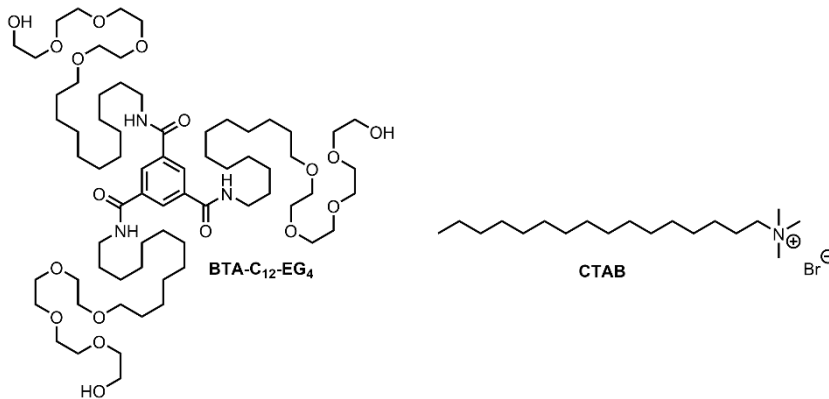
Figure 1. Chemical structure of **BTA-C$_{12}$-EG$_4$** and CTAB.

First, the interaction between **BTA-C$_{12}$-EG$_4$** and CTAB was studied with UV and ^{1}H NMR spectroscopy. All experiments were conducted at a BTA concentration of 250 µM to prevent micellization of CTAB (CAC = 1 mM)[41] and to ensure its interaction with the BTAs. The UV spectrum of **BTA-C$_{12}$-EG$_4$** in the absence of CTAB is characterized by absorption maxima at 211 and 229 nm.[40] These maxima remain present when 1 equivalent of CTAB is added, but the maximum at 229 nm starts to decrease with 2 equivalents of CTAB (Figure 2A). The spectrum completely shifts and only shows a maximum at 194 nm with 3 equivalents of CTAB. This spectrum does not match with the molecularly dissolved state of **BTA-C$_{12}$-EG$_4$**, suggesting that the aggregation state of the BTA has changed upon addition of 3 equivalents of CTAB. The ^{1}H NMR spectrum of **BTA-C$_{12}$-EG$_4$** in D$_2$O does not show any resonance peaks as the BTAs are contained in larger assemblies, whereas the spectrum of CTAB below its CAC contains sharp, well-defined peaks (Figure 2B). The peaks of CTAB disappear when 1 equivalent of this surfactant is added to the BTA, indicating that the surfactant is taken up in the BTA assemblies. However, broad signals of both the BTA and CTAB become visible upon increasing the amount of CTAB. It seems that CTAB is completely incorporated into the BTA fibers up to 1 equivalent, but at higher equivalents both molecules show a higher tumbling rate, revealing the presence of smaller assemblies.
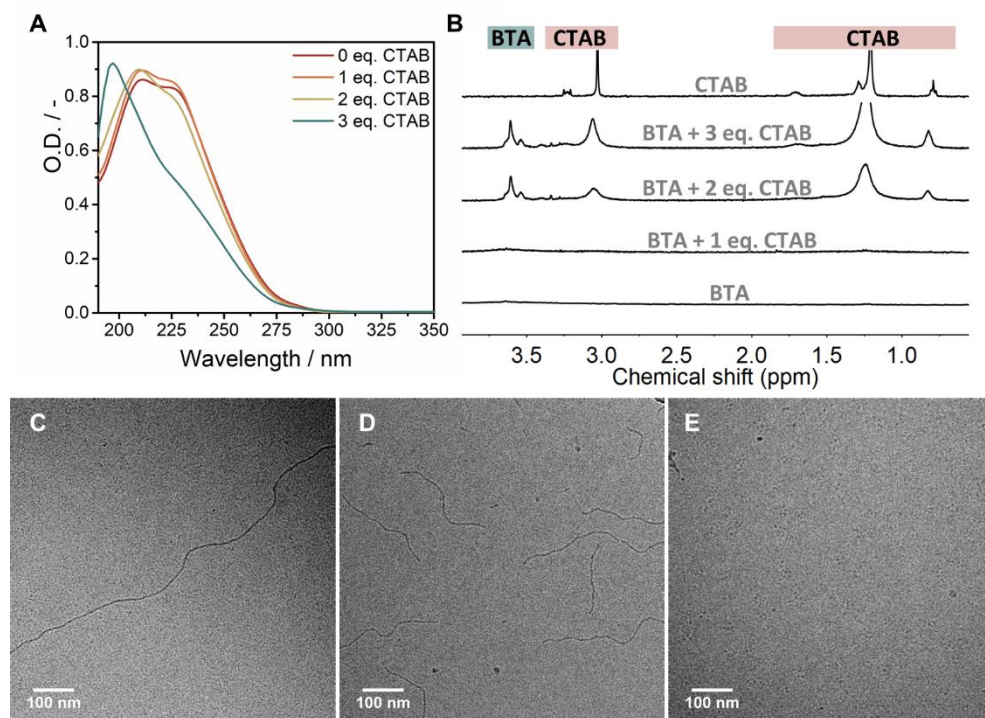
Figure 2. (A) UV spectrum of **BTA-C$_{12}$-EG$_4$** in water with different equivalents of CTAB (c_{BTA} = 250 µM, l = 1 mm, T = 20 °C). (B) ^{1}H NMR (400 MHz) of CTAB (c = 250 µM) and **BTA-C$_{12}$-EG$_4$** (c = 250 µM) with 0, 1, 2 and 3 equivalents of CTAB in D$_2$O (T = 20 °C). (C-E) CryoTEM images of **BTA-C$_{12}$-EG$_4$** in water with (C) 1, (D) 2 and (E) 3 equivalents of CTAB (c_{BTA} = 250 µM).

Cryogenic transmission electron microscopy (cryoTEM) was used to study changes in the morphology of the supramolecular polymers when mixed with CTAB. Micrometer long supramolecular polymers are observed when 1 equivalent of CTAB was added (Figure 2C), resembling images made in the absence of CTAB (Chapter 2). The polymers become significantly shorter, only a few hundreds of nanometers in length, when the amount of CTAB is increased to 2 equivalents (Figure 2D). At 3 equivalents only small spherical assemblies are observed (Figure 2E) and occasionally a short fiber. The combined spectroscopy and microscopy results indicate that **BTA-C$_{12}$-EG$_4$** can accommodate one equivalent of CTAB without disruption of the polymers. Aggregation is still observed with 2 equivalents of CTAB, although microscopy reveals shorter assemblies and ^{1}H NMR suggests that not all BTAs are confined in ordered supramolecular polymers. Finally, with 3 equivalents of CTAB the polymers of **BTA-C$_{12}$-EG$_4$** seem to be disrupted into small micellar aggregates. The disruption of the fibers is attributed to repulsion of the charged headgroups of the surfactants, which come in close proximity when interacting with the BTAs. Small micelles are formed when the

charge repulsion becomes too strong at high surfactant concentrations as the charge separation is more efficient in this morphology.

Surprisingly, the disruption of the fibers by CTAB was found to be reversible upon dilution. The typical UV absorption bands of **BTA-C$_{12}$-EG$_4$** at 211 and 229 nm reappear upon 2-fold or 5-fold dilution of a sample containing 3 equivalents of CTAB (Figure 3A). The ratio between the two peaks has not fully recovered after overnight equilibration, which suggests that aggregation has not fully recovered. The reformation of the supramolecular polymers was confirmed with cryoTEM (Figure 3B). It is hypothesized that CTAB is released upon dilution as the overall concentration decreases, thereby enabling the elongation of the BTA fibers over time. The higher the dilution ratio, the faster the recovery of the supramolecular polymers is observed. Such a dilution-induced supramolecular polymerization[42] has not yet been described in water.
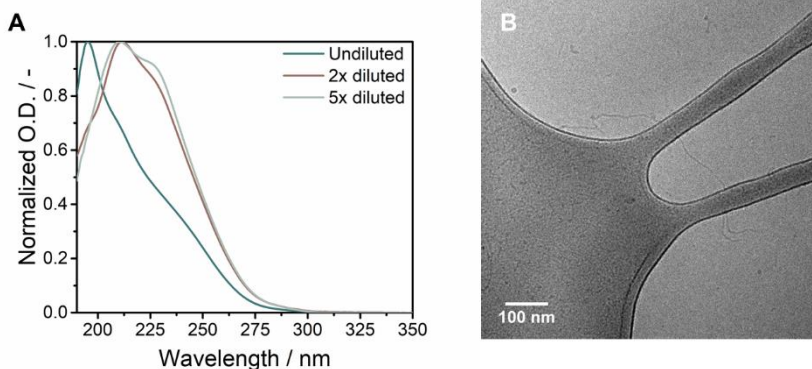
Figure 3. (A) Normalized UV spectrum of **BTA-C$_{12}$-EG$_4$** in water with 3 equivalents of CTAB before and after dilution ($c_{BTA, initial}$ = 250 μM, $c_{CTAB, initial}$ = 750 μM, l = 1mm or 1 cm, T = 20 °C). (B) CryoTEM image of a 2-fold diluted sample of **BTA-C$_{12}$-EG$_4$** in water with 3 equivalents of CTAB ($c_{BTA, initial}$ = 250 μM, $c_{CTAB, initial}$ = 750 μM). All samples were equilibrated overnight.

Several cationic surfactants with shorter hydrophobic chains and an anionic surfactant were selected to study if the disruption of the supramolecular polymers and the subsequent dilution-induced supramolecular polymerization is a generally applicable phenomenon (Figure 4A). All surfactants were used below their CAC. UV and ^{1}H NMR spectra of **BTA-C$_{12}$-EG$_4$** with hexyltrimethylammonium bromide (HTAB), octyltrimethylammonium bromide (OTAB) and dodecyltrimethylammonium bromide (DTAB) show that the BTA molecules are assembled in large structures, even in the presence of 10 equivalents of surfactant. CryoTEM images indeed reveal that the long supramolecular polymers of **BTA-C$_{12}$-EG$_4$** are still present when 10 equivalents of these surfactant are added (Figure 4B-D). It should be noted that the ends of a few fibers can be observed in all images, indicating a slight decrease in the length of the supramolecular polymers due to interaction with the surfactants. The addition of 1 equivalent of sodium dodecyl sulfate (SDS, CAC = 8.2 mM[43]) does not seem to affect the UV spectrum of **BTA-C$_{12}$-EG$_4$** (Figure 4E) but cryoTEM images show that the fibers are

significantly shorter at this concentration (Figure 4F). The absorbance maximum at 229 nm decreases when the amount of SDS is increased and a shoulder starts to appear at 195 nm in the sample with 8 equivalents of surfactant. When 9 or 10 equivalents of SDS are added the UV spectrum is characterized by a maximum at 195 nm, resembling the spectrum of **BTA-C$_{12}$-EG$_4$** with 3 equivalents of CTAB. CryoTEM images confirm the absence of supramolecular polymers when the BTA is mixed with 10 equivalents of SDS (Figure 4G). The disruption of the supramolecular polymers by 10 equivalents of SDS allows for dilution-induced supramolecular polymerization, as is evidenced by UV spectroscopy (Figure 4E). The diluted sample with SDS has to be equilibrated for 1 week for the recovery of the typical spectrum of supramolecular polymers.
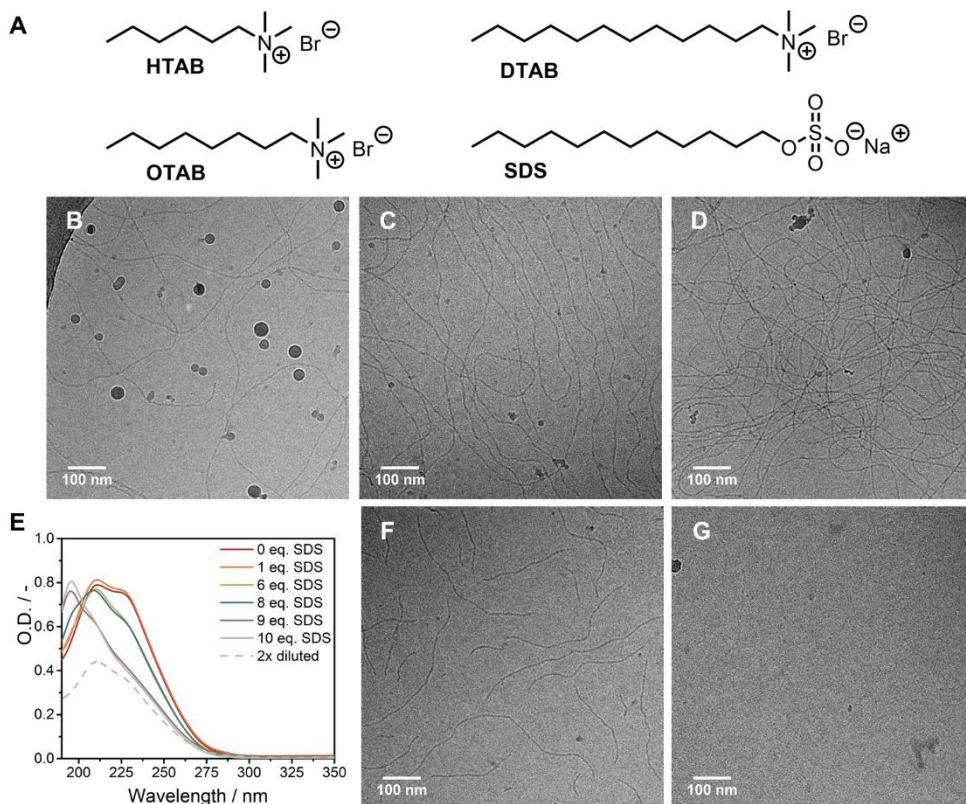
Figure 4. (A) Chemical structure of HTAB, OTAB, DTAB and SDS. (B-D) CryoTEM images of **BTA-C$_{12}$-EG$_4$** in water with 10 equivalents (B) HTAB, (C) OTAB and (D) DTAB (c_{BTA} = 250 μM, $c_{surfactant}$ = 2.5 mM). The dark spherical objects are crystalline ice particles. (E) UV spectrum of **BTA-C$_{12}$-EG$_4$** in water with different equivalents of SDS (c_{BTA} = 250 μM, l = 1 mm, T = 20 °C). The sample with 10 equivalents of SDS was diluted 2-fold and the spectrum was recorded after 1 week of equilibration ($c_{BTA, initial}$ = 250 μM, $c_{SDS, initial}$ = 2.5 mM, l = 1 mm, T = 20 °C). (F-G) CryoTEM images of **BTA-C$_{12}$-EG$_4$** in water with (F) 1 and (G) 10 equivalents of SDS (c_{BTA} = 250 μM).

In conclusion, several charged surfactants were shown to interact with **BTA-C$_{12}$-EG$_4$**. **BTA-C$_{12}$-EG$_4$** is not charged at the conditions studied here, suggesting that the interactions between the BTA and the surfactants come from hydrophobic interactions between the hydrophobic pocket of the BTA and the alkyl chain of the surfactants. From the cationic surfactants studied here, only CTAB was able to disrupt the supramolecular polymers, whereas shorter surfactants only slightly decreased the polymer length. This indicates that the length of the alkyl chain of the surfactant determines the capability of the surfactant to disrupt the polymers. The cationic surfactant DTAB cannot break the supramolecular assemblies, whereas the anionic surfactant SDS can. Both surfactants have the same hydrophobic chain length, indicating that also the charged groups influence the disruption of the assemblies. The charge on CTAB is fixed on the nitrogen atom, whereas the charge on SDS can be delocalized between three oxygen atoms. This latter arrangement results in a better spread and a higher accessibility of the charge which could be beneficial for the disruption of supramolecular assemblies. An anionic surfactant with hexadecyl chain may have stronger hydrophobic interactions with the supramolecular polymer but the CAC of the surfactants drastically decreases when increasing the length of the alkyl chain, complicating the analysis in solution. Both SDS and CTAB can be used for dilution-induced supramolecular polymerization, although more equivalents of SDS are needed and the subsequent polymerization takes longer due to a difference in molecular structure. By varying the hydrophobic chain length and the nature of the polar headgroups of the surfactants, various stimuli-responsive materials can be obtained as will be illustrated in Chapter 8.

7.3 The surfactant-assisted assembly of *C*$_3$-symmetrical charged BTAs

So far, it has been shown that the addition of a charged surfactant to BTA-based polymers leads to the disassembly of the supramolecular polymer. We wondered if the opposite can also be achieved, namely to use surfactants to induce the formation of large supramolecular assemblies. We envisioned that charged surfactants could stimulate the assembly of oppositely charged supramolecular building blocks. Charged moieties have previously been used as the water-soluble periphery for peptide amphiphiles,[44,45] rosette nanotubes[46,47] and discotic-based supramolecular polymers.[16,48] An advantage of the introduction of charged groups is that they enable control over the degree of supramolecular aggregation and the morphology of the assemblies with variations in pH[16,18,48–55] and ionic strength.[16,18,22,56,57] Such stimuli-responsiveness has not been introduced into our water-compatible BTA-based supramolecular polymers yet but could be a valuable tool in the creation of multicomponent biomaterials. Additionally, it could stimulate the cellular uptake of our supramolecular assemblies.[14,58] The design of the BTAs was therefore adapted to contain three charged groups at the end of their hydrophobic chains. For simplicity,

charged groups that do not respond to variations in pH will be used, such as trimethylammonium (TMA) and sulfonate groups. The self-assembly of these new BTAs will be studied here in presence of salts and oppositely charged surfactants.

C_3-symmetrical charged BTAs were synthesized by dr. Lu Su and dr. Jesús Mosquera with thiol-ene click chemistry as it is a straightforward method for the introduction of small functional groups.[59–61] This requires a BTA platform with alkene groups at the end of each arm. A side chain with alkene and amine functionality was obtained via Gabriel synthesis on the bromide of 11-bromo-1-undecene, affording **1** (Scheme 1), followed by its reaction with hydrazine to yield primary amine **2**. The side chains were then coupled to 1,3,5-benzenetricarbonyl trichloride, yielding BTA click platform **3**. Thiol-functionalized charged moieties were subsequently coupled to this platform via thiol-ene click chemistry using 2-dimethoxy-2-phenylacetophenone (DMPA) as a photoinitiator and by irritating the reaction mixture with UV light of 365 nm. A BTA with three TMA groups was obtained following the reaction of **3** with thiocholine chloride **4**, yielding **BTA-C$_{11}$-TMA$_3$** (Scheme 1). These new compounds were fully characterized with ^{1}H NMR, ^{13}C NMR, FT-IR spectroscopy and mass spectrometry (see section 7.6.3).
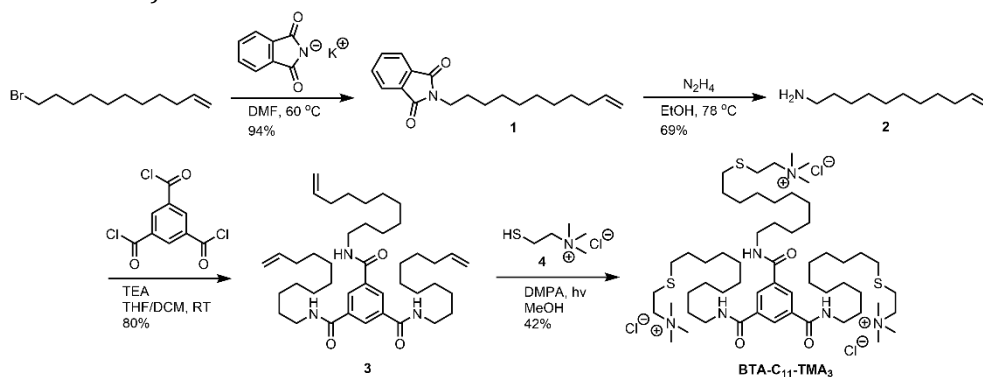
Scheme 1. Synthesis of **BTA-C$_{11}$-TMA$_3$** via thiol-ene click chemistry.

The self-assembly of the newly synthesized **BTA-C$_{11}$-TMA$_3$** was first tested in pure water with UV spectroscopy and static light scattering (SLS). A maximum UV absorbance is observed at 206 nm (Figure 5A), which does not correspond to previously studied elongated supramolecular polymers. However, this spectrum in does not overlap with the spectrum of the molecularly dissolved state in ACN, indicating that there is some aggregation of **BTA-C$_{11}$-TMA$_3$** molecules in water. SLS showed the presence of small anisotropic assemblies (Figure 5B). The repulsive electrostatic interactions between the trimethylammonium groups of **BTA-C$_{11}$-TMA$_3$** thus hamper elongation of the assemblies into supramolecular polymers. Small micellar BTA assemblies are formed instead as this allows for distribution of the charge in more directions.

Various salts were added to **BTA-C₁₁-TMA₃** in an attempt to screen the repulsive charges between the side chains. The absorption maximum remains at 206 nm upon addition of 10 mM NaCl or NaOAc, whereas it shifts to 202 nm in the presence of 10 mM Na_2SO_4 (Figure 5A). The size of the assemblies does not increase upon addition of any of the salts as is corroborated with SLS (Figure 5B). Similar results were obtained for other concentrations of salts in the range from 0.5 mM to 1 M, corresponding to Debye screening lengths from 13.6 nm to 0.3 nm as calculated with equation 7.1. The screening of the electrostatic interactions between the TMA groups seems to be insufficient to diminish the repulsive interactions and for the attractive interactions to dominate the self-assembly.
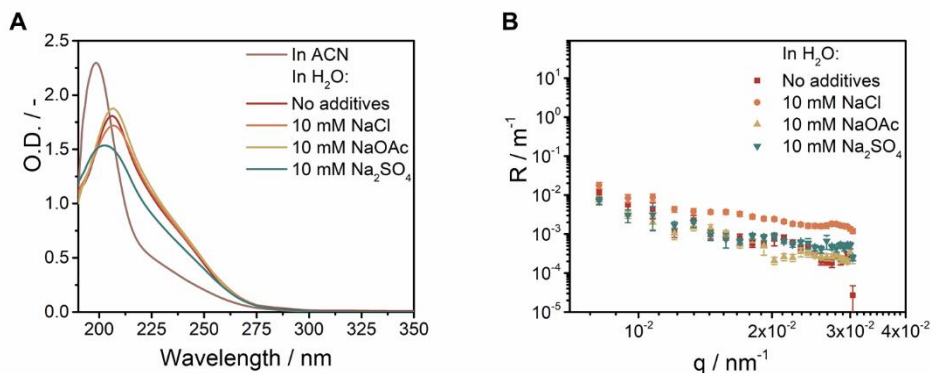
Figure 5. (A) UV spectrum of **BTA-C₁₁-TMA₃** in ACN (c_{BTA} = 50 μM, l = 1 cm, T = 20 °C) and in water with various salts (c_{BTA} = 500 μM, l = 1 mm, T = 20 °C). (B) Rayleigh ratio as a function of the scattering vector for **BTA-C₁₁-TMA₃** in water with various salts (c_{BTA} = 500 μM, l = 1 cm, λ = 532 nm, T = 20 °C).

We hypothesize that the intermolecular hydrogen bonds between **BTA-C₁₁-TMA₃** molecules are not sufficiently protected by a hydrophobic pocket to allow for the formation of elongated supramolecular assemblies. The alkyl chains of surfactants could in theory provide some additional hydrophobic interactions that promote the formation of larger assemblies. Therefore, an anionic surfactant such as SDS may compensate for the charge repulsion in **BTA-C₁₁-TMA₃** assemblies and at the same time induce additional hydrophobic interactions such that larger assemblies will be formed. UV spectra of **BTA-C₁₁-TMA₃** reveal a shift of the absorption maximum from 206 nm to 193 nm upon addition of at least 1 equivalent of SDS (Figure 6A). SLS confirmed that large anisotropic assemblies are formed at all concentrations of SDS studied (Figure 6B), confirming that SDS promotes the formation of larger supramolecular assemblies.
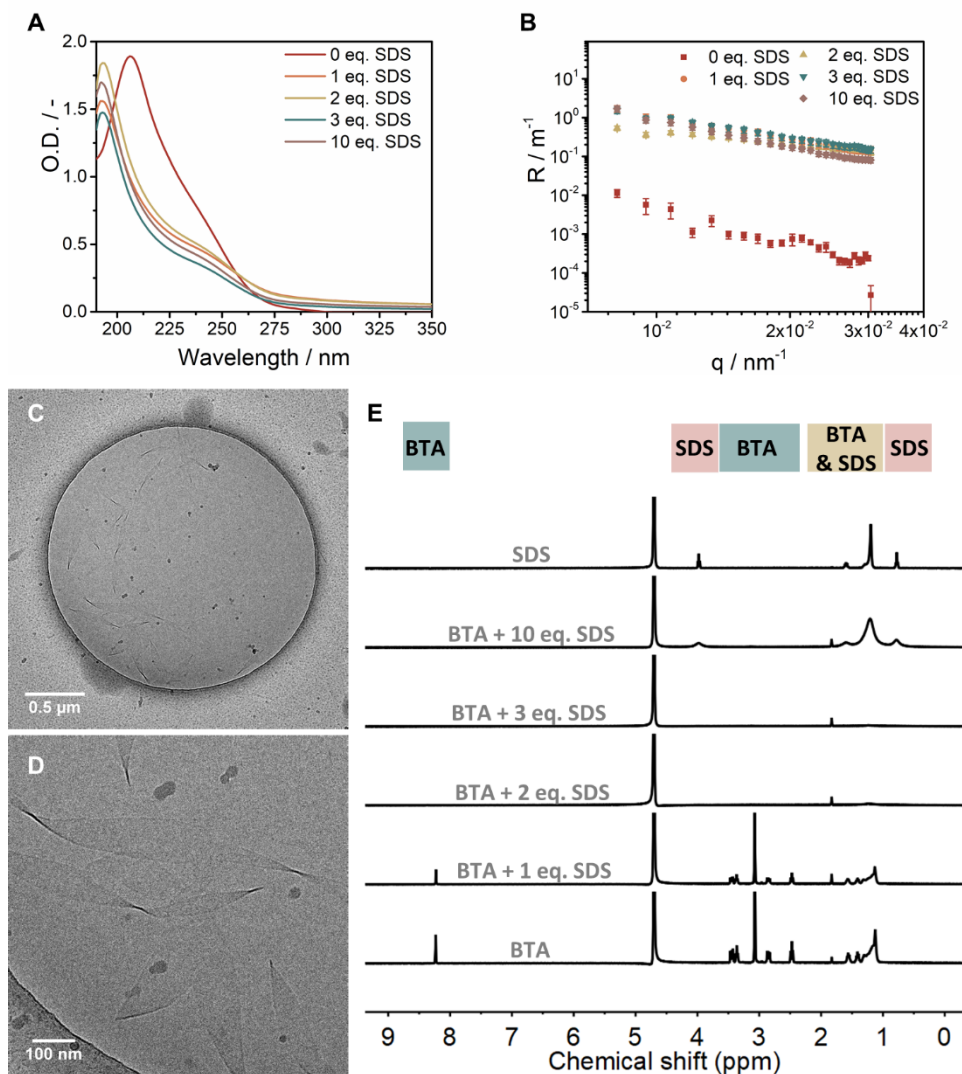
Figure 6. (A) UV spectrum of **BTA-C₁₁-TMA₃** in water with different equivalents of SDS (c_{BTA} = 500 μM, l = 1 mm, T = 20 °C). (B) Rayleigh ratio as a function of the scattering vector for **BTA-C₁₁-TMA₃** in water with various equivalents of SDS (c_{BTA} = 500 μM, l = 1 cm, λ = 532 nm, T = 20 °C). (C-D) CryoTEM images of **BTA-C₁₁-TMA₃** in water with 2 equivalents of SDS (c_{BTA} = 500 μM, c_{SDS} = 1 mM). (E) ^{1}H NMR (400 MHz) of SDS (c = 500 μM) and **BTA-C₁₁-TMA₃** (c = 500 μM) with different equivalents of SDS in D₂O (T = 20 ºC). The peak at 4.72 ppm corresponds to H₂O and the peak at 1.83 ppm to HOD.

Both the UV and SLS spectra of **BTA-C₁₁-TMA₃** with SDS suggest a morphology that differs from the double helix structures observed for **BTA-C₁₂-EG₄**, prompting us to further study the assemblies. CryoTEM images reveal the presence of twisted sheets

(Figure 6C-D) with large variations in their dimensions. The length of those assemblies ranges between 100 nm and several micrometers and the diameter between 30 and 100 nm. The interaction between the BTA and SDS was further studied with ^{1}H NMR spectroscopy. **BTA-C$_{11}$-TMA$_3$** and SDS both show sharp peaks in D$_2$O due to the absence of larger assemblies (Figure 6E). The characteristic peaks of SDS disappear when one equivalent is added to **BTA-C$_{11}$-TMA$_3$**, indicating that all of the SDS is taken up into larger BTA assemblies. However, the peaks of the BTA remain visible at this concentration, albeit with a lower intensity, from which it can be concluded that 1 equivalent of SDS is not sufficient to assemble all BTAs into the twisted sheets. The peaks of the BTA are absent with 2 and 3 equivalents of SDS, suggesting that all molecules are contained in the larger assemblies. Broader peaks of SDS reappear in the spectrum of **BTA-C$_{11}$-TMA$_3$** with 10 equivalents of SDS. From this spectrum it can be concluded that there is a limit to the amount of SDS that can be accommodated in the assemblies of the BTA. Since the peaks of the BTA are not observed in this spectrum it can be concluded that there is no disruption of assemblies due to an excess of surfactant.

The addition of SDS not only reduced the repulsive interactions between the charged BTAs, but it also provided additional attractive hydrophobic interactions such that the barrier for elongation was overcome. Based on the results we hypothesize that the surfactants assist the BTAs to stack on one another via intermolecular hydrogen bonding and that several of those BTA stacks interact laterally to create a sheet-like structure. The curvature in the sheet might originate from the angle between the hydrogen bonding amides of consecutive monomers. The lateral interactions between water-compatible BTAs, that result in the formation of sheet-like structures, have only been reported once before.[62]

The surfactant-assisted self-assembly is not limited to the cationic **BTA-C$_{11}$-TMA$_3$**. An anionic sulfonate group was introduced on BTA click-platform **3** to yield **BTA-C$_{11}$-Sulf$_3$** (Figure 7A). This BTA also does not assemble into larger structures in pure water or upon addition of salts. Only in the presence of CTAB the molecules assemble into twisted ribbons (Figure 7B). The length of those assemblies varies between 100 nm and several micrometers, similar to **BTA-C$_{11}$-TMA$_3$**. However, the diameter is around 10 nm hence the term ribbons instead of sheets as used for the cationic BTA. The difference in diameter of the assemblies of **BTA-C$_{11}$-TMA$_3$** and **BTA-C$_{11}$-Sulf$_3$** with surfactants could be related to the different presentation of the charges on the BTAs or the difference in the length of the alkyl chain on the surfactant. Further research is needed to determine the origin of this difference.

A similar thiol-ene click platform was designed for triphenylene-2,6,10-tricarboxamides (TTA) and trimethylammonium groups were attached to create **TTA-C$_{11}$-TMA$_3$** (Figure 7C). Since the molecule did not assemble into larger assemblies in pure water, SDS was added to assemble the TTAs into twisted ribbons (Figure 7D). The length of those assemblies, only a few hundred nanometers, is significantly shorter than of the BTAs. These shorter structures are a results of a lower aggregation propensity of

the TTAs compared to the BTAs since no longer assemblies have been observed for TTAs in water so far (Chapter 2). From these results it can be concluded that the surfactant-assisted assembly is not limited to BTA monomers but is applicable to other supramolecular building blocks as well.
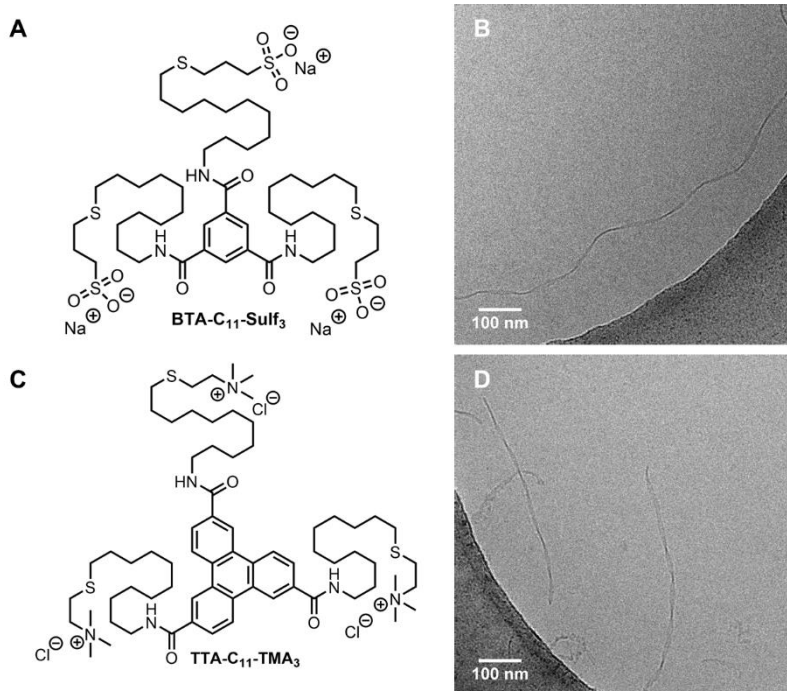
Figure 7. (A) Chemical structure of **BTA-C$_{11}$-Sulf$_3$**. (B) CryoTEM image of **BTA-C$_{11}$-Sulf$_3$** in water with 1 equivalent of CTAB (c$_{BTA}$ = 500 µM, c$_{CTAB}$ = 500 µM). (C) Chemical structure of **TTA-C$_{11}$-TMA$_3$**. (D) CryoTEM image of **TTA-C$_{11}$-TMA$_3$** in water with 1 equivalent of SDS (c$_{TTA}$ = 500 µM, c$_{SDS}$ = 500 µM).

7.4 The self-assembly of a surfactant-like BTA

Previous sections showed that surfactants can promote either disassembly or assembly of BTA-based supramolecular assemblies. The addition of surfactants can be used as a strategy to switch between small micelles and large elongated assemblies and vice versa. Whereas our systems are limited to two morphological states, van Esch *et al* reported controlled morphological transitions between tape-like structures, fibers and micelles using 1,3,5-cyclohexyltricarboxamides with a surfactant-like chain covalently attached to it.[63,64] These multisegmented building blocks assemble into tape-like structures via hydrogen bonding of the core amides and hydrophobic interactions of their octyl chain. The hydrophobic interactions were turned off upon addition of the surfactant tetra(ethylene glycol) mono-octyl ether, resulting in fiberous structures. Finally, hexafluorisopropyl alcohol disrupted the intermolecular hydrogen bonds,

leading to the formation of small micelles via hydrophobic interactions of the octyl chain.[64] Similarly, the group of Brendel synthesized BTAs with one hydrophilic side chain and two linear alkyl chains.[65] They showed that these molecules assemble as a surfactant with a morphology that depends on the packing parameter as determined by the length of the hydrophobic chains. Inspired by these publications we redesigned our BTA with sulfonate groups to comprise one hydrophobic (S)-dihydrocitronellyl chain (**BTA-C₁₁-Sulf₂**, Scheme 2). This C_2-symmetric BTA resembles a surfactant with one hydrophobic chain and two hydrophilic headgroups. We hypothesize that this BTA comprises the ability to assemble via intermolecular hydrogen bonds of the BTA core and via hydrophobic interactions of the (S)-dihydrocitronellol chain. We aim to obtain new morphologies based on both interactions, which can be switched by external stimuli such as salt and surfactant concentration.

7.4.1 Synthesis of BTA-C₁₁-Sulf₂ and its self-assembly in water

The synthesis of **BTA-C₁₁-Sulf₂** was performed by dr. Pongphak Chidchob and is based on thiol-ene click chemistry, similar to the synthesis of the C_3-symmetrical charged BTAs. Two alkene-functionalized side chains **2** were coupled to the carboxylic acids of 5-methoxycarbonyl-benzene-1,3-dicarboxylic acid, yielding **5** (Scheme 2). After deprotection of the third carboxylic acid group a (S)-dihydrocitronellol chain was coupled to **6**, resulting in click platform **7**. Finally, **BTA-C₁₁-Sulf₂** was obtained after the coupling of 3-mercapto-1-propanesulfonate to **7** via thiol-ene click chemistry with DMPA as photoinitiator. These new compounds were fully characterized with ¹H NMR, ¹³C NMR, FT-IR spectroscopy and mass spectrometry (see section 7.6.3).
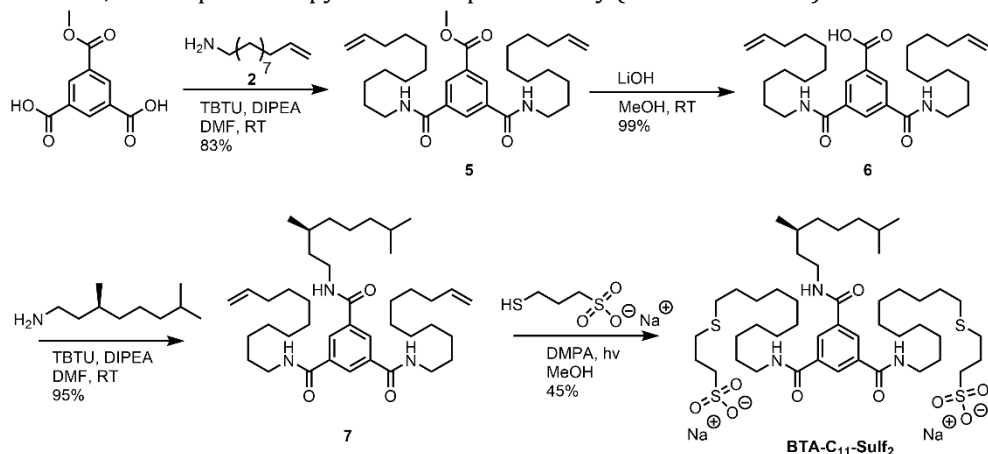
Scheme 2. Synthesis of **BTA-C₁₁-Sulf₂**.

First, the self-assembly of **BTA-C₁₁-Sulf₂** was studied without additives. This BTA shows a broad absorbance peak with a maximum at 198 nm in water and a narrower absorbance peak at 207 nm in the molecularly dissolved state in MeOH (Figure 8A). The

difference between those UV spectra suggests that **BTA-C₁₁-Sulf₂** aggregates in water but the origin of this aggregation requires investigation. The introduction of the (S)-dihydrocitronellol chain makes it possible to use CD spectroscopy for the characterization of the assemblies. **BTA-C₁₁-Sulf₂** shows a small exciton coupled Cotton effect with a positive CD signal at 198 nm and a negative CD signal at 225 nm; such distinct signals are absent in MeOH (Figure 8B). SLS measurements of aqueous samples reveal the formation of small assemblies, as is confirmed by cryoTEM (Figure 8C). The microscopy images reveal that **BTA-C₁₁-Sulf₂** assembles into small micelles in water. The presence of a CD signal and the difference in absorption spectra between water and MeOH suggest that the formation of the micelles is driven by weak hydrogen bonds between the BTA cores, rather than via hydrophobic interactions of the (S)-dihydrocitronellol chain.
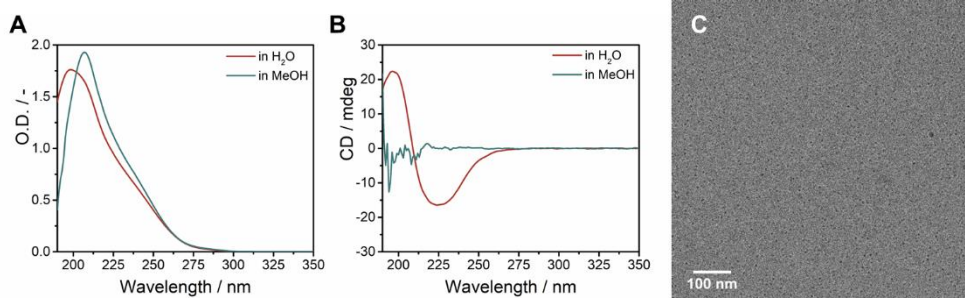
Figure 8. (A) UV spectrum of **BTA-C₁₁-Sulf₂** in water and MeOH (c_{BTA} = 500 μM, l = 1 mm, T = 20 °C). (B) CD spectrum of **BTA-C₁₁-Sulf₂** in water and MeOH (c_{BTA} = 500 μM, l = 1 mm, T = 20 °C). (C) CryoTEM image of **BTA-C₁₁-Sulf₂** in water (c_{BTA} = 500 μM). The larger black sphere on the right is a crystalline ice particle.

7.4.2 The assembly of BTA-C₁₁-Sulf₂ with salts

We expect that **BTA-C₁₁-Sulf₂** cannot assemble into larger structures due to insufficient screening of the charge repulsion, similar to the C_3-symmetrical charged BTAs. We therefore studied if additional salts can screen the electrostatic interactions and stimulate the formation of larger assemblies. First, the addition of different amounts of NaCl to a 500 μM sample of **BTA-C₁₁-Sulf₂** in water was evaluated with UV and CD spectroscopy (Figure 9A-B). The UV spectrum shifts to a narrower band with a maximum at 196 nm upon addition of 1 or 2 mM of NaCl and the CD signal slightly increases in intensity. Shoulders appear in the UV spectrum at 211 and 230 nm with 10 mM of NaCl but the maximum remains at 196 nm. The CD signal has increased and completely shifted at this concentration of NaCl to a positive signal at 209 nm, negative signal at 230 nm and a small positive signal at 263 nm. Further increase of the NaCl concentration to 25 mM or 50 mM results in clear absorption maxima at 196 nm, 209 nm and 230 nm, and a further increase of the CD signal. No linear dichroism (LD) signal was observed, indicating that this high CD signal is not an artefact.[66]
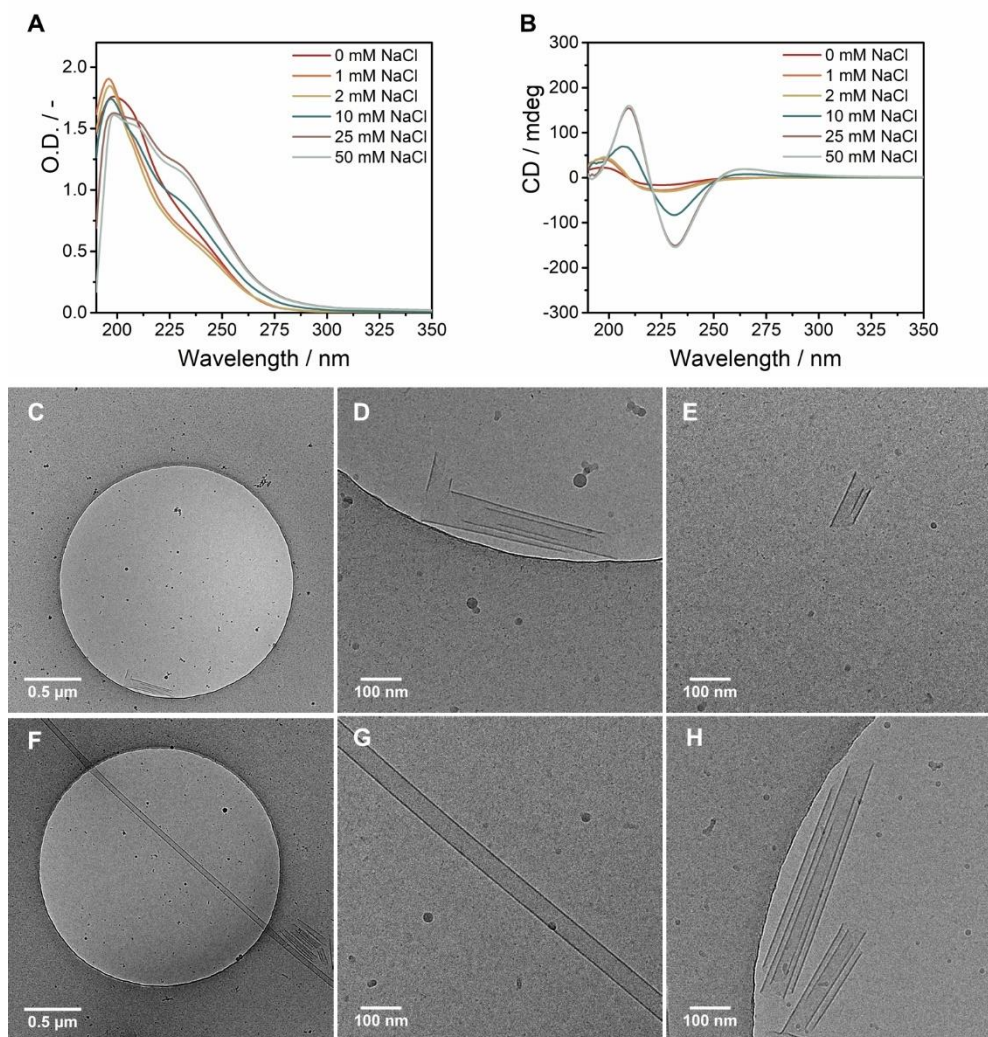
Figure 9. (A) UV spectrum of **BTA-C$_{11}$-Sulf$_2$** in water with various concentrations of NaCl (c_{BTA} = 500 μM, l = 1 mm, T = 20 °C). NaCl absorbs below 200 nm at high concentrations. (B) CD spectrum of **BTA-C$_{11}$-Sulf$_2$** in water with various concentrations of NaCl (c_{BTA} = 500 μM, l = 1 mm, T = 20 °C). (C-E) CryoTEM images of **BTA-C$_{11}$-Sulf$_2$** in water with 25 mM NaCl after 1 day of equilibration (c_{BTA} = 500 μM, c_{NaCl} = 25 mM). (F-H) CryoTEM images of **BTA-C$_{11}$-Sulf$_2$** in water with 25 mM NaCl after 4 weeks of equilibration (c_{BTA} = 500 μM, c_{NaCl} = 25 mM). Dark spherical objects are crystalline ice particles.

The changes in UV and CD spectra of **BTA-C$_{11}$-Sulf$_2$** upon addition of NaCl suggest the formation of a different aggregation state than the micelles observed in pure water. A sample with 500 μM BTA and 25 mM NaCl was imaged with cryoTEM after 1 day of equilibration, revealing the presence of sheets that are rolling up towards tubular

structures (Figure 9C-E). The majority of the assemblies is several hundred nanometers long (Figure 9D) but a few have a length of less than 100 nanometers (Figure 9E). The sample was then equilibrated for 4 weeks before new images were made that reveal the presence of micrometer long tubes with straight edges and a uniform diameter (Figure 9F-G). Additionally, the sheets can still be observed (Figure 9H). Several samples with the same composition were imaged, but none of them contained the long tubes after 1 day of equilibration, only after several weeks, indicating that the tubes form over time from the sheets. Similar UV and CD spectra were found when KCl or CsBr were added to **BTA-C$_{11}$-Sulf$_2$**. The rolled up sheets that change into tubes were also visualized in those samples with cryoTEM, demonstrating that the monovalent salts all induce the same morphological transition from micelles to sheets to tubes. The assemblies formed by **BTA-C$_{11}$-Sulf$_2$** are still dynamic, as evidenced by their morphological transition from sheets to tubes, although the process is slow and does not reach completion in 4 weeks.

It seems that the addition of 10 mM of a monovalent salt is sufficient to screen the electrostatic interactions and to promote the formation of larger assemblies. The addition of more salts increases the aggregation. The Debye length is roughly 3 nm at a NaCl concentration of 10 mM as calculated with equation 7.1. Further increase of the salt concentration to 25 mM decreases the Debye length to roughly 1.9 nm at which the distance of the repulsive electrostatic interactions is small enough that all molecules assemble into sheets or tubes. Interestingly, no larger assemblies were observed for the C_3-symmetrical charged BTAs at the same salt concentration. This could be explained by a more favorable balance between attractive and repulsive interactions in case of **BTA-C$_{11}$-Sulf$_2$**. First of all, the molecule has less charged groups and therefore less repulsive electrostatic interactions that require screening. Secondly, **BTA-C$_{11}$-Sulf$_2$** contains additional attractive hydrophobic interactions, which are shown to stimulate the formation of larger assemblies. Finally, **BTA-C$_{11}$-Sulf$_2$** molecules adopt a different molecular packing, which might be more favorable for the distribution of charges. The arrangement of molecules within the tubes or sheets will be discussed in more detail later.

Multivalent salts are known to generate more complex systems since they do not follow the simple equation for the Debye length and their addition often results in complexation.[67] Slightly different behavior was observed compared to monovalent salts when MgCl$_2$ was added to the micelles of **BTA-C$_{11}$-Sulf$_2$** in water. The UV spectrum in the presence of 0.5 mM MgCl$_2$ contains maxima at 211 and 229 nm (Figure 10A). The CD spectrum of this sample shows already a large Cotton effect with a positive signal at 209 nm, a negative signal at 230 nm and a positive band around 263 nm (Figure 10B). Both spectra show a small increase in intensity when 2 mM of MgCl$_2$ was added, but at higher concentrations their intensities decreased. Above 2 mM of MgCl$_2$ precipitation was observed in the samples by eye, which results in the decreased intensities and the scattering at high wavelengths in the UV spectra. No peaks were observed in the LD spectrum, indicating that the high intensity in the CD spectra are not artefacts.[66]
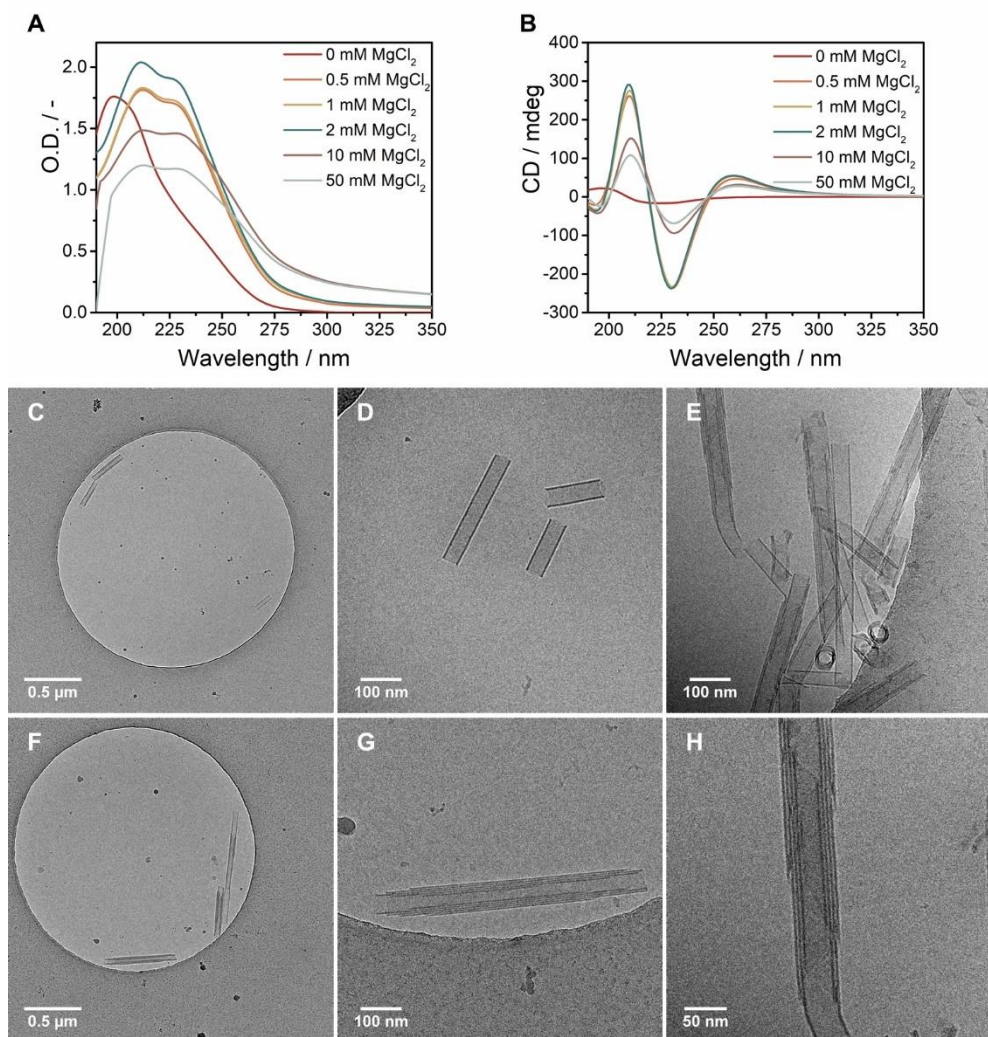
Figure 10. (A) UV spectrum of **BTA-C₁₁-Sulf₂** in water with various concentrations of MgCl₂ (c_{BTA} = 500 µM, l = 1 mm, T = 20 °C). MgCl₂ absorbs below 200 nm at high concentrations. (B) CD spectrum of **BTA-C₁₁-Sulf₂** in water with various concentrations of MgCl₂ (c_{BTA} = 500 µM, l = 1 mm, T = 20 °C). (C-E) CryoTEM images of **BTA-C₁₁-Sulf₂** in water with 2 mM MgCl₂ after 1 day of equilibration (c_{BTA} = 500 µM, c_{MgCl2} = 2 mM). (F-G) CryoTEM images of **BTA-C₁₁-Sulf₂** in water with 2 mM MgCl₂ after 4 weeks of equilibration (c_{BTA} = 500 µM, c_{MgCl2} = 2 mM). (H) Higher magnification cryoTEM image of a multilayered tube formed by **BTA-C₁₁-Sulf₂** in water with 2 mM MgCl₂ (c_{BTA} = 500 µM, c_{MgCl2} = 2 mM, 1 day of equilibration). Dark spherical objects are crystalline ice particles.

The UV and CD spectra of **BTA-C₁₁-Sulf₂** with MgCl₂ suggest the formation of larger assemblies which were further studied with cryoTEM using samples that contained 2

mM MgCl$_2$, since this concentration resulted in the highest intensities without precipitation. CryoTEM images showed the presence of tubular structures with lengths of several hundreds of nanometers to several micrometers after overnight equilibration of the sample (Figure 10C-E). Some tubes are lying perpendicular to the ice layer in the bottom of Figure 10E, confirming that the assemblies are hollow tubes. Some of those tubes have a straight thin wall (Figure 10D), whereas others have thicker irregular walls of multiple layers (Figure 10E). After 4 weeks of equilibration the majority of the assemblies contains those multilayered walls which are thicker than after 1 day of equilibration (Figure 10F-G). A zoom-in on such a multilayered tube reveals that it contains several layers that spiral around each other without covering the complete length of the tube (Figure 10H).

Samples of **BTA-C$_{11}$-Sulf$_2$** with 2 mM MgCl$_2$ were followed over time with cryoTEM to gain more insight into the formation process of the tubular structures. Short fibers of roughly 100 nm in length and a few small sheets are visible 2 minutes after the addition of MgCl$_2$ to a sample of the BTA in water (Figure 11A-B). It can be seen that the small sheet is curling up (Figure 11B), hinting that the tubes are formed from sheets. No fibers were observed at any later points in time and all sheets transitioned into tubes within 2 hours of which both the length and wall thickness increases over time. The first indications for the formation of multilayered tubes were observed after 30 minutes (Figure 11C). An extra sheet seems to be wrapped around a tube diagonally. These diagonal lines across the diameter of the tube have been observed at several timepoints (Figure 10) and suggest that tubes are formed by a mechanism that resembles that of closing coiled ribbons.[68–70] Based on those images we hypothesize that the micelles elongate upon addition of MgCl$_2$ to form a few fibers but mainly sheet-like structures. The fibers are quickly taken up by the sheets, which close into tubular structures. Multilayered walls grow when additional sheets wrap around the tubes.

Spectroscopy techniques were used to study the interactions that make **BTA-C$_{11}$-Sulf$_2$** assemble into the sheet and tubular structures. First, Fourier transform infrared (FT-IR) spectroscopy was used to investigate the presence of intermolecular hydrogen bonds between the amides in solution. Samples were prepared in deuterated methanol and D$_2$O to prevent overlap of the O-H vibrations with the amide I vibration of the BTAs.[71] The amide I vibration is positioned at 1648 cm^{-1} (Figure 11D) in MeOD, indicative for the absence of hydrogen. When the BTA is assembled in D$_2$O the amide I vibration is found at 1639 cm^{-1}, also in the presence of MgCl$_2$. The shift of the amide I vibration to lower wavenumbers indicates the presence of intermolecular hydrogen bonding, although not as strong as observed for the 1D supramolecular polymers (see Chapter 4 for example). The presence of hydrogen bonds in pure D$_2$O further strengthens our hypothesis that the micelles in pure water are not typical surfactant micelles but resemble the short stacks previously observed for BTAs (see Chapter 2 and 5 for examples). No further shift of the amide I vibration is observed when MgCl$_2$ is added to the sample, suggesting that the tubular structures are not formed by additional

hydrogen bonds. Secondly, CD spectroscopy was used to investigate the interactions in the multilayered tubes. The large CD signal is formed within minutes after the addition of MgCl$_2$ to **BTA-C$_{11}$-Sulf$_2$**. CryoTEM images revealed that the majority of the BTAs is contained in multilayered tubes after 4 weeks but this transition only leads to a small increase in intensity and a shift of 1 nm in the CD spectrum (Figure 11E). It can be concluded from these measurements that the formation of the multilayered tubes is based on interactions of the side chains rather than interactions of the BTA cores.
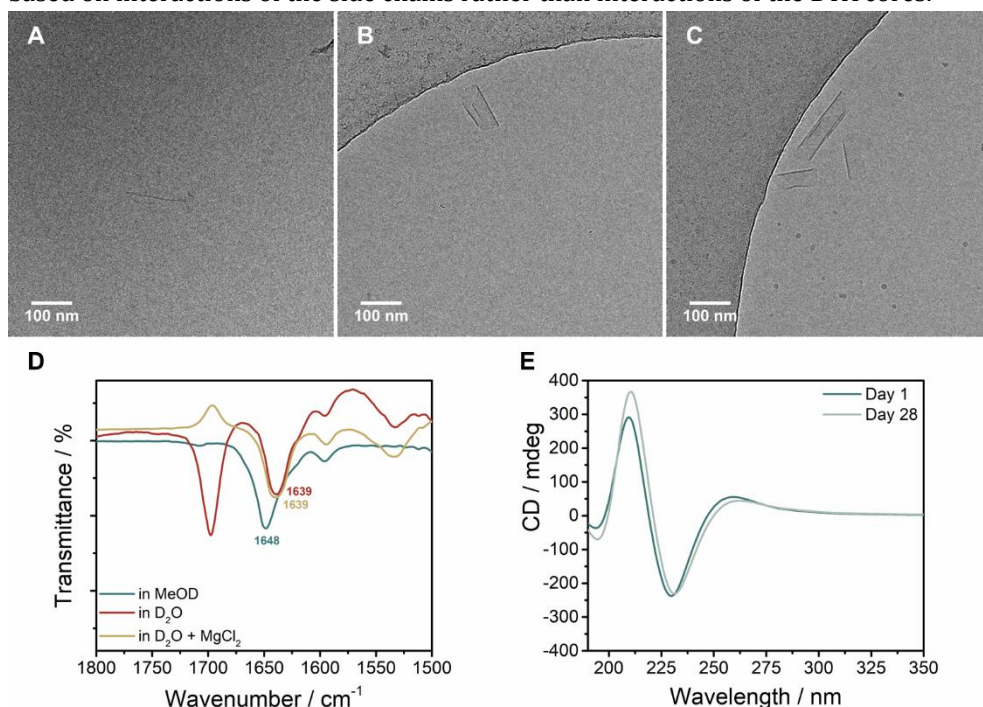
Figure 11. (A-B) CryoTEM images of **BTA-C$_{11}$-Sulf$_2$** in water with 2 mM MgCl$_2$ after 2 minutes of equilibration (c_{BTA} = 500 µM, c_{MgCl2} = 2 mM). (C) CryoTEM image of **BTA-C$_{11}$-Sulf$_2$** in water with 2 mM MgCl$_2$ after 30 minutes of equilibration (c_{BTA} = 500 µM, c_{MgCl2} = 2 mM). (D) Zoom of the FT-IR spectrum of the amide I vibration of **BTA-C$_{11}$-Sulf$_2$** in MeOD and D$_2$O with MgCl$_2$ (c_{BTA} = 20 mg/mL, c_{MgCl2} = 80 mg/mL, l = 0.05 mm, T = room temperature). The vibrations at 1697 cm^{-1} originate from the C=O vibration of acetone which was used to clean the cuvette.[72] (E) CD spectrum of **BTA-C$_{11}$-Sulf$_2$** in water with 2 mM MgCl$_2$ after 1 day and after 4 weeks of equilibration (c_{BTA} = 500 µM, c_{MgCl2} = 2 mM, l = 1 mm, T = 20 °C).

Based on the experiments presented above, we hypothesize that **BTA-C$_{11}$-Sulf$_2$** assembles into a bilayer due to hydrophobic interactions with the water-compatible charged groups facing towards the solvent in the presence of enough salts to screen the electrostatic interactions. These bilayers are elongated by aggregation of the BTA cores, as is evidenced by spectroscopic studies, resulting in larger sheets. Based on the UV spectra we hypothesize that the molecules aggregate with the same zig-zag hydrogen

pattern as described for **BTA-(S)-D-C$_{12}$-EG$_4$** in Chapter 4. The rotation of the amides then leads to a curvature in the sheets such that they can close into tubular structures. Interestingly, the UV spectra of **BTA-C$_{11}$-Sulf$_2$** with MgCl$_2$ resemble that of **BTA-C$_{12}$-EG$_4$**, whereas the CD spectra resemble that of **BTA-C$_{11}$-Sulf$_2$** with high concentrations of NaCl. However, only 1 equivalent of MgCl$_2$ was needed to obtain the maximum intensity instead of the 50 equivalents of NaCl$_2$. Samples of **BTA-C$_{11}$-Sulf$_2$** with CaCl$_2$ showed even higher CD signals when 0.5 or 1 mM of CaCl$_2$ was added and precipitation occurred already at 1.5 mM CaCl$_2$. CryoTEM images of a sample with 1 mM CaCl$_2$ contained tubes with thick multilayered walls after one day of equilibration. None of the samples with NaCl, KCl or CsBr contained the multilayered tubes that were found for samples with MgCl$_2$ or CaCl$_2$, suggesting that the addition of monovalent or multivalent salts results in the formation of different morphologies. The monovalent salts can only efficiently compensate for one layer of BTAs, whereas multivalent salts can accommodate another sheet of charged BTAs through complexation. This results in a thick wall with layers of BTAs separated by thin layers of counterions. The multilayered tubes with MgCl$_2$ seem to be less prone to morphological transitions over time than the tubes with NaCl, probably because of strong interactions and restricted movement of ions between the layers. Molecular modeling studies are currently conducted to test if the experiments match with the molecular picture drawn here.

7.4.3 The co-assembly of BTA-C$_{11}$-Sulf$_2$ with CTAB

BTA-C$_{11}$-Sulf$_2$ seems to assemble into sheets and tubes as if it is a surfactant. If these assemblies are indeed based on hydrophobic interactions, then we can turn these interactions off by addition of a surfactant similar to previous work by van Esch *et al.*.[64] The cationic surfactant CTAB was selected for mixing with **BTA-C$_{11}$-Sulf$_2$** and all experiments were performed below the CAC of CTAB (1 mM).

First, the effect of 1 equivalent of CTAB on **BTA-C$_{11}$-Sulf$_2$** in water is studied. Maxima are observed at 207 and 229 nm in the UV spectrum upon addition of 1 equivalent CTAB (Figure 12A). The CD spectrum contains positive signals at 212 and 265 nm and a negative signal at 233 nm (Figure 12B). Both spectra resemble that of the sheets and tubes formed by **BTA-C$_{11}$-Sulf$_2$** with salts. SLS measurements confirm the formation of large anisotropic assemblies, although the Rayleigh ratio is smaller than observed for the tubes formed in the presence of MgCl$_2$ (Figure 12C). Surprisingly, two morphologies are observed with cryoTEM; sheets and fibers (Figure 12D). The CD and UV spectra already suggested the presence of the sheets, but the high intensities in those spectra probably masked the peaks corresponding to the fibers. Although the addition of 1 equivalent of CTAB results in the formation of several supramolecular polymers, it seems that this is not enough to fully remove all hydrophobic interactions between the **BTA-C$_{11}$-Sulf$_2$** molecules.
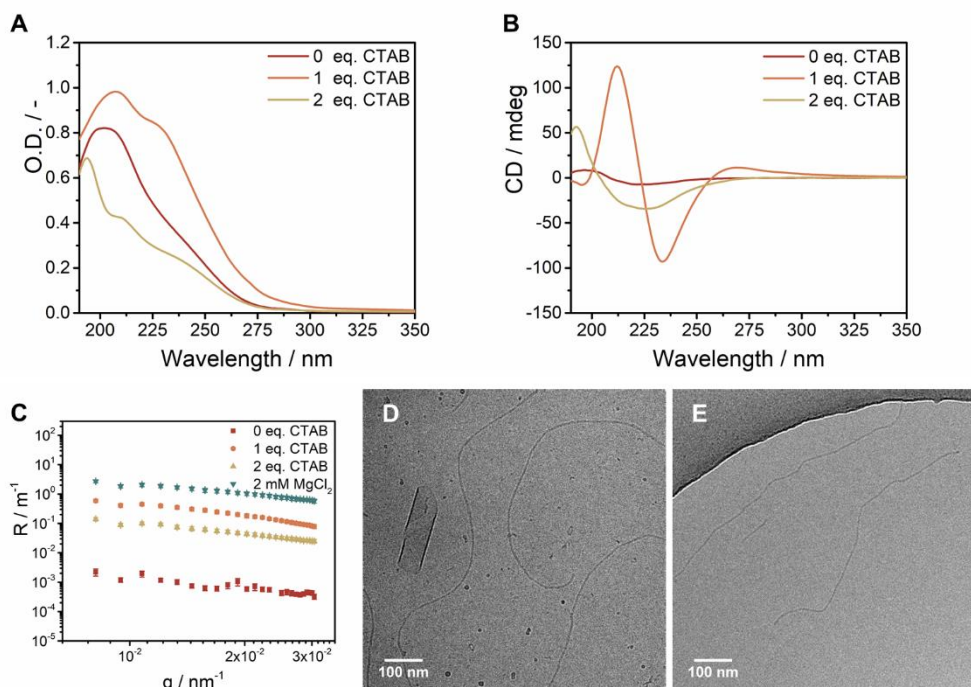
Figure 12. (A) UV spectrum of **BTA-C₁₁-Sulf₂** in water with different equivalents of CTAB (c_{BTA} = 250 μM, l = 1 mm, T = 20 °C). (B) CD spectrum of **BTA-C₁₁-Sulf₂** in water with different equivalents of CTAB (c_{BTA} = 250 μM, l = 1 mm, T = 20 °C). (C) Rayleigh ratio as a function of the scattering vector for **BTA-C₁₁-Sulf₂** in water with 0, 1 or 2 equivalents of CTAB (c_{BTA} = 250 μM, l = 1 cm, λ = 532 nm, T = 20 °C). The spectrum of 500 μM **BTA-C₁₁-Sulf₂** with 2 mM MgCl₂ was added as a reference. (D) CryoTEM image of **BTA-C₁₁-Sulf₂** with 1 equivalent of CTAB (c_{BTA} = 250 μM, c_{CTAB} = 250 μM). (E) CryoTEM image of **BTA-C₁₁-Sulf₂** with 2 equivalents of CTAB (c_{BTA} = 250 μM, c_{CTAB} = 500 μM).

An additional equivalent of CTAB was added to **BTA-C₁₁-Sulf₂** to study if this would break up all sheet-like structures. The UV spectrum of this BTA with 2 equivalents of CTAB shows large differences to previous spectra with its maximum at 193 and shoulders at 210 and 235 nm. The CD spectrum displays a positive signal at 193 nm and a broad negative signal centered around 220 nm. SLS reveals that the formed assemblies are smaller than in the sample with 1 equivalent of CTAB. Fibers of various lengths are observed with cryoTEM (Figure 12E). The fibers seemed to be thinner than those of for example **BTA-C₁₂-EG₄** but additional experiments are required to confirm that they do not possess a double helix structure. No sheets or tubes were found with cryoTEM. Given the results presented above, we conclude that CTAB is able to interact with **BTA-C₁₁-Sulf₂** and can turn off the hydrophobic interactions of the (S)-dihydrocitronellol chains such that the molecules assemble into supramolecular polymers via hydrogen bonding. This strengthens our hypothesis that **BTA-C₁₁-Sulf₂**

can assemble into bilayers via hydrophobic interactions. Additionally, it illustrates that the morphology of the assemblies can be controlled by the addition of surfactants.

7.4.4 The co-assembly of two oppositely charged surfactant-like BTAs

A cationic surfactant-like BTA was synthesized to study the generality of the results presented above. **BTA-C₁₁-TMA₂** (Figure 13A) was synthesized in collaboration with Stefan Maessen. This molecule assembles into small micelles in pure water without a CD signal (Figure 13B-D). Addition of high concentrations of salts barely stimulated the formation of larger assemblies and addition of SDS resulted in multiple morphologies even at concentrations close to the CAC of SDS. The balance between attractive and repulsive interactions could not be tuned in favor of elongated assemblies as was the case for **BTA-C₁₁-Sulf₂**. This could be related to the different presentation of charge on sulfonate groups compared to trimethylammonium groups.

Given their opposite charges, we wondered if the electrostatic interactions can be used as attractive forces by mixing **BTA-C₁₁-Sulf₂** with **BTA-C₁₁-TMA₂**. The equimolar mixture of **BTA-C₁₁-Sulf₂**:**BTA-C₁₁-TMA₂** is studied first. The UV spectrum of this sample shows two distinct maxima at 209 and 229 nm (Figure 13B), and the CD spectrum contains positive signals at 209 and around 260 nm and a negative signal at 228 nm (Figure 13C). SLS spectra confirm that anisotropic assemblies are formed that are larger than the assemblies of the individual BTAs (Figure 13D). All spectra resemble the spectra of previously studied sheet-like structures. CryoTEM images confirm the presence of clustered tubes in the equimolar sample (Figure 13E-G). These assemblies show variations in both length and diameter and some defects are visible (Figure 13G). We expect that **BTA-C₁₁-Sulf₂** and **BTA-C₁₁-TMA₂** can compensate each other's charge such that they can co-assemble into bilayers that form tubes.

Different ratios of **BTA-C₁₁-Sulf₂** and **BTA-C₁₁-TMA₂** were studied to get an idea of the organization of molecules within the tubes (Figure 13B-D). The UV spectra of samples with an excess of **BTA-C₁₁-Sulf₂** have a maximum around 194 nm and shoulders at 209 and 230 nm. A negative CD signal appears at 230 nm in the 9:1 sample. This signal increases in intensity in the 7:3 sample in which also a positive signal at 211 nm appears, resembling the spectrum of the equimolar mixture but with a lower intensity. Adding **BTA-C₁₁-TMA₂** to **BTA-C₁₁-Sulf₂** until equimolar ratio thus results in less micelles and more tubular structures being formed. An excess of **BTA-C₁₁-TMA₂** results in UV spectra with peaks at 196 nm and 209 nm and a shoulder around 230 nm. The CD spectrum of the 3:7 sample has a positive signal at 211 nm and a negative signal at 230 nm, similar to the 7:3 and 5:5 sample. The 1:9 sample has a broad CD signal around 228 nm, which resembles that of **BTA-C₁₁-Sulf₂**. SLS spectra confirm that different structures than micelles are formed at all ratios, with the largest assemblies in the 7:3, 5:5 and 3:7 samples.
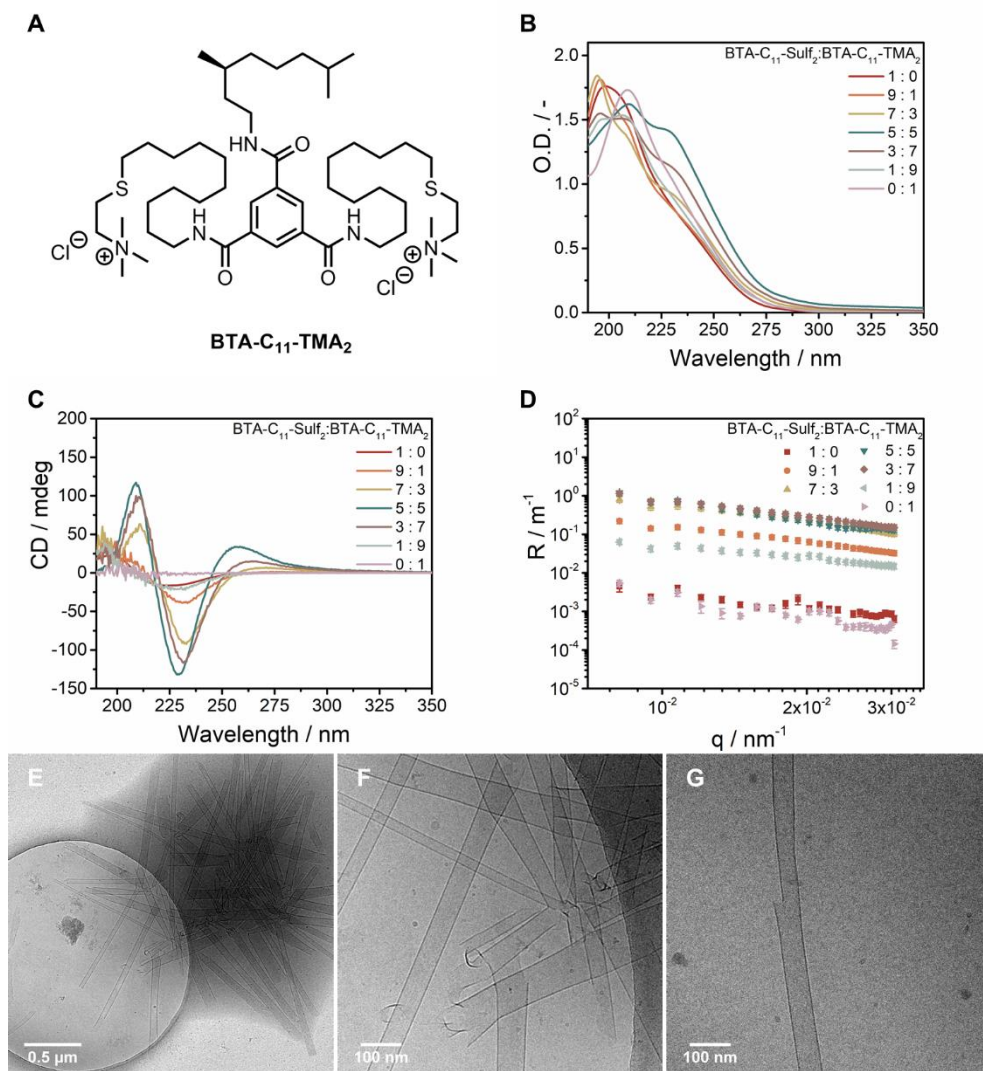
Figure 13. (A) Chemical structure of **BTA-C₁₁-TMA₂**. (B) UV spectrum of various mixtures of **BTA-C₁₁-Sulf₂** with **BTA-C₁₁-TMA₂** in water ($c_{BTA,total}$ = 500 µM, l = 1 mm, T = 20 °C). (C) CD spectrum of various mixtures of **BTA-C₁₁-Sulf₂** with **BTA-C₁₁-TMA₂** in water ($c_{BTA,total}$ = 500 µM, l = 1 mm, T = 20 °C). (D) Rayleigh ratio as a function of the scattering vector for various mixtures of **BTA-C₁₁-Sulf₂** with **BTA-C₁₁-TMA₂** in water ($c_{BTA,total}$ = 500 µM, l = 1 cm, λ = 532 nm, T = 20 °C). (E-G) CryoTEM images of the equimolar mixture of **BTA-C₁₁-Sulf₂** with **BTA-C₁₁-TMA₂** in water ($c_{BTA,total}$ = 500 µM).

These results show that **BTA-C₁₁-Sulf₂** and **BTA-C₁₁-TMA₂** co-assemble into larger structures at all ratios studied here. Previous work on BTAs decorated with oppositely charged amino acids showed that these molecules copolymerize in an alternating

fashion.[48,51] Based on these results, we expect that these oppositely charged surfactant-like BTAs also assemble in an alternating pattern. At an equimolar ratio all electrostatic interactions can be matched to a BTA of opposite charge, although there are some defects visible (Figure 13G). Tubular assemblies are also formed in the other samples although in a lower quantity than when one of the molecules is in access and requires screening of its charge to diminish repulsive interactions. The remaining molecules form micelles as is evidenced by the absorbance peaks below 200 nm.

7.5 Conclusions

Interesting new properties can be obtained by the combination of water-compatible BTAs and surfactants. The ability of those molecules to interact was shown in the first part, in which supramolecular polymers with an tetra(ethylene glycol) periphery were disrupted by charged surfactants. Through a serendipitous discovery, we observed that the supramolecular polymers can be reformed upon dilution, a phenomenon that was later observed for several surfactants. This dilution-induced supramolecular polymerization holds great potential for the creation of new stimuli-responsive materials and its application in functional materials will be discussed in more detail in Chapter 8.

The second part of this chapter showed the ability of surfactants to promote the formation of larger assemblies. C_3-symmetrical BTAs with charged end groups were previously believed to be unable to assemble into larger assemblies as their repulsive electrostatic interactions are not sufficiently screened by salts. Addition of oppositely charged surfactants to those BTAs resulted in micrometer-long twisted sheets and ribbons due to the introduction of attractive hydrophobic interactions. The addition of surfactants presents a new method to form larger assemblies from molecules with a disbalance in their attractive and repulsive interactions. It was already shown in this chapter that this strategy is not limited to supramolecular building blocks with a BTA core and it is likely that molecules without charges also benefit from this approach.

Finally, BTAs and surfactants can be covalently connected such that a supramolecular building blocks is obtained that can assemble via the different interactions it inherited from its two parent molecules. The molecule presented in this chapter assembles into small micelles via poorly protected hydrogen bonds in pure water. The repulsive electrostatic interactions are screened by the addition of salts such that the molecule assembles into a bilayer as if it is a surfactant when the Debye length is sufficiently small. These assemblies are shown to be dynamic and undergo morphological changes over time from sheets to tubes in the presence of monovalent salts. Multivalent salts on the other hand provide a strong complexation such that multilayered tubes are formed with confined layers of counterions between the sheets. The hydrophobic interactions were turned off by the addition of a surfactant, such that the molecule assembles into a supramolecular polymer via hydrogen bonding of the

BTA cores. With this new method we can obtain multiple morphologies from the same building block by controlling the concentration of additives in the solution.

In conclusion, the various interactions between water-compatible BTAs and surfactants can be used to obtain stimuli-responsive materials. The introduction of charges adds a new challenge to supramolecular self-assembly as it requires an understanding of the attractive and repulsive interactions that determine the degree of aggregation. The examples of frustrated self-assembly in this chapter show that the screening of charges with salts is not always sufficient to promote self-assembly as there should also be enough attractive non-covalent interactions to promote elongation. Surfactants are useful additives as they screen the charges and provide additional hydrophobic interactions such that the degree of aggregation and shape of the assemblies can be controlled. Although only a few BTAs and surfactants were studied here, we envision that the large variety of surfactants available should make it possible to apply this strategy to other supramolecular assemblies as well.

7.6 Experimental section

7.6.1 Materials and Methods

All solvents and chemicals used were of reagent grade quality or better and purchased from Biosolve or Sigma-Aldrich at the highest purity available and used without further purification unless otherwise noted. **BTA-C$_{12}$-EG$_4$** was synthesized according to literature procedures.[40] Water for aqueous samples was purified on an EMD Millipore Milli-Q Integral Water Purification System.

Sample preparation of BTA-C$_{12}$-EG$_4$ with surfactants: the solid **BTA-C$_{12}$-EG$_4$** was weighed into a glass vial equipped with a magnetic stirring bar. MQ-water was added to obtain a 500 µM concentration in H$_2$O. The sample was subsequently stirred at 80 °C for 15 minutes and the hot and hazy sample was vortexed immediately afterwards for 15 seconds. Surfactants were weighed into a glass vial and MQ-water was added to obtain a concentration of 25 mM. Both the BTA and surfactant stock solutions were left to equilibrate at room temperature for at least one night. Samples with HTAB and OTAB were prepared by mixing the BTA stock solution with MQ-water in a separate glass vial equipped with magnetic stirring bar such that the concentration of BTA was just above 250 µM. The sample was subsequently stirred at 80 °C for 15 minutes and the hot and hazy sample was vortexed immediately afterwards for 15 seconds. HTAB or OTAB were added in the desired ratio after cooling for one hour to yield a final BTA concentration of 250 µM. Samples with DTAB, CTAB and SDS were prepared by mixing the BTA stock solution, the surfactant stock solution and MQ-water in a separate glass vial with magnetic stirring bar to yield a sample with a BTA concentration of 250 µM and the desired ratio of surfactants. The sample was subsequently stirred at 80 °C for 15 minutes and the hot and hazy sample was vortexed immediately afterwards for 15 seconds. All samples with surfactants were left to equilibrate at room temperature overnight. Samples for NMR were prepared with the same method but with D$_2$O instead of MQ-water.

Sample preparation of BTAs and TTAs with trimethylammonium or sulfonate end groups: the solid material was weighed into a glass vial. MQ-water was added to obtain the desired concentration. Salts were added from 100 mM stock solutions in MQ-water, CTAB was added

from a 1 mM stock solution in MQ-water or SDS was added from a 5 mM stock solution in MQ-water. The volume of MQ-water was adapted to the volume of stock solution added to always yield sample with a BTA/TTA concentration of 250 or 500 µM. The samples were vortexed for 15 seconds and were subsequently left to equilibrate overnight. Samples in ACN were prepared by directly dissolving the molecules in ACN and equilibrating overnight. Samples for NMR were prepared with the same method but with D_2O instead of MQ-water.

Sample preparation for mixtures of BTA-C$_{11}$-Sulf$_2$ and BTA-C$_{11}$-TMA$_2$: the solid materials were weighed into separate glass vials. MQ-water was added to obtain a concentration of 500 µM and to dissolve both molecules. The stock solutions were vortexed for 15 seconds and were left to equilibrate for 1 hour at room temperature before combining them at the desired ratio in a new glass vial with magnetic stirring bar. The sample was subsequently stirred at 80 °C for 15 minutes and the hot and hazy sample was vortexed immediately afterwards for 15 seconds. The samples were left to equilibrate at room temperature overnight.

7.6.2 Instrumentation

Newly synthesis molecules were characterized with nuclear magnetic resonance (NMR), solid-state Fourier-transform infrared (FT-IR), liquid chromatography mass spectroscopy (LC-MS) and matrix assisted laser absorption/ionization mass time of flight mass spectroscopy (MALDI-TOF-MS) using the instruments described in Chapter 2.

Column chromatography was performed with the instruments described in Chapter 2. Reactions were followed by thin-layer chromatography (TLC) using 60-F$_{254}$ silica gel plates from Merck and visualized by UV light at 254 nm and/or staining (ninhydrin, bromocresol green, potassium permanganate, iodine chamber).

Ultraviolet-visible (UV-visible) absorbance spectra were recorded with the instruments described in Chapter 3.

Static light scattering (SLS) measurements were performed on the instruments described in Chapter 5.

Cryogenic transmission electron microscopy (cryoTEM) images were obtained with the instrument described in Chapter 2.

Fourier-Transform infrared (FT-IR) spectra in solution were recorded with the instruments and methods described in Chapter 4. All materials were dissolved in D_2O without heating-cooling.

Circular dichroism (CD) and linear dichroism (LD) spectra were measured on the instruments described in Chapter 4.

7.6.3 Synthetic procedures

2-(Undec-10-en-1-yl)isoindoline-1,3-dione (1)

The synthesis was adapted from a literature protocol.[73] 11-bromo-1-undecene (10.0 g, 43.1 mmol) was added to a solution of potassium phthalimide (12.0 g, 64.6 mmol) in 30 mL of DMF. The reaction mixture was heated to 60 °C under an atmosphere of dry argon and stirred for 4 h. DCM (30 mL) and HCl (aq. pH = 2) were added and the reaction mixture was extracted three times with DCM. The organic layers were collected and dried with MgSO$_4$, followed by the filtration and concentration *in vacuo* to afford a wax-like solid (12.3 g, 94%). ^{1}H NMR (400 MHz, CDCl$_3$ δ): 7.84 (dd, 2H, phthalimide), 7.71 (dd, 2H, phthalimide), 5.80 (m, 1H, CH$_2$C<u>H</u>=CH$_2$), 5.02-4.89 (m, 2H, CH$_2$CH=C<u>H</u>$_2$), 3.70-3.65 (m, 2H, CH$_2$C<u>H</u>$_2$N), 2.02 (m, 2H, C<u>H</u>$_2$CH=CH$_2$), 1.67 (m, 2H, C<u>H</u>$_2$CH$_2$N).

1.42-1.21 (m, 12H, aliphatic). ^{13}C NMR (400 MHz, CDCl$_3$ δ): 168.46, 139.20, 133.82, 132.18, 123.57, 123.14, 114.10, 38.08, 33.79, 29.41, 29.38, 29.16, 29.08, 28.90, 28.60, 26.85.

Undec-10-en-1-amine (2)

The synthesis was adapted from a literature protocol.[73] To a solution of **1** (10.0 g, 33.4 mmol) in 100 mL of ethanol, hydrazine monohydrate (5.0 g, 100.2 mmol) was added. The reaction mixture was allowed to stir for 30 min at reflux. DCM (50 mL) and NaOH (aq. 1 M, 100 mL) were added and the reaction mixture was extracted three times. The organic layers were collected and dried with MgSO$_4$, followed by the filtration and concentration *in vacuo* to afford a yellowish liquid. The crude liquid was distilled for further purification and a colorless liquid was obtained with some crystal in it (3.9 g, 69%). The material was used without further purification. ^{1}H NMR (400 MHz, CDCl$_3$ δ): 5.80 (m, 1H, CH$_2$CH=CH$_2$), 5.02-4.89 (m, 2H, CH$_2$CH=CH$_2$), 2.67 (t, 2H, CH$_2$CH$_2$NH$_2$), 2.03 (m, 2H, CH$_2$CH=CH$_2$), 1.67 (m, 2H, CH$_2$CH$_2$NH$_2$). 1.48-1.23 (m, 14H, aliphatic).

N^1,N^3,N^5-Tri(undec-10-en-1-yl)benzene-1,3,5-tricarboxamide (3)

A round bottom flask was charged with **2** (430 mg, 2.54 mmol), triethylamine (0.4 mL, 2.6 mmol) and 5 mL THF. 1,3,5-benzenetricarbonyl trichloride (200 mg, 753 μmol) was dissolved in 1 mL THF and was added dropwise to the solution. 5 mL of DCM was added and the reaction mixture was allowed to stir overnight. The reaction mixture was concentrated *in vacuo*. The crude was dissolved in CHCl$_3$ and washed with HCl (1M, 75 mL), NaOH (1 M, 75 mL) and brine (75 mL). The organic phase was then dried over MgSO$_4$, the drying agent was filtered off and crude compound was obtained by concentrating *in vacuo*. The product was purified with silica-gel column chromatography (MeOH/DCM 0/100 – 10/90) to give 402 mg of white solid (402 mg, 80%). ^{1}H NMR (400 MHz, CDCl$_3$ δ): 8.33 (s, 3H, Ar), 6.38 (t, 3H, amide), 5.87-5.74 (m, 3H, CH$_2$CH=CH$_2$), 5.03-4.89 (m, 6H, CH$_2$CH=CH$_2$), 3.47 (m, 6H, CH$_2$CH$_2$N), 2.03 (m, 6H, CH$_2$CH=CH$_2$), 1.61 (m, 6H, CH$_2$CH$_2$N), 1.36-1.10 (m, 36H, aliphatic). ^{13}C NMR (400 MHz, CDCl$_3$ δ): 165.58, 139.21, 135.26, 127.88, 114.13, 40.41, 33.80, 29.54, 29.46, 29.42, 29.28, 29.10, 28.91, 26.98. FT-IR (ATR) ν (cm^{-1}): 3240, 3076, 2924, 2854, 1731, 1637, 1557, 1465, 1439, 1378, 1366, 1296, 1262, 1198, 1169, 1143, 1062, 992, 908, 800, 723, 691, 639, 594, 555, 510. MALDI-TOF-MS: *m/z* calculated for C$_{42}$H$_{69}$N$_3$O$_3$+H$^+$: 644.54 [M+H]$^+$; observed 664.57; *m/z* calculated for C$_{42}$H$_{69}$N$_3$O$_3$+Na$^+$: 686.52 [M+Na]$^+$; observed 686.56.
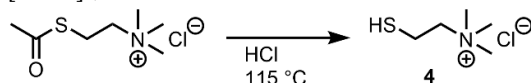
Thiocholine chloride (4)

The synthesis was adapted from a literature protocol.[74] Acetylthiocholine chloride (1.128 g, 5.06 mmol) was dissolved in 1 M HCl (6 mL) and refluxed at 115°C under nitrogen atmosphere. After 24 hours, the reaction was suspended and acetic acid, HCl and H$_2$O were removed by multiple washing steps with H$_2$O and subsequent solvent removal *in vacuo*. The obtained white crystalline solid was used without further purification. ^{1}H NMR (400 MHz, MeOD δ): 3.57 – 3.48 (m, 2H, CH$_2$CH$_2$N), 3.15 (s, 9H, CH$_3$), 2.97 – 2.88 (m, 2H, CH$_2$CH$_2$N).

BTA-C$_{11}$-TMA$_3$

A 15 mL glass vial was charged with **3** (50 mg, 75 μmol), DMPA (29 mg, 113 μmol), **4** (106 mg, 678 μmol) and 5 mL of deoxygenated methanol. A rubber lid was placed on top of the glass vial

and the reaction mixture was allowed to stir under nitrogen atmosphere for 5 minutes. The reaction vial was transferred to a UV chamber and stirred for 2 h with 365 nm (315-400 nm) UV light. Subsequently, the solvent was removed *in vacuo.* The crude product was purified by reversed-phase chromatography (H$_2$O/ACN 95/5–25/75 v/v) to give a white solid after lyophilization. At this point, ^{1}H NMR showed that the product was contaminated with the thiolated reagent. To remove such an impurity, the material was purified by dialysis against water (molecular weight cut-off (MWCO) = 100-500 Da, Spectra/Por Biotech CE Membranes), after which the material was dried by lyophilization, yielding **BTA-C$_{11}$-TMA$_3$** as a fluffy white material (35 mg, 42%). ^{1}H NMR (400 MHz, DMSO-d$_6$ δ): 8.98 (t, 3H, amide), 8.55 (s, 3H, Ar), 3.55-3.48 (m, 6H, SCH$_2$C$\underline{H}_2$N), 3.31-3.23 (m, 6H, CH$_2$C$\underline{H}_2$NH), 3.08 (s, 27H, C$\underline{H}_3$), 2.91 – 2.83 (m, 6H, SC$\underline{H}_2$CH$_2$N), 2.57 (t, 6H, CH$_2$C$\underline{H}_2$S), 1.59 – 1.46 (m, 12H, aliphatic), 1.38-1.20 (m, 42H, aliphatic) ^{13}C NMR (400 MHz, DMSO-d$_6$ δ): 165.70, 135.28, 128.94, 64.83, 52.59, 52.55, 52.51, 31.36, 29.47, 29.44, 29.26, 29.06, 28.64, 26.98, 23.82. FT-IR (ATR) ν (cm^{-1}): 3322, 3074, 3027, 2923, 2852, 2133, 1645, 1598, 1539, 1479, 1468, 1435, 1372, 1329, 1291, 1047, 1014,972, 945, 905, 703, 633, 615, 568, 545, 526, 516, 475, 457. LC-MS: *m/z* calculated for C$_{57}$H$_{111}$N$_6$O$_3$S$_3^{3+}$: 341.26 [M]$^{3+}$; observed 341.25; *m/z* calculated for C$_{57}$H$_{111}$N$_6$O$_3$S$_3^{3+}$+Cl$^-$: 529.63 [M+Cl]$^{2+}$; observed 529.33.
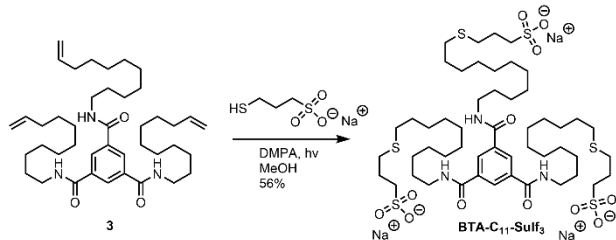
BTA-C$_{11}$-Sulf$_3$

A 15 mL glass vial was charged with **3** (104 mg, 157 μmol), DMPA (65 mg, 253 μmol), sodium 3-mercapto-1-propanesulfonate (257 mg, 1.44 mmol) and 10 mL of deoxygenated methanol. A rubber lid was placed on top of the glass vial and the reaction mixture was allowed to stir under nitrogen atmosphere for 5 minutes. The reaction vial was transferred to a UV chamber and stirred for 2 h with 365 nm (315-400 nm) UV light. The solids were collected by vacuum filtration, washed with methanol and dried. The material was purified by dialysis against water (molecular weight cut-off (MWCO) = 100-500 Da, Spectra/Por Biotech CE Membranes), after which the material was dried by lyophilization, yielding **BTA-C$_{11}$-Sulf$_3$** as a fluffy white material (99 mg, 56%). ^{1}H NMR (400 MHz, DMSO-d$_6$ δ): 8.65 (t, 3H, amide), 8.34 (s, 3H, Ar), 3.29-3.21 (d, 6H, CH$_2$C$\underline{H}_2$NH), 2.58-2.39 (m, 12H, C$\underline{H}_2$SC$\underline{H}_2$), 1.78 (p, 6H, SCH$_2$C$\underline{H}_2$CH$_2$S), 1.57-1.41 (m, 12H, aliphatic), 1.38-1.20 (m, 45H, aliphatic, SCH$_2$CH$_2$C$\underline{H}_2$S) ^{13}C NMR (400 MHz, DMSO-d$_6$ δ): 165.95, 135.58, 128.73, 50.76, 40.46, 40.25, 40.04, 39.83, 39.62, 39.41, 39.20, 31.35, 30.82, 29.57, 29.41, 29.38, 29.22, 29.04, 28.65, 26.92, 25.85. FT-IR (ATR) ν (cm^{-1}): 3288, 3075, 2920, 2851, 1643, 1596, 1543, 1466, 1454, 1435, 1179, 1056, 912, 855, 736, 720, 654, 604, 526, 475, 457. MALDI-TOF-MS: *m/z* calculated for C$_{51}$H$_{90}$N$_3$O$_{12}$S$_6^{3-}$+2H$^+$: 1130.51 [M+2H]$^-$; observed 1130.51; *m/z* calculated for C$_{51}$H$_{90}$N$_3$O$_{12}$S$_6^{3-}$+H$^+$+Na$^+$: 1152.49 [M+H+Na]$^-$; observed 1152.50; *m/z* calculated for C$_{51}$H$_{90}$N$_3$O$_{12}$S$_6^{3-}$+2Na$^+$: 1174.47 [M+2Na]$^-$; observed 1174.49;
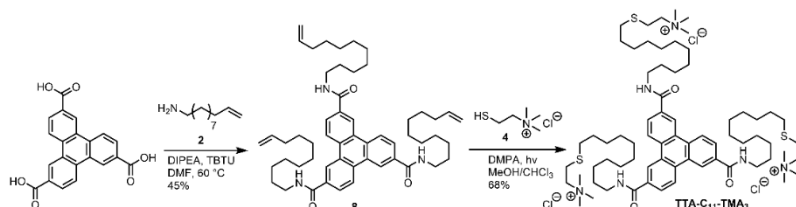
N^2,N^6,N^{10}-Tri(undec-10-en-1-yl)triphenylene-2,6,10-tricarboxamide (8)

2,6,10-Triphenylenetricarboxylic acid[75] (100 mg, 0.28 mmol) was dissolved in 4 mL of dry DMF at 60 °C under argon atmosphere. Then 4 equivalents of DIPEA (0.193 mL, 1.11 mmol) and TBTU (0.300 g, 0.92 mmol) dissolved in 0.5 mL of DMF were added. Subsequently, **2** (0.151 g, 0.88 mmol) was added and the mixture was stirred for 15 minutes at 60 °C and was then cooled down to room temperature. The resulting yellow solution was diluted with 50 mL of chloroform and was washed with water (50 mL), two times 0.5 M HCl (50 mL), 1 M NaOH (50 mL), water (50 mL) and brine (50 mL). The organic phase was then dried over MgSO$_4$, filtered and the solvent was removed *in vacuo*. The product was purified by silica-gel column chromatography starting at 100% of ethyl acetate to remove a yellow fluorescent impurity. Once such an impurity left the column, the product was isolated using a gradient of 10% methanol in chloroform resulting in **8** as a white solid (102 mg, 45%). ^{1}H NMR (400 MHz, DMSO-d$_6$ δ): 9.29 (s, 3H, triphenylene), 9.00 (d, 3H, triphenylene), 8.89 (d, 3H, triphenylene), 8.27 (m, 3H, amides), 5.83-5.69 (m, 3H, CH$_2$C$\underline{H}$=CH$_2$), 5.02-4.87 (m, 6H, CH$_2$CH=C$\underline{H}_2$), 3.39 (t, 6H, NHC$\underline{H}_2$CH$_2$), 1.99 (m, 6H, C$\underline{H}_2$CH=CH$_2$), 1.67-1.57 (m, 6H, NHCH$_2$C$\underline{H}_2$), 1.45-1.17 (m, 36H, aliphatic). ^{13}C NMR (400 MHz, DMSO-d$_6$ δ): 165.95, 139.26, 134.08, 131.98, 128.97, 127.47, 124.57, 123.18, 115.06, 33.63, 29.69, 29.43, 29.30, 29.28, 28.99, 28.74, 27.05. FT-IR (ATR) ν (cm^{-1}): 3243, 3075, 2923, 2853, 1894, 1792, 1717, 1631, 1576, 1547, 1497, 1463, 1439, 1409, 1395, 1371, 1339, 1313, 1282, 1150, 1091, 1062, 1030, 993, 908, 891, 838, 823, 787, 740, 704, 647, 631, 555, 526, 495, 475. MALDI-TOF-MS: *m/z* calculated for C$_{54}$H$_{75}$N$_3$O$_3$+H$^+$: 814.59 [M+H]$^+$; observed 814.60; *m/z* calculated for C$_{54}$H$_{75}$N$_3$O$_3$+Na$^+$: 836.57 [M+Na]$^+$; observed 836.61;

TTA-C$_{11}$-TMA$_3$

A 15 mL glass vial was charged with **8** (60 mg, 74 µmol), DMPA (28 mg, 110 µmol), **4** (103 mg, 663 µmol), 1 mL deoxygenated chloroform and 4 mL of deoxygenated methanol. A rubber lid was placed on top of the glass vial and the reaction mixture was allowed to stir under nitrogen atmosphere for 5 minutes. The reaction vial was transferred to a UV chamber and stirred for 2 hours with 365 nm (315-400 nm) UV light. Subsequently, the solvent was removed *in vacuo*. The crude product was purified by reverse-phase column chromatography (H$_2$O/ACN 95/5–20/80 v/v) to yield **TTA-C$_{11}$-TMA$_3$** as a white solid after lyophilization (64 mg, 68%). ^{1}H NMR (400 MHz, DMSO-d$_6$ δ): 9.37 (s, 3H , triphenylene), 9.09 (d, 3H, triphenylene), 9.07 (s, 3H, triphenylene), 8.29 (m, 3H, amides), 3.56-3.46 (m, 6H, SCH$_2$C$\underline{H}_2$N), 3.44-3.32 (m, 6H, NHC$\underline{H}_2$CH$_2$), 3.14 (m, 3H), 3.09 (s, 27H, C$\underline{H}_3$), 2.92-2.80 (m, 6H, SC$\underline{H}_2$CH$_2$N), 2.55 (t, 6H, CH$_2$C$\underline{H}_2$S), 1.69-1.57 (m, 6H, C$\underline{H}_2$CH$_2$S), 1.56-1.43 (m, 6H, NHCH$_2$C$\underline{H}_2$), 1.41-1.17 (m, 36H, aliphatic). ^{13}C NMR (400 MHz, DMSO-d$_6$ δ): 165.91, 134.03, 132.04, 129.01, 127.55, 124.74, 123.28, 64.83, 52.59, 52.55, 52.51, 31.36, 29.72, 29.47, 29.32, 29.08, 28.65, 27.09, 23.82. FT-IR (ATR) ν (cm^{-1}): 3339, 32062923, 2852, 1633, 1573, 1544, 1492, 1467, 1437, 1371, 1316, 1277, 1154, 1092, 1047, 972, 946, 903, 848, 752, 721, 672, 635, 565, 524, 507, 486, 457. LC-MS: *m/z* calculated for C$_{69}$H$_{117}$N$_6$O$_3$S$_3$$^{3+}$: 391.28 [M]$^{3+}$; observed 391.33; *m/z* calculated for C$_{69}$H$_{117}$N$_6$O$_3$S$_3$$^{3+}$+Cl$^-$: 604.65 [M+Cl]$^{2+}$; observed 604.75.

Methyl 3,5-bis(undec-10-en-1-ylcarbamoyl)benzoate (5)

5-methoxycarbonyl-benzene-1,3-dicarboxylic acid[76] (250 mg, 1.12 mmol) and TBTU (788 mg, 2.45 mmol) were dissolved in 10 mL DMF. DIPEA (0.6 mL, 3.46 mmol) was added and the mixture turned dark brown. The mixture was stirred for 5 minutes before **2** (430 mg, 2.54 mmol) was added in 2 mL DMF. The reaction mixture was stirred for 2 hours at room temperature. The reaction mixture was diluted with CHCl$_3$ (100mL), washed 3 times with water (100 mL), two times with 1M HCl (100 mL) and brine (100 mL). The organic phase was dried with MgSO$_4$, filtered and the solvent was removed *in vacuo*, yielding a brown oil. The crude was purified with silica-gel column chromatography (MeOH/CHCl$_3$ 0/100 – 10/90 v/v), yielding **5** as a yellow solid (487 mg, 83%). ^{1}H NMR (400 MHz, CDCl$_3$ δ): 8.52 (d, 2H, Ar), 8.41 (s, 1H, Ar), 6.28 (t, 2H, amides), 5.81 (m, 2H, CH$_2$CH=CH$_2$), 5.04-4.87 (m, 4H, CH$_2$CH=CH$_2$), 3.18 (s, 3H, CH$_3$), 3.48 (m, 4H, NHCH$_2$CH$_2$), 2.09-1.98 (m, 4H, CH$_2$CH=CH$_2$), 1.69-1.58 (m, 4H, NHCH$_2$CH$_2$), 1.45-1.22 (m, 24H, aliphatic). ^{13}C NMR (400 MHz, CDCl$_3$ δ): 165.80, 165.56, 139.20, 135.55, 131.02, 130.33, 129.73, 114.13, 52.63, 40.40, 38.62, 33.80, 29.58, 29.47, 29.42, 29.29, 29.10, 28.91, 26.99. MALDI-TOF-MS: *m/z* calculated for C$_{32}$H$_{50}$N$_2$O$_4$+H$^+$: 527.39 [M+H]$^+$; observed 527.39; *m/z* calculated for C$_{32}$H$_{50}$N$_2$O$_4$+Na$^+$: 549.37 [M+Na]$^+$; observed 549.40.

3,5-Bis(undec-10-en-1-ylcarbamoyl)benzoic acid (6)

5 (470 mg, 0.89 mmol) was dissolved in 20 mL MeOH. LiOH (77 mg, 3.21 mmol) was added but the material did not solubilize. LiOH monohydrate (135 mg, 3.21 mmol) was added with an additional 20 mL MeOH to dissolve all material. The reaction mixture was stirred overnight. The solvent was removed *in vacuo*. The crude was dissolved in 100 mL ethyl acetate, washed with 2 times 1M HCl (100 mL), water (100 mL) and brine (100 mL). The organic phase was dried with MgSO$_4$, filtered and the solvent was removed *in vacuo*, yielding **6** as a yellow solid (455 mg, 99%) which was used without further purification. ^{1}H NMR (400 MHz, CDCl$_3$ δ): 8.59-8.42 (m, 3H, Ar), 5.79 (m, 2H, CH$_2$CH=CH$_2$), 5.03-4.86 (m, 4H, CH$_2$CH=CH$_2$), 3.47 (m, 4H, NHCH$_2$CH$_2$), 2.09-1.94 (m, 4H, CH$_2$CH=CH$_2$), 1.80-1.52 (m, 4H, NHCH$_2$CH$_2$), 1.50-1.04 (m, 24H, aliphatic).

(S)-N^1-(3,7-Dimethyloctyl)-N^3,N^5-di(undec-10-en-1-yl)benzene-1,3,5-tricarboxamide (7)

6 (450 mg, 0.88 mmol) and TBTU (327 mg, 1.02 mmol) were dissolved in 12 mL DMF. DIPEA (0.23 mL, 1.32 mmol) was added and the reaction mixture turned dark brown. After 5 minutes, (S)-3,7-dimethyloctan-1-amine[77] (166 mg, 1.05 mmol) was added from a solution in DMF. The reaction mixture was stirred overnight at room temperature. The mixture was then diluted with 100 mL CHCl$_3$, washed three times with water (100 mL), two times with 1M HCl (100 mL) and brine (100 mL). The organic phase was dried with MgSO$_4$, filtered and the solvent was removed *in vacuo*. The crude was purified with silica-gel column chromatography (MeOH/CHCl$_3$ 0/100 – 10/90 v/v), yielding **5** as a yellow/orange wax (544 mg, 95%). ^{1}H NMR (400 MHz, CDCl$_3$ δ): 8.33 (s, 3H, Ar), 6.40 (m, 3H, amides), 5.81 (m, 2H, CH$_2$CH=CH$_2$), 5.03-4.89 (m, 4H, CH$_2$CH=CH$_2$), 3.48 (m, 6H, NHCH$_2$CH$_2$), 2.08-1.98 (m, 4H, CH$_2$CH=CH$_2$), 1.69-1.06 (m, 38H, aliphatic), 0.95 (d, 3H, CH$_3$), 0.87 (d, 6H, CH(CH$_3$)$_2$). ^{13}C NMR (400 MHz, CDCl$_3$ δ): 165.56, 139.21, 135.28, 127.86, 114.13, 40.40, 39.25, 38.53, 37.12, 36.63, 33.80, 30.74, 29.55, 29.46, 29.42, 29.28, 29.10, 28.91, 27.96, 26.98, 24.63, 22.70, 22.60, 19.49. FT-IR (ATR) ν (cm^{-1}): 3239, 3075, 2924, 2854 1824, 1637, 1557, 1464, 1439, 1378, 1366, 1296, 1169, 1145, 1105, 1063, 992, 908, 857, 798, 728, 691, 637, 598, 555, 525, 516, 474, 467, 457. MALDI-TOF-MS: *m/z* calculated for C$_{41}$H$_{69}$N$_3$O$_3$+H$^+$: 652.54 [M+H]$^+$; observed 652.54; *m/z* calculated for C$_{32}$H$_{50}$N$_2$O$_4$+Na$^+$: 674.52 [M+Na]$^+$; observed 674.54.

BTA-C₁₁-Sulf₂

BTA-C$_{11}$-Sulf$_2$

A 15 mL glass vial was charged with **7** (203 mg, 0.31 mmol), DMPA (127 mg, 0.49 mmol), sodium 3-mercapto-1-propanesulfonate (329 mg, 1.84 mmol) and 12 mL deoxygenated methanol. The reaction mixture was transferred to a UV chamber and stirred for 2 hours with 365 nm (315-400 nm) UV light, yielding a light yellow suspension with some white solids. Subsequently, the solvent was removed *in vacuo*. The material was dispersed in 30 mL water and dialyzed against water (MWCO = 100-500 Da, Spectra/Por Biotech CE Membranes), after which the material was lyophilized, yielding a fluffy white material. The crude product was further purified by reversed-phase chromatography (H$_2$O/ACN 95/5–10/90 v/v) to give a white solid after lyophilization (138 mg, 45%). ^{1}H NMR (400 MHz, DMSO-d$_6$ δ): 8.64 (m, 3H, Ar), 8.35 (s, 3H, amides), 3.27 (m, 6H, NHC$\underline{H}_2$CH$_2$), 2.56-2.39 (m, 12H, C$\underline{H}_2$SC$\underline{H}_2$, C$\underline{H}_2$SO$_3^-$), 1.79 (q, 4H, SCH$_2$C$\underline{H}_2$CH$_2$S), 1.61-1.07 (m, 46H, aliphatic), 0.90 (d, 3H, C$\underline{H}_3$), 0.83 (d, 6H, CH(C$\underline{H}_3$)$_2$). ^{13}C NMR (400 MHz, DMSO-d$_6$ δ): 165.86, 165.80, 135.58, 128.75, 79.76, 79.43, 50.81, 37.87, 37.06, 36.52, 31.35, 30.89, 30.42, 28.67, 27.85, 26.96, 26.02, 24.50, 23.03, 22.95, 19.98. FT-IR (ATR) ν (cm^{-1}): 3299, 3075, 3923, 2852, 1643, 1595, 1542, 1536, 1466, 1437, 1365, 1291, 1267, 1188, 1052, 915, 856, 708, 634, 604, 527, 474, 467, 461. MALDI-TOF: *m/z* calculated for C$_{47}$H$_{83}$N$_3$O$_9$S$_4$$^{2-}$+H$^+$: 962.51 [M+H]$^-$; observed 962.52; *m/z* calculated for C$_{47}$H$_{83}$N$_3$O$_9$S$_4$$^{2-}$+Na$^+$: 984.49 [M+Na]$^-$; observed 984.52;

BTA-C$_{11}$-TMA$_2$
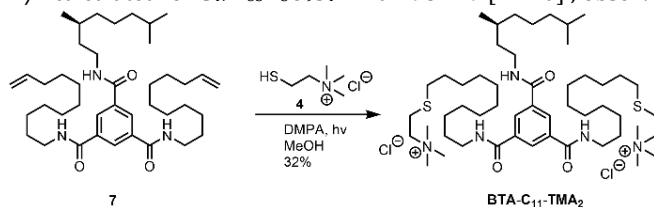
BTA-C₁₁-TMA₂

BTA-C$_{11}$-TMA$_2$

A 15 mL glass vial was charged with **7** (137 mg, 0.21 mmol), DMPA (119 mg, 0.46 mmol), **4** (382 mg, 2.45 mmol) and 5 mL deoxygenated methanol. The reaction mixture was transferred to a UV chamber and stirred for 2.5 hours with 365 nm (315-400 nm) UV light. Subsequently, the solvent was removed *in vacuo*, yielding a yellow solid. The crude product was purified by reversed-phase chromatography (H$_2$O/ACN 95/5–10/90 v/v) twice to give a white fluffy solid after lyophilization (65 mg, 32%). ^{1}H NMR (400 MHz, CD$_3$OD δ): 8.28 (m, 3H, Ar), 3.48-3.40 (m, 4H, SCH$_2$C$\underline{H}_2$N), 3.38-3.25 (m, 6H, NHC$\underline{H}_2$CH$_2$), 3.06 (s, 18H, C$\underline{H}_3$), 2.88-2.79 (m, 4H, SC$\underline{H}_2$CH$_2$N), 2.52 (t, 4H, CH$_2$C$\underline{H}_2$S), 1.61-1.02 (m, 46H, aliphatic), 0.87 (d, 3H, C$\underline{H}_3$), 0.78 (d, 6H, CH(C$\underline{H}_3$)$_2$). ^{13}C NMR (400 MHz, CD$_3$OD δ): 169.58, 169.53, 137.86, 130.76, 130.68, 119.18, 68.06, 68.04, 68.02, 54.60, 54.56, 54.52, 42.18, 41.44, 40.33, 39.29, 38.49, 33.99, 32.89, 31.62, 29.06, 26.78, 26.15, 24.09, 24.00, 20.97. FT-IR (ATR) ν (cm^{-1}): 3303, 3074, 3026, 2923, 2853, 1643, 1596, 1535, 1478, 1467, 1435, 1366, 1330, 1290, 1267, 1199, 1150, 1121, 1048, 1014, 972, 945, 905, 783, 702, 636, 591, 526, 488, 475, 457. MALDI-TOF-MS: *m/z* calculated for C$_{51}$H$_{97}$N$_5$O$_3$S$_2$$^{2+}$+Cl$^+$: 927.16 [M+Cl]$^+$; observed 926.71.

7.7 References

1   S. J. J. Singer and G. L. L. Nicolson, *Science*, 1972, **175**, 720–731.
2   M. R. Krause and S. L. Regen, *Acc. Chem. Res.*, 2014, **47**, 3512–3521.
3   P. Y. W. Dankers and E. W. Meijer, *Bull. Chem. Soc. Jpn.*, 2007, **80**, 2047–2073.
4   K. Petkau-Milroy, M. H. Sonntag and L. Brunsveld, *Chem. - A Eur. J.*, 2013, **19**, 10786–10793.
5   O. J. G. M. Goor, S. I. S. Hendrikse, P. Y. W. Dankers and E. W. Meijer, *Chem. Soc. Rev.*, 2017, **46**, 6621–6637.
6   A. Mata, Y. Geng, K. J. Henrikson, C. Aparicio, S. R. Stock, R. L. Satcher and S. I. Stupp, *Biomaterials*,

2010, **31**, 6004–6012.

7   N. A. Mansukhani, E. B. Peters, M. M. So, M. S. Albaghdadi, Z. Wang, M. R. Karver, T. D. Clemons, J. P. Laux, N. D. Tsihlis, S. I. Stupp and M. R. Kibbe, *Macromol. Biosci.*, 2019, **19**, 1900066.

8   D. Straßburger, N. Stergiou, M. Urschbach, H. Yurugi, D. Spitzer, D. Schollmeyer, E. Schmitt and P. Besenius, *ChemBioChem*, 2018, **19**, 912–916.

9   B. J. Cafferty, I. Gállego, M. C. Chen, K. I. Farley, R. Eritja and N. V. Hud, *J. Am. Chem. Soc.*, 2013, **135**, 2447–2450.

10   B. Liu, C. G. Pappas, J. Ottelé, G. Schaeffer, C. Jurissek, P. F. Pieters, M. Altay, I. Marić, M. C. A. Stuart and S. Otto, *J. Am. Chem. Soc.*, 2020, **142**, 4184–4192.

11   S. C. Karunakaran, B. J. Cafferty, A. Weigert-Muñoz, G. B. Schuster and N. V. Hud, *Angew. Chemie - Int. Ed.*, 2019, **58**, 1453–1457.

12   J. N. Israelachvili, D. J. Mitchell and B. W. Ninham, *Biochim. Biophys. Acta - Biomembr.*, 1977, **470**, 185–201.

13   X. Ma and H. Tian, *Acc. Chem. Res.*, 2014, **47**, 1971–1981.

14   E. Fröhlich, *Int. J. Nanomedicine*, 2012, **7**, 5577–5591.

15   L. C. Palmer, Y. S. Velichko, M. O. De La Cruz and S. I. Stupp, *Philos. Trans. R. Soc. A Math. Phys. Eng. Sci.*, 2007, **365**, 1417–1433.

16   M. Von Gröning, I. De Feijter, M. C. A. Stuart, I. K. Voets and P. Besenius, *J. Mater. Chem. B*, 2013, **1**, 2008–2012.

17   R. Appel, J. Fuchs, S. M. Tyrrell, P. A. Korevaar, M. C. A. Stuart, I. K. Voets, M. Schönhoff and P. Besenius, *Chem. - A Eur. J.*, 2015, **21**, 19257–19264.

18   R. Appel, S. Tacke, J. Klingauf and P. Besenius, *Org. Biomol. Chem.*, 2015, **13**, 1030–1039.

19   P. Besenius, G. Portale, P. H. H. Bomans, H. M. Janssen, A. R. A. Palmans and E. W. Meijer, *Proc. Natl. Acad. Sci.*, 2010, **107**, 17888–17893.

20   L. C. Palmer and S. I. Stupp, *Acc. Chem. Res.*, 2008, **41**, 1674–1684.

21   H. Dong, S. E. Paramonov, L. Aulisa, E. L. Bakota and J. D. Hartgerink, *J. Am. Chem. Soc.*, 2007, **129**, 12468–12472.

22   C. Schaefer, I. K. Voets, E. W. Meijer, P. Van Der Schoot and P. Besenius, *ACS Macro Lett.*, 2012, **1**, 830–833.

23   T. Imae and S. Ikeda, *Colloid Polym. Sci.*, 1987, **265**, 1090–1098.

24   F. C. Mackintosh, A. Safran and P. A. Pincus, *Epl*, 1990, **12**, 697–702.

25   A. Shukla and H. Rehage, *Langmuir*, 2008, **24**, 8507–8513.

26   H. Mattoussi, F. E. Karasz and K. H. Langley, *J. Chem. Phys.*, 1990, **93**, 3593–3603.

27   M. M. Kohonen, M. E. Karaman and R. M. Pashley, *Langmuir*, 2000, **16**, 5749–5753.

28   F. Hofmeister, *Arch. für Exp. Pathol. und Pharmakologie*, 1888, **25**, 1–30.

29   B. Kang, H. Tang, Z. Zhao and S. Song, *ACS Omega*, 2020, **5**, 6229–6239.

30   R. Perez-Jimenez, R. Godoy-Ruiz, B. Ibarra-Molero and J. M. Sanchez-Ruiz, *Biophys. J.*, 2004, **86**, 2414–2429.

31   Y. Zhang and P. S. Cremer, *Curr. Opin. Chem. Biol.*, 2006, **10**, 658–663.

32   P. Y. W. Dankers, M. C. Harmsen, L. A. Brouwer, M. J. A. Van Luyn and E. W. Meijer, *Nat. Mater.*, 2005, **4**, 568–574.

33   Y. Li, L. Dubreucq, B. G. Alvarenga, M. Raynal and L. Bouteiller, *Chem. - A Eur. J.*, 2019, **25**, 10650–10661.

34   L. N. J. De Windt, C. Kulkarni, H. M. M. Ten Eikelder, A. J. Markvoort, E. W. Meijer and A. R. A. Palmans, *Macromolecules*, 2019, **52**, 7430–7438.

35   A. Heeres, C. Van Der Pol, M. Stuart, A. Friggeri, B. L. Feringa and J. Van Esch, *J. Am. Chem. Soc.*, 2003, **125**, 14252–14253.

36   A. Brizard, M. Stuart, K. Van Bommel, A. Friggeri, M. De Jong and J. Van Esch, *Angew. Chemie - Int. Ed.*, 2008, **47**, 2063–2066.

37   A. M. Brizard, M. C. A. Stuart and J. H. Van Esch, *Faraday Discuss.*, 2009, **143**, 345–357.

38   J. Boekhoven, A. M. Brizard, M. C. A. Stuart, L. Florusse, G. Raffy, A. Del Guerzo and J. H. Van Esch, *Chem. Sci.*, 2016, **7**, 6021–6031.

39   C. M. A. Leenders, M. B. Baker, I. A. B. Pijpers, R. P. M. Lafleur, L. Albertazzi, A. R. A. Palmans and E. W. Meijer, *Soft Matter*, 2016, **12**, 2887–2893.

40   C. M. A. Leenders, L. Albertazzi, T. Mes, M. M. E. Koenigs, A. R. A. Palmans and E. W. Meijer, *Chem. Commun.*, 2013, **49**, 1963–1965.

41   J. M. Goronja, A. M. J. Ležaić, B. M. Dimitrijević, A. M. Malenović, D. R. Stanisavljev and N. D. Pejić, *Hem. Ind.*, 2016, **70**, 485–492.
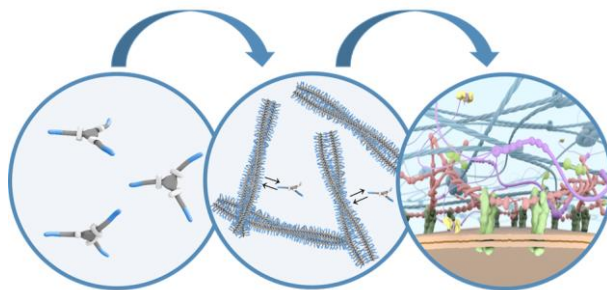
42   F. Helmich, C. C. Lee, M. M. L. Nieuwenhuizen, J. C. Gielen, P. C. M. Christianen, A. Larsen, G. Fytas, P. E. L. G. Leclère, A. P. H. J. Schenning and E. W. Meijer, *Angew. Chemie - Int. Ed.*, 2010, **49**, 3939–3942.

43   Y. Moroi, K. Motomura and R. Matuura, *J. Colloid Interface Sci.*, 1974, **46**, 111–117.

44   J. D. Hartgerink, E. Beniash and S. I. Stupp, *Science*, 2001, **294**, 1684–1688.

45   J. D. Hartgerink, E. Beniash and S. I. Stupp, *Proc. Natl. Acad. Sci.*, 2002, **99**, 5133–5138.

46   H. Fenniri, P. Mathivanan, K. L. Vidale, D. M. Sherman, K. Hallenga, K. V. Wood and J. G. Stowell, *J. Am. Chem. Soc.*, 2001, **123**, 3854–3855.

47   H. Fenniri, B. L. Deng and A. E. Ribbe, *J. Am. Chem. Soc.*, 2002, **124**, 11064–11072.

48   H. Frisch, J. P. Unsleber, D. Lüdeker, M. Peterlechner, G. Brunklaus, M. Waller and P. Besenius, *Angew. Chemie - Int. Ed.*, 2013, **52**, 10097–10101.

49   T. J. Moyer, J. A. Finbloom, F. Chen, D. J. Toft, V. L. Cryns and S. I. Stupp, *J. Am. Chem. Soc.*, 2014, **136**, 14746–14752.

50   D. Spitzer, L. L. Rodrigues, D. Straßburger, M. Mezger and P. Besenius, *Angew. Chemie - Int. Ed.*, 2017, **56**, 15461–15465.

51   H. Frisch, Y. Nie, S. Raunser and P. Besenius, *Chem. - A Eur. J.*, 2015, **21**, 3304–3309.

52   P. Ahlers, H. Frisch and P. Besenius, *Polym. Chem.*, 2015, **6**, 7245–7250.

53   B. J. Cafferty, R. R. Avirah, G. B. Schuster and N. V. Hud, *Chem. Sci.*, 2014, **5**, 4681–4686.

54   K. J. C. Van Bommel, C. Van Der Pol, I. Muizebelt, A. Friggeri, A. Heeres, A. Meetsma, B. L. Feringa and J. Van Esch, *Angew. Chemie - Int. Ed.*, 2004, **43**, 1663–1667.

55   A. Sarkar, J. C. Kölsch, C. M. Berač, A. Venugopal, R. Sasmal, R. Otter, P. Besenius and S. J. George, *ChemistryOpen*, 2020, **9**, 346–350.

56   S. Ghosh, V. Yesilyurt, E. N. Savariar, K. Irvin and S. . Thayumanavan, *J. Polym. Sci. Part A Polym. Chem.*, 2009, **47**, 1052–1060.

57   A. Pal, S. Shrivastava and J. Dey, *Chem. Commun.*, 2009, 6997–6999.

58   K. Petkau-Milroy, M. H. Sonntag, A. H. A. M. Van Onzen and L. Brunsveld, *J. Am. Chem. Soc.*, 2012, **134**, 8086–8089.

59   C. E. Hoyle, A. B. Lowe and C. N. Bowman, *Chem. Soc. Rev.*, 2010, **39**, 1355–1387.

60   A. B. Lowe, *Polym. Chem.*, 2010, **1**, 17–36.

61   C. E. Hoyle and C. N. Bowman, *Angew. Chemie - Int. Ed.*, 2010, **49**, 1540–1573.

62   N. M. Matsumoto, R. P. M. Lafleur, K. Lou, K. C. Shih, S. P. W. Wijnands, C. Guibert, J. W. A. M. Van Rosendaal, I. K. Voets, A. R. A. Palmans, Y. Lin and E. W. Meijer, *J. Am. Chem. Soc.*, 2018, **140**, 13308–13316.

63   J. Boekhoven, P. Van Rijn, A. M. Brizard, M. C. A. Stuart and J. H. Van Esch, *Chem. Commun.*, 2010, **46**, 3490–3492.

64   J. Boekhoven, A. M. Brizard, P. Van Rijn, M. C. A. Stuart, R. Eelkema and J. H. Van Esch, *Angew. Chemie - Int. Ed.*, 2011, **50**, 12285–12289.

65   T. Klein, F. V. Gruschwitz, S. Rogers, S. Hoeppener, I. Nischang and J. C. Brendel, *J. Colloid Interface Sci.*, 2019, **557**, 488–497.

66   M. Wolffs, S. J. George, Ž. Tomović, S. C. J. Meskers, A. P. H. J. Schenning and E. W. Meijer, *Angew. Chemie - Int. Ed.*, 2007, **46**, 8203–8205.

67   F. Wurm, B. Rietzler, T. Pham and T. Bechtold, *Molecules*, 2020, **25**, 1840.

68   T. Shimizu, M. Masuda and H. Minamikawa, *Chem. Rev.*, 2005, **105**, 1401–1443.

69   C. Boettcher, B. Schade and J. H. Fuhrhop, *Langmuir*, 2001, **17**, 873–877.

70   H. Weissman and B. Rybtchinski, *Curr. Opin. Colloid Interface Sci.*, 2012, **17**, 330–342.

71   J. J. Max and C. Chapados, *J. Chem. Phys.*, 2009, **131**, 184505.

72   J. J. Max and C. Chapados, *J. Chem. Phys.*, 2003, **119**, 5632–5643.

73   M. Tanaka, T. Sawaguchi, Y. Sato, K. Yoshioka and O. Niwa, *Langmuir*, 2011, **27**, 170–178.

74   B. J. Walker, G. P. Nair, L. F. Marshall and V. Bulovic, *J. Am. Chem. Soc.*, 2009, **131**, 9624–9625.

75   Y. N. Gong, X. W. Wei, L. H. He, Y. Q. Wen, Y. W. Ren, Y. R. Xie and D. C. Zhong, *Dalt. Trans.*, 2017, **46**, 7403–7407.

76   J. Roosma, T. Mes, P. Leclère, A. R. A. Palmans and E. W. Meijer, *J. Am. Chem. Soc.*, 2008, **130**, 1120–1121.

77   G. Koeckelberghs, L. De Cremer, W. Vanormelingen, W. Dehaen, T. Verbiest, A. Persons and C. Samyn, *Tetrahedron*, 2005, **61**, 687–691.

Chapter 8

Towards the Application of Benzene-1,3,5-Tricarboxamides as Functional Materials

Abstract: In previous chapters fundamental studies on the structure and dynamics of supramolecular polymers and the interplay between those properties were presented. Function has to be incorporated in those polymers by the addition of bioactive functional monomers. However, the influence of these functional groups on the structure and dynamics of supramolecular polymers is yet to be elucidated. Therefore, some examples will be presented in this chapter in which functionality was introduced in benzene-1,3,5-tricarboxamides (BTAs). In the first section, the structure and dynamics of supramolecular copolymers with covalently attached functional groups will be described. These functional monomers change the hydrophilic/hydrophobic balance and as a result the supramolecular polymers are shortened and their exchange dynamics are increased. Similar findings are reported upon addition of the non-covalent dye Nile Red. Next, it will be shown that the supramolecular polymers can maintain their fiber-like morphology in protein-rich media, albeit with a shorter length due to interactions with the protein. Finally, the structure of BTAs in a stimuli-responsive hydrogel will be elucidated. With the new insights presented in this chapter, the first steps can be made towards functional materials based on BTAs.

8.1 Introduction

In the previous chapters, the relationship between the structure and dynamics of supramolecular polymers based on benzene-1,3,5-tricarboxamide (BTA) derivatives has been studied. These results illustrate that BTA-based polymers are promising for application in biomaterials as their structure and dynamics both resemble those of natural fibers. However, the use of BTA-based biomaterials is still in its infancy compared to the well-studied peptide amphiphiles[1–5] and ureidopyrimidinones.[6–9] This is partly due to a lack of detailed knowledge on how these supramolecular materials behave in physiological environments after the introduction of functional groups and how they interact with biological species such as cells and proteins.

As discussed in the first chapter of this thesis, understanding and controlling the structure-dynamics-function relationship is central to achieve successful applications as biocompatible materials. So far, the interplay between structure and dynamics has mainly been studied for BTAs in pure water and without functional moieties attached. The examples presented in previous chapters have made it clear that small chemical modifications to the structure of the monomer can drastically affect the morphologies and dynamics of the supramolecular polymer because of the delicate balance between hydrophilic and hydrophobic forces. The introduction of function, either via chemical modifications of the monomers or by placing the polymers in a biological environment, will without a doubt influence the morphology and dynamics of the supramolecular polymers. More systematic and fundamental studies are therefore required to gain a control over the influence of function in the structure-dynamics-function relationship.

In this chapter, some preliminary examples of functional materials based on water-compatible BTAs are presented with the aim to elucidate the effect of the functional groups on the structural and dynamic behavior of the resulting supramolecular (co)polymers. The focus in these examples lies on the characterization of the structure with cryogenic transmission electron microscopy (cryoTEM) and the dynamics with hydrogen/deuterium exchange followed by mass spectrometry (HDX-MS). In the first section, monomers are covalently functionalized with biologically relevant groups and the effect of their copolymerization with conventional monomers is subsequently studied. Additionally, an example is presented in which a small functional molecule is non-covalently bound to the supramolecular polymers. It has previously been confirmed that BTAs are compatible with cells,[10] but in this chapter also the compatibility of BTAs with protein-rich cell growing media is explored to asses if BTAs can be used as support materials during cell growth. Finally, stimuli-responsive hydrogels based on the dilution-induced supramolecular polymerization presented in Chapter 7 are introduced. The examples in this chapter provide some insights into the structure-dynamics-function relationship which should be used in the design of new biomaterials.

8.2 Copolymerization with covalently functionalized monomers

The copolymerization of unfunctionalized and functionalized monomers is an strategy often used to create supramolecular polymers with tunable numbers of functional groups presented on their surface.[11,12] However, the introduction of a functional moiety may change the self-assembly behavior of the monomers. In this section a few examples will be presented in which it is studied if and how copolymerization with functionalized monomers influences the supramolecular polymers of water-compatible BTAs.

Cyanine dyes have been covalently attached to BTAs to study the dynamics of the supramolecular polymers with stochastic optical reconstruction microscopy or Förster resonance energy transfer (FRET).[13–16] In most experiments **BTA-C$_{12}$-EG$_4$** and dye-labeled BTAs such as **BTA-C$_{12}$-EG$_4$-Cy3** (Figure 1A) were mixed to obtain a sample in which 5% of the molecules is labeled with a dye. CryoTEM images show that this copolymerization does not change the length of the supramolecular polymers as they are still micrometer long, similar to homopolymers of **BTA-C$_{12}$-EG$_4$**. Analysis of the images confirms that the BTAs still assemble into a double helix structure, with a slight decrease of the half helical pitch from 19.9 ± 0.4 nm before copolymerization (Chapter 2) to 19.5 ± 0.4 nm after copolymerization (Figure 1B). Dye-labeled samples are often equilibrated for 4 weeks before imaging with fluorescent microscopy as this was found to improve the visibility of the supramolecular polymers. A slight reduction of the half helical pitch is observed after the equilibration time (Figure 1C), but this difference is not as drastic as observed for **BTA-(S)-D-C$_{12}$-EG$_4$** as described in Chapter 4.

In contrast, HDX-MS experiments reveal an increase in the molecular exchange dynamics of the dye-labeled sample. Already in the first hours the percentage of fully deuterated **BTA-C$_{12}$-EG$_4$** in the copolymers exceeds that of the homopolymers (Figure 1D). After 72 hours, 77.8% of **BTA-C$_{12}$-EG$_4$** in the copolymers is fully deuterated whereas this is 70.4% in the homopolymers. The functionalization of a small amount of monomers with Cy3 does not result in a change of the supramolecular structure but does result in an increase of the exchange dynamics. Additionally, it should be noted that the H/D exchange of **BTA-C$_{12}$-EG$_4$** and **BTA-C$_{12}$-EG$_4$-Cy3** in the copolymers overlaps. It can therefore be concluded that the dynamics of **BTA-C$_{12}$-EG$_4$-Cy3**, provide a good representation of all molecules in the polymer.
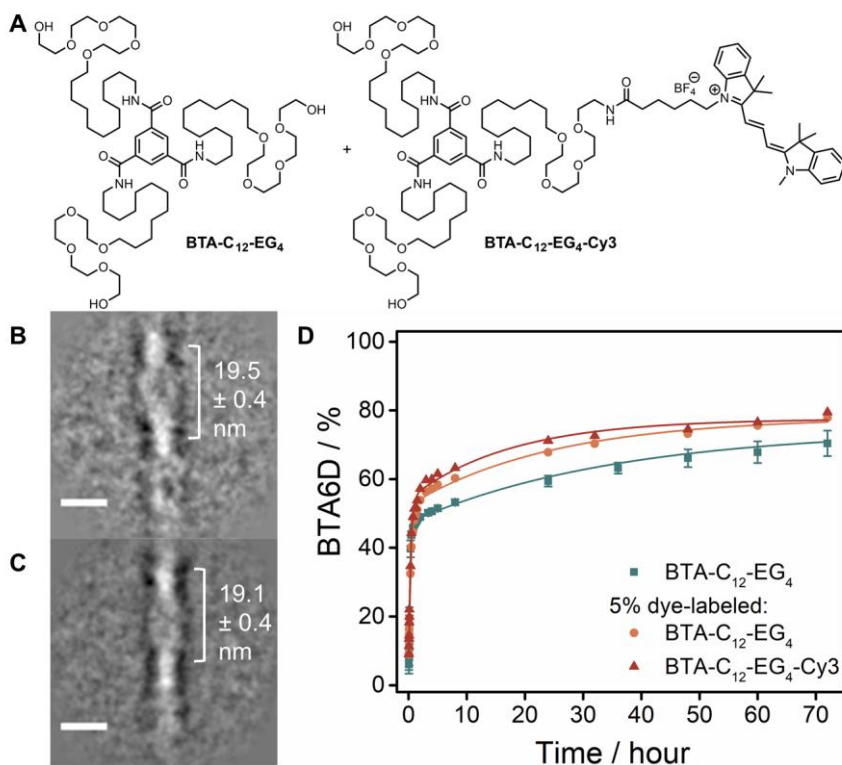
Figure 1. (A) Chemical structure of **BTA-C$_{12}$-EG$_4$** and **BTA-C$_{12}$-EG$_4$-Cy3**. (B-C) Class sum image of aligned image extracts of a sample of **BTA-C$_{12}$-EG$_4$** with 5% **BTA-C$_{12}$-EG$_4$-Cy3** after (B) 1 day of equilibration and (C) 4 weeks of equilibration ($c_{BTA, total}$ = 500 µM). (D) The percentage of fully deuterated BTAs in samples of **BTA-C$_{12}$-EG$_4$** with and without 5% **BTA-C$_{12}$-EG$_4$-Cy3** as a function of time after 100x dilution of aqueous 500 µM samples into D$_2$O (T = room temperature). The sample was equilibrated overnight before dilution into D$_2$O. The lines represent a bi-exponential growth function.

Next, the difference between monofunctionalized and trifunctionalized monomers was studied with choline-functionalized BTAs (Figure 2A). These BTAs were designed by Ir. Marle Vleugels and were used to create a multivalent platform for pathogen binding. The choline-functionalized BTAs do not homopolymerize due to charge repulsion, similar to the charged BTAs in Chapter 7. However, copolymerization with **BTA-C$_{12}$-EG$_4$** yields supramolecular polymers as is evidenced by cryoTEM images. The 8:1 mixture of **BTA-C$_{12}$-EG$_4$:BTA-C$_{12}$-EG$_4$-Chol$_1$** contains micrometer long supramolecular polymers (Figure 2B). In contrast to the homopolymers with **BTA-C$_{12}$-EG$_4$**, chain ends are observed in the images of the copolymers, which indicates that the polymer length has decreased upon copolymerization. More ends are observed in the 8:1 mixture of **BTA-C$_{12}$-EG$_4$:BTA-C$_{12}$-EG$_4$-Chol$_3$** (Figure 2C), which could be related to an increase of the electrostatic repulsions within the polymers due to the presentation

of three charged groups per monomer. Increasing the amount of **BTA-C$_{12}$-EG$_4$-Chol$_3$** to a 2:1 ratio results in fibers of less than a micrometer in length (Figure 2D). These results indicate that the length of the supramolecular polymers decreases upon copolymerization with a functionalized BTA with charges. The more charges presented on the monomer and the more functional monomers, the shorter the polymers become.
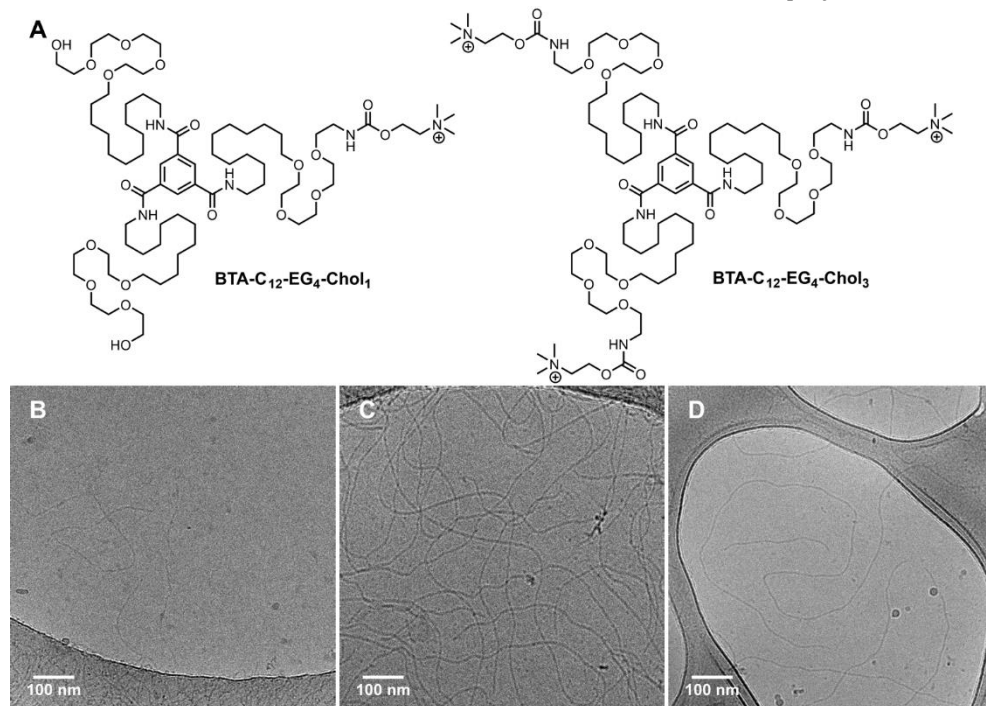
Figure 2. (A) Chemical structure of **BTA-C$_{12}$-EG$_4$-Chol$_1$** and **BTA-C$_{12}$-EG$_4$-Chol$_3$**. (B) CryoTEM image of a 8:1 mixture of **BTA-C$_{12}$-EG$_4$** and **BTA-C$_{12}$-EG$_4$-Chol$_1$** in water (c$_{BTA, total}$ = 500 µM). (C) CryoTEM image of a 8:1 mixture of **BTA-C$_{12}$-EG$_4$** and **BTA-C$_{12}$-EG$_4$-Chol$_3$** in water (c$_{BTA, total}$ = 500 µM). (D) CryoTEM image of a 2:1 mixture of **BTA-C$_{12}$-EG$_4$** and **BTA-C$_{12}$-EG$_4$-Chol$_3$** in water (c$_{BTA, total}$ = 500 µM).

The effect of the copolymerization of **BA-C$_{12}$-EG$_4$** with **BTA-C$_{12}$-EG$_4$-Chol$_3$** on the exchange dynamics was elucidated with HDX-MS. All labile hydrogen atoms of **BTA-C$_{12}$-EG$_4$-Chol$_3$** are immediately deuterated upon dilution into D$_2$O as this BTA forms shorts stacks on its own (Figure 3). The H/D exchange of the amide hydrogen atoms of this functional BTA is delayed upon mixing with **BTA-C$_{12}$-EG$_4$** due to its incorporation into the supramolecular polymers. However, both BTAs in the copolymer show more H/D exchange than the homopolymers of **BTA-C$_{12}$-EG$_4$**, especially in the first hours of the experiment. After 72 hours, 82.6% of **BTA-C$_{12}$-EG$_4$** and 80.7% of **BTA-C$_{12}$-EG$_4$-Chol$_3$** is fully deuterated. It can therefore be concluded that copolymerization increases the exchange dynamics in this example.

Figure 3. The percentage of fully deuterated BTAs before and after copolymerization of **BTA-C$_{12}$-EG$_4$** and **BTA-C$_{12}$-EG$_4$-Chol$_3$** as a function of time after 10x dilution of aqueous 500 µM samples into D$_2$O (T = room temperature). The sample was equilibrated overnight before dilution into D$_2$O. The lines represent a bi-exponential growth function.
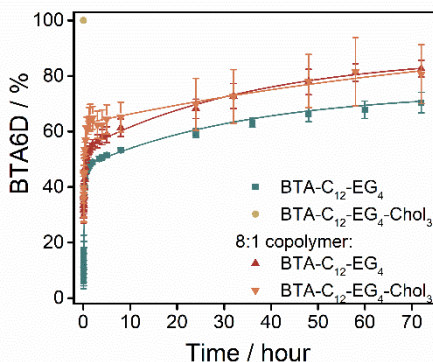
A similar shortening of supramolecular polymers was observed when dr. Giulia Morgese copolymerized a BTA functionalized with benzoxaborole (**BTA-C$_{12}$-EG$_4$-BA**, Figure 4A) with **BTA-C$_{12}$-EG$_4$**. The multivalent presentation of benzoxaborole on the supramolecular copolymers allows them to bind to human red blood cells via interactions with sialic acid.[17] CryoTEM images of the 9:1 mixture of **BTA-C$_{12}$-EG$_4$:BTA-C$_{12}$-EG$_4$-BA** show micrometer long supramolecular polymers, but ends are visible (Figure 4B) indicating a shortening of the fibers compared to the homopolymers of **BTA-C$_{12}$-EG$_4$**. Shortening of the polymers is therefore not only induced by repulsive electrostatic interactions. In this example with benzoxaborole the change in the hydrophilic/hydrophobic balance of the functional monomers is likely responsible for the change in the structure of the supramolecular polymers.
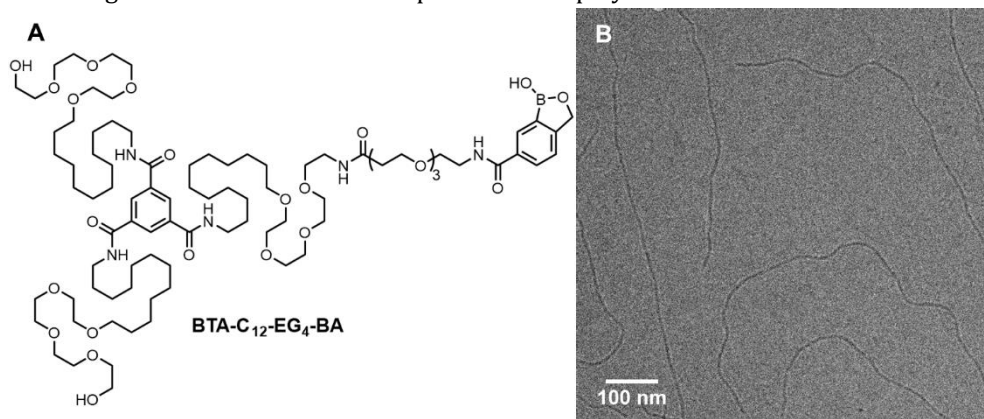
Figure 4. (A) Chemical structure of **BTA-C$_{12}$-EG$_4$-BA**. (B) CryoTEM image of a 9:1 mixture of **BTA-C$_{12}$-EG$_4$** and **BTA-C$_{12}$-EG$_4$-BA** in phosphate buffered saline ($c_{BTA, total}$ = 500 µM, pH 7.4).

In a final example, dr. Silvia Varela-Aramburu combined **BTA-C₁₂-EG₄** with hyaluronic acid (**HA** 10kDa, Figure 5A) to create a dynamic biocompatible hydrogel. **HA** is one of the main components of the extracellular matrix (ECM) and can bind to glycoproteins and receptors involved in inflammation processes, cell migration and cell proliferation. Here, the structure of BTA assemblies was studied at low concentration in the presence of **HA** to investigate the compatibility of the two components. Only short fibers of a few hundreds of nanometers in length are observed when a small weight percentage of HA is added to **BTA-C₁₂-EG₄** (Figure 5B). Since this co-assembly of **BTA-C₁₂-EG₄** and HA leads to a shorter and more polydisperse polymers, HA was covalently functionalized with BTAs (**BTA-C₁₂-EG₄-HA**, Figure 5C). The BTAs in this molecule cannot stack on their own due to the increased hydrophilicity and were therefore co-assembled with **BTA-C₁₂-EG₄**. This copolymerization results in the formation of supramolecular polymers that are longer than observed for the mixture with free **HA** (Figure 5D), but shorter than for the homopolymers of **BTA-C₁₂-EG₄**. Nevertheless, at high concentrations stronger hydrogels were obtained than for **BTA-C₁₂-EG₄** alone due to **BTA-C₁₂-EG₄-HA** crosslinking the polymers.
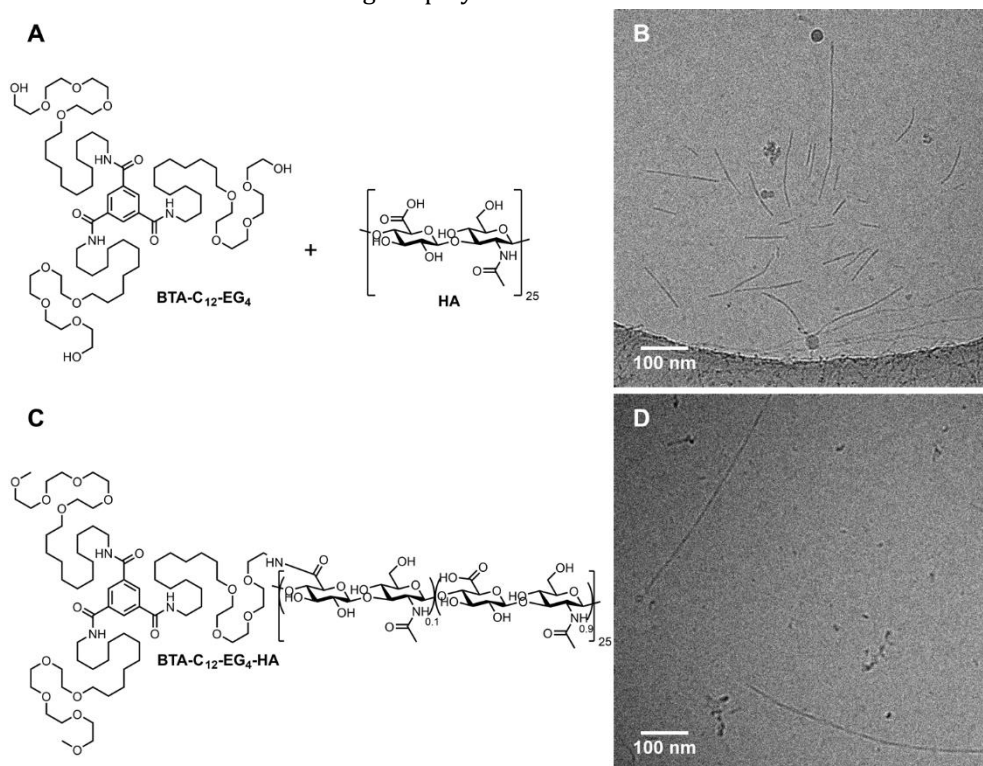
Figure 5. (A) Chemical structure of **BTA-C₁₂-EG₄** and hyaluronic acid (**HA**, 10 kDa). (B) CryoTEM image of a mixture of **BTA-C₁₂-EG₄** and **HA** at a 2:1 weight ratio in water (c_{BTA} = 500 μM). (C) Chemical structure of **BTA-C₁₂-EG₄-HA**. (D) CryoTEM image of a mixture of **BTA-C₁₂-EG₄** and **BTA-C₁₂-EG₄-HA** in a 1:1 weight ratio in water (c_{BTA} = 500 μM).

The examples presented here all comprise BTAs with covalently attached functional groups that increase the hydrophilicity of the monomers. The examples presented in previous chapters already illustrated that changes in the hydrophilic/hydrophobic balance of the monomers alter the structure and dynamics of the resulting supramolecular polymers. The introduction of functionality is no exception to this as the copolymerization with functional monomers often leads to the shortening of the polymers and an increase in exchange dynamics due to additional hydrophilic interactions with the solvent. The more hydrophilic groups are introduced, the shorter the supramolecular polymers become.

8.3 The effect of the addition of small hydrophobic molecules

Not only functional moieties that are covalently attached to supramolecular polymers can influence the supramolecular polymers, but also functional moieties that interact via non-covalent interactions. The surfactants presented in Chapter 7 and the **HA** used in the previous subsection both decrease the length of the supramolecular polymers based on **BTA-C$_{12}$-EG$_4$**. Here, the effect of small hydrophobic molecules on the structure and dynamics of the supramolecular polymers will be studied by adding the solvatochromic dye Nile Red (Figure 6A) to supramolecular polymers of **BTA-C$_{12}$-EG$_4$**. This dye is known to intercalate in the hydrophobic pocket of the BTAs and is therefore often used to probe the hydrophobicity of the polymer interior and as a non-covalent dye for the visualization of supramolecular structures.[18,19] CryoTEM images reveal that the length of the supramolecular polymers of **BTA-C$_{12}$-EG$_4$** has drastically decreased to only a few hundreds of nanometers upon 5% labeling with Nile Red (Figure 6B). The image analysis method described in Chapter 2 reveals the presence of a double helix structure with diameter of 8.2 ± 0.4 nm. The half helical pitch is increased from 19.9 ± 0.4 nm in the absence of Nile Red to 23.0 ± 0.4 nm in the presence of Nile Red (Figure 6C), indicating that Nile Red not only shortens the fibers, but also unravels the double helix.

HDX-MS was employed to elucidate the impact of Nile Red on the molecular exchange dynamics of **BTA-C$_{12}$-EG$_4$**. The percentage of fully deuterated BTA increases faster in the first hour, which could indicate the formation of more defects (Figure 6D). When Nile Red is added, 81.1% of the BTAs is fully deuterated after 56 hours. In contrast, 70.4% of the molecules is fully deuterated after 72 hours in the absence of Nile Red. These results indicate that the molecular exchange dynamics of **BTA-C$_{12}$-EG$_4$** are increased by the addition of Nile Red, especially in the first hours. This increase in H/D exchange in combination with the shortening of the fibers, illustrate that the structure and dynamics of supramolecular polymers are not independent variables and should be evaluated simultaneously. UV-Vis spectroscopy and Fourier-transform infrared (FT-IR) spectroscopy revealed that the BTAs do not lose their aggregation ability or hydrogen bond pattern upon addition of Nile Red, suggesting that the dye does not

interact with the amides but via hydrophobic interactions. The group of Hud reported that a similar dye, Nile Blue, could disrupt their supramolecular polymers due to its hydrophobic interactions with the hydrophobic surface of their macrocycles.[20] Based on these results, we expect that Nile Red interacts with the hydrophobic BTA core or the alkyl chains, thereby disturbing their hydrophobic interactions. The findings presented here should be kept in mind when Nile Red is used for the characterization of supramolecular polymers.
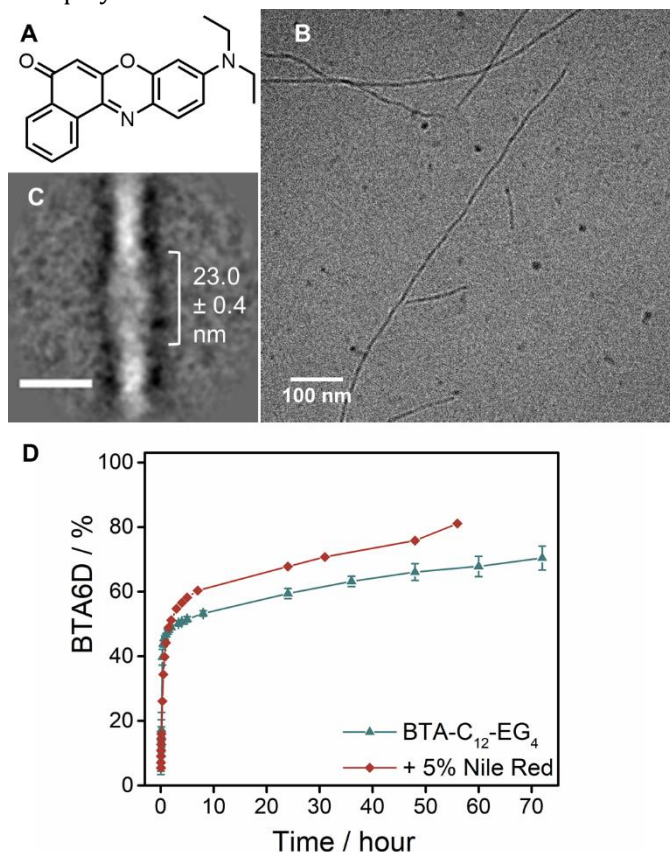
Figure 6. (A) Chemical structure of Nile Red. (B) CryoTEM image of **BTA-C$_{12}$-EG$_4$** with 5% Nile Red in water (c$_{BTA}$ = 500 µM, c$_{NR}$ = 25 µM). Dark spherical objects are crystalline ice particles. (C) Class sum image of aligned image extracts of a sample of **BTA-C$_{12}$-EG$_4$** in water with 5% Nile Red (c$_{BTA}$ = 500 µM, c$_{NR}$ = 25 µM). The scale bar is 10 nm. (D) The percentage of fully deuterated **BTA-C$_{12}$-EG$_4$** in the absence and presence of 5% Nile Red as a function of time after the 100x dilution of aqueous 500 µM samples into D$_2$O (T = room temperature). Lines are added to guide the eye.

8.4 The impact of proteins on the polymer structure

Protein adsorption onto materials is generally the first event occurring between synthetic biomaterials and biological systems.[21] The protein-compatibility of BTAs was

therefore investigated in collaboration with dr. Silvia Varela-Aramburu and dr. Giulia Morgese by incubating **BTA-C₁₂-EG₄** with a physiologically relevant concentration of the protein bovine serum albumin (BSA).[10] CryoTEM images confirm that the BTAs retain their micrometer long fiber-like morphology after overnight incubation with the protein (Figure 7A). Nevertheless, some polymer ends can be observed, which does not occur for **BTA-C₁₂-EG₄** in pure water. This indicates that the length of the polymers is slightly shortened by interaction with the protein. Molecular simulations in collaboration with the group of prof. dr. Giovanni Pavan revealed that this is due to the protein directly interacting with the fibers and subsequently taking up a few monomers into its hydrophobic interior.[10]

The compatibility of BTAs with cell-growing media was explored by equilibrating **BTA-C₁₂-EG₄** polymers in Eagle's Minimum Essential Medium (MEM) and Dulbecco's Modified Eagle Medium (DMEM). Both media contain 10% of fetal bovine serum (FBS), a complex biological serum containing many proteins and growth factors used for the growth of eukaryotic cells. Supramolecular polymers of micrometer length are found in DMEM (Figure 7B) and of only a few hundred of nanometers in MEM (Figure 7C). Additionally, in both media some BTAs seem to be present in small micelles. However, many of the BTAs maintains a fiber-like morphology even in these complex media with high protein concentration, albeit with a shorter length due to protein interactions. No cytotoxicity was observed when cells were grown on the BTA polymers.[10]
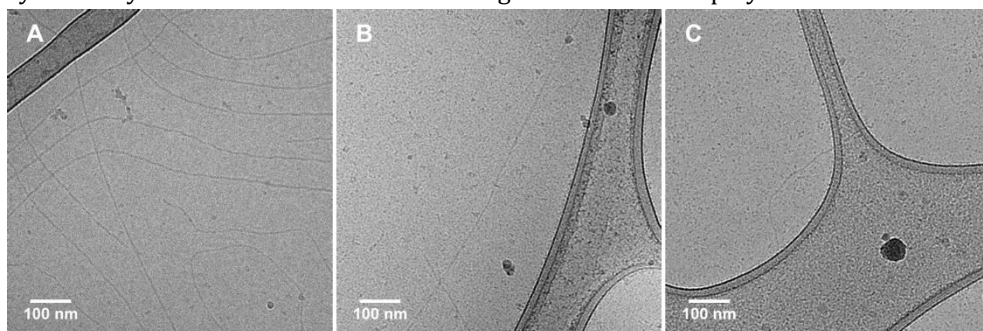
Figure 7. (A) CryoTEM images of **BTA-C₁₂-EG₄** after overnight incubation with BSA in phosphate buffered saline (c_{BTA} = 250 μM, c_{BSA} = 20 mg/mL). (B) CryoTEM image of **BTA-C₁₂-EG₄** in DMEM (c_{BTA} = 250 μM, 10% FBS). (C) CryoTEM image of **BTA-C₁₂-EG₄** in MEM (c_{BTA} = 250 μM, 10% FBS). Dark spherical objects are crystalline ice particles.

8.5 BTAs in stimuli-responsive hydrogels

BTA-C₁₂-EG₄ can form a hydrogel at concentrations above 1 wt% due to fiber entanglements (Figure 8A).[22] It was shown in Chapter 7 that supramolecular polymers can be disrupted by the addition of surfactants and can be reobtained upon dilution. This can be used as a strategy to control the formation of hydrogels. Together with Dr. Jesús Mosquera, Dr. Lu Su and Cyprien Muller it was shown that the supramolecular polymers in a 4 wt% solution of **BTA-C₁₂-EG₄** are disrupted by the addition of 6.5

equivalents of octyltrimethylammonium bromide (OTAB, Figure 8B). As a result, a solution was obtained instead of a viscous hydrogel. The 2-fold dilution of the sample results in the reformation of the supramolecular polymers and already 5 minutes after dilution a transparent hydrogel was obtained. Further dilution of this solution would lead to a solution again due to a loss of fiber entanglements at low concentration, thereby presenting a method to obtain a sol-gel-sol transition by dilution.
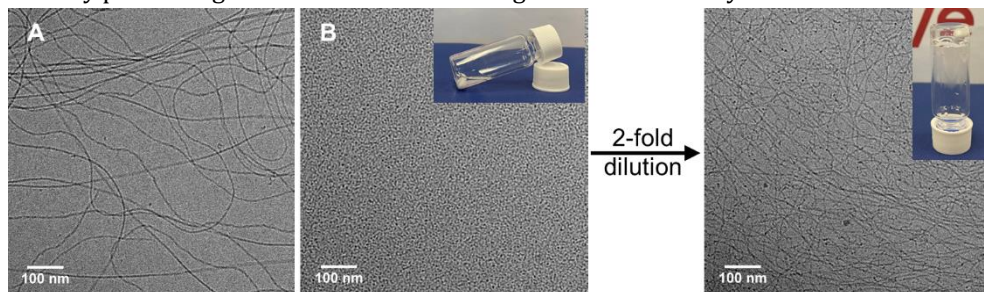
Figure 8. (A) CryoTEM image of a 2 wt% hydrogel of **BTA-C$_{12}$-EG$_4$** in water (c = 15.5 mM). (B) CryoTEM image of **BTA-C$_{12}$-EG$_4$** with 6.5 equivalents of OTAB in water before (c_{BTA} = 31 mM (4 wt%), c_{OTAB} = 204 mM) and after 2-fold dilution (c_{BTA} = 15.5 mM (2 wt%), c_{OTAB} = 102 mM, 5 minutes equilibration). The insets show macroscopic images of the BTA solution.

Dr. Lu Su combined **BTA-C$_{12}$-EG$_4$** with the polymeric surfactant octyl poly(ethylene glycol) (OPEG). The long 2k PEG chain of this surfactant enables micelle fusion at high concentrations above the critical micelle concentration (CMC, around 42 mM). Additionally, OPEG has an octyl chain for hydrophobic interactions with the BTA. Similar to the charged surfactant, this surfactant is able to disrupt the supramolecular polymers, which is reversible by dilution. The combination of **BTA-C$_{12}$-EG$_4$** and OPEG leads to the creation of a gel-sol-gel-sol transition of which the different states were visualized with cryoTEM (Figure 9). When **BTA-C$_{12}$-EG$_4$** and OPEG are combined in a 2:3 ratio at a high concentration of c_{BTA} = 80 mM, an opaque hydrogel is obtained (Gel 1) with a storage modulus (G') of 2 kPa. The fibers observed in this network are composed of fused micelles of **BTA-C$_{12}$-EG$_4$** with OPEG. Upon dilution to c_{BTA} = 45 mM, the fused micelles break apart and a clear solution is obtained (Sol 1). A second dilution step to c_{BTA} = 23 mM, which is below the CMC of OPEG, leads to the dissociation of **BTA-C$_{12}$-EG$_4$** and OPEG. A weaker hydrogel (Gel 2) with a G' of 5 Pa is formed within minutes due to reformation of the **BTA-C$_{12}$-EG$_4$** polymers and there subsequent entanglement. A final dilution step to c_{BTA} = 0.8 mM removes the entanglements of the BTA polymers and yields a solution again (Sol 2). The gel-sol-gel-sol transition of **BTA-C$_{12}$-EG$_4$** and OPEG can also be obtained in media such as phosphate buffered saline (PBS) and in DMEM. This results in a stimuli-responsive biocompatible hydrogel which we envision will be a useful as support material for the growth of cells.
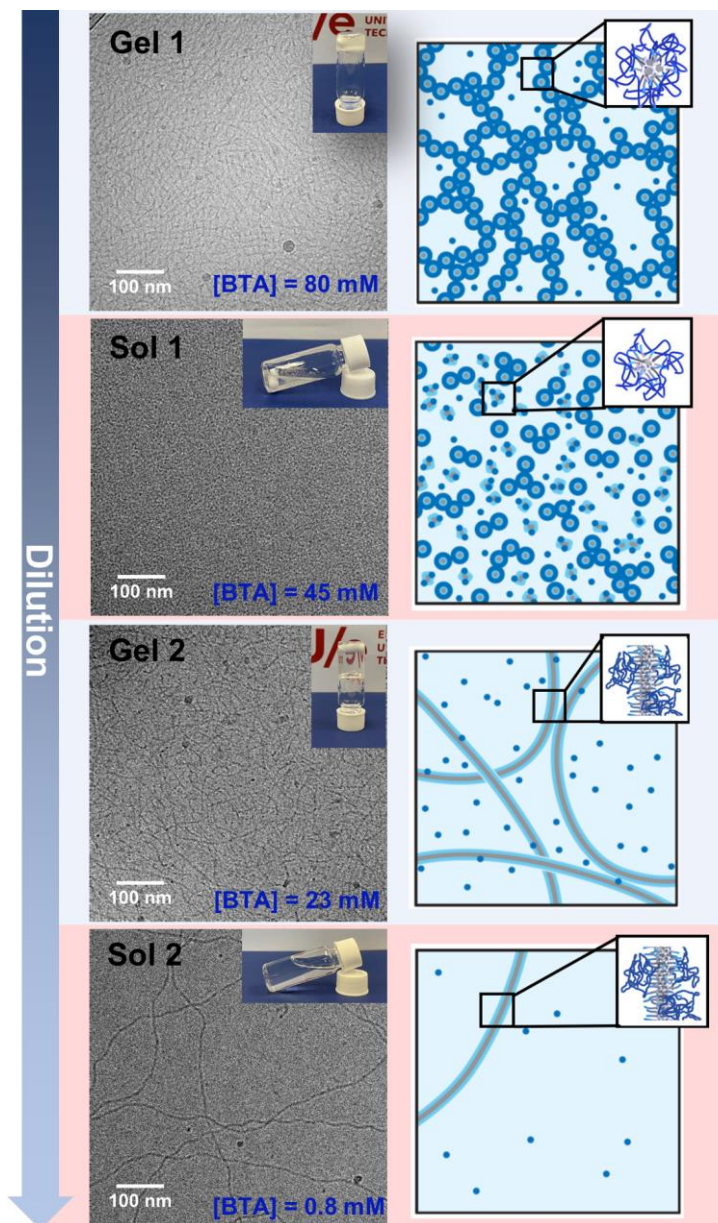
Figure 9. CryoTEM images and schematic representation of the gel-sol-gel-sol transitions of a two-component system of **BTA-C$_{12}$-EG$_4$**:OPEG 2:3 upon dilution. Insets show the macroscopic images of the samples.

8.6 Conclusions

The analytical techniques described in Chapter 2 and 3 for the characterization of supramolecular structure and dynamics have been applied to various examples of

functionalized materials based on BTAs. In the first examples, BTAs were covalently functionalized with a fluorescent dye or biologically relevant groups. The introduction of 5% Cy3-labeled BTA does not result in significant changes in the structure of the polymers, but their dynamics are increased. In other examples, motifs that can interact with biological matter are covalently coupled to some BTAs to allow the binding of the supramolecular polymers to, for example, bacteria and red blood cells. In all examples the length of the supramolecular polymers is decreased upon copolymerization and the more functional groups are present, the shorter the polymers become. Moreover, the copolymerization with choline-functionalized BTAs increases the exchange dynamics. In all cases the delicate balance between hydrophilic and hydrophobic components is changed in the functionalized monomers which affects the supramolecular copolymers. Additionally, the introduction of a functional moiety via non-covalent interactions leads to a similar shortening of the polymers and an increase of their exchange dynamic, as exemplified by the addition of Nile Red. The effect of introducing functionality on structure and dynamics should therefore be evaluated in the design of new supramolecular polymers and a trade-off should be made between the optimal number of functional motifs presented and the optimal length and dynamicity of the polymers.

Additionally, we evaluated if BTAs can be used as biomaterials during cell growth by studying their compatibility with proteins and cell-growing media rich in proteins. The polymers are able to maintain their fibrous structure in the vicinity of proteins. However, the interactions of the polymers with the proteins lead to a decrease of the polymer length. Still, subsequent cell experiments showed that the BTA polymers are compatible with several cell lines, underlining their potential as synthetic biomaterials.

In a final study, stimuli-responsive hydrogels are obtained by the combination of BTAs with surfactants. Poly(ethylene glycol)-functionalized surfactants allow for dilution-induced gel-sol-gel-sol transitions by the switching between fused micelle polymers and BTA-based supramolecular polymers as is illustrated with cryoTEM. We envision that this is a useful strategy for the growth of cells on top of the supramolecular polymers as no conditions that can damage the cells are acquired to assemble or remove the polymers in the presence of the cells.

8.7 Some general conclusions and future outlook

In the last part of this thesis, we revisit the aim as described in the introduction of this thesis. In Chapter 1, a bottom-up approach was proposed to benefit the design of supramolecular monomers with the aim to control the interplay between structure, dynamics and function of the resulting (co)polymers. Previously published work mainly focused the importance of the structure-function relationship, which is now well-recognized. In this thesis, the focus has been on the structure-dynamics relationship. In Chapter 2 and 3, cryoTEM and HDX-MS were presented as the characterization techniques of choice to study these two properties as they cause only minimal

perturbations during the measurements compared to the native assemblies in water. In subsequent chapters the impact of small chemical modifications - the introduction of stereogenic centrers, using monosaccharides as water-compatible periphery, changing the connectivity of amide bonds or adding charges - on the structure and dynamics of the supramolecular polymers was studied.

One of the main challenges in the field remains to rationally design monomers to come to a supramolecular polymers with the desired properties. Designing supramolecular motifs for self-assembly in water might, at some times, feel like walking on a tightrope; add too many hydrophilic or too many hydrophobic components and the balance between well-ordered supramolecular polymers and small ill-defined micelles is lost. However, the results presented in this thesis might provide some general design principles. In case of BTAs, dynamic micrometer long supramolecular polymers with double helix structure are obtained with linear side chains comprising a dodecyl chain and tetra(ethylene glycol) chain. In Chapter 4 it was described that increasing the order through the introduction of stereogenic centers tightens the packing of the molecules and decreases their dynamics. Branching in the side chains enhances the directionally and pattern of the hydrogen bonds, resulting in single fibers with a faster molecular exchange on long timescales. The introduction of a second hydrophilic group in the side chains results in the formation of small micelles, as is evidenced by the attachment of monosaccharides to the tetra(ethylene glycol) chains of BTAs in Chapter 5. In case of design flaws that result in a molecule assembling into small micelles, supramolecular polymerization can still be induced by copolymerization, as is shown in Chapter 6, or by additives that compensate repulsive interactions and increase the attractive interactions, as is shown in Chapter 7. We anticipate that the insights obtained in this work can also be applied in other supramolecular systems.

Over the years, we have expanded our toolbox of supramolecular building blocks and self-assembly strategies with the aim to create multicomponent, adaptive and functional biomaterials. In this chapter, it was already shown that the introduction of functional groups reduces the length of the supramolecular polymers and increases their dynamics. However, we are not there yet as many open questions still remain to be answered. Most importantly, one part of the structure-dynamics-function relationship remains to be studied, that is the interplay between function and dynamics. The examples described at the beginning of this chapter are still rather simple as they describe the structure and dynamics of supramolecular polymers in the absence of any interaction between their functional groups and biological species. It remains to be elucidated if and how the monomers rearrange upon multivalent binding, if the dynamics of supramolecular polymers change upon binding and if binding results in a change of the dynamics of bound monomers compared to the unbound monomers. We envision that an understanding of the structure-dynamics-function relationship paves the way towards the application of supramolecular polymers as synthetic biomaterials.

8.8 Experimental section

8.8.1 Materials and Methods

All solvents and chemicals used were of reagent grade quality or better and purchased from Biosolve or Sigma-Aldrich at the highest purity available and used without further purification unless otherwise noted. Dulbecco's Modified Eagle Medium (DMEM), Eagle's Minimum Essential Medium (MEM) and fetal bovine serum (FBS) were purchased from Gibco (Life Technologies). Phosphate buffer saline (PBS) and bovine serum albumin (BSA) were purchased from Sigma-Aldrich. **BTA-C$_{12}$-EG$_4$**,[19] **BTA-C$_{12}$-EG$_4$-Cy3**,[13] and **BTA-C$_{12}$-EG$_4$-BA**[17] were synthesized according to literature procedure. Water for aqueous samples was purified on an EMD Millipore Milli-Q Integral Water Purification System.

Sample preparation of BTA-C$_{12}$-EG$_4$ in water: the solid material was weighed into a glass vial equipped with a magnetic stirring bar. MQ-water was added to obtain the desired concentration. The sample was subsequently stirred at 80 °C for 15 minutes and the hot and hazy sample was vortexed immediately afterwards for 15 seconds. All samples were left to equilibrate overnight at room temperature.

Sample preparation of BTA-C$_{12}$-EG$_4$ with BTA-C$_{12}$-EG$_4$-Cy3: samples of the homopolymer of **BTA-C$_{12}$-EG$_4$** were prepared with the previously described protocol. The hot and hazy samples were vortexed for 15 seconds before **BTA-C$_{12}$-EG$_4$-Cy3** was added from a 1 mM stock solution in MeOH in the desired concentration. The samples were equilibrated at a temperature of 45 °C for 60 minutes, without stirring. The samples were left to equilibrate at room temperature overnight.

Sample preparation of BTA-C$_{12}$-EG$_4$ with BTA-C$_{12}$-EG$_4$-Chol$_1$ or BTA-C$_{12}$-EG$_4$-Chol$_3$: the solid **BTA-C$_{12}$-EG$_4$** was weighed into a glass vial equipped with a magnetic stirring bar. **BTA-C$_{12}$-EG$_4$-Chol$_1$** or **BTA-C$_{12}$-EG$_4$-Chol$_3$** were added from a 500 µM stock solution in MeOH. The solvent was removed with a N$_2$ (g) stream after which MQ-water was added to obtain the desired concentration. The sample was subsequently stirred at 80 °C for 15 minutes and the hot and hazy sample was vortexed immediately afterwards for 15 seconds. All samples were left to equilibrate overnight at room temperature.

Sample preparation of BTA-C$_{12}$-EG$_4$ with BTA-C$_{12}$-EG$_4$-BA, HA or BTA-C$_{12}$-EG$_4$-HA: the solid materials were weighed into a glass vial equipped with a magnetic stirring bar. MQ-water was added to obtain the desired concentration. The sample was subsequently stirred at 80 °C for 15 minutes and the hot and hazy sample was vortexed immediately afterwards for 15 seconds. All samples were left to equilibrate overnight at room temperature.

Sample preparation of BTA-C$_{12}$-EG$_4$ with Nile Red: Samples of 500 µM BTA in water were prepared by the standard protocol and were equilibrated overnight. Nile Red was added from a 25 mM stock solution in ACN 1 hour prior to the measurements to yield a sample with a BTA concentration of 500 µM and a Nile Red concentration of 25 µM (= 5% labeling).

Sample preparation of BTA-C$_{12}$-EG$_4$ with BSA: Samples of the BTA in water were prepared by the standard protocol and were incubated overnight at 37 °C with 20 mg/mL (303 µM) BSA in PBS. Samples were studied the next day.

Sample preparation of BTA-C$_{12}$-EG$_4$ in MEM and DMEM: 1 mM samples of the BTA in water were prepared with the previously described protocol. After 8 hours of equilibration the samples were diluted into MEM or DMEM (containing 10% FBS) to yield a final BTA concentration of 250 µM. The samples were allowed to equilibrate in the fridge overnight.

Sample preparation of BTA-C$_{12}$-EG$_4$ hydrogels with surfactants: the solid materials were weighed into a glas vial equipped with magnetic stirring bar in the desired ratio. MQ-water was

added to obtain the desired concentration. The sample was subsequently stirred at 80 °C for 15 minutes. The resulting mixture was allowed to equilibrate at room temperature overnight. Samples were diluted by adding the desired amount of MQ-water.

8.8.2 Instrumentation

Cryogenic transmission electron microscopy (cryoTEM) images were obtained with the instrumentation described in Chapter 2. Images of highly concentrated viscous hydrogels were obtained by applying 2 μL of sample and blotting for 5 seconds.

2D image reconstruction was performed in Berlin in collaboration with Dr. Christoph Böttcher and Dr. Svenja Herziger based on the instrumentation and methodology described in Chapter 2.

Hydrogen deuterium exchange experiments with electrospray ionization were carried out with the instruments described in Chapter 3.

8.8.3 Details on the HDX-MS analysis

All HDX-MS experiments were performed under similar conditions to eliminate influences from the environment, for example temperature. The measurements were performed by diluting a sample of self-assembled supramolecular building-blocks in H_2O 100x or 10x into D_2O. 0.5 mM sodium acetate was added to the D_2O prior to the dilution to facilitate the detection. For **BTA-C$_{12}$-EG$_4$-Cy3** the distribution with one sodium ion was used for the calculations and for **BTA-C$_{12}$-EG$_4$-Chol$_3$** the distribution with 3 charges. In all other cases the distributions with two sodium ions were used for the calculations. All calculations are based on the method presented in Chapter 3. The equations used for samples of **BTA-C$_{12}$-EG$_4$** are given in section 3.9.3.

Isotope correction for **BTA-C$_{12}$-EG$_4$-Cy3** is based on the following set of equations:

$I_{BTA1D\_c} = I_{875.11}$

$I_{BTA2D\_c} = I_{875.61} - 1.15 I_{BTA1D\_c}$

$I_{BTA3D\_c} = I_{876.11} - 1.15 I_{BTA2D\_c} - 0.70 I_{BTA1D\_c}$

$I_{BTA4D\_c} = I_{876.62} - 1.15 I_{BTA3D\_c} - 0.70 I_{BTA2D\_c} - 0.29 I_{BTA1D\_c}$

$I_{BTA5D\_c} = I_{877.12} - 1.15 I_{BTA4D\_c} - 0.70 I_{BTA3D\_c} - 0.29 I_{BTA2D\_c} - 0.09 I_{BTA1D\_c}$

$I_{BTA6D\_c} = I_{877.62} - 1.15 I_{BTA5D\_c} - 0.70 I_{BTA4D\_c} - 0.29 I_{BTA3D\_c} - 0.09 I_{BTA2D\_c} - 0.03 I_{BTA1D\_c}$

with $I_{875.11}$, $I_{875.61}$, $I_{876.11}$, $I_{876.62}$, $I_{877.12}$ and $I_{877.62}$ the intensity at m/z = 875.11, 875.61, 876.11, 876.62, 877.12 and 877.62, respectively.

The correction for the presence of 1 vol% H_2O can be calculated with the following set of equations:

$I_{BTA1D} = I_{BTA1D\_c} - 6.31 \times 10^{-10} I_{BTA6D\_c} - 3.06 \times 10^{-4} I_{BTA3D\_c}$

$I_{BTA2D} = I_{BTA2D\_c} - 1.56 \times 10^{-7} I_{BTA6D\_c} - 3.03 \times 10^{-2} I_{BTA3D\_c}$

$I_{BTA3D} = I_{BTA3D\_c} - 2.06 \times 10^{-5} I_{BTA6D\_c} + (3.06 \times 10^{-4} + 3.03 \times 10^{-2}) I_{BTA3D\_c}$

$I_{BTA4D} = I_{BTA4D\_c} - 1.53 \times 10^{-3} I_{BTA6D\_c}$

$I_{BTA5D} = I_{BTA5D\_c} - 6.06 \times 10^{-2} I_{BTA6D\_c}$

$I_{BTA6D} = I_{BTA6D\_c} + (6.31 \times 10^{-10} + 1.56 \times 10^{-7} + 2.06 \times 10^{-5} + 1.53 \times 10^{-3} + 6.06 \times 10^{-2}) I_{BTA6D\_c}$

Isotope correction for **BTA-C$_{12}$-EG$_4$-Chol$_3$** is based on the following set of equations:

$I_{BTA1D\_c} = I_{558.75}$

$I_{BTA2D\_c} = I_{559.08} - 1.03 I_{BTA1D\_c}$

$I_{BTA3D\_c} = I_{559.42} - 1.03 I_{BTA2D\_c} - 0.57 I_{BTA1D\_c}$

$I_{BTA4D\_c} = I_{560.09} - 1.03 I_{BTA3D\_c} - 0.57 I_{BTA2D\_c} - 0.22 I_{BTA1D\_c}$

$I_{BTA5D\_c} = I_{560.09} - 1.03 I_{BTA4D\_c} - 0.57 I_{BTA3D\_c} - 0.22 I_{BTA2D\_c} - 0.07 I_{BTA1D\_c}$

$I_{BTA6D\_c} = I_{560.42} - 1.03 I_{BTA5D\_c} - 0.57 I_{BTA4D\_c} - 0.22 I_{BTA3D\_c} - 0.07 I_{BTA2D\_c} - 0.02 I_{BTA1D\_c}$

With $I_{558.75}$, $I_{559.08}$, $I_{559.42}$, $I_{559.75}$, $I_{560.09}$ and $I_{560.42}$ the intensity at m/z = 558.75, 559.08, 559.42, 559.75, 560.09 and 560.42, respectively.

The correction for the presence of 10 vol% H_2O in the measurements with the 8:1 copolymers of **BTA-C$_{12}$-EG$_4$** and **BTA-C$_{12}$-EG$_4$-Chol$_3$** can be calculated with the following set of equations:

$I_{BTA1D} = I_{BTA1D\_c} - 1.02 \times 10^{-4} I_{BTA6D\_c} - 3.70 \times 10^{-2} I_{BTA3D\_c}$

$I_{BTA2D} = I_{BTA2D\_c} - 2.29 \times 10^{-3} I_{BTA6D\_c} - 3.33 \times 10^{-1} I_{BTA3D\_c}$

$I_{BTA3D} = I_{BTA3D\_c} - 2.74 \times 10^{-2} I_{BTA6D\_c} + (3.70 \times 10^{-2} + 3.33 \times 10^{-1}) I_{BTA3D\_c}$

$I_{BTA4D} = I_{BTA4D\_c} - 1.85 \times 10^{-1} I_{BTA6D\_c}$

$I_{BTA5D} = I_{BTA5D\_c} - 6.67 \times 10^{-1} I_{BTA6D\_c}$

$I_{BTA6D} = I_{BTA6D\_c} + (1.02 \times 10^{-4} + 2.29 \times 10^{-3} + 2.74 \times 10^{-2} + 1.85 \times 10^{-1} + 6.67 \times 10^{-1}) I_{BTA6D\_c}$

The percentage of the deuterated analogues can be calculated:

$$\%BTAnD = \frac{I_{BTAnD}}{\sum_{k=1}^{6} I_{BTAkD}} \times 100\%$$

with $\sum_{k=1}^{6} I_{BTAkD}$ the sum of all intensities. The percentage of deuterated analogues was calculated for several time points and plotted as a function of time in this chapter.

8.9 References

1   J. J. Greene, M. T. McClendon, N. Stephanopoulos, Z. Álvarez, S. I. Stupp and C. P. Richter, *J. Tissue Eng. Regen. Med.*, 2018, **12**, 1389–1401.

2   R. Dobbs, S. Choe, E. Kalmanek, D. A. Harrington, S. I. Stupp, K. T. McVary and C. A. Podlasek, *Nanomedicine Nanotechnology, Biol. Med.*, 2018, **14**, 2087–2094.

3   J. B. Matson, R. H. Zha and S. I. Stupp, *Curr. Opin. Solid State Mater. Sci.*, 2011, **15**, 225–235.

4   A. Mata, Y. Geng, K. J. Henrikson, C. Aparicio, S. R. Stock, R. L. Satcher and S. I. Stupp, *Biomaterials*, 2010, **31**, 6004–6012.

5   R. Mammadov, B. Mammadov, S. Toksoz, B. Aydin, R. Yagci, A. B. Tekinay and M. O. Guler, *Biomacromolecules*, 2011, **12**, 3508–3519.

6   R. C. van Gaal, B. D. Ippel, S. Spaans, M. I. Komil and P. Y. W. Dankers, *J. Polym. Sci.*, 2021, **59**, 1253–1266.

7   P. J. Besseling, T. Mes, A. W. Bosman, J. W. Peeters, H. M. Janssen, M. H. Bakker, J. O. Fledderus, M. Teraa, M. C. Verhaar, H. Gremmels and P. Y. W. Dankers, *J. Polym. Sci.*, 2021, **59**, 1267–1277.

8   M. J. G. Schotman, M. M. C. Peters, G. C. Krijger, I. van Adrichem, R. de Roos, J. L. M. Bemelmans, M. J. Pouderoijen, M. G. T. A. Rutten, K. Neef, S. A. J. Chamuleau and P. Y. W. Dankers, *Adv. Healthc. Mater.*, 2021, **10**, 1001987.

9   M. M. C. Bastings, S. Koudstaal, R. E. Kieltyka, Y. Nakano, A. C. H. Pape, D. A. M. Feyen, F. J. van Slochteren, P. A. Doevendans, J. P. G. Sluijter, E. W. Meijer, S. A. J. Chamuleau and P. Y. W. Dankers, *Adv. Healthc. Mater.*, 2014, **3**, 70–78.

10   S. Varela-Aramburu, G. Morgese, L. Su, S. M. C. Schoenmakers, M. Perrone, L. Leanza, C. Perego, G. M. Pavan, A. R. A. Palmans and E. W. Meijer, *Biomacromolecules*, 2020, **21**, 4105–4115.

11   K. Petkau-Milroy, M. H. Sonntag and L. Brunsveld, *Chem. - A Eur. J.*, 2013, **19**, 10786–10793.

12   P. Y. W. Dankers, M. C. Harmsen, L. A. Brouwer, M. J. A. Van Luyn and E. W. Meijer, *Nat. Mater.*, 2005, **4**, 568–574.

13   L. Albertazzi, D. van der Zwaag, C. M. A. Leenders, R. Fitzner, R. W. van der Hofstad and E. W.

Meijer, *Science*, 2014, **344**, 491–495.

14   L. Albertazzi, F. J. Martinez-Veracoechea, C. M. A. Leenders, I. K. Voets, D. Frenkel and E. W. Meijer, *Proc. Natl. Acad. Sci.*, 2013, **110**, 12203–12208.

15   C. M. A. Leenders, M. B. Baker, I. A. B. Pijpers, R. P. M. Lafleur, L. Albertazzi, A. R. A. Palmans and E. W. Meijer, *Soft Matter*, 2016, **12**, 2887–2893.

16   M. B. Baker, L. Albertazzi, I. K. Voets, C. M. A. Leenders, A. R. A. Palmans, G. M. Pavan and E. W. Meijer, *Nat. Commun.*, 2015, **6**, 6234.

17   G. Morgese, B. F. M. Waal, S. Varela-Aramburu, A. R. A. Palmans, L. Albertazzi and E. W. Meijer, *Angew. Chemie*, 2020, **132**, 17382–17386.

18   M. C. A. Stuart, J. C. Van De Pas and J. B. F. N. Engberts, *J. Phys. Org. Chem.*, 2005, **18**, 929–934.

19   C. M. A. Leenders, L. Albertazzi, T. Mes, M. M. E. Koenigs, A. R. A. Palmans and E. W. Meijer, *Chem. Commun.*, 2013, **49**, 1963–1965.

20   S. C. Karunakaran, B. J. Cafferty, M. Peláez-Fernández, K. Neselu, I. Schmidt-Krey, A. Fernandez-Nieves, G. B. Schuster and N. V. Hud, *Polym. Chem.*, 2018, **9**, 5268–5277.

21   Z. Othman, B. Cillero Pastor, S. van Rijt and P. Habibovic, *Biomaterials*, 2018, **167**, 191–204.

22   C. M. A. Leenders, T. Mes, M. B. Baker, M. M. E. Koenigs, P. Besenius, A. R. A. Palmans and E. W. Meijer, *Mater. Horiz.*, 2014, **1**, 116–120.

Summary
Supramolecular Polymers under the Magnifying Glass

Water-compatible supramolecular polymers are able to mimic the structural and dynamic properties of natural materials through an interplay of several non-covalent interactions, making them promising candidates for the formation of synthetic biomaterials. To create such multifaceted materials a bottom-up approach is required in which first a fundamental understanding of the self-assembly properties of the supramolecular polymers is obtained before the complexity of the material is increased. In this thesis a structure-dynamics-function relationship is presented for supramolecular polymers. Whereas structure and function of supramolecular polymers are well-studied in literature, the number of studies that describes their interplay with the dynamics is still limited. In this thesis the structure and dynamics of various supramolecular polymers is studied in detail with the aim to gain a better understanding of the structure-dynamics-function relationship.

The concept of supramolecular polymerization in water is introduced in **Chapter 1**. Examples of supramolecular polymers found in literature are presented, with a focus on the impact of chemical modification on the supramolecular structure and function. Subsequently, some recently developed experimental techniques for the characterization of supramolecular dynamics are described.

Cryogenic transmission electron microscopy (cryoTEM) is presented in **Chapter 2** as the method of choice for the visualization of supramolecular assemblies as it allows to study them in their hydrated near-native state. With this technique, we confirm the formation of supramolecular polymers based on new synthetic building blocks. Additionally, the secondary structure of supramolecular polymers based on benzene-1,3,5-tricarboxamides (BTAs) is elucidated with an image analysis technique that is based on single-particle analysis. With this technique the double helix structure within the supramolecular polymers is revealed and the half helical pitch is studied after chemical modifications and mixing.

In **Chapter 3**, hydrogen/deuterium exchange followed by mass spectrometry (HDX-MS) is discussed as a tool for the characterization of the molecular exchange dynamics. The technique is applied to a library of molecules to demonstrate that the dynamics of supramolecular polymers are influenced by the mechanism of self-assembly and the internal order within the polymers. Additionally, HDX-MS is shown to be a valuable technique to confirm copolymerization and to evaluate the dynamics of the different components within a copolymer.

The techniques introduced in the first chapters are applied in the next chapters of this thesis to elucidate the structure and dynamics of supramolecular polymers based on BTAs. In **Chapter 4** the effect of the introduction of stereogenic centers is explored.

The double helix structure and the dynamic behavior are initially maintained when deuterium atoms are introduced as stereogenic centers. However, an increase in order is revealed over time which is accompanied by a decrease in the half helical pitch and exchange dynamics. A single stack of molecules is obtained for a BTA with methyl groups as stereogenic centers. Finally, it is shown that the helicity of the stacks can be inversed through mixing with the BTA with stereogenic methyl groups.

The possibility to use saccharides as water-compatible periphery is explored in **Chapter 5**. Bundled supramolecular polymers with increased monomer exchange dynamics are found when monosaccharides replace the previously used tetra(ethylene glycol) periphery. Molecular dynamics simulations are used to reveal the presence of numerous hydrogen bonds between the saccharides, explaining the bundling of the supramolecular polymers and their increased dynamics. In contrast, small BTA micelles are formed when the monosaccharides are attached to the tetra(ethylene glycol). These BTAs can still be incorporated into a supramolecular polymer via copolymerization such that these functional moieties are expressed on the polymer.

An alternative route for the selective introduction of functional groups onto BTAs is presented in **Chapter 6**. The use of a commercially available desymmetrised core eliminates statistical reactions and reduces the number of synthetic steps. However, this approach inevitably leads to the inversion of one of the amide bonds on the benzene core. It is confirmed that these molecules can still form supramolecular polymers via intermolecular hydrogen bonds and that they can copolymerize with conventional BTAs without altering their structure and dynamics. Super-resolution microscopy confirms the successful incorporation of dye-labeled monomers into BTA polymers.

In **Chapter 7**, BTAs are combined with linear charged surfactants in various settings to create responsive materials. Supramolecular polymers with a tetra(ethylene glycol) periphery are disrupted by the charged surfactants but can be reobtained via dilution-induced supramolecular polymerization. BTAs with a charged periphery, on the other hand, assemble into short stacks due to charge repulsion and can only form elongated assemblies in the presence of oppositely charged surfactants. Finally, a BTA is studied with one hydrophobic side chain and two hydrophilic charged side chains. This molecule assembles into sheets and tubes as if it is a surfactant when salts are added, but these surfactant interactions can be turned off by the addition of a linear charged surfactant such that supramolecular polymers are obtained.

This thesis concludes with some examples in which functionality is introduced into BTA-based supramolecular polymers. The structure and dynamics of supramolecular copolymers containing covalently functionalized monomers is studied in **Chapter 8** to reveal that these biologically relevant groups slightly shorten the supramolecular polymers and slightly increase their exchange dynamics. BTA-based supramolecular polymers are also shown to be compatible with cell growth media. Finally, BTAs are incorporated in a stimuli-responsive hydrogel, highlighting their potential as responsive, functional biomaterials.

Samenvatting
Supramoleculaire Polymeren onder het Vergrootglas

Supramoleculaire polymeren die geassembleerd zijn in water zijn in staat om de structuur en dynamiek van natuurlijke materialen na te bootsen door een samenspel van niet-covalente interacties. Dit maakt hen veelbelovende kandidaten voor het maken van synthetische biomaterialen. Een bottom-up aanpak is hiervoor vereist waarbij eerst een fundamenteel begrip van de zelf-assemblage eigenschappen wordt verkregen voordat de complexiteit van het materiaal toeneemt. In dit proefschrift wordt de relatie tussen de structuur, dynamiek en functie van supramoleculaire polymeren besproken. De structuur en functie van supramoleculaire polymeren worden vaak beschreven in de literatuur, terwijl het aantal studies die de dynamiek van supramoleculaire polymeren beschrijft gelimiteerd is. In dit proefschrift worden de structuur en dynamiek van verschillende supramoleculaire polymeren bestudeerd om een beter begrip te krijgen van de structuur-dynamiek-functie relatie.

In **Hoofdstuk 1** wordt het concept van supramoleculaire polymerisatie in water geïntroduceerd. Hiervoor worden voorbeelden uit de literatuur aangehaald en wordt er gefocust op de impact van chemische modificaties op de supramoleculaire structuur en functie. Daarna worden recentelijk gevonden experimentele technieken besproken voor het meten van de dynamiek van de supramoleculaire polymeren.

De visualisatie van supramoleculaire assemblages onder condities vergelijkbaar met die in oplossing door middel van cryogene transmissie elektronenmicroscopie (cryoTEM) wordt besproken in **Hoofdstuk 2**. Met deze technieken kan de vorming van supramoleculaire polymeren door nieuwe bouwstenen bevestigd worden. Door middel van beeldanalyse wordt de secondaire structuur van supramoleculaire polymeren op basis van benzeen-1,3,5-tricarboxamides (BTAs) opgehelderd. Deze analyse toont aan dat de supramoleculaire polymeren bestaan uit twee ketens van moleculen die om elkaar heen draaien als een dubbele helix. De pitch van deze helix kan aangepast worden door chemische modificaties of door het mengen van monomeren.

In **Hoofdstuk 3** wordt waterstof/deuterium uitwisseling met massa spectrometrie (HDX-MS) geïntroduceerd als een techniek voor het meten van de beweging van moleculen tussen polymeren. Deze techniek is toegepast op een aantal verschillende moleculen om aan te tonen dat de dynamiek van supramoleculaire polymeren beïnvloed wordt door het mechanisme van zelf-assemblage en de mate van orde in het polymeer. Daarnaast is HDX-MS een waardevolle techniek voor het bevestigen van copolymerisatie en om de dynamiek van de moleculen in de copolymeren te meten.

De technieken geïntroduceerd in het begin van deze thesis worden vervolgens toegepast om de structuur en dynamiek van supramoleculaire polymeren gebaseerd op BTAs te bestuderen. In **Hoofdstuk 4** wordt het effect van stereocentra onderzocht.

Wanneer deuterium atomen worden gebruikt om stereocentra te introduceren blijft de dubbele helix structuur en dynamiek in eerste instantie behouden. Echter neemt de orde in het polymeer toe over tijd wat gepaard gaat met een afname in de pitch van de dubbele helix en een langzamere uitwisseling van moleculen. Methyl groepen als stereocentra resulteren in een enkele keten van moleculen en door het inmengen van dit molecuul kan de heliciteit van andere ketens omgedraaid worden.

In **Hoofdstuk 5** wordt onderzocht of sachariden gebruikt kunnen worden om supramoleculaire polymeren compatibel te maken met water. Wanneer monosachariden de eerder gebruikte tetra(ethyleen glycol) vervangen worden gebundelde supramoleculaire polymeren waargenomen met een snellere dynamiek. Deze observatie kan verklaard worden met computer simulaties die wijzen op de aanwezigheid van vele waterstofbruggen tussen de sachariden. Wanneer de monosachariden echter bevestigd worden aan de tetra(ethyleen glycol) worden er kleine BTA micellen gevormd. Deze BTAs kunnen nog steeds ingemengd worden in een copolymeer zodat hun functionele groepen aanwezig zijn op het polymeer.

Een alternatieve route voor het selectief introduceren van functionele groepen in BTAs wordt gepresenteerd in **Hoofdstuk 6**. Door het gebruik van een commercieel verkrijgbaar asymmetrische startmateriaal worden statistische reacties vermeden en het aantal synthetische stappen beperkt. Hierdoor wordt tevens een van de amides van de BTA omgedraaid, maar dit hindert de vorming van waterstofbruggen in de supramoleculaire polymeren niet. Deze moleculen kunnen met of zonder functionele groep copolymeriseren met traditionele BTAs zonder hun structuur en dynamiek te veranderen zoals onder anderen wordt aangetoond met hoge resolutie microscopie.

In **Hoofdstuk 7** worden BTAs gecombineerd met geladen surfactanten om responsieve materialen te maken. Supramoleculaire polymeren met tetra(ethyleen glycol) ketens worden afgebroken door de geladen surfactanten, maar kunnen opnieuw gevormd worden na verdunning. BTAs met geladen groepen kunnen geen grote assemblages vormen door afstotende ladingen tenzij surfactanten met een tegenovergestelde ladingen worden toegevoegd. Tot slot wordt er een BTA met één hydrofobe zijstaarten en twee hydrofiele, geladen zijstaarten onderzocht. Wanneer zouten worden toegevoegd vormt deze BTA dubbellaagse structuren alsof het een surfactant is, maar deze interacties kunnen uitgezet worden door het toevoegen van een lineaire surfactant zodat supramoleculaire polymeren gevormd worden.

Tot slot worden er in dit proefschrift voorbeelden besproken waarin functie wordt geïntroduceerd in supramoleculaire polymeren gebaseerd op BTAs. In **Hoofdstuk 8** wordt aangetoond dat de supramoleculaire polymeren iets korter en meer dynamisch worden na copolymerisatie met covalent gefunctionaliseerde monomeren. Daarnaast wordt getoond dat supramoleculaire polymeren op basis van BTAs compatibel zijn met de omstandigheden waarin cellen groeien en dat ze gebruikt kunnen worden in een responsieve hydrogel om hun potentie als functionele biomaterialen nogmaals te onderstrepen.

Curriculum Vitae

Sandra Schoenmakers was born on June 15th, 1994 in Goirle, the Netherlands. After completing her secondary education at the Mill-Hill college in Goirle in 2012, she studied Biomedical Engineering at the Eindhoven University of Technology (TU/e). She obtained her bachelor's degree *(with great appreciation)* after a research project in the group of prof. dr. ir. A.R.A. Palmans and prof. dr. E.W. Meijer in which she worked on the introduction of spin labels in supramolecular polymers. She continued with her master's studies in Biomedical Engineering at TU/e, which included a research internship at the Radboud University Nijmegen in the group of dr. ir. P.A. Korevaar and prof. dr. W.T.S. Huck. Her graduation project at TU/e in the research group of prof. dr. ir. A.R.A. Palmans and prof. dr. E.W Meijer focused on the characterization of the dynamics of supramolecular (co)polymers in water. This work was awarded with a prize for the best master thesis of the faculty Biomedical Engineering and was nominated for a prize for the best master thesis at TU/e in 2017. After obtaining her master's degree (*cum laude*) in 2017, she started her PhD work in the laboratory for Macromolecular and Organic Chemistry under the supervision of prof. dr. ir. A.R.A. Palmans and prof. dr. E.W. Meijer. Her research focused on the characterization of the structure and dynamics of supramolecular polymers in water. The most important results are presented in this thesis.

Sandra Schoenmakers werd geboren op 15 juni 1994 in Goirle. Na het afronden van haar Gymnasium opleiding aan het Mill-Hill college in Goirle in 2012 is ze Biomedische Technology gaan studeren aan de Technische Universiteit Eindhoven (TU/e). Ze behaalde haar bachelor diploma *met grote waardering* na een onderzoeksproject in de groep van prof. dr. ir. A.R.A. Palmans en prof. dr. E.W. Meijer waarin ze werkte aan de introductie van spin labels in supramoleculaire polymeren. Vervolgens begon ze aan haar masteropleiding in Biomedische Technology aan de TU/e, inclusief een onderzoeksstage aan de Radboud Universiteit Nijmegen in de groep van dr. ir. P.A. Korevaar en prof. dr. W.T.S. Huck. Haar afstudeerproject aan de TU/e in de onderzoeksgroep van prof. dr. ir. A.R.A. Palmans en prof. dr. E.W. Meijer betrof de karakterisatie van de dynamiek van supramoleculaire (co)polymeren in water. Voor dit werk ontving ze een prijs voor de beste master thesis van de faculteit Biomedische Technology en werd ze genomineerd voor een prijs voor de beste master thesis van de TU/e in 2017. Nadat ze haar master diploma *cum laude* had behaald, startte ze in 2017 met haar promotieonderzoek in de capaciteitsgroep Macromoleculaire en Organische Chemie onder begeleiding van prof. dr. ir. Palmans en prof. dr. E.W. Meijer. Tijdens dit project onderzocht ze de structuur en dynamiek van verschillende supramoleculaire polymeren in water. De belangrijkste resultaten staan beschreven in dit proefschrift.

List of Publications

S.M.C. Schoenmakers, A.J.H. Spiering, A.R.A. Palmans, E.W. Meijer, Amplification of Asymmetry in Supramolecular Polymers: Wait and See, *Manuscript in preparation*

L. Su*, J. Mosquera*, M.F.J. Mabesoone, S.M.C. Schoenmakers, C. Muller, M.E.J. Vleugels, S. Dhiman, A.R.A. Palmans, E.W. Meijer, Dilution-induced gel-sol-gel-sol transitions by competitive supramolecular pathways in water, *Manuscript in preparation*

M.E.J. Vleugels, S. Varela-Aramburu, B.F.M. de Waal, S.M.C. Schoenmakers, B. Maestro, A.R.A. Palmans, J.M. Sanz, E.W. Meijer, Introducing choline and atropine into supramolecular polymers in water: towards antimicrobial activity, *Submitted*

R. Surís-Valls, S.M.C. Schoenmakers, L.G. Milroy, I.K. Voets, Inhibition of ice recrystallization by nanotube-forming cyclic peptides, *Submitted*

S. Varela-Aramburu, L. Su, J. Mosquera, G. Morgese, S.M.C. Schoenmakers, R. Cardineals, A.R.A. Palmans, E.W. Meijer, Introducing hyaluronic acid into supramolecular polymers and hydrogels, *Biomacromolecules*, **2021**, DOI: 10.1021/acs.biomac.1c00927

S.M.C. Schoenmakers*, B.W.L. van den Bersselaar*, S. Dhiman, L. Su, A.R.A. Palmans, Facilitating functionalization of benzene-1,3,5-tricarboxamides by switching amide connectivity, *Org. Biomol. Chem.*, **2021**, 19, 8281-8294

E.M. Timmers, P.M. Fransen, A. González Garciá, S.M.C. Schoenmakers, J.R. Magana, J.W. Peeters, R. Tennebroek, I. van Casteren, R. Tuinier, H.M. Janssen, I.K. Voets, Co-assembly of precision polyurethane ionomers reveals role of and interplay between individual components, *Polymer Chemistry*, **2021**, 12, 2891-2903

L. Gascoigne, J.R. Magana, D.L. Atkins, C.C.M. Sproncken, B. Gumi-Audenis, S.M.C. Schoenmakers, D. Wadeham, E.J. Wanless, I.K. Voets, Fractal-like R5 assembly promote the condensation of silicic acid into silica particles, *J. Colloid Interface Sci.*, **2021**, 598, 206-212

X. Lou*, S.M.C. Schoenmakers*, J.L.J. van Dongen, M. Garcia-Iglesias, N.M. Casellas, M. Fernández-Castaño Romera, R.P. Sijbesma, E.W. Meijer, A.R.A. Palmans, Elucidating dynamic behavior of synthetic supramolecular polymers in water by hydrogen/deuterium exchange mass spectrometry, *J. Pol. Sci*, **2021**, 59 (12), 1151-1161

B.A.G. Lamers, A. Herdlitschka, T. Schnitzer, M.F.J. Mabesoone, S.M.C. Schoenmakers, B.F.M. de Waal, A.R.A. Palmans, H. Wennemers, E.W. Meijer, Oligodimethylsiloxane-Oligoproline Block Co-Oligomers: The Interplay between Aggregation and Phase Segregation in Bulk and Solution, *J. Am. Chem. Soc.*, **2021**, 143 (10), 4032-4042

E.M. Timmers, J.R. Magana, S.M.C. Schoenmakers, P.M. Fransen, H.M. Janssen, I.K. Voets, Sequence of polyurethane ionomers determinative for core structure of surfactant-copolymer complexes, *Int. J. Mol. Sci.*, **2021**, 22 (1), 337

S. Varela-Aramburu*, G. Morgese*, L. Su, S.M.C. Schoenmakers, M. Perrone, L. Leanza, C. Perego, G.M. Pavan, A.R.A. Palmans, E.W. Meijer, Exploring the Potential of Benzene-1,3,5-tricarboxamide Supramolecular Polymers as Biomaterials, *Biomacromolecules*, **2020**, 21 (10), 4105-4115

R.P.M. Lafleur*, S. Herziger*, S.M.C. Schoenmakers, A.D.A. Keizer, J. Jahzerah, B.N.S. Thota, L. Su, P.H.H. Bomans, N.A.J.M Sommerdijk, A.R.A. Palmans, R. Haag, H. Friedrich, C. Böttcher, E.W. Meijer, Supramolecular Double Helices from Small C3-symmetrical Molecules Aggregated in Water, *J. Am. Chem. Soc.*, **2020**, 142 (41), 17644-17652

A. van der Weijden, M. Winkens, S.M.C. Schoenmakers, W.T.S. Huck, P.A. Korevaar, Autonomous mesoscale positioning emerging from myelin filament self-organization and Marangoni flows, *Nat. Commun.,* **2020**, 11, 4800

R.P.M. Lafleur, S.M.C. Schoenmakers, P. Madhikar, D. Bochicchio, B. Baumeier, A.R.A. Palmans, G.M. Pavan, E.W. Meijer, Insights into the kinetics of supramolecular comonomer incorporation in water, *Macromolecules*, **2019**, 52 (8), 3049-3055

S.M.C. Schoenmakers, C.M.A. Leenders, R.P.M. Lafleur, X. Lou, E.W. Meijer, G.M. Pavan, A.R.A. Palmans, Impact of the water-compatible periphery on the dynamic and structural properties of benzene-1,3,5-tricarboxamide based amphiphiles, *Chem. Commun.*, **2018**, 54, 11128-11131

X. Lou*, R.P.M. Lafleur*, C.M.A. Leenders, S.M.C. Schoenmakers, N.M. Matsumoto, M.B. Baker, J.L.J. van Dongen, A.R.A. Palmans, E.W. Meijer, Dynamic diversity of synthetic supramolecular polymers in water as revealed by hydrogen/deuterium exchange, *Nat. Commun.*, **2017**, 8, 15420

* Equal contribution

Acknowledgements/Dankwoord

Met dit proefschrift komt er een einde aan vier mooie en leerzame jaren die voorbij zijn gevlogen. Een proefschrift schrijf je niet alleen en ik wil daarom de mensen bedanken die mij hierbij geholpen hebben.

Ten eerste mijn promotoren. Bert, ik wil je bedanken voor de fijne begeleiding de afgelopen jaren. Met de jaren wordt het alleen maar duidelijker wat voor unieke kansen jij voor ons gecreëerd hebt in deze onderzoeksgroep. Een promotie draait niet alleen om heel veel tijd op het lab doorbrengen, maar ook om persoonlijke ontwikkeling en ik ben dankbaar dat je daar zoveel ruimte voor geeft. Bedankt dat je mijn sterke punten altijd eerder zag dan ikzelf.

Ik had het geluk om niet één, maar twee promotoren te hebben. Anja, bedankt dat je mij als BMT-meisje hebt geaccepteerd binnen de groep. Bij jou kon ik echt altijd binnenlopen voor een vraag, een praatje of als ik een kritische blik nodig had voor mijn (niet zo sexy) TOCs. Bedankt dat je altijd je eerlijke mening gaf en mij met precies de juiste vragen weer de goede kant uit stuurde. Ik heb ook genoten van alle pubquiz-avondjes samen met Bas, Jolanda en Sjef. Hopelijk kunnen we dat snel weer eens doen!

I want to thank my committee members for carefully reading my manuscript and providing valuable feedback. Prof. Besenius, I really enjoyed meeting you at various conferences during my PhD. I have always considered your work as an inspiration and I want to thank you for your enthusiasm about my work. Prof. Pochan, unfortunately you cannot come to Eindhoven but I hope we can meet in person in the future. De colleges en onderzoeksprojecten van prof. Dankers en prof. Sijbesma hebben mij tijdens mijn bachelor en master al geïnspireerd om supramoleculaire polymeren te bestuderen. Bedankt dat jullie nu deel uit willen maken van mijn promotiecommissie. I also want to thank dr. Albertazzi for fruitful discussions during my PhD.

Jolanda en Marle, bedankt dat jullie tijdens mijn verdediging naast mij willen staan als paranimfen. Ik hoop dat er met jullie allebei een vriendschap is ontstaan die ook blijft bestaan na mijn promotie. Jolanda, ik wil jou bedanken voor zo veel meer dan alleen maar het draaiende houden van het lab en het maken van mooie moleculen. De afgelopen vier jaar hebben wij samen heel wat tijd doorgebracht op het lab, achter het kolomapparaat en aan de koffietafel voor een fruit- en theemomentje. Bedankt dat je altijd voor iedereen klaar staat, dat je altijd een luisterend oor hebt, dat je altijd klaar staat met praktische oplossingen en dat je het nooit hebt opgegeven om mij wat synthese kennis bij te brengen. En natuurlijk bedankt voor het lenen van die 10% ACN oplossing. Marle, bedankt dat jij mijn BTA-maatje wilde zijn! Er is niemand in de groep

die zo goed begrijpt wat ik doe als jij en die haar onderzoek met net zo veel precisie uitvoert. Ik heb altijd genoten van onze discussies (die vaak al heel snel van werk naar een persoonlijk onderwerp gingen). Heel veel succes met het afronden van je eigen onderzoek en ik weet zeker dat dat een heel mooi boekje wordt.

Lu, we started around the same time and I had the pleasure to collaborate with you many times. Together with Marle and Shikha we formed the "BTA dream team" and I think this team was so successful thanks to your constant motivation and creativity. Unfortunately, you cannot be here for my defense, but I know how hard you have worked for your new position and I wish you all the best in China. Shikha, I'm still amazed by the speed with which you developed your lipid bilayer setup. Thank you for the nice collaboration on the iBTA project. René, van jou heb ik tijdens mijn master ongelofelijk veel geleerd over BTAs, maar ook aan het begin van mijn PhD hebben we nog samengewerkt aan mijn eerste artikelen. Heel erg leuk dat je nu toch weer bij mijn verdediging kunt zijn. Jesús and Pongphak, I want to thank you for initiating the project with the surfactant-like BTAs and for letting me continue it. I hope you like all the new results. I want to thank all the other members of the 'Supramolecular Chemistry and Polymers in Water' subgroup, Simone, Sjors, Giulia, Silvia, Marle, Jolanda, Laura, Kasper, Tomo, Takuya, Misha, Hailin, Kaho and Huachuan, for the nice and supportive lunchmeetings.

Tijdens mijn PhD heb ik samen mogen werken met een aantal studenten. Als eerste Yvonne; heel erg knap hoeveel analysetechnieken jij hebt geleerd tijdens je BEP. Jolanda en ik denken soms nog steeds dat kolommen beter gaat als jij erbij bent. Laura, door jouw motivatie hebben we nu een goede basis voor onze geladen BTAs. Met jouw enthousiasme moet het helemaal goedkomen met je eigen PhD. Gilian, jij hebt aan een zeer uitdagend onderwerp gewerkt, maar het heeft uiteindelijk toch een plekje in mijn thesis gekregen. Bedankt dat je nog iets langer wilde blijven om een extra molecuul te maken. Koen, bedankt voor al je droge humor. Ik weet dat je intussen iets heel anders doet, maar ik hoop dat je toch positief terugkijkt op je tijd in het lab. Bart, stiekem was ik best wel blij dat je je moleculen niet binnen een maand af had, want ik vond het veel te gezellig om samen te werken. Bedankt voor alle keren dat je bij mij "advies" kwam vragen over je synthese (we weten allebei dat dat meer voor de gezelligheid was) en dat je ook tijdens je PhD nog zo veel tijd in het iBTA project hebt gestopt zodat we het toch maar mooi hebben kunnen publiceren. En tot slot Stefan, wat was jij gedreven om elk detail van je molecuul uit te zoeken! Ik wens je heel veel succes met het afronden van je studie. Ik hoop dat jullie allemaal net zo veel van mij hebben geleerd als ik van jullie.

I also had the pleasure to be involved in many collaborations outside of our own group. Lou, thank you for your constant enthusiasm about HDX-MS. I know how long

those measurements can take but you keep promoting the technique and keep testing new molecules. Miguel, Nicolas and Marcos, thank you for sending your molecules to Eindhoven, it really helped to illustrate the usefulness of HDX-MS. I'm very grateful that I was able to travel to Berlin a few times to learn more about cryoTEM and image analysis from Svenja Herziger and Christoph Böttcher. Thanks to you we finally found the prove for the double helix structure. I also want to thank prof. Giovanni Pavan and his group for all the simulations of the BTA fibers. Henk, Michel en Ilja, bedankt voor de vlotte samenwerking voor de verschillende cryoTEM plaatjes.

SMO zou niets zijn zonder alle mensen die er achter de schermen voor zorgen dat alles op rolletjes loopt. Martina, Carla, Margot, de coronatijd heeft echt laten zien hoe verloren wij zijn zonder jullie organisatorische vaardigheden. Ik ben blij dat jullie weer gezellig in Helix zijn. Bas, Hans en Marcel, bedankt dat jullie samen met Jolanda de labs draaiende houden. Uiteraard gaat mijn dank uit naar Ralf, Lou en Joost voor het onderhoud van het analytische lab, maar vooral naar Joost voor het ontstoppen van de Q-TOF. Net zo belangrijk voor dit onderzoek waren Rick, Paul en Anne; bedankt dat jullie zo veel tijd nemen om jullie kennis over (cryo)TEM te delen en dat jullie altijd klaar staan om problemen op te lossen (zelfs als dat erg vroeg in de ochtend is).

Ik wil een aantal collega's in het bijzonder bedanken voor de onvergetelijke tijd de afgelopen vier jaar. Bas, jij bent waarschijnlijk in alles mijn tegenpool, maar toch was je vijf jaar lang mijn maatje binnen SMO. Bedankt voor alle kopjes thee, chocola en opbeurende knuffels de afgelopen jaren. Niet schrikken als ik af en toe een etentje in je agenda zet. Martin, bedankt dat je me altijd aan het lachen maakt, ook op de meest ongemakkelijke momenten. Annelore, jij bent met gemak de meest kleurrijke persoon binnen SMO! Een gesprek met jou gaat altijd gepaard met een grote lach en weet ieders dag weer op te fleuren. Tijdens mijn PhD heb ik heel wat kopjes thee mogen drinken aan de koffietafel met de SyMO-Chem-mannen, Michel, Joris en Maarten, natuurlijk onder leiding van Henk. Bedankt voor de diverse gesprekken en alle koekjes. Het was niet alleen gezellig aan de koffietafel, maar zeker ook op kantoor. Ghislaine, Chidambar and Lafayette, you were my officemates at the start of my PhD. I definitely learned a lot from all of your different personalities. Eveline, jij was mijn kantoorgenoot tijdens de coronatijd en wat was dat een feestje! We hebben heel wat afgelachen in ons kantoortje achter het lab. Als we straks allemaal ergens anders gaan werken moeten we onze lunchafspraken misschien maar omzetten in dinerafspraken. Kasper, ik kwam misschien niet zo heel enthousiast over toen je de eerste keer binnenkwam, maar dat was ik zeker wel! Als we begonnen met kletsen kwamen de meest uiteenlopende onderwerpen voorbij en waren we al snel een uur verder. Bedankt voor al je steun tijdens het schrijven. Ik ben trots op je dat je de moeilijke beslissing hebt genomen om te stoppen met je PhD en ik wens je heel veel geluk toe met je volgende stap. Giulia, Kaho and Huachuan, we only shared an office for the last few months, but I really enjoy

our chats. Enjoy your stay in the group! Christiaan, Freek, Joost, Marco, Stef, Fabian, Hao, Tobias, Linlin, Anjana, Ramkrishna, Stefan, Julian, Nate, Gijs, Andreas, Elisabeth, Brigitte, Mathijs, Marcin, Beatrice, Hailong, Katja, Diederik, Patricia, Jie, Soumabrata, Huiyi, Paul, Muhabbat and Maaike; Unfortunately, I do not have the space here to thank you all personally, but I am very happy that I met all of you and I want to thank you for helping me with eating all of my homemade cakes. Uiteraard gaat er ook een bedankje naar alle studenten voor het voorzetten van wat misschien wel mijn beste uitvinding ooit is: maandag bakdag. Bedankt voor alle keren dat ik nog mee mocht proeven!

Ik will ook graag alle vrienden van buiten het lab bedanken voor de nodige afleiding. Pascal, Saskia, Nick, Melanie, Marjolein, Koert, Iris, Tom, Nimke, Sanne en Mathijs; bedankt voor alle maandelijkse spelletjesavonden waarbij we vaak zoveel kletste dat er geen tijd meer was voor spelletjes. Iedereen is bezig met zijn eigen avontuur, maar ik hoop dat dat ons er niet van weerhoudt om regelmatig samen te komen. Een speciaal bedankje gaat uit naar Saskia, Melanie en Marjolein. Bedankt voor alle ontspannende kopjes thee waarbij we helemaal onszelf konden zijn!

Tot slot wil ik graag mijn familie bedanken voor hun onvoorwaardelijke steun en interesse. Papa en mama, bedankt dat jullie altijd voor mij klaar staan. Ik ben blij dat jullie deur nog steeds wagenwijd open staat voor mij, al is het maar om even met Happy te komen knuffelen. Remco en Jessica, bedankt voor alle afleiding en dat jullie altijd blijven proberen om te begrijpen wat ik nu eigenlijk doe. Zonder al jullie steun en vertrouwen was me dit allemaal niet gelukt. En tot slot Tobias en Jip: ook al doen jullie er geen moeite voor, jullie kunnen mij altijd opvrolijken. Ik ben er trots op dat ik jullie tante mag zijn.

Liefs,
Sandra